



The University of
Nottingham

UNITED KINGDOM • CHINA • MALAYSIA

Influence of Microstructure on Cavitation Erosion Resistance of Laser-surface-melted Ni-WC Composites

Rui Yang

Thesis submitted for the degree of Doctor of Philosophy

Department of Mechanical, Materials and Manufacturing Engineering,

Faculty of Science and Engineering,

University of Nottingham Ningbo China

April 2023

Preface

This thesis is submitted to the University of Nottingham Ningbo China (UNNC) for the degree of Doctor of Philosophy. The examined copy is also submitted to the Ningbo Institute of Materials Technology and Engineering (NIMTE), Chinese Academy of Sciences (CAS) for the completion of the UNNC-NIMTE Doctoral Training Partnership (DTP) programme (Dec. 2018 entry).

The research project was carried out under the supervision of Dr. Hao Chen (Mechanical, Materials and Manufacturing Engineering, Faculty of Science and Engineering, UNNC) and Prof. Hua Li (Advanced Coatings and Additive Manufacturing Research Group, NIMTE, CAS).

Related publications and patent:

R. Yang, N. Huang, Y. Tian, J. Qing, P. Lu, H. Chen, H. Li, and X. Chen. Insights into the cavitation erosion behaviour of laser surface melted Ni-WC composites: The effects of WC morphology and distribution, *Surf. Coat. Technol.* 444 (2022) 128685.

Y. Tian, **R. Yang**, Z. Gu, H. Zhao, X. Wu, S. T. Dehaghani, H. Chen, X. Liu, T. Xiao, A. McDonald, H. Li, and X. Chen. Ultrahigh cavitation erosion resistant metal-matrix composites with biomimetic hierarchical structure, *Compos. B. Eng.* 234 (2022) 109730.

R. Yang, Y. Tian, N. Huang, P. Lu, H. Chen, H. Li, and X. Chen. Effects of CeO₂ addition on microstructure and cavitation erosion resistance of laser-processed Ni-WC composites, *Mater. Lett.* 311 (2022) 131583.

X. Chen, **R. Yang**, Y. Tian, N. Huang, J. Huang, X. Liu, B. Zhang, P. Zhou, Y. Dan, S. Wu, X. Feng, and H. Li. Cavitation-corrosion-resistant metal-ceramic matrix composite material and preparation method, State Intellectual Property Office of P.R.China, authorisation of CN114214555A.

Acknowledgement

I would like to express my sincerest gratitude to my supervisors, Dr. Hao Chen and Prof. Hua Li, for their invaluable guidance and constant support over the past four years. I also would like to thank Dr. Xiuyong Chen for his great assistance on my research projects. I also wish to thank my internal assessor, Prof. Xiaogang Yang, and external assessor, Prof. Xiaofeng Zhao, for their constructive and positive feedback on this work. My thanks also to Prof. André McDonald and Dr. Shahed Taghian Dehaghani at the University of Alberta for their assistance in cold spraying and revising my papers. Lastly, I will remain forever thankful to UNNC and NIMTE for providing this DTP programme.

I also would like to extend my gratitude to the many professional technical staff that I have had the pleasure of working with during this fruitful journey. They are Ms. Rongrong Jiang, Ms. Yirong Yao, Dr. Haichen Wu, Dr. Zihou Li, Mr. Mingxin Hao, Ms. Mingzhu Zhang, Mr. Gongjun Zhang, Mr. Zhe Sang, Ms. Xiaoxue Shui, Mr. Jiacheng Liu, Ms. Chunting Wang at NIMTE, and Mr. Weiqiang Zhu at UNNC. I thank them for their knowledge and assistance in material characterisations, mechanical tests, and sample preparations.

My sincerest thanks to my colleagues in the Advanced Coatings and Additive Manufacturing Research Group for their unfailing support and friendship. My special thanks to Mr. Ye Tian, a team player and loyal friend, who helped me unreservedly during my research projects as well as during this phase of life. My special thanks also to Dr. Yaoyao Fu and Ms. Haijun Zhang for their inspiring mentorship in the first two years.

I remain forever thankful to my parents, whose lasting faith and unconditional love have supported me to become the budding academic I am today.

Finally, my deepest love and apologies to my wife, Yu Liu. I started my PhD study on the day we registered our marriage. Since then, we have lived in two cities and rarely seen each other, which we never experienced in the past six years we spent together. I appreciate and repent for the tremendous sacrifice she made to support my PhD study. The depth of the stress and loneliness she endured due to my absence and my immersion in my study is still beyond my imagination, but she never failed to encourage me during my moments of doubt and frustration. I hope what I am to accomplish is worthy of everything she did for me, and I wish, now that this study has concluded, we will never be apart again.

List of abbreviations

A/N	Amorphous/nanocrystalline
ASS	Austenitic stainless steel
BCC	Body-centred cubic
BSE	Backscattered electron
CE	Cavitation erosion
CER	Cavitation erosion resistance
DSS	Duplex stainless steel
E	Elastic modulus
EIT	Indentation modulus (by nanoindentation test)
EBSD	Electron backscattered diffraction
EDX	Energy dispersive X-ray spectroscopy
FCC	Face-centred cubic
HAADF	High-angle annular dark field
FESEM	Field-emission scanning electron microscope
H	Hardness
HIT	Indentation hardness (by nanoindentation test)
HCP	Hexagonal close-packed
HDPE	High-density polyethylene
HRTEM	High-resolution transmission electron microscope/microscopy
HVAF	High-velocity air-fuel (spraying)
HVOF	High-velocity oxygen-fuel (spraying)
IPF	Inverse pole figure
LSM	Laser surface melting; Laser-surface-melted
MDE	Mean depth of erosion
MDER	Mean depth of erosion rate
MMC	Metal matrix composite
MSS	Martensitic stainless steel
NAB	Nickel-aluminium-bronze
ORH	Orthorhombic
SAED	Selected area electron diffraction
SE	Secondary electron
SEM	Scanning electron microscope/microscopy
SFE	Stacking-fault energy
SS	Stainless steel
STEM	Scanning transmission electron microscope/microscopy
TEM	Transmission electron microscope/microscopy
VHS	Vacuum hot-pressing sintering
XRD	X-ray diffraction/diffractometry
YSZ	Yttria-stabilised zirconia

Abstract

Cavitation erosion (CE) is a type of wear that frequently occurs to the components operating in a fluid, such as propeller, rudder, impeller, pump, and pipeline. Failures caused by CE can result in significant economic losses in civil fields and can also pose a risk to national security in other sensitive fields, such as nuclear engineering and coastal defence.

Therefore, research into materials with effective cavitation erosion resistance (CER) has become imperative. Over the past two decades, WC-based cermet composites have been extensively utilised for resisting CE. However, further improvements in CER are still necessary. Many studies have focused on enhancing mechanical properties to achieve effective CER, but these studies have unintentionally neglected the effect of microstructure on CER.

In this study, cold-sprayed Ni-WC metal matrix composites (MMCs) were post-treated by laser surface melting (LSM), resulting in excellent CER compared to other common engineering materials such as WC-based cermet composites and 316L stainless steel. Scanning electron microscopy (SEM) images revealed that the LSM cold-sprayed Ni-WC MMCs had a hypoeutectic microstructure, where the eutectic Ni-WC network divided the primary Ni grain into many cells. Examination of post-mortem samples indicated that the eutectic Ni-WC network could restrict microcrack growth within the cells, providing a damage-control effect. Additionally, the experimental results suggested that mechanical properties may not be a reliable predictor of CER.

The excellent CER of the LSM Ni-WC MMCs warranted further exploration and optimisation. The microstructural evolution of the LSM sintered Ni-WC MMCs was investigated by taking a series of SEM images from the same positions after different CE test intervals. The results demonstrated

that the eutectic Ni-WC network was effective in constraining CE. Numerical simulation results also indicated that the hierarchically layered WC lamellae in the eutectic Ni-WC region could mitigate cavitation impacts. Hence, the exceptional CER of the LSM Ni-WC MMCs was attributed to the altered microstructure.

To optimise the LSM Ni-WC MMCs and further enhance CER, CeO₂ and Cr were introduced in this study. The LSM Ni-WC-CeO₂ MMCs exhibited refined Ni grains and significantly higher microhardness than the LSM Ni-WC MMCs, and the distribution and morphology of the WC lamellae were also altered. However, the addition of CeO₂ did not guarantee an increase in CER. SEM observations suggested that the microstructure played a dominant role in determining CER, and only MMCs with a continuous eutectic Ni-WC network and hierarchically interlocked WC lamellae exhibited the best CER. Numerical simulation results also indicated that the morphology and distribution of the WC lamellae could influence the stress and energy in the material when subjected to cavitation impacts.

For the LSM NiCr-WC MMCs, they exhibited either a hypoeutectic structure similar to the LSM Ni-WC MMCs or a fully eutectic structure depending on the Cr content. Meanwhile, the addition of Cr significantly enhanced the CER. The LSM NiCr-WC MMCs showed 10-h CE that was only 10-20% that of the LSM Ni-WC MMCs. SEM observations indicated that a lamellar eutectic with finely and densely distributed carbide lamellae may be the most optimal microstructure for resisting CE among the ones presented in this study.

Contents

Preface.....	I
Acknowledgement.....	II
List of abbreviations	III
Abstract.....	IV
Contents.....	VI
List of figures.....	X
List of tables	XV
Chapter 1 Introduction.....	1
1.1 Background	1
1.2 Aims and objectives	5
1.3 Scope of the thesis.....	6
Chapter 2 Literature review	9
2.1 Introduction	9
2.2 Cavitation and cavitation erosion	9
2.2.1 Cavitation	9
2.2.2 Cavitation erosion	14
2.3 Evaluating cavitation erosion performance	19
2.3.1 Standard test method for cavitation erosion using vibratory apparatus.....	19
2.3.2 Mean depth of erosion and stages of cavitation erosion	26
2.4 Cavitation-erosion-resistant alloys	32
2.4.1 Stainless steels	33
2.4.2 Nickel-aluminium-bronzes.....	37
2.5 Cavitation-erosion-resistant coatings	42
2.5.1 Coating techniques	42
2.5.2 Inorganic coatings based on commercially available alloys ..	48
2.5.3 WC-based cermet coatings.....	52
2.5.4 Fe-based amorphous/nanocrystalline coatings.....	62
2.5.5 Other ceramic/cermet coatings	65
2.6 Improving cavitation erosion resistance	66
2.7 Summary of the literature review.....	71
2.7.1 Strategies for achieving good cavitation erosion resistance..	71
2.7.2 Research gaps.....	72
2.7.3 Selection of materials and processing methods.....	74
Chapter 3 Materials and experimental methods	76
3.1 Materials	76
3.2 Cold spraying	77
3.3 Vacuum hot-pressing sintering (VHS)	78
3.4 Laser surface melting	79
3.5 Characterisations and tests.....	81

3.5.1	<i>Sample preparation</i>	81
3.5.2	<i>X-ray diffraction (XRD)</i>	82
3.5.3	<i>Scanning electron microscopy (SEM)</i>	82
3.5.4	<i>Electron backscattered diffraction (EBSD)</i>	83
3.5.5	<i>Transmission electron microscopy (TEM)</i>	84
3.5.6	<i>Microhardness and nanoindentation tests</i>	84
3.6	Evaluation of cavitation erosion performance.....	86
3.6.1	<i>Cavitation erosion test</i>	86
3.6.2	<i>Surface profile</i>	88
3.6.3	<i>Scanning electron microscopy observation at the same site</i>	88
Chapter 4 Cavitation erosion of LSM cold-sprayed Ni-WC coating		89
4.1	Introduction	89
4.2	Characterisation of the cold-sprayed Ni-WC coating.....	91
4.3	Microstructure characterisation of the LSM cold-sprayed Ni-WC coatings.....	93
4.3.1	<i>XRD results</i>	93
4.3.2	<i>SEM results</i>	94
4.3.3	<i>EBSD results and grain size</i>	98
4.3.4	<i>TEM results</i>	101
4.4	Mechanical properties	103
4.4.1	<i>Microhardness results</i>	103
4.4.2	<i>Nanoindentation results</i>	105
4.5	Cavitation erosion performance	107
4.5.1	<i>Cavitation erosion and erosion rate</i>	107
4.5.2	<i>SEM characterisation of the eroded samples</i>	110
4.5.3	<i>Profilometry of the eroded samples</i>	111
4.6	Discussion.....	113
4.6.1	<i>Effects of LSM on cold-sprayed Ni-WC coating</i>	113
4.6.2	<i>Possible reasons for the formation of lamellar WC</i>	114
4.6.3	<i>Mechanical properties and cavitation erosion resistance</i>	115
4.6.4	<i>Microstructure and cavitation erosion resistance</i>	116
4.6.5	<i>Defects and cavitation erosion resistance</i>	119
4.6.6	<i>Cavitation erosion and fatigue failure</i>	120
4.7	Summary.....	123
Chapter 5 Cavitation erosion of sintered Ni-WC MMCs treated by LSM		125
5.1	Introduction	125
5.2	Characterisation of sintered Ni-WC	126
5.3	Characterisation of LSM sintered Ni-WC	127
5.3.1	<i>XRD results</i>	127
5.3.2	<i>SEM results</i>	128
5.3.3	<i>EBSD results and grain size</i>	132

5.3.4 Microhardness	132
5.4 Cavitation erosion and erosion rate.....	133
5.5 SEM observation of the samples exposed to cavitation erosion at different test intervals	134
5.5.1 Ni matrix and Ni-WC eutectic in Ni-WC hypoeutectic.....	134
5.5.2 Other microstructural features.....	137
5.6 Numerical simulation	140
5.6.1 Model establishment	140
5.6.2 Simulation results.....	142
5.7 Discussion.....	146
5.7.1 Sintering as an alternative to spraying for pre-deposition ...	146
5.7.2 Effect of eutectic Ni-WC on cavitation erosion resistance ...	147
5.7.3 Behaviour of primary Ni phase in response to cavitation ...	149
5.7.4 Defects and cavitation erosion resistance	149
5.8 Summary.....	151
Chapter 6 Effects of CeO₂ addition on cavitation erosion of LSM Ni- WC-CeO₂ MMCs.....	152
6.1 Introduction	152
6.2 Sample information	153
6.3 Characterisation of the sintered Ni-WC-CeO ₂	154
6.4 Characterisation of LSM sintered Ni-WC-CeO ₂	155
6.4.1 XRD results.....	155
6.4.2 SEM results.....	156
6.4.3 EBSD results.....	159
6.4.4 Grain size and microhardness	161
6.5 Cavitation erosion and erosion rate.....	163
6.6 SEM observation of the samples exposed to cavitation erosion at different test intervals	165
6.6.1 Specimens with 0.9wt.% CeO ₂	165
6.6.2 Specimens with 1.8wt.% CeO ₂	166
6.6.3 Specimens with 2.7wt.% CeO ₂	167
6.7 Numerical simulation	170
6.7.1 Model establishment	170
6.7.2 Simulation results.....	171
6.8 Discussion.....	175
6.8.1 Effect of CeO ₂ addition on the microstructure of LSM Ni-WC MMCs	175
6.8.2 Microstructure and cavitation erosion resistance	177
6.9 Summary.....	181
Chapter 7 Effects of Cr addition on cavitation erosion of LSM NiCr- WC MMCs	183
7.1 Introduction	183

7.2 Sample information	184
7.3 Characterisation of the sintered Ni-WC-Cr	185
7.4 Characterisation of LSM NiCr-WC	186
7.4.1 SEM results.....	186
7.4.2 SEM-EDX results	191
7.4.3 EBSD results.....	192
7.5 Cavitation erosion	194
7.6 SEM observation of the samples exposed to cavitation erosion at different test intervals	195
7.6.1 Specimens with 10 vol.% Cr	195
7.6.2 Specimens with 20 vol.% Cr	196
7.6.3 Specimens with 30 vol.% Cr	198
7.6.4 Other microstructural features.....	198
7.6.5 Large pre-existing cracks	199
7.7 Discussion.....	201
7.7.1 Effect of Cr addition on the microstructure of LSM NiCr-WC MMCs	201
7.7.2 Microstructure and cavitation erosion resistance	203
7.7.3 Ideal microstructure for resisting cavitation erosion	204
7.8 Summary.....	206
Chapter 8 Conclusions	208
Chapter 9 Future work	212
References.....	215
Appendix A – Excerpt of the product specification sheet of Belzona®- 2141	248
Appendix B – Physical properties of the materials in this thesis	249
Appendix C – The CS-400 sample processed by focused ion beam ..	249
Appendix D – Cavitation erosion test on abalone shells	250
Appendix E – Ni-20/30vol.%Cr-WC MMCs treated by a 500-W laser .	251
Appendix F – Benchmarking the LSM MMCs against some engineering materials	252

List of figures

Fig. 2.1 – Schematic phase diagram of water.	10
Fig. 2.2 – A trail of cavities behind a spinning propeller [36].	11
Fig. 2.3 – Schematic of the lifetime of a cavitation bubble.	11
Fig. 2.4 – The relationship of the flow velocity and the distance to the blade surface of a spinning propeller.	12
Fig. 2.5 – Cavitation erosion on different components.	15
Fig. 2.6 – Major types of hydrodynamic cavitation [52].	16
Fig. 2.7 – Various types of cavitation occurring on a propeller [53].	16
Fig. 2.8 – Photos of cavitation on a propeller [54].	17
Fig. 2.9 – Photos and schematics of sheet and cloud cavitation on a hydrofoil.	18
Fig. 2.10 – Schematic of ultrasonic vibratory cavitation erosion apparatus [71].	20
Fig. 2.11 – Important parameters for ASTM G32 [71].	20
Fig. 2.12 – Schematic of direct and indirect vibratory cavitation erosion tests.	22
Fig. 2.13 – Plots of the cumulative erosion-time curve and the erosion rate-time curve [71].	28
Fig. 2.14 – Microstructure and cavitation erosion of 13Cr4Ni stainless steel.	33
Fig. 2.15 – SEM images and XRD patterns of 304 and 316L austenitic stainless steels after cavitation erosion [80, 103].	35
Fig. 2.16 – Microstructure and cavitation erosion behaviour of duplex stainless steel [114].	36
Fig. 2.17 – SEM image and schematic of nickel-aluminium-bronze [123, 125].	38
Fig. 2.18 – Cavitation erosion behaviour of nickel-aluminium-bronze [64, 135].	40
Fig. 2.19 – Schematic of an HVOF spraying gun [142].	44
Fig. 2.20 – Schematic of a cold spraying gun [143].	45
Fig. 2.21 – Schematic of various laser surface modification techniques [145].	46
Fig. 2.22 – Schematic of laser surface melting process.	47
Fig. 2.23 – Schematic of a vacuum hot-pressing sintering device	48
Fig. 2.24 – The weld overlay of CaviTec and the HVOF-sprayed CaviTec coating subjected to cavitation erosion [157, 159].	49
Fig. 2.25 – The weld overlays of two Stellite alloys subjected to cavitation erosion [164, 165].	50
Fig. 2.26 – HVOF-sprayed WC-CoCr coatings subjected to cavitation erosion [193, 194, 202].	55

Fig. 2.27 – HVOF-sprayed and post-melted WC-CoNiCr coatings subjected to cavitation erosion [201].	57
Fig. 2.28 – WC-CoCr coatings deposited by HVOF spraying using gas and liquid fuels subjected to cavitation erosion [194].	58
Fig. 2.29 – HVOF-sprayed WC-CoCr coatings with different WC size distributions subjected to cavitation erosion [203].	59
Fig. 2.30 – HVOF-sprayed WC-CoCr and WC-Ni coatings subjected to cavitation erosion [200].	60
Fig. 2.31 – HVOF-sprayed Fe-based A/N coating subjected to cavitation erosion [232].	63
Fig. 2.32 – Microstructure and cavitation erosion behaviour of NiTi alloys with and without heat-treatment [261].	67
Fig. 2.33 – Microstructure and cavitation erosion behaviour of nickel-aluminium-bronzes post-treated by different method [139].	68
Fig. 2.34 – Microstructural evolution of pure copper and aluminium-bronze exposed to cavitation for different durations [267].	69
Fig. 3.1 – Temperature control of the furnace for the sintered Ni-WC(-CeO ₂).	79
Fig. 3.2 – Schematic showing the laser surface melting process in this work.	80
Fig. 3.3 – The indentation sites for the hardness and the nanoindentation tests	85
Fig. 3.4 – A photograph of the vibratory cavitation erosion apparatus used in this research.	87
Fig. 4.1 – SEM images showing the cross-section of the cold-sprayed Ni-WC coating on the 316L ASS substrate.	91
Fig. 4.2 – XRD spectrum of the cold-sprayed Ni-WC coating.	92
Fig. 4.3 – EBSD mapping of the cold-sprayed Ni-WC coating.	92
Fig. 4.4 – XRD spectra of the cold-sprayed and the LSM Ni-WC coatings.	93
Fig. 4.5 – SEM images showing the cross-sections of the LSM Ni-WC coatings treated by different laser powers.	95
Fig. 4.6 – SEM images showing the etched surfaces of the as-LSM Ni-WC coatings.	96
Fig. 4.7 – EBSD results of the cross-section of the LSM Ni-WC coatings.	99
Fig. 4.8 – Grain size of the cold-sprayed and the LSM samples.	100
Fig. 4.9 – EBSD results of the surface of the LSM Ni-WC coatings.	100
Fig. 4.10 – STEM characterisation of the CS-400 sample and the corresponding TEM-EDX results.	101
Fig. 4.11 – HRTEM images and SAED patterns of the CS-400 sample.	102

Fig. 4.12 – Microhardness of 316L ASS, cold-sprayed coating, and LSM coatings.....	103
Fig. 4.13 – SEM images of the indented cross-section of the cold-sprayed and the LSM coatings subjected to the microhardness test. .	104
Fig. 4.14 – Nanoindentation results of the 316L ASS, the cold-sprayed coating, and the LSM coatings.....	105
Fig. 4.15 – SEM images of the indented cross-section of the cold-sprayed and the LSM coatings subjected to the nanoindentation test.	107
Fig. 4.16 – Cavitation erosion results of the 316L ASS, the cold-sprayed coating, and the LSM coatings.....	108
Fig. 4.17 – Erosion and the average erosion rate of the 316L ASS, the cold-sprayed coating, and the LSM coatings.	108
Fig. 4.18 – SEM images showing the surface of the cold-sprayed and the LSM samples after the exposure to cavitation for 10 h.	109
Fig. 4.19 – SEM images showing the cross-section near the surface of the cold-sprayed and the LSM samples after the exposure to cavitation for 10 h.....	110
Fig. 4.20 – Surface and linear profiles of the cold-sprayed and the LSM samples after the exposure to cavitation for 10 h.....	112
Fig. 4.21 – The depth distribution of the craters/pits of the cold-sprayed and the LSM samples after the exposure to cavitation for 10 h.	113
Fig. 4.22 – SEM images of the cast Ni-WC ingot before and after laser surface melted by 400 W laser.....	115
Fig. 5.1 – SEM images of the cross-section of the sintered Ni-WC MMC.	126
Fig. 5.2 – XRD spectrum of the sintered Ni-WC MMC.	127
Fig. 5.3 – XRD spectra of the LSM sintered Ni-WC MMC.....	128
Fig. 5.4 – SEM images showing the cross-sections of the LSM Ni-WC MMCs treated by different laser powers.....	129
Fig. 5.5 – EBSD results of the cross-section of the LSM Ni-WC MMCs.	131
Fig. 5.6 – Grain size of the LSM sintered MMCs.....	132
Fig. 5.7 – Microhardness of the LSM sintered MMCs.	133
Fig. 5.8 – Cavitation erosion results of the LSM sintered MMCs.....	134
Fig. 5.9 – Total erosion and the average erosion rate of the LSM sintered MMCs.....	134
Fig. 5.10 – Microstructural evolution of hypoeutectic Ni-WC in S0-300 sample during cavitation erosion.....	136
Fig. 5.11 – Microstructural evolution of hypoeutectic Ni-WC in S0-400 sample during cavitation erosion.....	136
Fig. 5.12 – Microstructural evolution of hypoeutectic Ni-WC in S0-500 sample during cavitation erosion.....	137

Fig. 5.13 – Microstructural evolution of a WC-free region in S0-300 sample during cavitation erosion.....	138
Fig. 5.14 – Microstructural evolution of pre-existing pores in S0-300 sample during cavitation erosion.....	139
Fig. 5.15 – Microstructural evolution of granular WC grains in S0-300 sample during cavitation erosion.....	140
Fig. 5.16 – Numerical models of pure Ni and Ni-WC structures and STEM image of Ni-WC structure.	141
Fig. 5.17 – Impact applied during numerical simulation.	141
Fig. 5.18 – Stress evolution of the pure Ni and the Ni-WC structures .	143
Fig. 5.19 – Stress and kinetic energy of the pure Ni structure and the Ni-WC structure.	144
Fig. 5.20 – Element failure of the pure Ni and the Ni-WC structures...	145
Fig. 6.1 – SEM images of the cross-section of the sintered Ni-WC-(CeO ₂) MMCs.....	154
Fig. 6.2 – XRD spectra of the sintered Ni-WC-CeO ₂ MMCs.....	155
Fig. 6.3 – XRD spectra of the LSM sintered Ni-WC MMC.....	155
Fig. 6.4 – Cross-sections of the LSM Ni-WC-1.8wt.%CeO ₂ MMCs treated by different laser powers.	156
Fig. 6.5 – Cross-sections of the LSM Ni-WC-1.8wt.%CeO ₂ MMCs treated by different laser powers.	157
Fig. 6.6 – Cross-sections of the LSM Ni-WC-2.7wt.%CeO ₂ MMCs treated by different laser powers.	158
Fig. 6.7 – EBSD results of the cross-section of the LSM Ni-WC-CeO ₂ MMCs.....	160
Fig. 6.8 – Ni grain size and microhardness of the LSM Ni-WC-CeO ₂ MMCs.....	161
Fig. 6.9 – Erosion of the LSM Ni-WC-CeO ₂ MMCs after 10-hour cavitation erosion test.	163
Fig. 6.10 – Erosion rate of the LSM Ni-WC-CeO ₂ MMCs in terms of MDER.	164
Fig. 6.11 – Cavitation erosion rate of the LSM Ni-WC-CeO ₂ MMCs....	164
Fig. 6.12 – Microstructural evolution of the LSM MMCs with 0.9 wt.% CeO ₂ during cavitation erosion.....	165
Fig. 6.13 – Microstructural evolution of the LSM MMCs with 1.8 wt.% CeO ₂ during cavitation erosion.....	167
Fig. 6.14 – Microstructural evolution of the LSM MMCs with 2.7 wt.% CeO ₂ treated by a laser of 300 W during cavitation erosion.....	168
Fig. 6.15 – Microstructural evolution of the LSM MMCs with 2.7 wt.% CeO ₂ treated by a laser of 400 W during cavitation erosion.....	168
Fig. 6.16 – Microstructural evolution of the LSM MMCs with 2.7 wt.% CeO ₂ treated by a laser of 500 W during cavitation erosion.....	169

Fig. 6.17 – Numerical models of the pure Ni structure and the Ni-WC structures with different dimensions and distributions of WC lamellae.	171
Fig. 6.18 – Stress evolution of the pure Ni structure and the Ni-WC structures with different dimensions and distributions of WC lamellae.	172
Fig. 6.19 – Stress and kinetic energy of the pure Ni structure and the Ni-WC structures with different dimensions and distributions of WC lamellae.	173
Fig. 7.1 – SEM images of the cross-section of the sintered NiCr-WC MMCs.	185
Fig. 7.2 – SEM images showing the cross-sections of the LSM NiCr-WC MMCs (with 10 vol.% of Cr) treated by different laser powers.	186
Fig. 7.3 – SEM images showing the cross-sections of the LSM NiCr-WC MMCs (with 20 vol.% of Cr) treated by different laser powers.	187
Fig. 7.4 – SEM images showing the cross-sections of the LSM NiCr-WC MMCs (with 30 vol.% of Cr) treated by different laser powers.	188
Fig. 7.5 – SEM image showing the large cracks and microcracks on the surface of LSM NiCr-WC MMCs with 20 and 30 vol.% of Cr treated by 400-W laser.	189
Fig. 7.6 – Cross-sectional SEM image showing the cracks in the LSM NiCr-WC MMCs with 20 and 30 vol.% of Cr.	190
Fig. 7.7 – SEM-EDX results of various microstructure features in the LSM NiCr-WC MMCs.	191
Fig. 7.8 – EBSD results of various microstructure features in the LSM NiCr-WC MMCs.	193
Fig. 7.9 – Erosion of LSM NiCr-WC MMCs after 10-hour cavitation erosion test.	194
Fig. 7.10 – Microstructural evolution of the LSM MMCs with 10 vol.% Cr during cavitation erosion.	195
Fig. 7.11 – Microstructural evolution of the LSM MMCs with 20 vol.% Cr during cavitation erosion.	196
Fig. 7.12 – Microstructural evolution of the LSM MMCs with 30 vol.% Cr during cavitation erosion.	197
Fig. 7.13 – Microstructural evolution of the other interested features in the LSM NiCr-WC MMCs during cavitation erosion.	199
Fig. 7.14 – Microstructural evolution of the crack crossing the edge of the molten pool in the LSM NiCr-WC MMC during cavitation erosion.	200
Fig. 7.15 – Microstructural evolution of the crack crossing the eutectic matrix in the LSM NiCr-WC MMC during cavitation erosion.	200

List of tables

Table 2.1 – Comparison of the direct and the indirect cavitation approaches.	23
Table 3.1 – Feedstocks for cold spraying and sintering.....	76
Table 3.2 – Spraying parameters for depositing Ni-WC coating.....	77
Table 3.3 – Chemical composition of the sintered MMCs.....	78
Table 3.4 – Processing parameters of laser remelting.	80
Table 3.5 – Parameters of cavitation erosion test.....	87
Table 5.1 – Physical parameters of Ni and WC for numerical simulation.	142
Table 6.1 – Chemical composition and process parameters of Ni-WC-CeO ₂ MMCs.....	153
Table 7.1 – Chemical composition and process parameters of NiCr-WC MMCs.....	184
Table 7.2 – Summary of the carbides in the LSM NiCr-WC.	194

Chapter 1

Introduction

1.1 Background

History of cavitation

Cavitation is a phenomenon known to occur when the local pressure of a fluid drops below its vapour pressure, resulting in the generation of vapour bubbles, termed cavities or cavitation bubbles. Then, when being subjected to higher pressure, these cavitation bubbles collapse and can release micro jets and shock waves with intense energy [1, 2]. This phenomenon is concerned in various disciplines, such as hydropower engineering, marine engineering, pipeline transportation, vehicle engineering, and aerospace engineering. Since about 1890, scientists and engineers have been struggling with the problems brought by cavitation, such as noise, vibration, surface erosion, and efficiency reduction of machineries [3].

The history of cavitation can be traced back to 1754, when it was the first time that the existence of cavitation was considered by the Swiss mathematician Leonhard Euler, who came up with a theory of hydraulic machines. In his memoir, Euler predicted the formation of a cavitation bubble and described it as a 'void'. In 1847, the Anglo-Irish mathematician

George Stokes raised a problem about the instantaneous pressure upon the collapse and the duration of the annihilation of a cavity [4], to which a solution was published by the English mathematician William Henry Besant in 1859 [5]. In 1894, the Irish fluid dynamicist Osborne Reynolds investigated the life of vapour bubbles in boiling liquids and in tubular constrictions [6, 7].

Then in 1895, the term 'cavitation', coined by the British engineer Robert Edmund Froude, first appeared in a paper, *Torpedo-boat destroyers*, by the English shipbuilder John Isaac Thornycroft and the British naval architect Sydney Walker Barnaby [8, 9]. For the first time in history, Thornycroft and Barnaby observed cavitation on the back sides of propeller blades, and their work [8], in which a significant efficiency reduction of a propeller operating at high speed due to cavitation was reported, gave the real impetus for the research of cavitation. Since then, the British physicist Lord Rayleigh [10], the British engineer Stanley Smith Cook [11], the American fluid dynamicist and acoustician Mark Harrison [12], the German physicist and acoustician Wernfried Güth [13], the Soviet scientists Mark Iosifovich Kornfeld, L. Suvorov, and Prof. V.F. Minin [14, 15], the fluid dynamicists Maurice Rattray Jr., Charles F. Naudé, and, Albert T. Ellis at the California Institute of Technology [16, 17], and many other researchers have made significant progress in the exploration of

cavitation.

Cavitation erosion and cavitation-erosion-resistant materials

Accompanied by the extensive studies of cavitation, cavitation erosion (CE), one of the most unpleasant outcomes of cavitation, also gradually attracted attention and has been widely researched. Upon the implosion of a cavitation bubble, an intense micro jet and shock waves are released. When the micro jet and shock waves strike the surface of a material, highly localised surface stresses are accumulated. Then, the repeated impacts from the collapse of cavitation bubbles to the material can cause plastic deformation and ultimately result in the detachment of pieces of material by local surface fatigue failure. Such surface wear caused by the collapse of cavitation bubbles is known as CE [2], which frequently occurs to the components operating with a high-velocity flow, including propeller, rudder, impeller, pump, and pipeline [18-23].

The issues caused by CE draws much attention in recent years due to the call of carbon neutrality. As the backbone of low-carbon electricity generation, hydropower generated about 17% of the global electricity (in 2020) [24], and hence stable functioning and service life extension for hydro turbines are required. However, CE (together with silt erosion) frequently occurs to the blades of hydro turbines, resulting in reduction in

efficiency, suspension of operation, and compromise of durability. On the other hand, in marine engineering, CE also frequently occurs to the blades of propellers and rudders, causing similar issues and extra fuel consumption due to the increased drag force by the rough eroded surface of the blades. Such extra fuel consumption can significantly affect the environment, as the maritime shipping industry consumes a significant portion of global transportation energy [25] and emits a considerable amount of CO₂, NO_x, and SO_x [26].

Therefore, researchers have been searching for effective methods against CE since the last century. A proper mechanical design can significantly reduce the occurrence of cavitation. However, it is inevitable for many components, such as the back sides of impeller blades and the geometrically changed sites of pipelines, to be exposed to cavitation [27]. Thus, many materials are developed to effectively resist CE in recent decades. Martensitic stainless steels [28-31] and nickel aluminium bronzes [32, 33] are the most representative materials with good cavitation erosion resistance (CER), and they are commonly used for manufacturing the components in hydropower and marine engineering. Nevertheless, it is still necessary to apply protective coatings when these components operate in a complex environment. For example, WC-based cermet coatings deposited by high-velocity oxygen-fuel spraying are

frequently used to protect the surface of impeller blades in a hydraulic turbine from cavitation erosion and silt erosion [34, 35].

At present, much effort has been put into the research and development of CE-resistant materials, and hundreds of studies report numerous materials that have some potential in resisting CE. However, in practice, martensitic stainless steels, nickel-aluminium-bronzes, and WC-based cermet coatings are still irreplaceable for resisting CE. Furthermore, most of the studies suggest that mechanical properties are strongly correlated to CER. Therefore, these studies devoted many resources to achieving good mechanical properties but somehow neglected the role of microstructure in resisting CE. Hence, new perspectives on developing CE-resistant materials are required.

1.2 Aims and objectives

This research project aims to develop novel CE-resistant WC-based materials and investigate their microstructural evolution during CE. The specific objectives are proposed as follows to address the research gaps:

1. To prepare several Ni-WC composites post-treated by laser surface melting (LSM) at different laser powers, which outperform the existing HVOF-sprayed WC-based cermet coating in CER.
2. To study whether the CE performance of these LSM Ni-WC

composites is dominated by mechanical properties or microstructure.

3. To seek further enhanced CER of the LSM Ni-WC composites by adding other alloying elements (such as CeO₂ and Cr).
4. To investigate the microstructural evolution of the LSM Ni-WC composites (with and without additives) during the CE test and understand the effect of their microstructure on the CE performance, in an attempt to develop novel microstructure with effective CER.

1.3 Scope of the thesis

Chapter 1 has given the general introduction.

Chapter 2 introduces the general concepts of cavitation and CE and extensively reviews the materials with effective cavitation erosion resistance. The chapter also summarises the strategies for achieving good CER and points out the research gap.

Chapter 3 presents the materials and demonstrates the experimental methods used in this work.

Chapter 4 presents a study on the LSM cold-sprayed Ni-WC composite coatings. The microstructure of the coatings was characterised, and the mechanical properties were measured. Then, the CER of the coatings was evaluated, followed by the examination on the eroded specimens subjected to 10-h CE.

Chapter 5 presents a study on the LSM sintered Ni-WC composites. The microstructure of the composites was characterised, and the microhardness was measured. Then, the CER of the composites was evaluated. Next, the specimens at different intervals of CE test (at the 0th, 2nd, 5th, and 7th h) at the same site were examined, investigating the behaviours of the featured microstructure and various defects in response to cavitation impacts. Finally, numerical simulation was conducted to investigate the stress and energy of the featured microstructure subjected to a cavitation impact.

Chapter 6 investigates the effect of CeO₂ addition on the LSM sintered Ni-WC composites. The microstructure of the composites was characterised, and the microhardness was measured. Then, the CER of the composites was evaluated. Next, the specimens at different intervals of CE test (at the 0th, 2nd, 5th, and 7th h) at the same site were examined, investigating the behaviours of different microstructures in response to cavitation impacts. Finally, numerical simulation was conducted to investigate the stress and energy of the microstructures with different carbide lamellae subjected to a cavitation impact.

Chapter 7 investigates the effect of Cr addition on the LSM sintered Ni-WC composites. The microstructure of the composites was characterised, followed by the evaluation of the CER. Then, the examination on the

specimens at different intervals of CE test (at the 0th, 2nd, 5th, and 7th h) at the same site demonstrated the behaviours of different microstructures in response to cavitation impacts.

Chapter 8 provides the overall conclusions of the thesis.

Chapter 9 provides some recommendations for future work.

Chapter 2

Literature review

2.1 Introduction

This chapter reviews the literature that is highly relevant to this thesis. Firstly, the basics of cavitation and cavitation erosion (CE) are briefly introduced. Next, the test methods for evaluating the CE performance are demonstrated. Subsequently, various alloys and coatings with effective cavitation erosion resistance (CER) are extensively reviewed. Finally, the strategies for achieving good CER are summarised, and the research gaps to be addressed are identified at the end of this chapter.

2.2 Cavitation and cavitation erosion

2.2.1 Cavitation

As cavitation commonly occurs in fluid, a basic knowledge of fluid dynamics is necessary to understand cavitation. The incompressible flow equation from Bernoulli's principle in **Eq. 2.1** demonstrates the relationship among flow velocity (v), the local fluid pressure (p), and the depth of the flow to the liquid level (h), where ρ is the density of the fluid and g is the local gravitational acceleration [3].

$$p + \frac{1}{2}\rho v^2 + \rho gh = \text{Constant} \quad \text{Eq. 2.1}$$

Assuming the depth of a submerged component exposed to the fluid is not changed, the term of the hydraulic head (ρgh) is constant. Hence, **Eq. 2.1** can be simplified as **Eq. 2.2**.

$$p + \frac{1}{2}\rho v^2 = \text{Constant} \quad \text{Eq. 2.2}$$

When a component operates in fluid, such as a propeller spinning in water, the velocity (v) of the water flow near the surface of the propeller blades is relatively high. Therefore, according to **Eq. 2.2**, the local pressure (p) of the water flow near the blade surface should be relatively low.

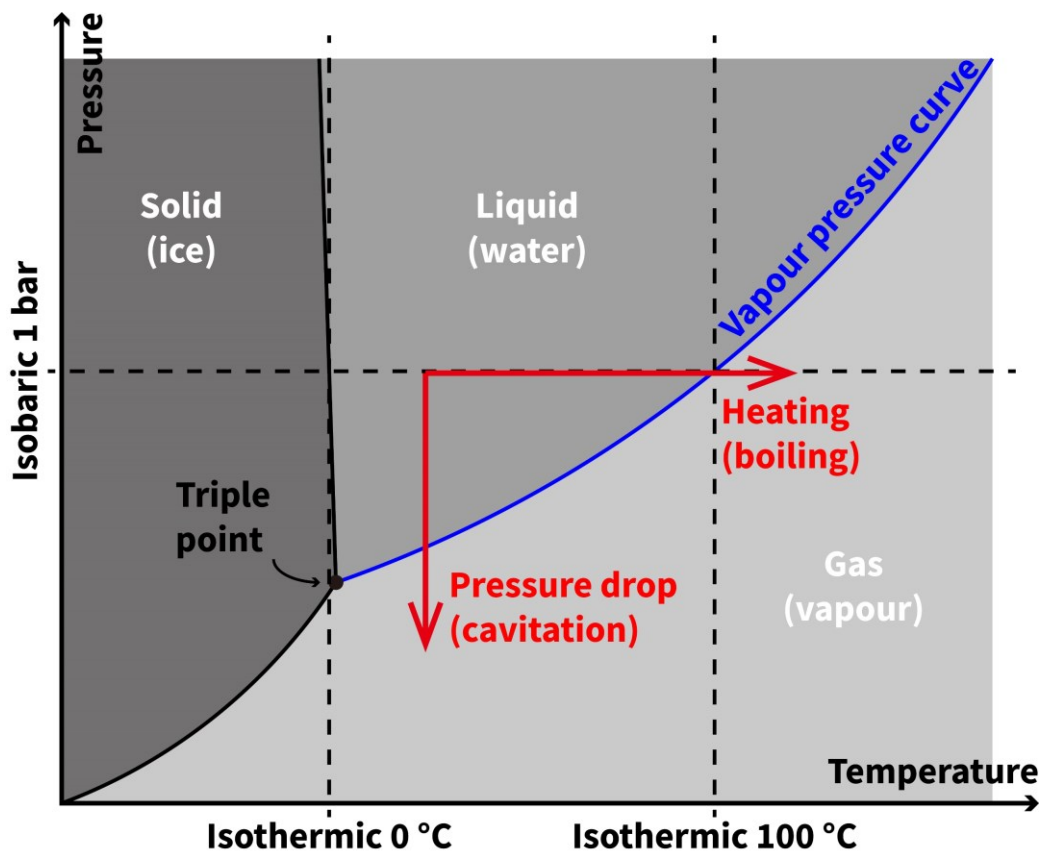


Fig. 2.1 – Schematic phase diagram of water.

Then, as the phase diagram of water (**Fig. 2.1**) shows, water can evaporate when the pressure isothermally drops below the vapour pressure curve. This process is very similar to boiling but results from a

decrease in pressure, while boiling is caused by temperature rising (Fig. 2.1). This phenomenon of the formation of the vapour-filled bubbles due to the local pressure drop is termed 'cavitation', and these bubbles are named as 'cavities' or 'cavitation bubbles' [3]. A typical example of cavitation is a trail of cavitation bubbles left behind a spinning propeller, as shown in Fig. 2.2.

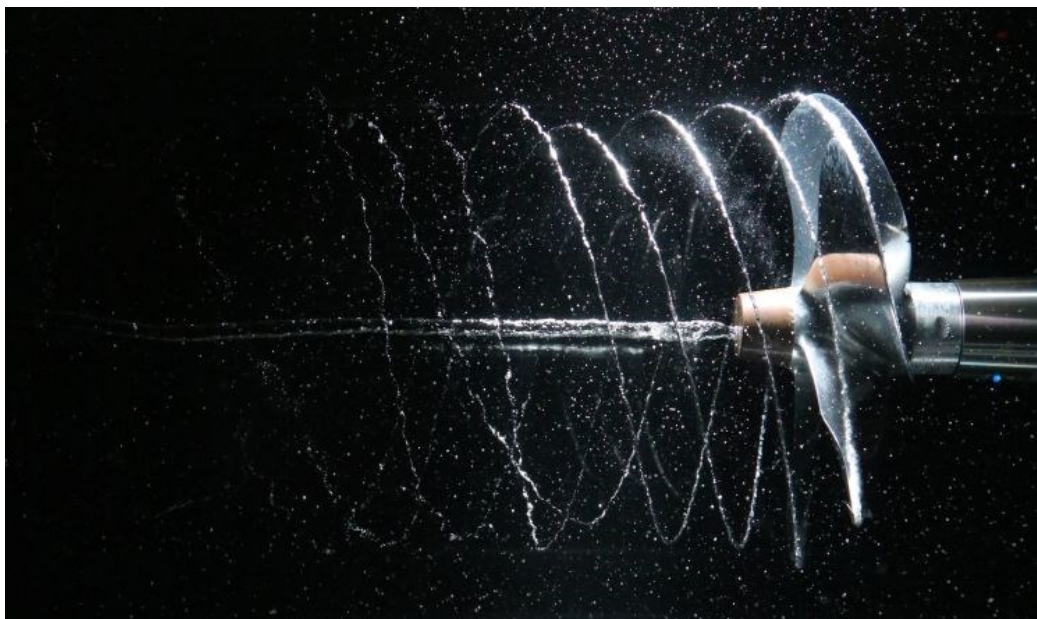


Fig. 2.2 – A trail of cavities behind a spinning propeller [36].

The lifetime of a cavitation bubble is schematically demonstrated in Fig. 2.3. Meanwhile, a plot presenting the flow velocity at different distances to the blade surface is shown in Fig. 2.4, which helps the understanding of the behaviour of a cavitation bubble. As mentioned in Eq. 2.2, the high

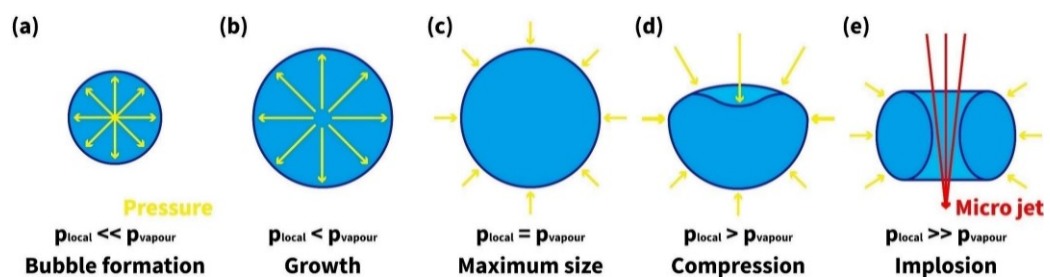


Fig. 2.3 – Schematic of the lifetime of a cavitation bubble.

velocity of the fluid near the blade surface results in the local pressure (p_{local}) of the fluid dropping below the vapour pressure (p_{vapour}), which leads to the formation (near the blade surface) and the growth of cavitation bubbles (**Fig. 2.3a-b**). While the cavitation bubble is growing, it is also moving away from the blade surface. As shown in **Fig. 2.4**, the flow away from the blade surface has a significantly lower velocity than the flow near the blade surface. Then, according to **Eq. 2.2** (the change in h is sufficiently small in **Eq. 2.1**, and thus the ρgh term is still a constant), the local pressure increases as the flow velocity decreases. Hence, the cavitation bubble is transported from the area with low local pressure to the area with high local pressure. When the cavitation bubble moves to the area where the local pressure equals the vapour pressure, it stops growing and reaches its maximum size (**Fig. 2.3c**). When the cavitation bubble moves further away from the blade surface, the local pressure

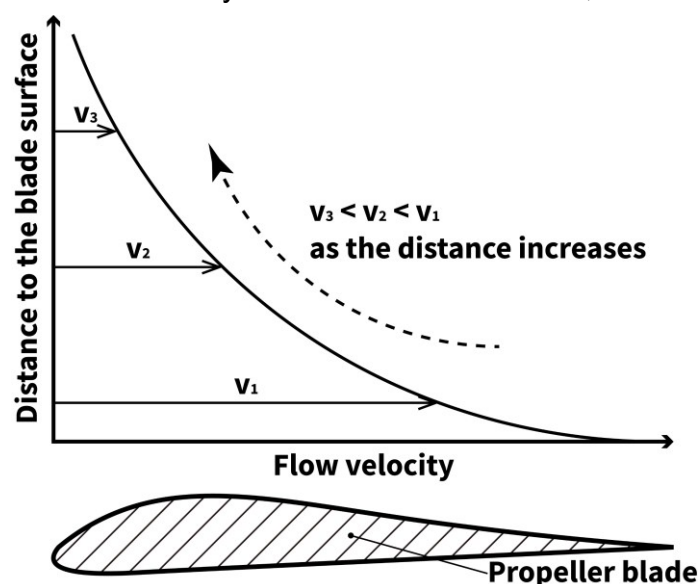


Fig. 2.4 – The relationship of the flow velocity and the distance to the blade surface of a spinning propeller.

exceeds the vapour pressure, and the weakest site is pressed (**Fig. 2.3d**).

Before the collapse, the cavitation bubble is pierced by a free surface-induced micro jet. Finally, the cavitation bubble becomes a torus and disintegrates (**Fig. 2.3e**). Meanwhile, shock waves and a high-velocity micro jet with intense energy are discharged upon the collapse [22, 37].

In addition, according to the generation pathways, cavitation can be sorted into hydrodynamic cavitation, acoustic cavitation, optical cavitation, particle cavitation, and steam bubbles cavitation. In hydrodynamic cavitation (such as the cavitation in a spinning propeller mentioned before) and acoustic cavitation, the fluctuation of the fluid velocity and pressure cause a decrease in the local pressure that results in the formation of cavitation bubbles [2, 38]. The difference is that hydrodynamic cavitation results from the motion of the component or fluid, while the vibration of a sonotrode induces acoustic cavitation. Optical cavitation and particle cavitation occur when a liquid is exposed to an intense energy deposition. In optical cavitation, bubbles are formed due to the breakdown of the liquid by highly intensive irradiation of photons. In particle cavitation, the breakdown of the liquid is accomplished by protons, neutrinos, and other types of particles [39]. Steam bubbles cavitation is caused by the direct injection of steam into a sub-cooled liquid providing collapse conditions, which is similar to hydrodynamic cavitation and acoustic cavitation [40].

2.2.2 Cavitation erosion

As mentioned previously, the micro jet and shock waves are released upon the implosion of a cavitation bubble. The velocity of the micro jet can reach 100-500 m/s (hydrodynamic cavitation [41, 42]) and may be up to 700-1300 m/s (acoustic cavitation [43, 44]), while the velocity of the shock waves can be up to 4000 m/s (acoustic cavitation [45]). Furthermore, the temperature of cavitation can achieve several thousands of K (5075 ± 156 K for acoustic cavitation by ultrasonic irradiation of silicone oil [46]). Thus, the micro jets and shock waves with such intense kinetic and thermal energies can cause damage when impacting on materials, and the damage caused by the implosion of cavitation bubbles in the vicinity of a solid surface is known as cavitation erosion (CE) [2].

Despite the debate about whether CE results from microjets or shock waves or both for many years [2], there is no doubt that the impact load by the collapse of cavitation bubbles is significant, which can range from several MPa to GPa [41, 47, 48]. The intense impact load by the implosion of a cavitation bubble near a solid surface can cause highly localised and transient stresses on the surface. Then, the repeated collapses apply the repeated impact loads to the surface, resulting in local surface fatigue and subsequently the erosion of material [2]. As shown in **Fig. 2.5**, severe CE occurred on various components operating with a high-velocity fluid.



Fig. 2.5 – Cavitation erosion on different components. a, The blades of a mixed flow pump impeller [2]; **b,** The blades at the discharge of a Francis turbine [49]; **c,** The blades of the propeller of a personal watercraft [50]; **d,** The blades of the propeller of a vessel [51].

Hydrodynamic cavitation can be sorted into five major types based on the operating conditions and fluid properties (**Fig. 2.6**). Meanwhile, these types of cavitation can be further categorised according to the parts of the propeller or impeller being exposed to the cavitation (**Fig. 2.7**). Here briefly introduces the sheet cavitation and the cloud cavitation that are usually inevitable and can cause severe erosion. Sheet cavitation (**Fig. 2.6a**) is a cluster of cavities staying approximately at a fixed region relative to the component, and thus sheet cavitation is also known as attached or fixed cavitation [2]. For a propeller, sheet cavitation usually occurs on the back side of the blade (**Fig. 2.7** and **Fig. 2.8**) due to the significant suction pressures around the leading edge of the blade.

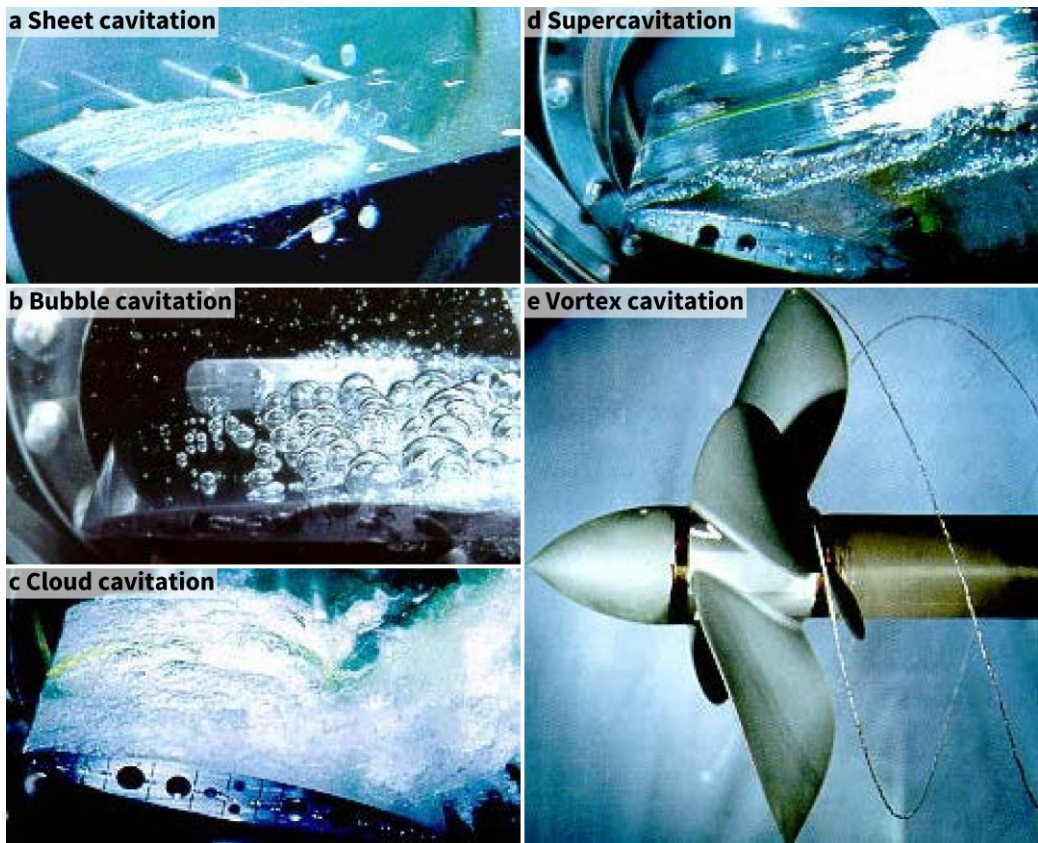


Fig. 2.6 – Major types of hydrodynamic cavitation [52].

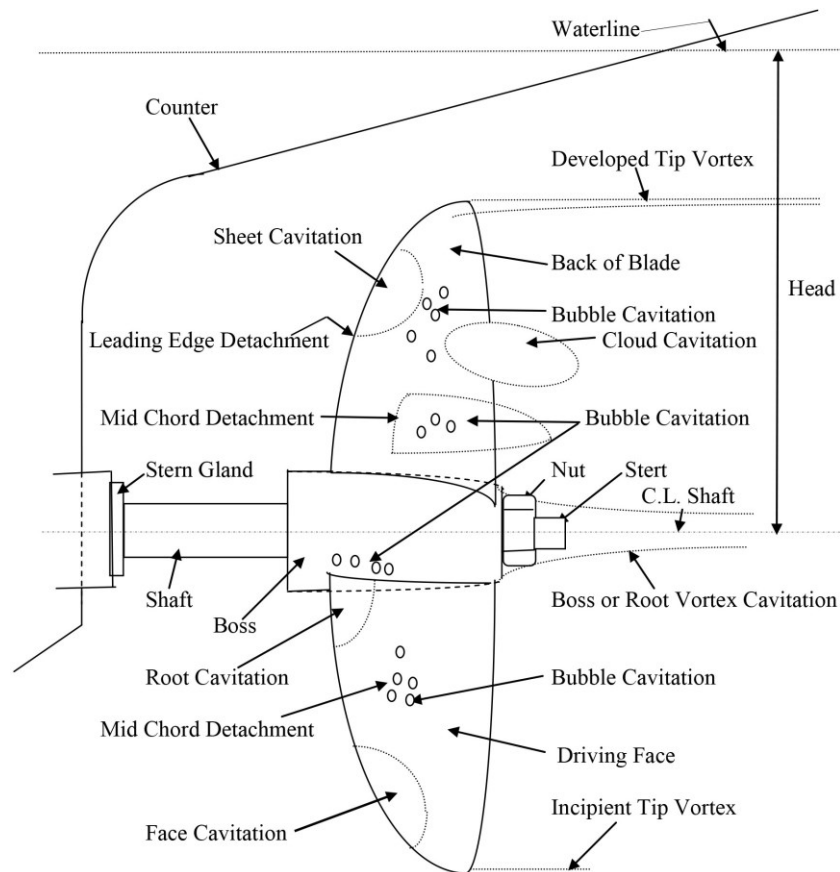


Fig. 2.7 – Various types of cavitation occurring on a propeller [53].

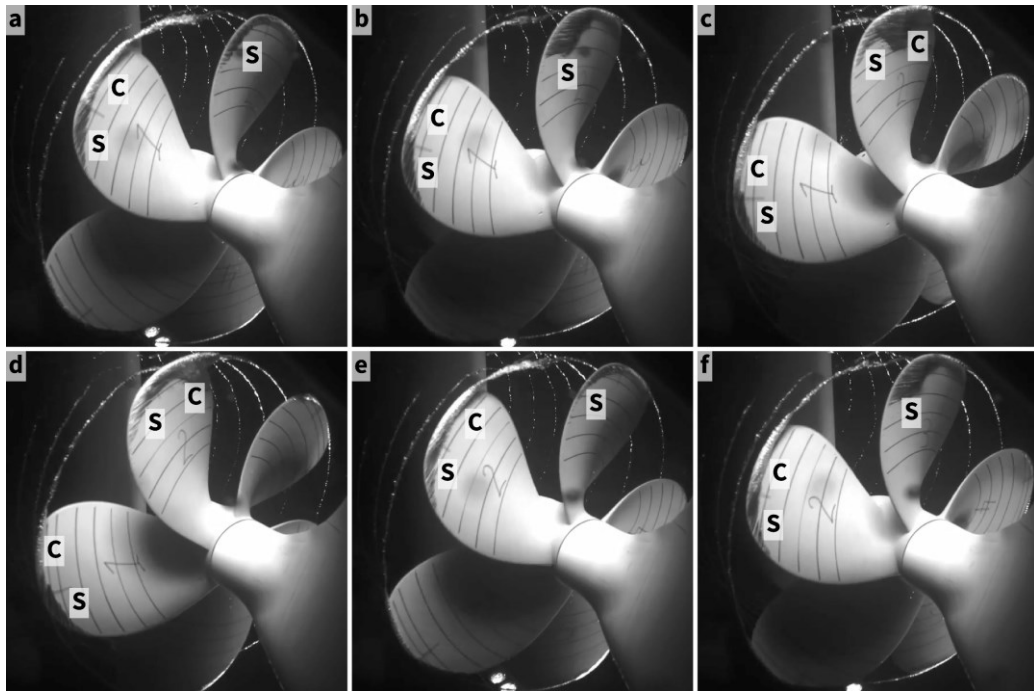


Fig. 2.8 – Photos of cavitation on a propeller [54]. The change in the region covered by sheet cavitation can be observed from the 2nd and 3rd blades as the propeller is spinning ('S' labels the sheet cavitation). It can be noticed that the extension of the sheet cavitation only occurs at the top blade because the local pressure near the liquid level is lower than the pressure at the deep. Cloud (labelled as 'C') and vortex (the spiral trails of bubbles) cavitation is also observed.

The CE can be trivial if the sheet cavitation remains stable. However, sheet cavitation can always be interfered periodically by the re-entrant turbulent flow at its end, resulting in vortex shedding and causing cloud cavitation (**Fig. 2.8** and **Fig. 2.9**) [2, 3]. Separated by the re-entrant flow, cloud cavitation can occur at some distance to the blade edge (**Fig. 2.8** and **Fig. 2.9**). As cloud cavitation is extremely aggressive due to the implosion of huge numbers of cavitation bubbles, severe erosion can happen. As shown in **Fig. 2.5**, massive erosion is commonly found at the back side of the blade. Meanwhile, the erosion near the edge is more significant than the erosion at the edge (**Fig. 2.5b-d**), and sometimes

erosion can only happen to the inner region of the blade (**Fig. 2.5a**), which is in accordance with the region that the cloud cavitation occurs.

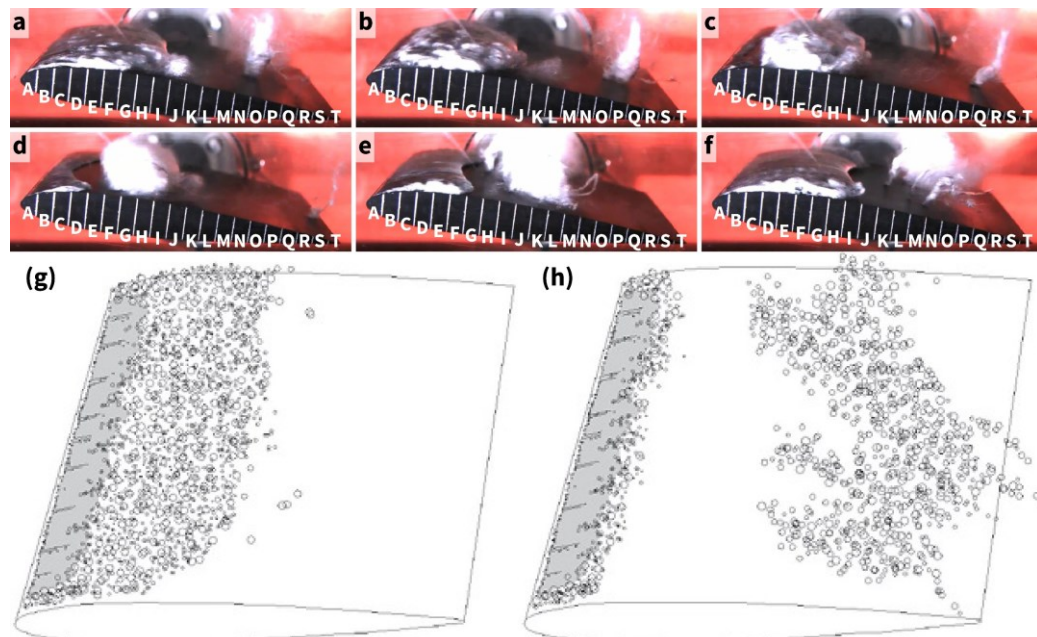


Fig. 2.9 – Photos and schematics of sheet and cloud cavitation on a hydrofoil. **a-f**, Photos showing sheet cavitation interfered by turbulent flows [55]: **a**, Sheet cavitation on the front part of the hydrofoil (region A-I); **b**, Sheet cavitation (A-B) and sheet cavitation interfered by turbulent flows forming cloud cavitation (C-I); **c**, Cloud cavitation (D-I) starting to detach (B-C) from sheet cavitation (A); **d**, Detachment of cloud cavitation (E-I) and restoring of sheet cavitation (A-D); **e**, Travelling of cloud cavitation (H-M) and further restoring of sheet cavitation (A-F); **f**, Fully restored sheet cavitation (A-I) and annihilation of cloud cavitation as it travelling to high pressure fluid (K-R). **g-h**, Schematics demonstrating the detachment of sheet cavitation due to turbulent flows and the formation of cloud cavitation [56].

The other types of cavitation shown in **Fig. 2.6** and **Fig. 2.7** usually do not cause severe erosion to the component, and the details can be found in these studies [2, 3, 53, 57]. Meanwhile, more incisive analysis about the erosion caused by the sheet and the cloud cavitation are reported in the literature by Bark et al. and Pelz et al. [58, 59].

Although this work only focuses on CE, it is worth mentioning that cavitation can exhibit synergistic effects with other types of wear. For

example, the coalesced effect of CE and silt (or sediment/slurry) erosion can significantly damage the materials [18, 21, 60, 61], as CE can compromise the integrity of the material structure and accelerate silt erosion, and vice versa. On the other hand, since cavitation can enhance chemical processes, the corrosion progress of the component operating in a corrosive liquid can be accelerated by cavitation, which in turn further aggravates CE. Therefore, the synergistic effect of cavitation erosion-corrosion is also extensively concerned [62-70].

2.3 Evaluating cavitation erosion performance

2.3.1 Standard test method for cavitation erosion using vibratory apparatus

ASTM G32 [71], G73 [72], and G134 [73] are the three standard test methods for evaluating the CE of materials. The most popular one is ASTM G32 due to the low cost and the simplicity of the test apparatus. The device is just a simplified version of an ultrasonic homogeniser that can generate acoustic cavitation (**Fig. 2.10**). Some important test parameters are given in **Fig. 2.11**. In this method, cavitation bubbles are induced by the high-frequency vibration of the horn (sonotrode) tip in the test medium, and the implosion of the bubbles near the specimen surface causes erosion.

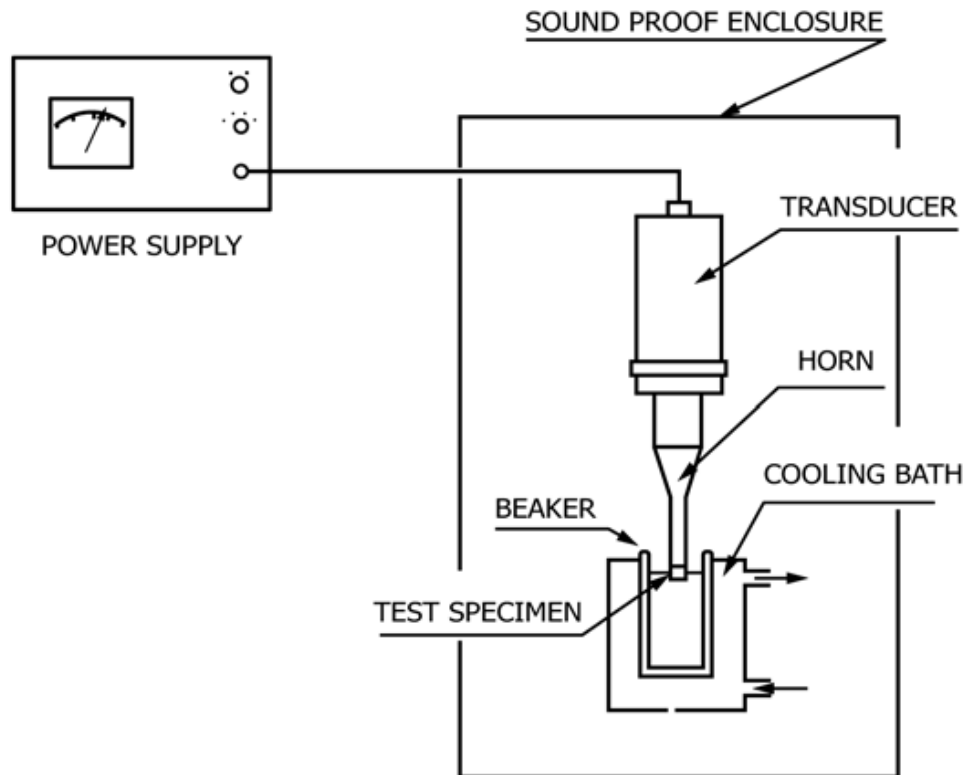


Fig. 2.10 – Schematic of ultrasonic vibratory cavitation erosion apparatus [71].

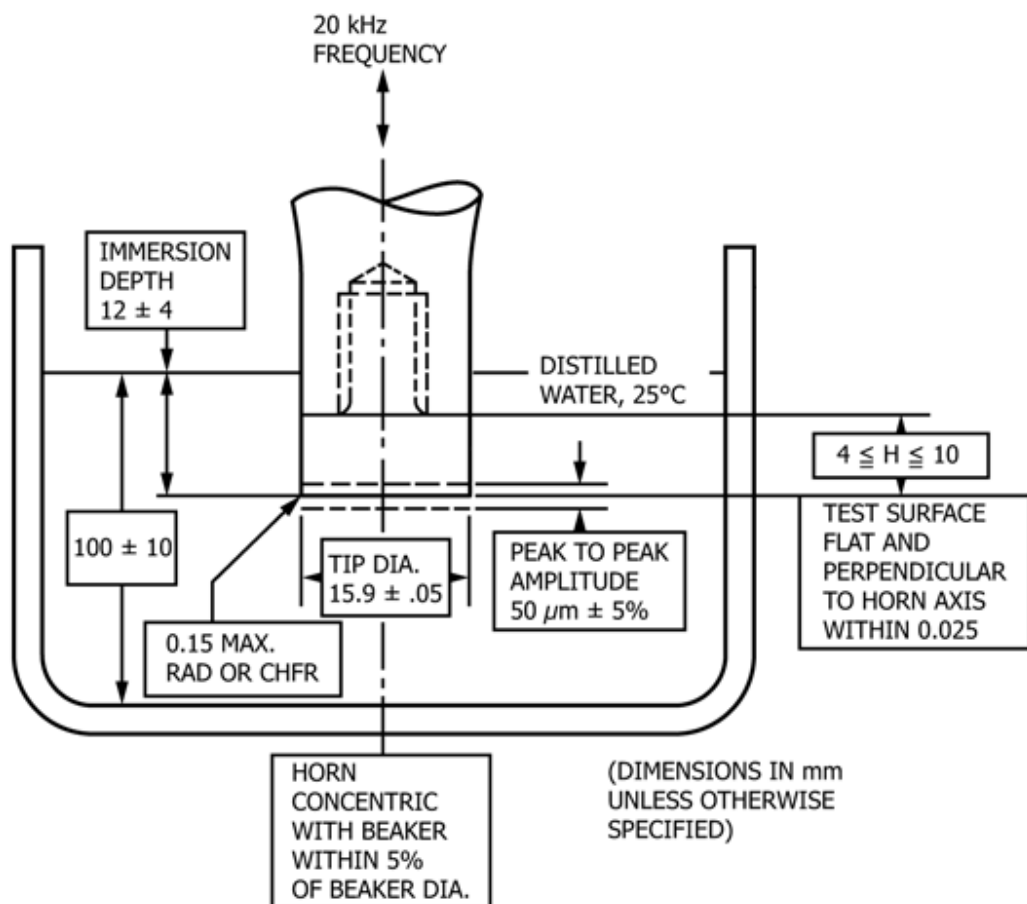


Fig. 2.11 – Important parameters for ASTM G32 [71].

It is worth noticing that the temperature control of the test medium is very important. As **Fig. 2.1** shows, the pressure drop required to form a cavitation bubble is highly correlated to the liquid temperature. Thus, failure to maintain a specified temperature can cause huge fluctuations [71, 74, 75]. For a specimen tested in distilled water, an increase of 1 °C (from the standard temperature of 25 °C to about 50 °C) may increase the CE rate by 1~2 % [71, 74, 76]. It is also worth mentioning that the CE rate reaches a maximum when the temperature of the test medium is about halfway between freezing and boiling point, and hence it may be economic incentive to perform the water test at 40~50 °C for materials that are exceptionally resistant to CE [71, 74, 77]. However, introducing a heating device to the testing apparatus can bring about more complexities to the test system, and thus the most frequent choices are just extending the test duration and using the specimens with a large radius (the recommended maximum radius is 20 mm [71]).

According to the position of the specimen, the test approaches of ASTM G32 can be sorted into direct cavitation and indirect cavitation (**Fig. 2.12**). The standard test method in ASTM G32 utilises the direct cavitation approach (**Fig. 2.12a**), as per which the specimen is tightly fastened to the horn via screw threads (**Fig. 2.11**). Thus, in the direct approach, cavitation is actually induced by the vibration of the specimen. A modified

version of ASTM G32 using the alternative indirect cavitation approach (also known as the 'stationary specimen' approach) is also acceptable (**Fig. 2.12b**). In this approach, the specimen is placed on or fastened to a holder and submerged in the testing medium. Meanwhile, the space between the horn tip and the surface of the specimen is in close proximity to ensure that the cavitation bubbles induced by the vibration of the horn can effectively act on the surface of the specimen.

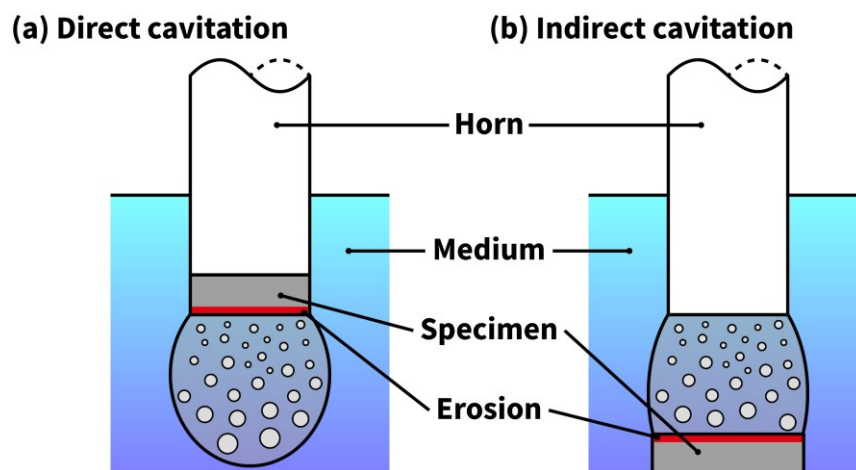


Fig. 2.12 – Schematic of direct and indirect vibratory cavitation erosion tests.

Literature shows that both approaches have advantages and limitations, summarised in **Table 2.1**. The erosion rate of the materials subjected to the direction cavitation is much higher than the indirection cavitation [78, 79]. The high erosion intensity by the direct approach not only shorten the test duration but also allow the evaluation of the materials with extremely high erosion resistance. For the indirect cavitation approach, it can take much time to reveal the CER of a material, and sometimes hundreds of hours may be required to evaluate the materials with extremely high CER.

Moreover, the horn tip has to be occasionally restored (usually by grinding or turning) after operating for dozens of hours, as cavitation can also damage the horn tip if the indirect approach is used. In addition, the resonance frequency of the horn will ultimately be out of the required frequency domain due to the shortened length, and the sonotrode needs to be replaced. For the direct cavitation approach, the horn is not exposed to cavitation, and thus the horn does not need maintenance very often unless fatigue failures happen to the thread.

Table 2.1 – Comparison of the direct and the indirect cavitation approaches. Summarised from the literature [71, 78] and the experience of the author.

Items	Direct approach	Indirect approach
Time taken	Short (due to high erosion intensity)	Long (due to low erosion intensity)
Maintenance frequency of horn	Low (but the horn is still at the risk of failure as the thread hole in the horn is subjected to fatigue by vibration)	High (the surface of the horn tip has to be periodically restored due to CE)
Usability in different materials	Poor (as the frequency has to be adjusted when testing materials with different dimensions and densities)	Good (as no adjustment needed except the horn-specimen space)
Main causes of errors	Frequency change due to inconsistent fastening torque Wear at the specimen thread during fastening	Adjusting the space between the horn tip and the specimen
Brittle materials	Not applicable (due to the difficulty in machining threads)	Applicable
Elastomeric/Compliant materials	Not applicable (as the compliance of the material can reduce the severity of vibration-induced cavitation)	Applicable
Coatings	Not applicable (as the oscillations can cause the detachment of the overlays)	Applicable

Despite having a good efficiency of testing and a low frequency of maintenance, the direct approach is not very often used in practice for the screening test on a large variety of materials due to its two greatest drawbacks. Firstly, as the specimen is fastened to the horn, the specimen and the horn are considered as a single sonotrode. This means that the resonance frequency of the sonotrode can vary if the specimens with different dimensions and densities are fastened to the horn, and thus the resonance frequency can be out of the required frequency domain for the test. As most of the commercial vibratory devices are designed to operate at a specific resonance frequency, evaluating the specimens with large differences in dimensions and densities requires a series of customised horns. In addition, the fastening torque of the specimen can also affect the frequency, which brings about extra errors. Meanwhile, even for a device whose output parameters of the transducer are adjustable, it is very challenging to configure the frequency and the amplitude to be within the required domains simultaneously. Hence, using the direct approach to evaluate many different specimens can be extremely inconvenient and costly.

Secondly, the direct approach only applies to a certain range of materials, except for brittle materials, elastomeric/compliant materials, and coatings [71, 78]. Brittle materials are difficult to be machined into threaded

specimens and thus cannot be fastened to the horn. Elastomers can reduce the severity of the vibration-induced cavitation due to their compliance. Hence, the cavitation intensity acts on elastomers is lower than that on the other materials even if the test parameters are the same, and thus the direct method cannot reveal the real CER of elastomers. For the coatings, especially the sprayed coatings, it is difficult to tell whether the material loss is due to the vibration-induced detachment of the splats or cavitation impacts. Despite the drawbacks, the direct approach is very suitable if the specimens are the same and the long-time continuous exposure to cavitation impacts is required to be evaluated.

Considering the limitations of the direct approach, many studies on the development and evaluation of CE-resistant materials used the indirect approach. As the specimen to be evaluated by the indirect approach does not need a machined thread, brittle materials can be tested via this approach. Meanwhile, since the cavitation is not induced by the vibration of the specimen, compliant materials and coatings are also applicable. Furthermore, identical sonotrodes can be used for different materials since the properties of the material do not influence the frequency of the sonotrode. The main problems with the indirect approach are brought by the separation distance between the horn tip and the specimen surface. Firstly, researchers have not reached a consensus about the most-

optimised distance for the indirect approach [71]. Although the approach is frequently used, comparing the results from different literature is discouraged as different separation distances (usually 0.5~2 mm) are chosen. This problem is partially solved by introducing reference specimens, which at least allows the comparison of the studies that use the same reference material. Secondly, it is difficult to adjust the separation distance between the horn tip and the specimen surface accurately, and thus the cavitation intensity can vary for each test, causing random errors. To address the problem, an add-on for precisely controlling the distance can be installed on the apparatus. In addition, a large separation distance can narrow the errors, but the test duration has to be extended due to the reduced cavitation intensity.

2.3.2 Mean depth of erosion and stages of cavitation erosion

After the material has been subjected to a CE test for some time, it can be weighed to find the mass loss caused by CE. However, it is inappropriate to compare the mass losses of different materials. For example, it is not a good practice to compare the CER of a polymer coating and a cermet coating based on the mass losses. Hence, the mass loss is usually converted into the mean depth of erosion (MDE) to allow the comparison among different materials [71], as demonstrated in **Eq.**

2.3, where the V_{loss} , A , m_{loss} , and ρ are the volume loss of the specimen, mass loss of the specimen, area of the specimen exposed to cavitation, and density of the specimen, respectively. Meanwhile, the erosion rate in terms of MDE (MDER) can be found by the quotient of the change in MDE and the duration of the corresponding test interval (**Eq. 2.4**).

$$MDE = \frac{V_{loss}}{A} = \frac{m_{loss}}{\rho \cdot A} \quad \text{Eq. 2.3}$$

$$MDER = \frac{\Delta MDE}{\Delta t} \quad \text{Eq. 2.4}$$

In practice, specimens should be polished before the test. The specimen is weighed after each test interval, and multiple test intervals are necessary to acquire the two curves of the cumulative erosion and the erosion rate versus the exposure time to cavitation. These two curves provide the most important quantitative results for evaluating the CER of a material. As presented in the schematic plots from **Fig. 2.13a**, the most preliminary result from a CE test is the cumulative erosion-time curve. Since mass losses are not meaningful when comparing materials with different densities, the quantity of the vertical axis should be MDE. As the plot of the cumulative erosion-time curves only allows the direct comparison of the losses of different materials subjected to CE, an engineering-meaningful approach to evaluate the CER of different materials is to compare the exposure times of reaching the same MDE.

For example, the time to 10 μm . On the other hand, a more frequently used approach in the laboratory is to compare the MDE after a set exposure time. For example, an exposure of 10 to 20 h is usually sufficient enough for the ASTM G32 method.

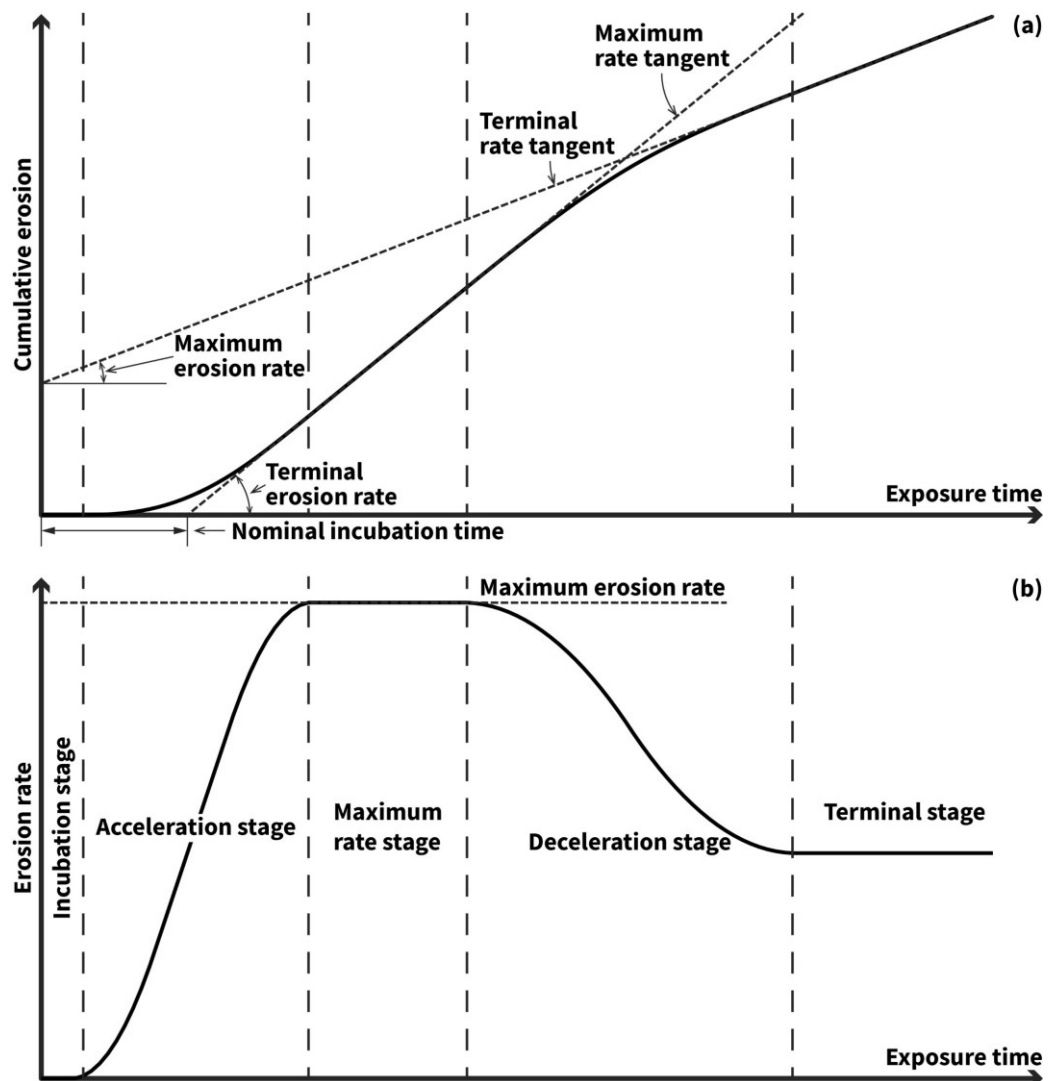


Fig. 2.13 – Plots of the cumulative erosion-time curve and the erosion rate-time curve [71].

However, the information provided by the cumulative erosion-time curve is very limited, and thus it is not easy to extract or extrapolate further outcomes. Hence, the erosion rate-time curve is used to analyse the CE behaviour further. As the schematic plot shown in **Fig. 2.13b**, the progress

of CE can be divided into various stages according to the pattern of the erosion rate-time curve.

The initial stage of CE is known as the incubation stage. At this stage, the compressive residual stress are accumulating on the material surface exposed to cavitation [71]. Meanwhile, dislocation, local displacement of the material, plastic deformation (i.e., cavitation pits), and the development of microcracks can also happen. Materials can exhibit a temporary hardness increase by the work-hardening effect due to the repeated impacts of cavitation, and some can also exhibit stress-induced phase transformation at this stage [80]. Therefore, researchers can take advantage of the accumulation of the residual stress (i.e., cavitation peening) to improve the fatigue strength of materials [81-84]. In addition, if the original surface is well-polished, small pits can be observed via profilometry [85-88], interferometry [89, 90], or scanning electron microscopy [47, 80, 90, 91], which can help the studies on the cavitation pitting progress [85-87, 89-92] and the cavitation impact load [47, 88, 92]. Since material removal barely occurs at this stage, the material loss is zero or negligible. Hence, the boundary between the incubation stage and the followed acceleration stage is not clear, resulting in the difficulty in the estimation of the incubation time. One approach is to take the total exposure time when the erosion rate reaches a threshold, but the

threshold value is not standardised. The other approach is to take the intersection of the maximum rate tangent and the horizontal axis in the cumulative erosion-time plot as the 'nominal incubation time' (**Fig. 2.13a**), but there could be some material losses at this time already. Thus, the length of the incubation time is still undefined [71]. Nevertheless, although the estimation of the incubation time can be important for the studies on the early stage of CE, it is not a crucial criterion for screening the CE-resistant materials from the perspective of engineering application, as the long-term durability is far more critical when the materials are put into use. When the material near the surface reaches its plastic limit, further exposure to cavitation impacts cannot harden it anymore and can cause fracture and erosion to the surface. This stage is named as the acceleration stage since the erosion rate is gradually increasing. The increased erosion rate may be attributed to the removal of the material at the surface which is previously work-hardened by the cavitation impacts, leaving the untreated material below directly subjected to cavitation. Meanwhile, the flow condition on a rough surface is different from that on a polished surface, and thus the similar work-hardening effect by cavitation is absent. Eventually, the erosion rate will reach its maximum. Then, it can exit from the maximum instantaneously or maintain the maximum for some time depending on the properties of the material, and

this stage is known as the maximum rate stage [71].

After reaching the maximum rate stage, the material can progress to the deceleration stage, in which the erosion decreases. During this stage, the surface properties are rebalanced because of the cavitation impacts on the newly exposed surface [93]. For example, the cavity dynamics can be affected by the surface roughness, and the cavitation pressure waves can be damped by the entrapped gas and liquid in the craters previously formed by cavitation impacts [93]. Once the equilibrium is achieved when the surface properties of the material have been sufficiently altered to restrict the change of the flow dynamics near the surface, the erosion rate becomes stable, and this stage is known as the terminal stage.

For the evaluation of CER, the steady-state erosion rate should be used. According to **Fig. 2.13**, it is the erosion rate at the terminal stage. Nevertheless, it can take an extremely long time for some materials to reach the terminal stage, which is impractical. Thus, the maximum erosion rate is also acceptable since the erosion rate can also be stable at this stage for some time. Meanwhile, the separation of the stages shown in **Fig. 2.13** highly depends on the material properties, and many materials may not exhibit all the stages. For example, the erosion rate-time curve of some materials may not have the deceleration stage and becomes stable at the maximum rate stage for a considerable duration. On the other hand,

the erosion rate may never be stable for other materials, such as elastomeric coatings [93]. Hence, extra caution about which erosion rates should be taken when different materials are evaluated. In addition, it is worth mentioning that the pattern of the curves (**Fig. 2.13**) for the same material tested by different methods can be very different. For example, the terminal erosion rate of some materials tested by cavitating jet follows a non-linear function of the erosion time.

2.4 Cavitation-erosion-resistant alloys

In the early twentieth century, the components of the machinery operating in fluids, such as propellers, rudders, impellers, and pipes, were made from copper alloys or cast irons. Then in the 1950s, stainless steels (SSs) gradually took their place for the application in non-corrosive environments and were found in a wide variety of hydraulic components, ranging from pipe and valve components to high-speed pump impellers. Martensitic stainless steel (MSS) 13Cr4Ni is a typical one that has good resistance to CE and has broad application areas in hydro turbines, pumps, and compressors. In corrosive environments, more specialised copper alloys such as aluminium-bronze and nickel-aluminium-bronze (NAB) are widely used. Meanwhile, as CER is generally correlated to the mechanical properties of the materials, such as hardness, elastic

modulus, ultimate tensile strength, ultimate resilience, and fatigue strength [94-97], other alloys with good mechanical properties are also of great potential for resisting CE. This section mainly reviews the CE performance and the failure mechanisms of some SSs and NABs. In addition, some other alloys with good CER are also briefly introduced.

2.4.1 Stainless steels

Martensitic stainless steels (MSSs)

MSSs exhibit a distorted body-centred cubic (BCC) crystal structure (martensite) and they can be hardened and tempered via various ways of heat treatment [98]. MSSs are widely applied for manufacturing the components of hydro turbines, and one of the most popular choices among the MSSs is 13Cr4Ni (**Fig. 2.14**), also known as the CA6NM hydro turbine steel.

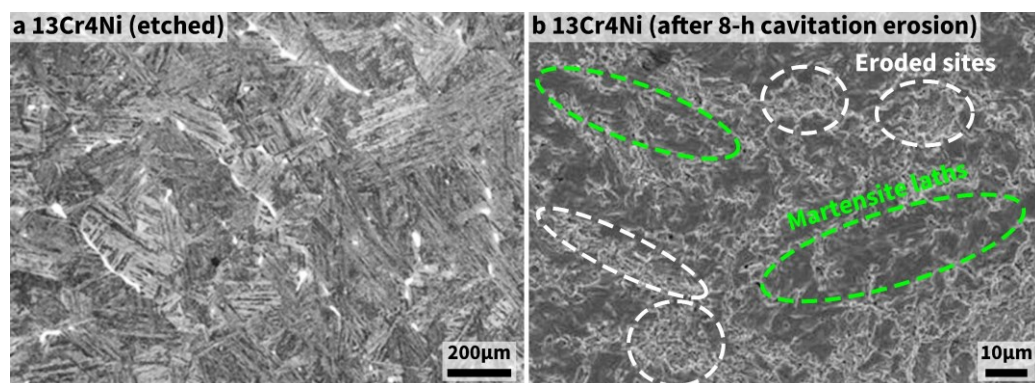


Fig. 2.14 – Microstructure and cavitation erosion of 13Cr4Ni stainless steel. **a**, The etched surface showing martensitic matrix (black laths) and δ -ferrite (white particles) [99]; **b**, The surface after 8 h of cavitation [100]. Only very minor erosion was found on the eroded surface, suggesting the good CER of 13Cr4Ni MSS. In addition, the erosion was less likely to occur in the martensite laths.

MSS 13Cr4Ni exhibits outstanding weldability, fracture toughness, corrosion resistance, and CER [28, 29]. Hence, MSS 13Cr4Ni is extensively applied for the hydro turbine components exposed to high-velocity flows, such as guide vanes, runners, and rotary labyrinths [29, 30]. Meanwhile, 13Cr4Ni MSS also has good workability even in a large scale [28], and its mechanical properties can be easily improved via simple heat treatment [101, 102], which further expands its application. Apart from 13Cr4Ni MSS, other MSSs such as 13Cr0.5Ni, 13Cr1Ni, 13Cr5Ni, 16Cr5Ni, and 18Cr8Ni, are also commonly applied in hydraulic engineering [28-31]. In addition, some researchers suggest that the good CER of MSSs can be partially attributed to the low stacking-fault energy (SFE) [30, 103].

Austenitic stainless steels (ASSs)

ASSs have a primary crystalline structure of face-centred cubic (FCC) austenite at room temperature, which is attained by the liberal addition of N, Mn, Ni, and other austenitising elements [98]. ASSs 304 (ASTM S30400) and 316L (similar to ASTM S31603) are commonly used as the references for evaluating the CER of other materials, and their erosion rates are close to MSS 410 (ASTM S41000, also commonly applied for hydrodynamic engineering) [104]. Meanwhile, 304 ASS can undergo

stress-induced phase transformation from austenite to martensite during CE (Fig. 2.15e), which results in a portion of the cavitation impact energy being consumed by phase transformation instead of by plastic deformation [80, 103, 105-107], while ASS 316L cannot [80, 103, 108]. In addition, the formation of the hard martensite can also inhibit crack generation and propagation [109, 110]. Therefore, ASS 304 has better CER than 316L ASS. However, it is worth mentioning that some studies suggest that the pitting potential and the stability of passive films are negatively correlated to the martensite content [111, 112], indicating the corrosion resistance and CER of ASS 304 can be compromised when ASS 304 is exposed to CE in corrosive media.

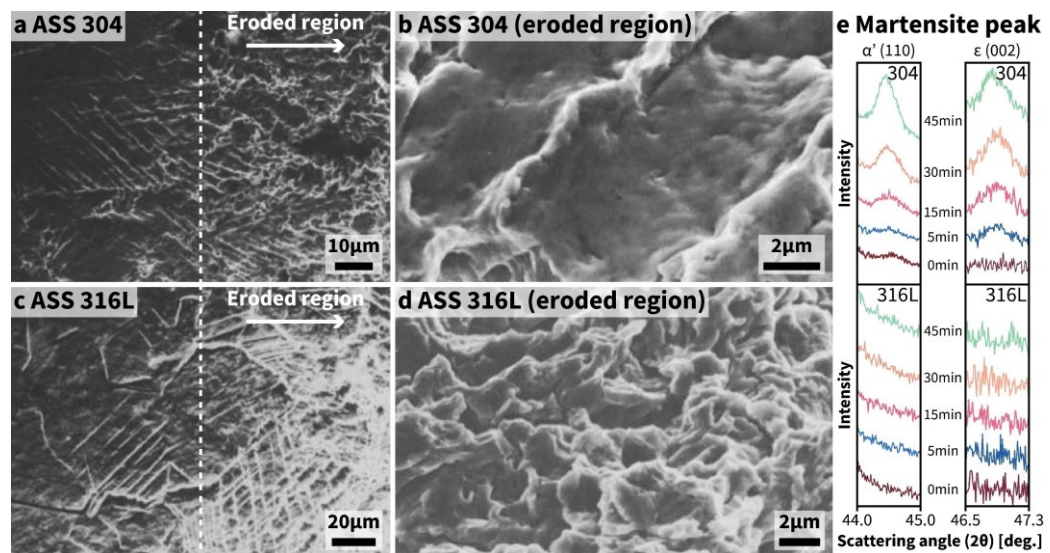


Fig. 2.15 – SEM images and XRD patterns of 304 and 316L austenitic stainless steels after cavitation erosion [80, 103]. a&c, SEM images at the edge of the eroded region; b, Eroded surface of 304 stainless steel showing the erosion at a protruding slip or twin boundary; d, Eroded surface of 316L ASS showing ductile rupture; e, XRD patterns of the ASSs before and after cavitation erosion for 5-45 min showing the 304 ASS exhibited martensitic transformation but 316L ASS did not.

Duplex stainless steels (DSSs)

DSSs are a family of SSs which consist of FCC austenite and BCC ferrite in approximately equal proportions (**Fig. 2.16a**) [98]. Generally, apart from Fe, the composition of the DSS includes 18–28% Cr, 1-9% Ni, Mo up to 5%, 0.05–0.50% N, and up to 0.05% C (in wt.%), and some may also contain Si, P, S, Mn, Co, Cu, and W [98, 113]. Since DSSs possess a low Ni content but good mechanical properties, specific strength, and corrosion resistance, researchers have been studying whether DSSs can be cost-effective substitutes for MSSs and ASSs in hydrodynamic engineering.

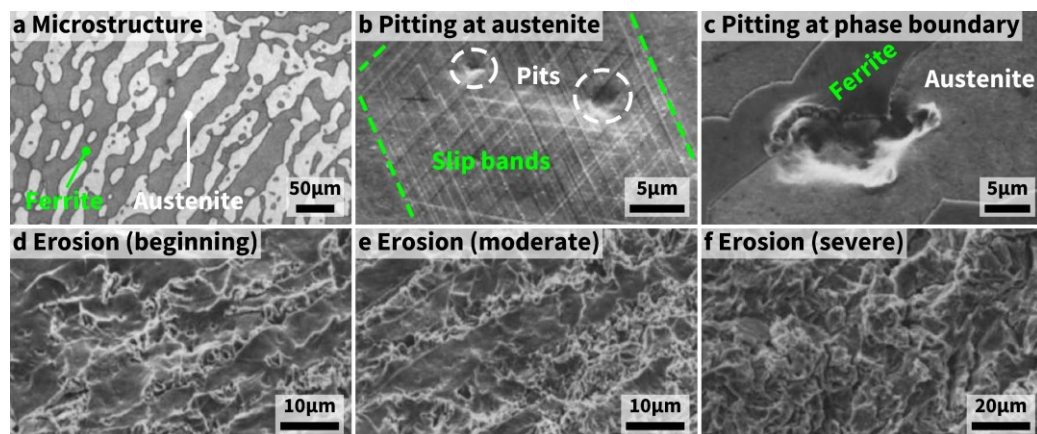


Fig. 2.16 – Microstructure and cavitation erosion behaviour of duplex stainless steel [114]. **a**, Light micrograph showing ferrite and austenite; **b**, Initial exposure to cavitation impacts (a few min) causing pits and cross slips in the austenite phase; **c**, Initial exposure to cavitation impacts causing a pit in the austenite at the phase boundary; **d-e**, Preferential damage in the austenite at the early stage of cavitation erosion; **f**, Detachment of ferrite after further exposure to cavitation impacts.

According to the literature, DSS CrMnN and super DSSs present promising outcomes. DSS CrMnN has better CER than the MSS 13Cr5Ni due to the high work-hardening ability of DSS CrMnN, and the Ni content

in CrMnN DSSs is extremely low, which considerably reduces the cost [115, 116]. Super DSSs such as ASTM S32750 and S32760 exhibit outstanding resistance to pitting corrosion and stress corrosion cracking [76, 117], and they have similar CER as ASS 304 and MSS 410 [104, 118, 119]. Meanwhile, super DSSs also show excellent resistance to cavitation erosion-corrosion [76], and thus they are potentially preferable in corrosive environments.

The material losses of the DSSs subjected to cavitation preferentially initiate at the austenite-ferrite phase boundaries (**Fig. 2.16c-e**), and the failure is mainly attributed to the brittle fracture of the hard ferrite (**Fig. 2.16f**) [114-116, 118-120]. Therefore, it is generally acknowledged that the CER of the DSSs is negatively correlated to increasing the ferrite content. On the other hand, since a certain ferrite content is beneficial to prevent thermal cracks for welding, DSSs can be promising welding materials for fluid machinery, but extra heat treatment is necessary to reduce the exceeded ferrite content [121, 122].

2.4.2 Nickel-aluminium-bronzes

Copper and copper alloys are known for good corrosion resistance, workability, thermal and electrical conductivity, and antimicrobial effect, which are beneficial to a vast range of industries. Among various copper

alloys, aluminium-bronze provides a combination of great mechanical properties and corrosion resistance and have found applications in marine, offshore, and shipboard components for many decades [32, 33]. Then, the development of the aluminium-bronze was catalysed by World War II, and nickel-aluminium-bronze (NAB), as a more developed series of aluminium-bronzes which outperform many SSs, brasses, and bronzes, gradually taken the portion of aluminium-bronze. For now, NABs are the most extensively used copper alloys in these fields [123].

NABs are composed of Cu, 6-13% Al, up to 7% each of Fe and Ni (in wt.%) and some minor alloying elements such as Si and Mn [124]. These alloying elements have different influences on the properties of NABs [123]. Al can improve strength and hardness but at the cost of reduced ductility. Ni further enhances the corrosion resistance and mechanical strength, improving the CER in high-velocity flows. The content of Fe is usually lower than Ni, and Fe can provide a refined microstructure and good toughness.

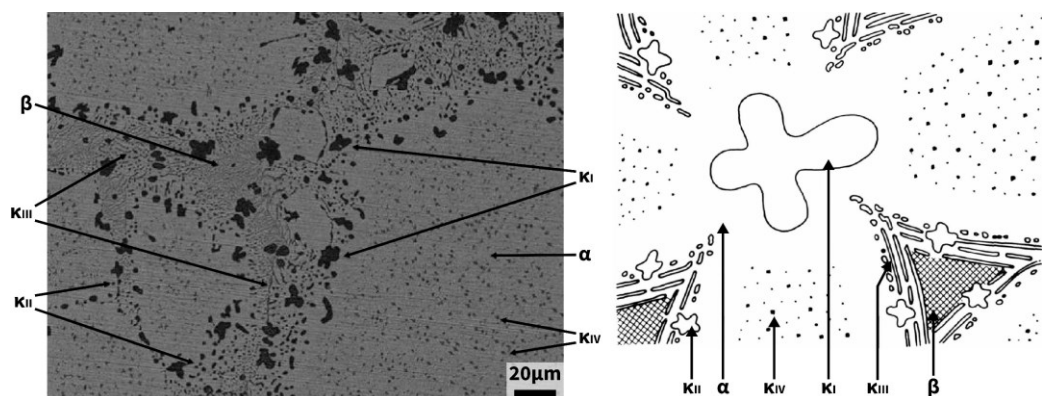


Fig. 2.17 – SEM image and schematic of nickel-aluminium-bronze [123, 125].

As shown in **Fig. 2.17**, the phase composition of NAB includes FCC copper-rich α phase, martensitic BCC copper-rich β phase, and intermetallic κ phases of various morphologies [125-129]. β phase appears at high temperature and has relatively high hardness. Similar to quench-hardening steels, NAB can undergo a martensitic phase transformation via rapid cooling, resulting in high strength and hardness but low ductility. Therefore, heat treatment can be employed to transform β phase to α/κ eutectoid to improve ductility. Sometimes there are a few β phases remained after the heat treatment as the cooling rate is not sufficiently slow, and these β phases are also known as the retained β' phase. Meanwhile, the secondary κ precipitates can form during the heat treatment, which also enhances the strength of NAB via precipitation hardening. Furthermore, κ phases can be further categorised according to morphology, location, and distribution. κ_I phases have a rosette form and are mainly composed of Fe or Fe_3Al . κ_{II} phases are also rosette-like or spheroidal NiAl-FeAl precipitates at the grain boundaries (mostly at the α/β phase boundaries). κ_{III} phases are lamellar, whose composition varies from NiAl to FeAl. κ_{IV} phases are fine needle-like precipitates formed within the α grains, and they are also based on Fe_3Al . In addition, these κ phases also exhibit different crystal structures [63, 126, 127]. κ_{III} phase has a BCC-based B_2 structure, while the rest of the κ phases present a

DO₃ structure. The complex composition in NABs by these phases with different chemical and crystallographic properties grants good corrosion resistance and causes selective phase corrosion [62-64, 130-134].

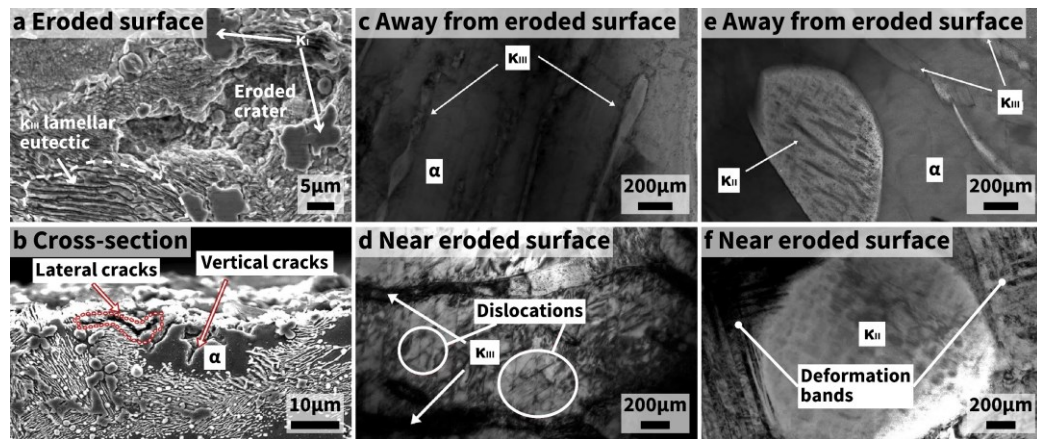


Fig. 2.18 – Cavitation erosion behaviour of nickel-aluminium-bronze [64, 135]. **a-b**, SEM images of the surface and the cross-section of NAB after cavitation erosion; **c-f**, TEM images of the cross-section away from (about 200 nm) and near (about 50 nm) the surface after 3 h of cavitation erosion.

NABs have excellent CER compared to many SSs and other copper alloys [136], which can be attributed to the strengthened structure by the hard β' and κ phases. During cavitation erosion, microcracks can frequently form at the α phase adjacent to κ precipitates instead of in the precipitate-free α phase or κ phases (**Fig. 2.18a**), and these microcracks often propagate along the α/κ phase boundary [62-64, 130, 131] and parallelly to the surface (**Fig. 2.18b**), which is attributed to both chemical (if in a corrosive medium) and physical attacks. Firstly, since the κ phase tends to have higher electronegativity than the α phase, localised galvanic corrosion can occur to the α phase at the α/κ phase boundary, where the α phase is coupled with the cathodic κ phase [63, 64, 130, 131]. Secondly, the low

SFE of the FCC α phase can improve the work-hardening ability [137, 138]. Meanwhile, since the FCC α phase also has low strain rate sensitivity and good ductility, dislocation and slip are more likely to occur (**Fig. 2.18c-f**). As the κ phases have high hardness, the movement of the crystal defects in the α phase is blocked by the α/κ phase boundary, resulting in plastic deformation and material rupture in the α phase at the α/κ phase boundary (**Fig. 2.18c-f**) [135].

Further exposure to cavitation impacts can result in the growth of microcracks and subsequent material losses, which mainly happen to the α phase, and then the exposed κ phases start to detach from the surface [62-64, 130, 131, 135]. Meanwhile, the detachment of the large κ_{I-III} phases can leave large craters and very rough surface, which not only aggravates the CE but also leaves a large area of the metal matrix for corrosion attack [139]. On the other hand, since there are numerous small but hard κ_{IV} phases embedded in the α phase, crack propagation can be inhibited by these κ_{IV} phases [135]. Meanwhile, the strength of the material beneath the surface can be greatly enhanced via the formation of dense dislocations and deformation twins due to the repeated cavitation impacts, which is beneficial to CER [135]. However, other studies argue that such a hardening effect in the subsurface can cause subsurface cracks due to the reduced fracture toughness [63, 131].

2.5 Cavitation-erosion-resistant coatings

In practice, CE is not the only concern for the hydrodynamic component. The materials can face silt erosion, corrosion, biofouling, and other issues depending on the working conditions and environments. Therefore, extra approaches are necessary to optimise and customise CE-resistant alloys reviewed previously for dealing with these issues. The most cost-effective and extensively used approach is applying protective coatings. This section reviews the commonly used coatings for fluid machinery and mainly focuses on their CE performance. These coatings can be sorted into organic and inorganic types. At present, most of the published studies on CE-resistant coatings focus on inorganic coatings. This section briefly introduces some coating techniques, followed by a review of various inorganic coatings.

2.5.1 Coating techniques

Generally, most CE-resistant coatings are deposited by thermal spraying. Thermal spraying refers to various techniques that spray melted or heated materials onto a substrate surface. Depending on the principles, the thermal spraying techniques can be classified into flame spraying, atmospheric plasma spraying, controlled-atmosphere plasma spraying, vacuum plasma spraying, arc spraying, detonation-gun spraying, high-

velocity oxygen-fuel (HVOF) spraying, high-velocity air-fuel (HVOF) spraying, cold spraying, and some other techniques developed recently. The detailed information about these thermal spraying techniques can be found in this literature [140]. In addition, some relevant techniques are briefly reviewed as follows.

High-velocity oxygen-fuel (HVOF) spraying

HVOF spraying is a feasible technique for depositing carbide and alloy coatings [140]. Most of the CE-resistant WC-based coatings are fabricated through HVOF spraying [34, 35]. A schematic of an HVOF spraying gun is shown in **Fig. 2.19**. During the HVOF spraying process, fuel is injected to an air- or water-cooled combustion chamber accompanied by oxygen. Then, the fuel-oxygen mixture is ignited, and the combustion and the exhaust gases are initiated, releasing a high-temperature (up to 3000 K) supersonic (up to 2000 m/s) jet. Next, the powder is fed into the jet, and the particles that become melted or partially melted are propelled through the nozzle. A portion of the inflight particles can eventually hit and adhere to the substrate, forming a coating [140]. If air is used instead of oxygen, the spraying process is high-velocity air-fuel (HVOF) spraying. Since the inflight time of the particles within the heat source is very short due to the acceleration by the supersonic jet, the particles exhibit low oxidation. Hence, the coating prepared by HVOF

tends to have a low oxide content, depending on the oxygen-to-fuel ratio [140]. In addition, the high particle velocity (up to 660 m/s for stainless steel particles) also provides a dense coating [141].

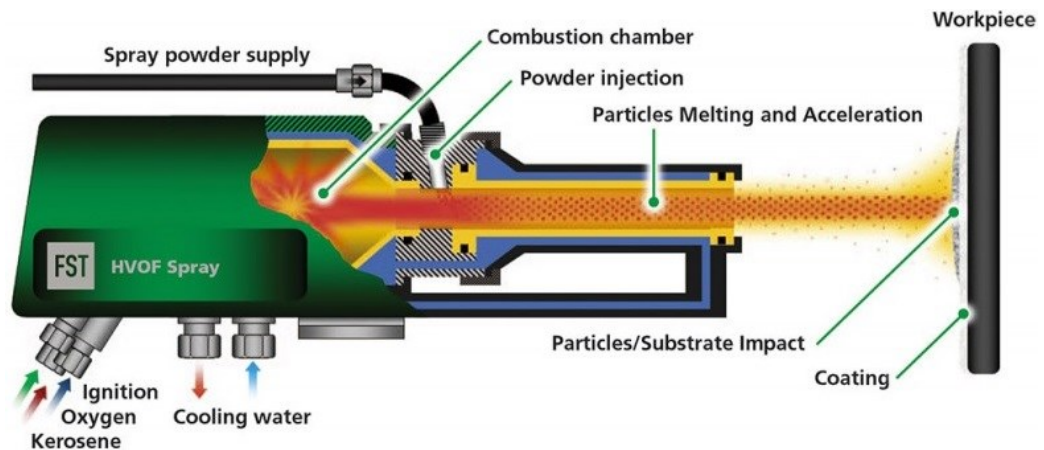


Fig. 2.19 – Schematic of an HVOF spraying gun [142].

Cold spraying

Cold spraying is very similar to HVOF spraying but with much lower thermal energy and higher kinetic energy. A schematic of a cold spraying gun is demonstrated in **Fig. 2.20**. During the cold spraying process, a stream of pre-heated (up to 600 K) high-pressure (several MPa) gas (nitrogen or helium) flows to the nozzle. Prior to the entrance of the nozzle, the compressed gas flow is further heated (up to 1500 K) by the heating element to achieve a higher flow velocity, and thus the injected powder accelerated by the compressed gas flow can reach a higher velocity. After exiting from the nozzle, some particles have gained sufficient kinetic energy (up to 1200 m/s), which guarantees the particles to exceed the

critical velocity and allows plastic deformation with a high strain rate to occur upon impact. These particles finally adhere to the surface of the substrate to form a coating [140].

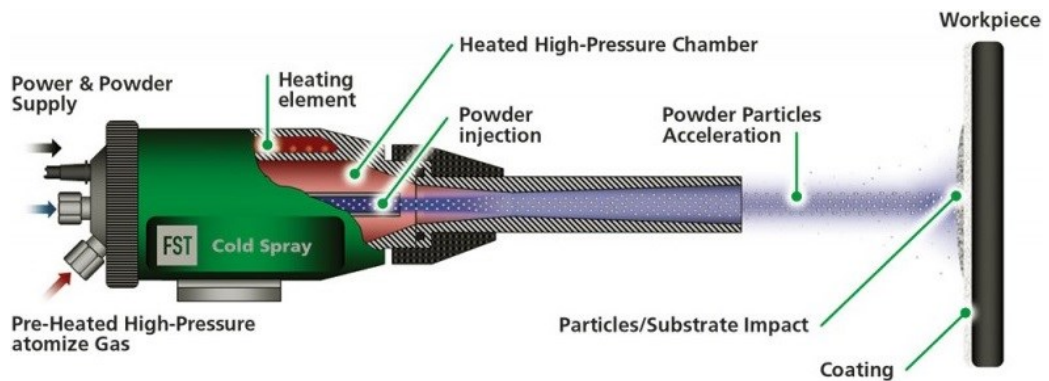


Fig. 2.20 – Schematic of a cold spraying gun [143].

Compared to HVOF spraying, the particles are subjected to much lower heat but achieve much higher velocity during the cold spraying process. Therefore, the cold-sprayed coating exhibits minimal oxide content and low porosity [144].

Laser surface melting (LSM)

Surface modification is commonly applied to improve the CER of a material since cavitation impacts only affect the surface. Compared to the conventional techniques, laser surface engineering is effective and flexible in enhancing the coating properties [145]. The input laser energy can be controlled to heat or melt the coating, providing a variety of surface treatments. As shown in **Fig. 2.21**, laser surface modification can be further sorted depending on the specific treatment applied. Laser

transformation hardening and laser surface melting (LSM) do not change the chemical composition of the material surface, while the rest of the techniques in **Fig. 2.21** will introduce new materials to the surface.

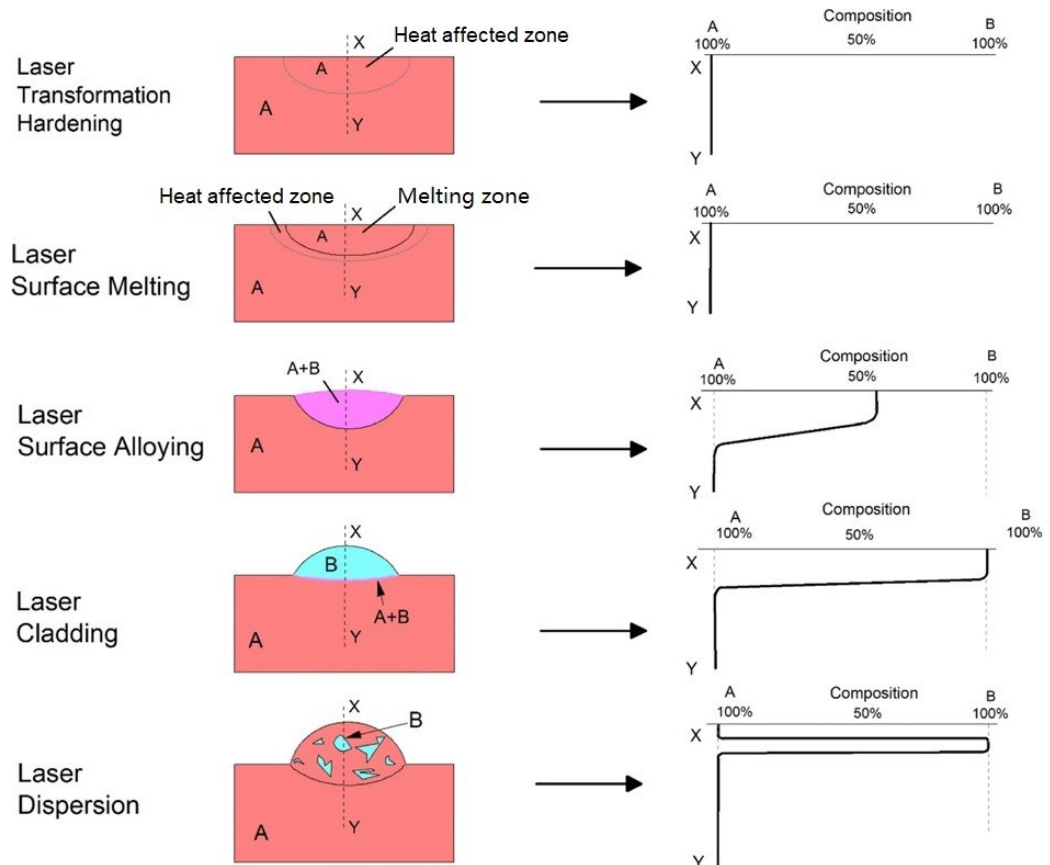


Fig. 2.21 – Schematic of various laser surface modification techniques [145].

Among these laser surface modification techniques, LSM is of particular interest in this work because the LSM process has been reported to have significant improvements in the CER of many materials. Cottam et al. reported a 1350% increase in the CER of NAB by LSM [146]. Song et al. also realised CER and corrosion resistance enhancement of cast NAB by LSM [147]. Tang et al. improved the CER and corrosion resistance of manganese-nickel-aluminium-bronze by LSM [148, 149]. Other materials,

such as cast iron [150], 316L ASS [151], and 420 MSS [152], were also found to have enhanced CER after being processed by LSM.

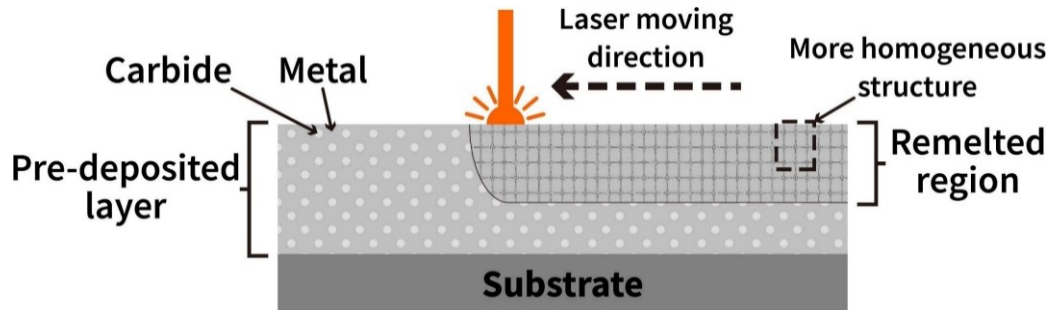


Fig. 2.22 – Schematic of laser surface melting process.

A schematic of the LSM process is demonstrated in **Fig. 2.22**. During the LSM process, the material surface is melted by a laser with high energy density. Meanwhile, the material below the surface is almost unaffected and can be regarded as a heat sink, resulting in rapid cooling (about 10^3 to 10^6 °C/s) and solidification of the molten pool [145]. Hence, a refined surface microstructure is achieved, and the microstructure is also homogenised. For example, coarse carbides in the coating can be converted into fine carbides [145].

Vacuum hot-pressing sintering (VHS)

Sintering is a heat treatment process during which loose material (a powder or a mixture of powders) is heated to a high temperature but not melted and then cooled to acquire a dense material with desired properties. A more densified material can be achieved by introducing pressure during the sintering process, and this pressurised sintering

process is known as hot-pressing. If the oxidation level of the final product is restricted, vacuum hot-pressing sintering (VHS) is a feasible method where the hot-pressing is conducted in vacuum [153]. In addition, since both high temperature and high pressure can be achieved, VHS is capable of processing carbide powders. Although only using VHS may not be able to prepare CE-resistant materials, VHS is an applicable method for making a composite with a desired chemical composition for further treatment. A schematic of a VHS device is shown in **Fig. 2.23**.

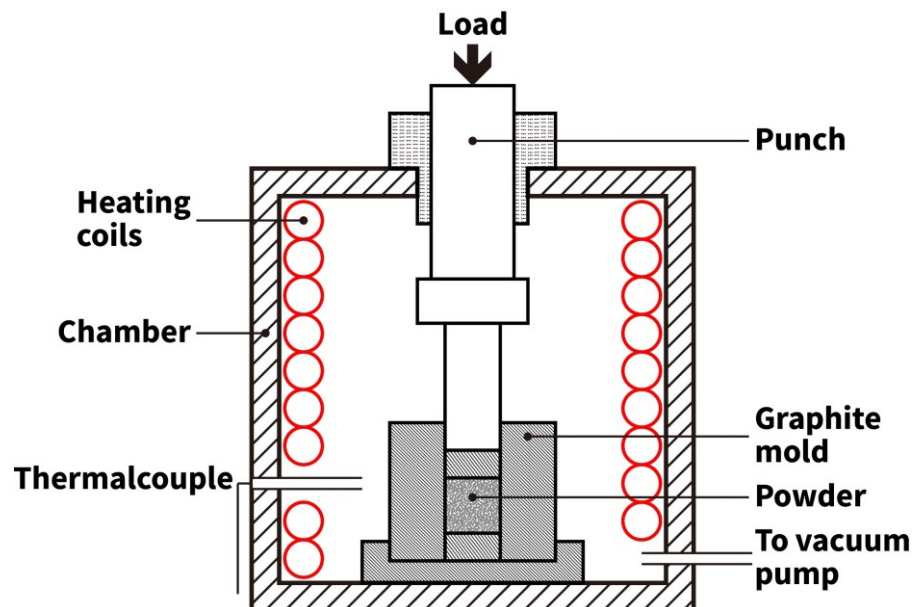


Fig. 2.23 – Schematic of a vacuum hot-pressing sintering device

2.5.2 Inorganic coatings based on commercially available alloys

CaviTec

CaviTec is an Fe-based austenitic alloy for repairing hydraulic turbines due to its good resistance to CE and corrosion [154, 155]. The weld overlays of CaviTec outperform many alloys and HVOF sprayed coatings

in CER [156-158]. The HVOF-sprayed CaviTec coating also exhibits good CER but is not as good as the weld overlays because of defects, oxides, and the removal of the splat prior to undergo structural phase transition due to weak adhesion at inter-splat boundaries (**Fig. 2.24**) [159].

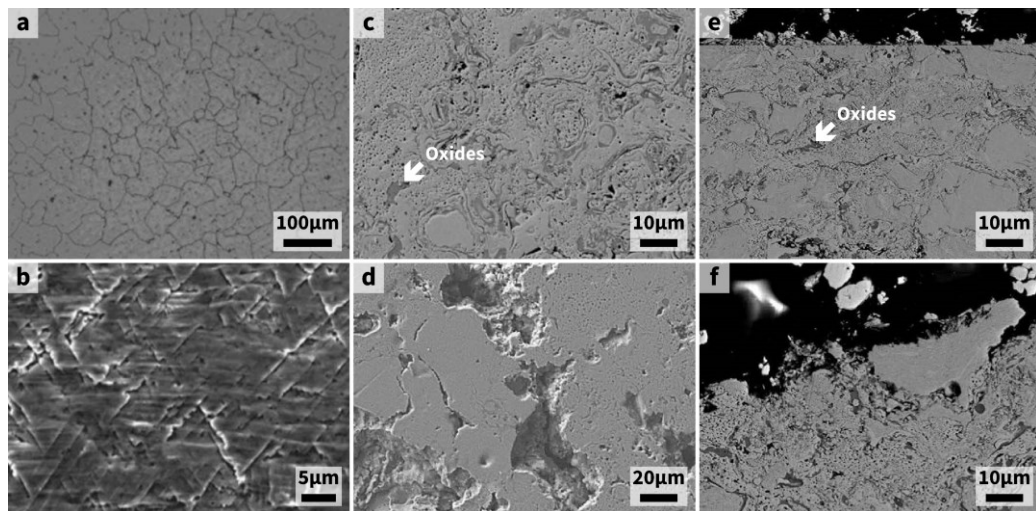


Fig. 2.24 – The weld overlay of CaviTec and the HVOF-sprayed CaviTec coating subjected to cavitation erosion [157, 159]. **a**, Light micrograph of CaviTec weld overlay; **b**, SEM image of CaviTec weld overlay after CE test for 10 h, where the triangular structures indicate the existence of phase transformation; **c&e**, SEM images of the surface and cross-section of the CaviTec coating; **d&f**, The CaviTec coating after 2-h CE test, where phase transformation was not observed.

Stellite

Stellite series are Co-based alloys with fine carbide microstructure which were originally developed as the materials for cutting tools around 1910 and were found to be wear-resistant around 1970 [160]. The subsequent studies suggest Stellite series also exhibit effective CER, possibly due to the low SFE and the energy absorption by the stress-induced phase transformation [161-163]. For the Stellite coatings, most of them are

based on Stellite 6. The HVOF-sprayed Stellite 6 coating has acceptable CER and good silt erosion resistance [156]. The weld overlay of the Stellite 6 has much better resistance to CE and silt erosion than its HVOF sprayed version and outperforms MSS 13Cr4Ni and other SSs for hydraulic components, and thus many researchers suggest that the weld overlay of Stellite 6 is applicable for repairing worn hydrodynamic components [164-166].

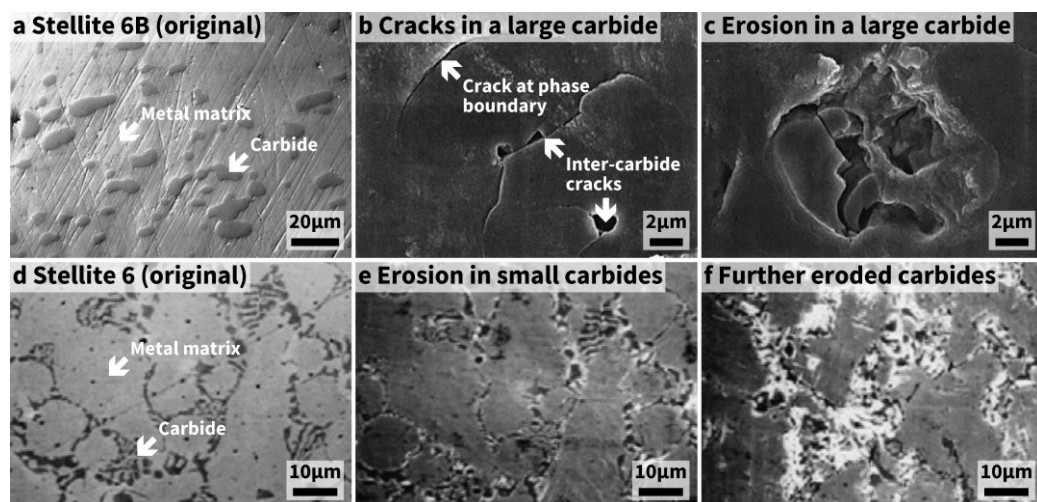


Fig. 2.25 – The weld overlays of two Stellite alloys subjected to cavitation erosion [164, 165]. a, Microstructure of Stellite 6B weld overlay with large carbides; **b,** Cracks in a large carbide after CE; **c,** A eroded large carbide after CE; **d,** Microstructure of Stellite 6 weld overlay with small carbides; **e-f,** After 5-h and 10-h CE tests.

According to the SEM images of the damaged surface from these studies (**Fig. 2.25**), it seems the coatings with large carbide particles [164] have more effective resistance than the coatings with the fine carbide microstructure at the inter-dendrite [165, 166], possibly attributed to the cracking at the inter-dendritic eutectic carbides due to the cooling process resulting in the eutectic carbides being preferentially eroded. However,

preferential erosion also frequently occurs to the Co-matrix at the phase boundaries and to the interface between two individual carbides, which subsequently causes the detachment of the carbides after further exposure to cavitation [164]. Apart from overlay welding, laser cladding can also deposit the Stellite 6 coating, whose resistance to CE, corrosion, and silt erosion is as good as the weld overlay [167, 168]. Meanwhile, some studies successfully improve the CER of the Stellite coatings by optimising the cladding process [169] and the mixed use of different Stellite products [170, 171]. In addition, it is worth mentioning that the study on the CE performance of the Stellite 6 coating in liquid sodium suggests the coating has a potential application in the centrifugal sodium pumps of a fast reactor [172].

Inconel

Inconel series are high-performance Ni-based superalloys with superior mechanical properties, corrosion resistance, and temperature endurance, which are commonly used in nuclear and aerospace industries [173, 174]. Studies have shown that some Inconel alloys also possess good CER attributed to the stress-induced twinning effect and high hardness [175-177]. For the weld overlays and the sprayed coatings, there are tremendous studies evidencing the good mechanical properties and

effective resistance to wear, erosion, corrosion, and erosion-corrosion [178-182]. Nevertheless, only a few studies investigate the CE behaviour [183-185]. Two studies deposited Inconel coatings onto the SS substrate by cold spraying, but the results show that the cold sprayed Inconel coating cannot resist CE effectively [183, 184]. Another study explored the feasibility of using the selective laser melted Inconel series as a low-cost alternative for the pipes that transport cryogenic fluids in rocket engines, and the results show that the selective laser melted Inconel 718 may have good CER [185]. The lack of the studies on the CE performance and the outstanding properties of the Inconel coatings suggests that further research on the CER of the Inconel coatings may be rewarding.

2.5.3 WC-based cermet coatings

As mentioned before, hydraulic components can face much more complex issues other than only CE. For hydro turbines, silt erosion is also a primary concern if the site is located at a sediment-rich river, which can cause severe erosion and performance degradation of the turbines [29, 34, 35]. WC-based cement coatings, especially those deposited by the HVOF spraying techniques, can provide excellent resistance to cavitation and slit erosion, and thus they are the most extensively used coatings for the protection of the hydro turbines [34, 35, 186-190]. Generally, the WC-Co

and the WC-CoCr coatings are the most commonly used HVOF-sprayed WC-based cermet coatings for resisting CE. In deionised water, the WC-Co and the WC-CoCr coatings have similar CER [191]. However, the WC-CoCr coatings are preferred for operating in corrosive environments because the WC-Co coatings can be easily damaged by the dissolve of Co matrix phase, while the WC-CoCr coatings can exhibit the formation of protective surface oxides [191]. For the application in the marine environment, biofouling is another critical concern. Despite there being very few studies on the anti-fouling ability of the WC-based cermet coatings, a recent field study reported that the HVOF-sprayed WC-based cermet coatings exhibited much better resistance to biofouling compared with the air-plasma-sprayed $\text{Al}_2\text{O}_3\text{-TiO}_2$ coating (a typical protective coating for hydraulic actuator piston rods in marine vessels) [192].

The outstanding CER of the HVOF-sprayed WC-based cermet coatings can be attributed to the combination of the hard WC phase and the ductile metallic binder phase. Ideally, the hard phase directly resists the cavitation impact, and the ductile phase dissipates the impact energy by forming dislocations, slips, twins, and the movement of these crystal defects (similar to DSS and NAB in **Fig. 2.17** and **Fig. 2.18**). Nevertheless, the inter-splat boundaries and the defects such as the pre-existing pores in the HVOF-sprayed WC-based cermet coatings can bring about various

failure modes.

Due to the weak adhesion at the inter-splat boundaries, cavitation impacts can cause the removal of the splat before the formation of dislocations, slips, and twins, in the ductile metal matrix. As a result, the metallic phase in the HVOF-sprayed WC-based coatings can be susceptible to cavitation impacts, and hence a typical failure mode for the HVOF-sprayed WC-based cermet coatings is the erosion of the binder phase followed by the microcrack propagation along with the phase boundaries causing the subsequent brittle detachment of the WC particles (**Fig. 2.26c**) [193-201]. On the other hand, as the adhesion strength at the phase boundary can be quite weak for the sprayed coatings, the other typical failure mode is the sudden detachment of the WC particles leaving the metallic binder phases beneath unprotected, which causes the accelerated erosion due to the unprotected metallic binder phases being severely eroded (**Fig. 2.26c**) [193, 197, 198]. Furthermore, the cavitation impact at the weak site or the pores on the coating surface can initiate the formation of microcrack, and further impacts can cause crack propagation. Although crack propagation can be hindered by the hard WC particles, the microcrack may grow along with the inter-splat boundaries and bypass the WC particles due to the weak adhesion at the inter-splat boundaries or the selective corrosion at the phase boundaries (if in corrosive

mediums), resulting in severe detachment of the surface material (**Fig. 2.26e-f**) [191, 193-196].

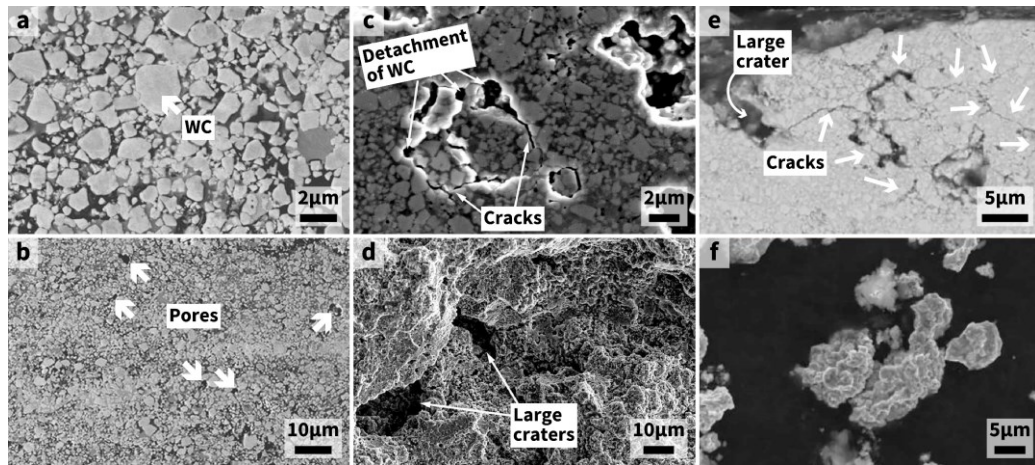


Fig. 2.26 – HVOF-sprayed WC-CoCr coatings subjected to cavitation erosion [193, 194, 202]. **a-b**, Cross-section of the coating in high and low magnifications; **c**, Mildly eroded surface; **d**, Severely eroded surface after 20-h CE test; **e**, Cross-section of the eroded coating; **f**, Debris from the eroded coating.

It is well acknowledged that microhardness, fracture toughness, and porosity are the most crucial factors correlated to the CER of the HVOF-sprayed WC-based coatings. High fracture toughness indicates a good adhesion strength at the interfaces, such as the phase and the inter-splat boundaries, and thus the sprayed coating with high fracture toughness can effectively absorb the cavitation impact energy and inhibit the formation and propagation of the microcracks [191, 201, 203-207]. The porosity of the coatings should be minimised since pores are usually considered the potential sites for crack nucleation and are preferentially damaged during CE [191, 196, 197, 205]. As for microhardness, it may not be a reliable criterion when comparing the coatings with different metallic binder phases [201]. However, many studies still took

microhardness into consideration and found it positively correlated to the CER of the HVOF-sprayed WC-based coatings because it indicates the content of the defects in the sprayed coatings to some extent [190, 191, 196-198, 207-209].

Therefore, improving the CER of the HVOF-sprayed WC-based cermet coatings is usually from the perspectives mentioned above, and numerous studies have given positive results via various approaches. Heat treatment can be the most straightforward post-deposition approach. For example, Du et al. reported that heat treatments could effectively reduce the porosity and improve the interface adhesion of the HVOF-sprayed WC-12Co coating, and the CE rate of the heat-treated coating was almost halved compared to the as-sprayed coating [209]. Post-melting is also an effective post-deposition approach for improving the CER of thermal-sprayed coatings. As mentioned before, the microcracks tend to form and propagate at the inter-splat boundaries, while post-melting can reduce the inter-splat boundaries and disrupt the intrinsic lamellar microstructure of the thermal sprayed coatings. Meanwhile, fracture toughness can be improved as well (**Fig. 2.27**) [201]. Therefore, post-melting is considered a feasible approach to enhance the CER of the thermal-sprayed coatings.

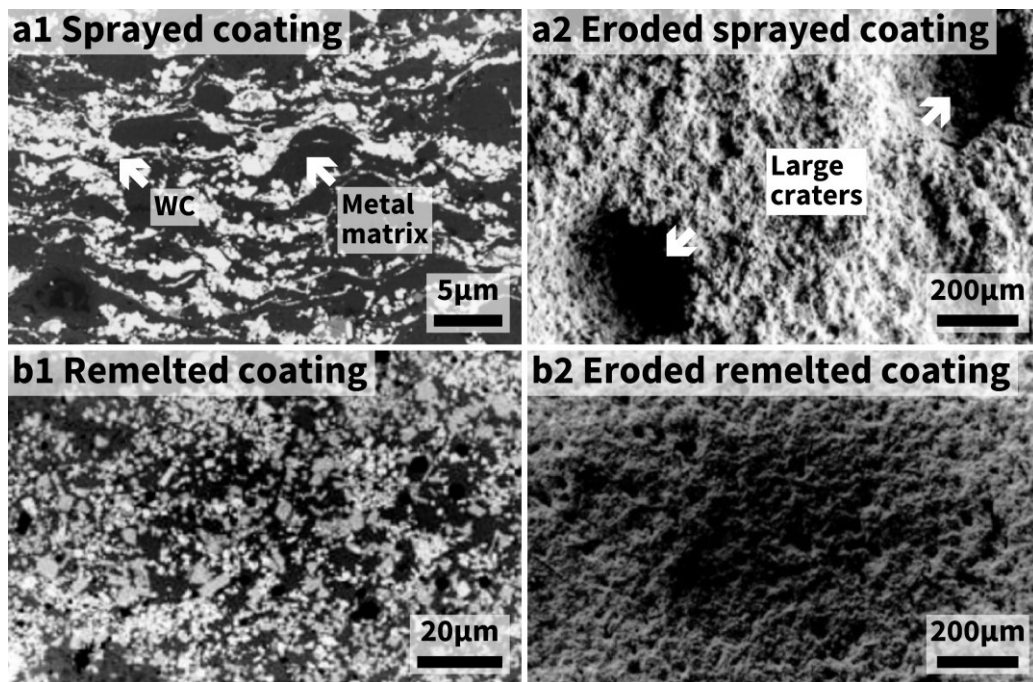


Fig. 2.27 – HVOF-sprayed and post-melted WC-CoNiCr coatings subjected to cavitation erosion [201]. a, The sprayed coating; b, The sprayed coating after post melting; 1, Cross-sections; 2, Eroded surfaces.

Optimising spraying parameters is a challenging but applicable approach to improving the quality of HVOF-sprayed WC-based cermet coating [202]. Kanno et al. found that the HVOF-sprayed WC-CoCr coating exhibited a dense microstructure and superior CER if the combustion pressure was 0.8 MPa during deposition [207]. Becker et al. reported that the oxygen-fuel ratio could greatly affect the CE of the HVOF-sprayed WC-20Cr₃C₂-7Ni coating [210]. Ding et al. suggested that using liquid fuel could provide HVOF-sprayed WC-10Co-4Cr coatings with lower porosity and better CER compared with gas fuel (**Fig. 2.28**) [194], and similar results were also found by Lamana et al. from the HVOF-sprayed WC-Co coatings [206]. Wang et al. reported that HVOF-sprayed WC-10Co-4Cr coating was less likely to undergo decarburisation and had lower porosity,

higher hardness, higher fracture toughness, and thus better CER than the HVOF-sprayed WC-10Co-4Cr coating [208]. Varis et al. evaluated the compressive residual stress of the HVOF- and the HVOF-sprayed WC-10Co-4Cr coatings and suggested that the higher compressive residual stress of the HVOF-sprayed coating might contribute to better CER [211].

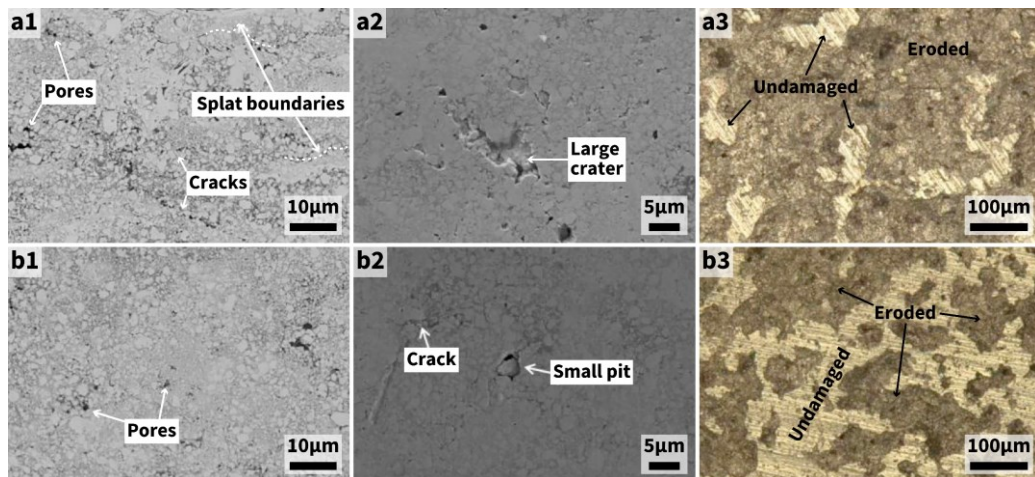


Fig. 2.28 – WC-CoCr coatings deposited by HVOF spraying using gas and liquid fuels subjected to cavitation erosion [194]. a, The coating prepared by using gas fuel; b, The coating prepared by using liquid fuel; 1, Cross-sections; 2, Surfaces at the beginning of CE test; 3, Eroded surfaces after 2-h CE test.

Apart from spraying parameters, many studies have suggested that the properties of the feedstock powder can have a significant influence on the CER of the HVOF-sprayed WC-based cermet coatings. Hong et al. deposited an HVOF-sprayed coating using a near-nanostructured WC-10Co-4Cr powder and suggested that the amorphous phase, high hardness, and high fracture toughness of the coating contributed to the good resistance to corrosion and CE [70, 198]. Li et al. prepared two HVOF-sprayed WC-10Co-4Cr coatings from a conventional micro powder and a nano-micron bimodal powder, finding that the bimodal coating had

lower porosity, higher hardness, and better CER in artificial seawater [196]. Ding et al. have performed a series of research on the HVOF-sprayed WC-based cermet coatings with WC particles of different sizes.

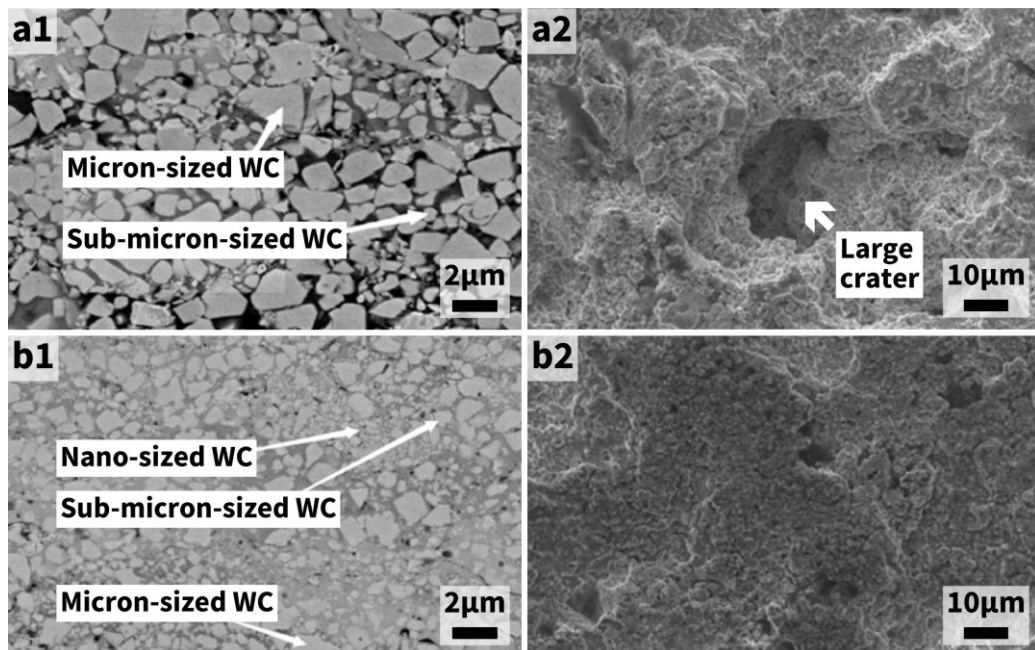


Fig. 2.29 – HVOF-sprayed WC-CoCr coatings with different WC size distributions subjected to cavitation erosion [203]. a, The conventional HVOF-sprayed WC-CoCr coating; b, The coating with WC particles whose size ranges from nano to micron; 1, Cross-sections; 2, Eroded surfaces.

The preliminary studies investigated the CER of the HVOF-sprayed WC-12Co using the WC-12Co powders with different WC size, indicating that CER was correlated to the size of the WC, and the coatings with large-sized WC particles had less effective CER than the other coatings with small-sized and mixed-sized WC particles [212, 213]. Recent studies by Ding et al. prepared various HVOF-sprayed WC-10Co-4Cr coatings using a nanostructured powder, a nano-micron bimodal powder, and a nano-submicron-micron multi-scaled powder, respectively, among which the coating with multi-scaled WC particles exhibited the best CER attributed

to its lowest porosity and highest fracture toughness (**Fig. 2.29**) [194, 203-205].

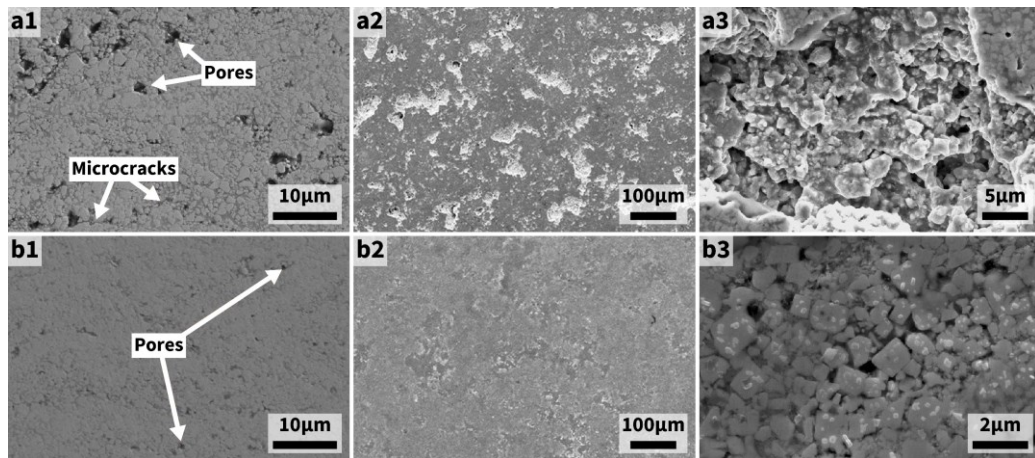


Fig. 2.30 – HVOF-sprayed WC-CoCr and WC-Ni coatings subjected to cavitation erosion [200]. **a**, HVOF-sprayed WC-CoCr coating; **b**, HVOF-sprayed WC-Ni coating; **1**, Cross-sections; **2**, Eroded surface after 6-h CE test (low magnification); **3**, Eroded surface after 6-h CE test (high magnification).

Altering the ratio and the chemical composition of the metallic binder phase is also an option to improve the CER of the HVOF-sprayed WC-based cermet coatings. Lamana et al. investigated the CER of the WC-12Co and the WC-17Co coatings sprayed by HVOF and found that the increased content of Co could provide improved fracture toughness and CER [206]. Lima et al. prepared HVOF-sprayed WC-based coatings using an equally blended powder of WC-12Co and NiCr [201]. The results showed that the CER of the WC-Co-NiCr coating was better than the WC-12Co coating due to the improved fracture toughness, and the CER of the

former was greatly enhanced after post-melting. Lin et al. reported that the HVOF-sprayed WC-10Ni coating exhibited higher elastic modulus and better CER than the WC-10Co-4Cr coating (**Fig. 2.30**) [200], while Hong et al. found that the CER of the HVOF-sprayed WC-20Cr₃C₂-7Ni slightly outperformed the WC-10Ni coating [214].

The above two studies also suggested that a high hardness (H) to elastic modulus (E) ratio and a high H^3/E^2 ratio had positive effects on the plasticity and elastic energy absorption during CE [200, 214]. Korobov et al. studied the CE performance of the HVAF-sprayed WC-10Co-4Cr and the WC-20Cr₃C₂-7Ni coatings in the alkaline environment, showing that the WC-20Cr₃C₂-7Ni coating had better CER attributed to the improved hardness and plasticity to the dissolution of Cr [215]. In addition, the materials for modification are not limited to metals or carbides. For example, Thakur et al. found that the HVOF-sprayed nano WC-10Co-4Cr coating modified by the multi-walled carbon nanotubes in the binder matrix could effectively increase the fracture toughness and the slit erosion resistance [216].

Apart from spraying techniques, laser processing techniques are applicable to fabricate WC-based coatings with good CER. Cheng et al. prepared laser surface alloyed 316L ASSs with WC-Ni and WC-Co powders [217]. The results show that the CER of the laser surface alloyed

316L ASSs was improved, and the best resistance was achieved by the sample alloyed with the WC-Co powder, possibly attributed to the low SFE and the presence of martensitic transformation by the Co-rich matrix. Lo et al. extended the previous study by laser surface alloying 316 ASSs with coarse [218] and fine [219] WC powders. The significantly enhanced CER was achieved due to the laser surface alloyed samples exhibiting a microstructure composed of dendritic carbides and eutectic inter-dendritic carbide/ γ -FeCrNiW, which could effectively resist cavitation damage. However, the large WC particles in the samples alloyed with the coarse WC powder could be subjected to severe brittle detachment [218]. Hence, the best CER was achieved by the sample alloyed with the fine WC powder, which was 30 times higher than the as-received 316 ASS [219]. Other studies have also reported the enhanced CER of various materials that were laser surface alloyed with WC or the WC-consisted materials [220-223]. Besides laser processing, there are other interesting techniques that fabricate WC-based cermet coatings with effective CER, such as chemical vapour deposition [224] and microwave cladding [225].

2.5.4 Fe-based amorphous/nanocrystalline coatings

Although the thermal-sprayed WC-based cermet coatings are most extensively used to protect hydrodynamic components, researchers are

seeking alternatives due to the high cost [35]. Thermal-sprayed Fe-based amorphous/nanocrystalline (A/N) coatings exhibit high wear and corrosion resistance and relatively low cost [226-230]. These papers also reviewed the effects of various spraying techniques [226, 228] and alloying elements [226, 227] on Fe-based A/N coatings, which may be valuable for the design and development of Fe-based A/N coatings. Despite literature reporting that the CER of the Fe-based A/N coatings could be lower than the WC-based cermet coatings in some cases [195, 231], thermal-sprayed Fe-based A/N coatings are still promising in the applications generally using WC-based cermet coatings.

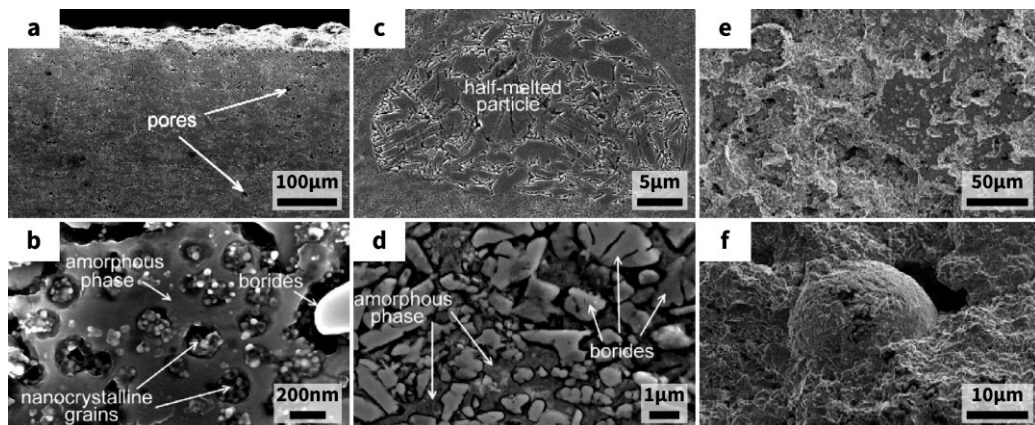


Fig. 2.31 – HVOF-sprayed Fe-based A/N coating subjected to cavitation erosion [232]. a, SEM image of the cross-section in low magnification; **b-d**, SEM images of the cross-section in high magnification showing the microstructures in the coating; **e**, Eroded surface; **f**, Erosion at the interface between amorphous matrix and a partially melted particle.

Wu et al. prepared HVOF-sprayed FeCrSiBMn A/N coating (**Fig. 2.31**), and the CER of the coating outperformed MSS 13Cr5Ni in a noncorrosive medium [232]. Wang et al. fabricated FeCrNiBSiNb, FeCrBSiWNb, and 18Cr9Ni coatings by high-velocity arc spraying, and the results showed

that both high-velocity-arc-sprayed Fe-based A/N coatings exhibited much better CER than the 18Cr9Ni coating [233]. The two preliminary studies also suggested that the cavitation damage tended to initiate at the edges of the pores and the interfaces of the splats [232, 233]. Kim et al. also reported similar results and found that the CER of the HVOF-sprayed Fe-based A/N coating was negatively correlated to porosity [234]. Meanwhile, the interfaces formed by the unmelted or partially melted particles were susceptible to CE [232-234].

Hong et al. and Qiao et al. have conducted a series of studies on the CE of the HVOF-sprayed Fe-based A/N coatings [195, 235, 236]. The preliminary study reported that the HVOF-sprayed Fe-based A/N coating had lower CER but higher corrosion resistance in 3.5 wt.% NaCl solution compared to the HVOF-sprayed WC-based cermet coating [195], suggesting the potential application of Fe-based A/N coatings in corrosive environments. Then, Hong et al. studied the influences of the spraying parameters on the microstructures and CER of the HVOF-sprayed Fe-based A/N coatings and found the most optimised spraying parameters that provided minimised porosity, highest hardness, and greatest CER [235]. Qiao et al. conducted a further study on the failure mechanism of the HVOF-sprayed Fe-based A/N coating exposed to CE [236]. Besides the results similar to the previous literature [232-234], the study found that

a part of the amorphous phase was subjected to nanocrystalline transformation first and then removed from the coating during CE [236]. Furthermore, the study pointed out that high fracture energy and small grain size were beneficial to improving the CER of the HVOF-sprayed Fe-based A/N coating.

2.5.5 Other ceramic/cermet coatings

As the cost of WC is a bit high, researchers have been screening other CE-resistant cermet coatings at a low cost. Cr₃C₂-based cermet coatings have corrosion, slit erosion, and CE resistance that is similar to the WC-based cermet coatings [191, 210, 237-242], and thus Cr₃C₂-based cermet coatings can be a possible low-cost substitute for the WC-based cermet coatings other than Fe-based A/N coatings. The good CER of the Cr₃C₂-based cermet coatings is attributed to the composition of the ductile and the brittle phases, and their failure mode also follows that of the WC-based cermet coatings [191, 237, 242].

The CE behaviour of yttria-stabilised zirconia (YSZ) and YSZ-based coatings is also investigated by some studies, as the bulk YSZ can undergo tetragonal-monoclinic martensitic phase transformation during CE [243]. Nevertheless, the CER of the YSZ and YSZ-based coatings was disappointing compared to the HVOF-sprayed WC-based cermet coatings

[244-246], possibly due to the adhesive failure [247].

The Al₂O₃-based coatings attract researchers by their extremely low cost, among which the Al₂O₃-TiO₂ coating is the most promising one due to the good mechanical properties and some antifouling ability [248-251]. Although many studies found the poor CER of the Al₂O₃-TiO₂ and other Al₂O₃-based coatings due to the poor adhesion [252-256], a few studies achieved acceptable CER of the Al₂O₃-based coatings, such as flame-sprayed Al₂O₃-40%TiO₂/NiMoAl coatings [257], Rodojet-sprayed Al₂O₃-50%TiO₂ coatings [258], and HVOF-sprayed Al₂O₃-40%YSZ/ZrO₂ coatings [259].

Laser surfacing with engineering ceramics can offer effective CER. Apart from WC and Cr₃C₂, Cheng et al. evaluated the CER of the ASS S31603 laser-surface-modified with SiC, TiC, CrB₂ and Cr₂O₃ [260], finding that the addition of CrB₂ improved the CER of the ASS S31603 by about 9 times. The ASS S31603 laser surface modified with the other engineering ceramics except for Cr₂O₃ also provided enhanced CER [260].

2.6 Improving cavitation erosion resistance

In previous **Subsection 2.5.3**, the approaches to improving the CER of WC-based coatings have been reviewed. This section reviews a few other studies where the change of microstructure is found to play an important

role in the enhancement of CER, as this thesis is particularly focused on the microstructural behaviours of the materials during CE. In addition, the materials which can potentially improve the CER of the coatings are briefly reviewed.

Cheng et al. applied heat-treatment to a austenitic NiTi alloy by aging at 200-600 °C, and their study pointed out that proper heat treatment could enable the coexistence of superelastic austenite and superplastic (large tensile elongation before failure) martensite in the NiTi alloy, providing exception long incubation period and remarkable CER (**Fig. 2.32**) [261].

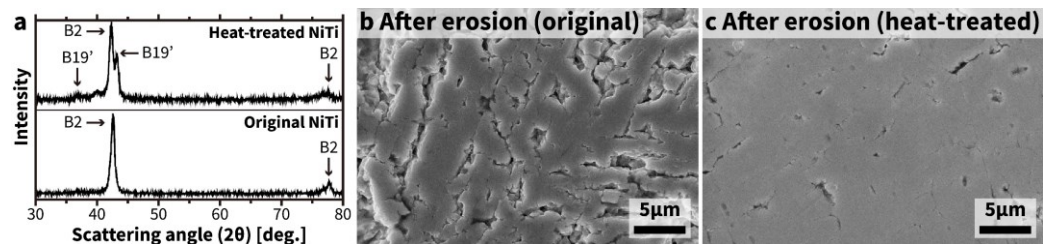


Fig. 2.32 – Microstructure and cavitation erosion behaviour of NiTi alloys with and without heat-treatment [261]. **a**, XRD results showing that the heat-treated NiTi alloy exhibits both austenite (B2) and martensite (B19') while the original NiTi alloy is fully austenite (B2); **b-c**, The surface of the NiTi alloys after CE test.

As reviewed in **Subsection 2.4.2**, the phases in NABs can affect the cavitation erosion-corrosion resistance. Therefore, the configuration of the microstructure of the NAB via certain treatments may enhance the resistance. Qin et al. found that the cavitation erosion-corrosion resistance of the cast NAB can be improved by heat treatments such as normalizing and quenching (**Fig. 2.33**) [139]. The quenched and the quenched-aged NABs do not have any large κ phases, which effectively minimises

selective phase corrosion (**Fig. 2.33c**). The homogenised and refined microstructure after the quenching or the quenching-ageing allows the uniform corrosion on the surface, and thus the formation of the passive protective film is in good condition. Meanwhile, the dense and homogeneous distribution of the hard β' and the κ phases can strengthen the resistance to cavitation impacts. In addition, the evenly dispersed κ phases with supersaturated Ni and Al also result in the formation of a uniform passive film. Wu et al. also reported similar findings from the heat-treated NAB [262]. In addition, the microstructure of NAB can be optimised for enhancing cavitation erosion-corrosion resistance via friction stir processing [263-266].

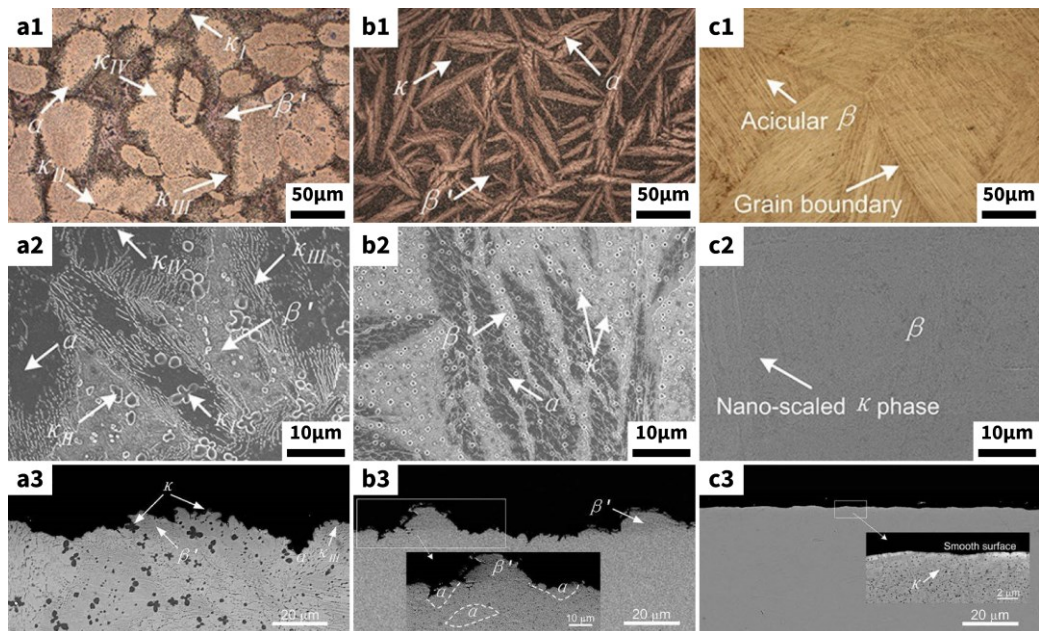


Fig. 2.33 – Microstructure and cavitation erosion behaviour of nickel-aluminium-bronzes post-treated by different method [139]. a, As-cast NAB; b, Normalized NAB; c, Quenched NAB; 1, Light micrographs of the cross-sections; 2, SEM images of the cross-sections; 3, SEM images of the eroded cross-section.

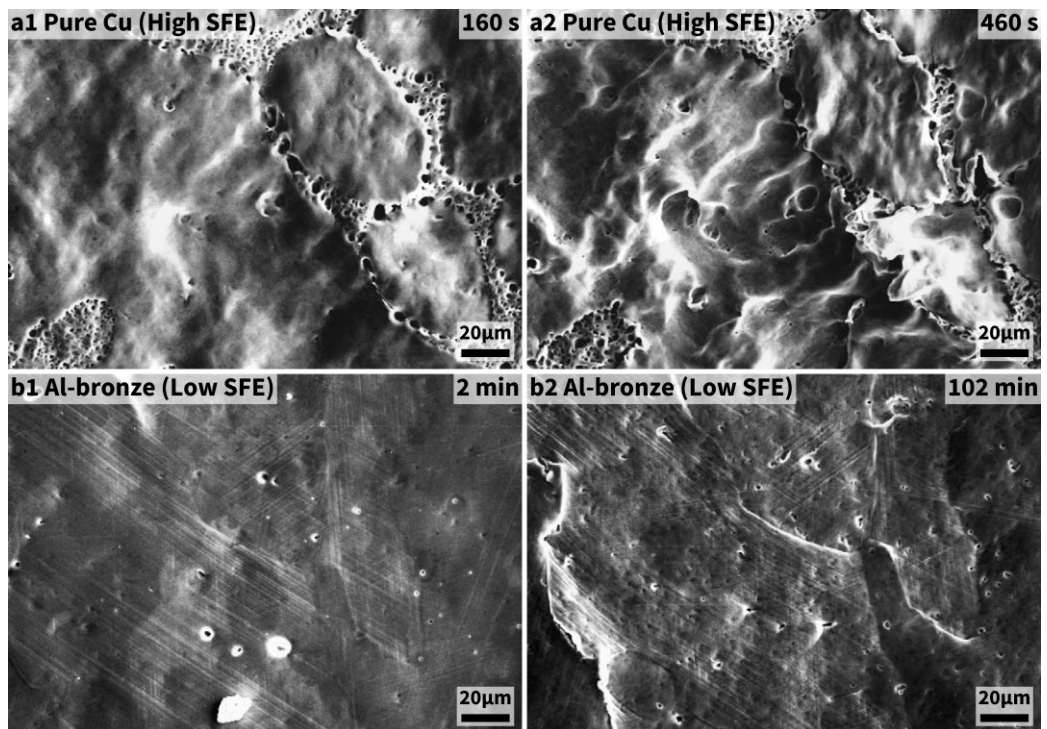


Fig. 2.34 – Microstructural evolution of pure copper and aluminium-bronze exposed to cavitation for different durations [267]. a, Pure copper; b, Aluminium-bronze.

As mentioned previously, the material with low SFE may have good CER.

Zhang et al. reduced the SFE of α -phase aluminium-bronzes to study the effects of SFE on CER by increasing the aluminium content [267]. The studied found that SFE was negatively correlated to CER. For the materials with high SFE, cross-slip is frequently formed during the exposure to cavitation, leading to the wavy slip mode of deformation (**Fig. 2.34a1**). Thus, highly localised plastic flow can occur at the early stage, which causes the formation, growth, coalescence of the microcracks (**Fig. 2.34a2**), resulting in a high erosion rate. The low SFE can inhibit the formation of cross-slip via preventing the recombination of partial dislocations [103]. Hence, different from the large craters in high SFE

materials (**Fig. 2.34a**), planar slip is the dominant plastic deformation mode in low SFE materials, and the erosion is very mild (**Fig. 2.34b**). The studies on other alloys also indicate that good CER is correlated to the low SFE [268, 269]. For example, a recent work by Szala et al. reports that nitrogen ion implantation can remarkably enhance the CER of the hot isostatically pressed Stellite 6 alloy because the nitrogen ion implantation converts the HCP (hexagonal close-packed) phase to the FCC phase with low SFE, which allows the Co-based matrix effectively to consume the cavitation impacts by work-hardening effect and stress-induced phase transformation [268].

For the WC-based coatings, apart from what have been mentioned in **Subsection 2.5.3**, the addition of Cr to the coatings may have positive effects on the CER. As an alloying element, Cr is known for its outstanding corrosion resistance and high hardness, which can effectively improve the corrosion and oxidation resistance of coatings [270, 271]. Bordeasu et al. found that the Ni-Cr ratio can affect the CER of steels [272]. St-Georges fabricated laser-cladded NiCr-WC coatings exhibited good abrasive wear resistance [273]. Tam et al. reported that the CER of laser-cladded NiCrFe-WC was much higher than that of brass [220].

Apart from Cr, adding rare earth elements during the fabrication of coatings may also improve the CER. Literature reported that when being

alloyed with metals, rare earth elements, such as Ce and La, can reduce the melting point of the alloy system and accelerate the nucleation rate [274]. For the Fe-based and the Ni-base coatings deposited via laser-cladding, the addition of Ce and La can greatly improve coating quality and thus enhances wear and corrosion resistance [275-277]. On the other hand, the addition of rare earth elements is found having a positive effect on the CER of DSS, NAB, and the HVOF-sprayed WC-10Co-4Cr coating [278-280].

2.7 Summary of the literature review

2.7.1 Strategies for achieving good cavitation erosion resistance

The followings are the strategies for achieving good CER concluded from the studies on the CE-resistant inorganic materials reviewed previously:

1. Low SFE

The material with low SFE can prevent the recombination of partial dislocations, resulting in the inhibition of the formation of cross-slip, and fatigue crack is less likely to occur. Meanwhile, the work-hardening ability is benefited from low SFE. Therefore, the low stacking fault energy usually indicates good CER.

2. Stress-induced phase transformation

Some materials exposed to cavitation impacts can exhibit stress-

induced phase transformation by consuming a portion of the impact energy. As a result, the deformation by the impact is reduced, and the severity of CE is mitigated.

3. Combination of ductile and hard phases

The high strength of the hard brittle phase can directly resist the cavitation impacts, while the ductile phase consumes the impact energy by forming dislocations, slips, twins, and the movement of these crystal defects. Therefore, good CER can be realised by combining ductile and hard phases.

4. Minimisation of defects

Defects, such as pre-existing pores and cracks, are negatively correlated to CER, since CE can preferentially attack defects. Hence, another frequently adopted strategy for enhancing the CER of the materials is minimising these defects.

2.7.2 Research gaps

In reviewing the literature about the development of the CE-resistant materials, the work presented in this thesis attempts to make progress towards the following aspects:

1. Enhancement in the CER of the WC-based coatings

The HVOF-sprayed WC-based cermet coatings are the most

successful ones in protecting hydrodynamic components against CE and have been extensively used for now. However, these WC-based cermet coatings are quite expensive [35]. Therefore, researchers have been seeking low-cost substitutes, such as Fe-based A/N coatings and other cermet coatings with inexpensive ceramics, but the application of these coatings has not been realised yet. On the other hand, a more conservative but effective choice is enhancing the CER of the WC-based coatings to extend the service life. Nevertheless, most relevant studies only achieved minor improvements in the CER of the WC-based coatings.

2. Relationship between microstructure and CE performance

Apart from what was mentioned in **Subsection 2.7.1**, the mechanical properties of the coatings, including microhardness and fracture toughness, are also correlated to the CER, but cannot dominate the CER. This is because the mechanical properties of the coatings are dependent upon the microstructural features and the defects of the coatings. Nevertheless, a considerable number of studies on the development of CE-resistant coatings pursued the accomplishment of excellent mechanical properties but unintentionally neglected the effect of microstructure on the CE

performance. In addition, although many studies investigated the behaviours of different microstructures in response to CE, the analyses were based on the post-mortem examination, leaving the microstructural evolution during CE unrevealed.

2.7.3 Selection of materials and processing methods

This research project aims to develop CE-resistant materials and investigate the effects of microstructure on the CE behaviours of the materials. As the combination of ductile and hard phases may provide good CER, the target materials are supposed to have ductile phases and hard phases. WC is selected as the hard phase since WC-based cermet coatings exhibit good CER. To minimise variables, the ductile phase of the material should be monoalloy, and Cr, Co, and Ni are the potential choices. Ni is selected in this work for two reasons. Firstly, Ni has an FCC structure which may exhibit low SFE. Secondly, there is an optimised method using cold spraying to pre-deposit Ni-WC composites with minimised oxide [281]. In addition, vacuum hot-pressing sintering (VHS) is also used to prepare Ni-WC composites.

As conventional heat-treatment techniques cannot significantly change the microstructure of WC-based composites, the post-treatment with a high energy input is required. Meanwhile, the post-treatment that can

introduce oxides or other impurities is unfavourable, as the materials with and without post-treatment are supposed to be compared. Therefore, laser surface melting (LSM) is selected as the post-treatment because the rapid solidification during LSM can provide altered microstructure with minimised oxide.

Chapter 3

Materials and experimental methods

3.1 Materials

In this work, laser surface melting (LSM) was introduced to the cold-sprayed Ni-WC composite coating and the sintered composites of Ni-WC, Ni-WC-CeO₂, and NiCr-WC. The cold-sprayed coating was deposited onto 316L austenitic stainless steel (ASS) substrate. The ASS 316L was also used as the reference material for evaluating cavitation erosion (CE) performance. Detailed information on the raw materials is listed in **Table 3.1**.

3.1.

Table 3.1 – Feedstocks for cold spraying and sintering.

Material	Use	Supplier	Note
Ni powder	Cold spraying	Centerline, Canada	Purity: 99.7%; Size: ~ 5 μm
WC powder	Cold spraying	Sulzer Metco, USA	Purity: 99.7%; Size: ~ 20 μm
Ni powder	Sintering	Changsha Tianjiu Metallics, China	Purity: 99.5%; Size: ~ 5 μm
WC powder	Sintering	Changsha Tianjiu Metallics, China	Purity: 99.5%; Size: ~ 3 μm
CeO ₂ powder	Sintering	Changsha Tianjiu Metallics, China	Purity: 99.5%; Size: ~ 3 μm
Cr powder	Sintering	Changsha Tianjiu Metallics, China	Purity: 99.5%; Size: ~ 3 μm
ASS 316L	Cold spraying	Xinghua Guojin Metallics, China	As substrate and reference

3.2 Cold spraying

Low-pressure cold-gas dynamic spraying (SST series P, CenterLine, Canada) was used to deposit Ni-WC coatings onto the top surface of 316L ASS substrates. The substrate was a solid cylinder of 20 mm in diameter and 10 mm in thickness. Prior to cold spraying, these substrates were grit-blasted by 24-grit alumina with 0.3-1.0 MPa compressed air for 1 min (Manus Abrasive Systems, Canada) and then cleaned in ethanol to increase the adhesion between the coating and substrate. The spraying parameters are given in **Table 3.2**.

Table 3.2 – Spraying parameters for depositing Ni-WC coating.

Length of nozzle [mm]	120
Entrance diameter of nozzle [mm]	4.46
Exit diameter of nozzle [mm]	6.40
Pressure of compressed Air [kPa]	634
Temperature of compressed air [°C]	550
Carrier gas	Argon
Pressure of carrier gas [kPa]	483
Volumetric flow rate of carrier gas [l/min]	7
Stand-off distance [mm]	5
Transverse velocity [mm/min]	300

A robot (Motoman HP-20, Yaskawa Electric, USA) was utilised for automatic control, to which the nozzle was installed. The Ni-WC powder blend, which was composed of mechanically blended Ni powder (8 wt.%) and WC powder (92 wt.%), was transported via a volumetric powder feeder (5MPE, Sulzer Metco, USA) to the nozzle by the carrier gas. The content of the WC in the as-sprayed coating was about 25 vol.% (36.7 wt.%) which was much lower than the Ni-WC powder blend due to the

relatively lower deposition efficiency of the WC powder than the Ni powder.

3.3 Vacuum hot-pressing sintering (VHS)

The sintered Ni-WC metal matrix composites (MMCs) were fabricated by vacuum hot-pressing sintering (VHS). The feedstocks were composed of mechanically blended powders. The volumetric ratio of the WC and the Ni in the feedstocks was 1:3 for the Ni-WC MMCs. The CeO₂ content in the Ni-WC-CeO₂ MMCs was 0.9, 1.8, and 2.7 wt.%, respectively. The WC content was 25 vol.%, and the content of the Cr was 10, 20, and 30 vol.%, respectively, for the NiCr-WC MMCs. A list of the composition of the sintered MMCs is tabulated in **Table 3.3**.

Table 3.3 – Chemical composition of the sintered MMCs.

Set	Composition (vol.%)				Composition (wt.%)			
	Ni	WC	CeO ₂	Cr	Ni	WC	CeO ₂	Cr
1	75.0	25.0	-	-	63.1	36.7	-	-
2	74.0	24.7	1.3	-	62.6	36.5	0.9	-
3	73.0	24.4	2.6	-	62.0	36.2	1.8	-
4	72.1	24.0	3.9	-	61.4	35.9	2.7	-
5	65.0	25.0	-	10.0	55.6	37.5	-	6.9
6	55.0	25.0	-	20.0	47.9	38.1	-	14.0
7	45.0	25.0	-	30.0	39.9	38.8	-	21.3

The blended feedstock was fed into the mould in a VHS furnace (ZT-25-20Y, Shanghai Chenhua Science Technology, China). Once the furnace was vacuumed to below 5 Pa at room temperature, the furnace started heating, and the temperature was controlled as per **Fig. 3.1**. Once the

temperature reached 800 °C, a load up to 40 MPa was applied to the powder mixture at a rate of 2 MPa/min, and the load was held until the furnace was cooled to room temperature.

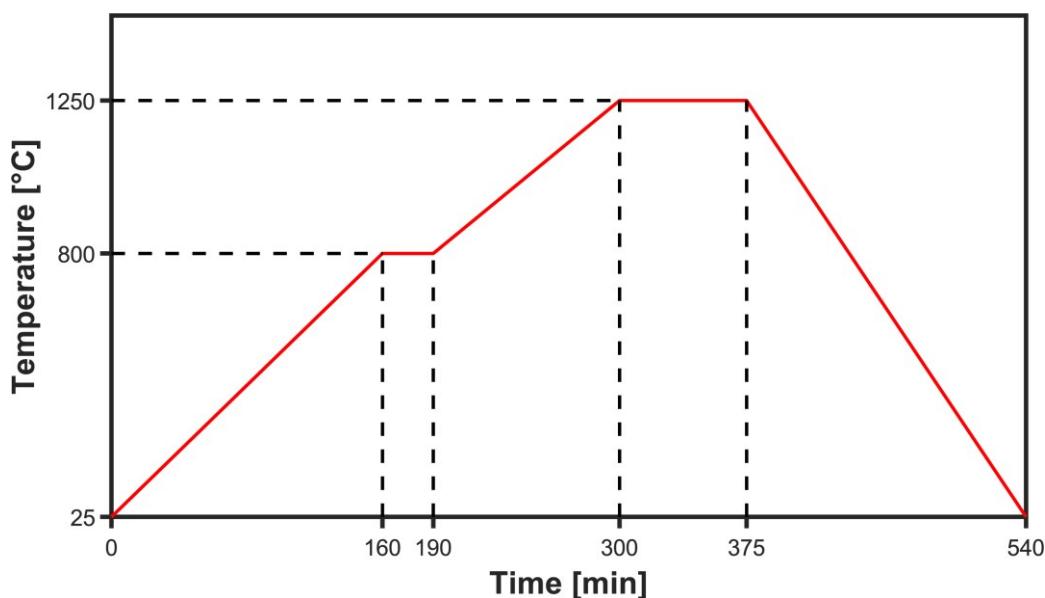


Fig. 3.1 – Temperature control of the furnace for the sintered Ni-WC(-CeO₂).

3.4 Laser surface melting

The as-sintered MMCs were cut into bars with a square cross-section of 10 x 10 mm via wire electrical discharge machining (MV2004S, Mitsubishi Electric, Japan). The as-sprayed coatings and the as-sintered MMC bars were grounded by 240-grit sandpaper. The as-grounded samples were cleaned in ethanol and dried in hot air. Then, these samples were processed by LSM. The LSM process was performed in a digital-controlled platform (Laser manufacturing centre, Hans Laser, China) with an ytterbium laser system (YLS-2000, IPG Photonics, USA). The

processing parameters of LSM are presented in **Table 3.4**, and a schematic demonstration is shown in **Fig. 3.2**.

Table 3.4 – Processing parameters of laser remelting.

Focus position	On the surface
Laser wavelength [nm]	1075
Spot size in diameter [mm]	0.5
Trace spacing [mm]	0.25
Power [W]	300, 400, and 500
Transverse speed [mm/min]	200
Shielding gas	Nitrogen
Shielding gas flow rate [L/min]	1.5

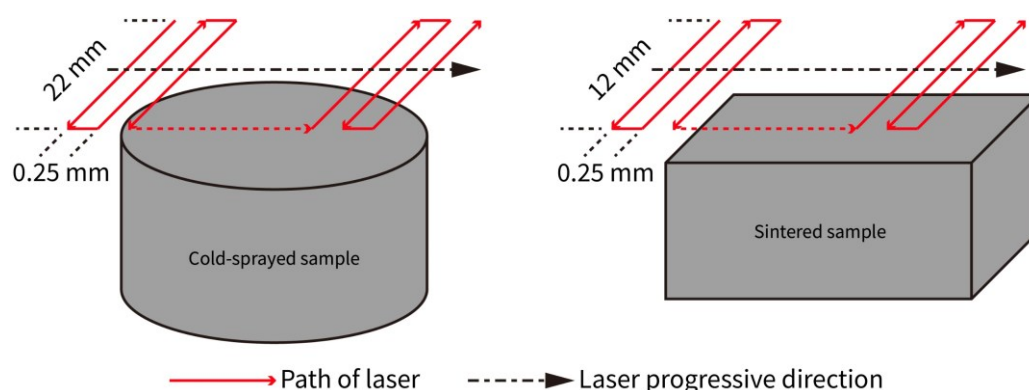


Fig. 3.2 – Schematic showing the laser surface melting process in this work.

In addition, a margin of 1 mm out of the sample periphery (a circumscribed square for the cold-sprayed sample) was kept for the laser-scanned region. Apart from being processed by 300-, 400-, and 500-W lasers, some Ni-WC samples were also treated by 200- and 600-W lasers. However, the 200-W laser could not melt the coating, while the 600-W laser caused serious damage. Thus, the results for the sample treated by 300-, 400-, and 500-W lasers are presented.

3.5 Characterisations and tests

3.5.1 Sample preparation

The as-remelted sintered MMC bars were cut into 10 mm cubes before the subsequent processing. The LSM surface of some as-remelted cold-sprayed cylindrical samples and as-remelted sintered cubic samples were grounded on 240-, 400-, 800-, 1200-, and 2000-grit SiC paper and then polished with 2.5 μm , 1 μm , and 0.25 μm diamond suspensions. The final surface finishing was accomplished by polishing with 0.02 μm colloidal silica suspension. The as-sprayed and the as-sintered samples were subjected to the same grinding and polishing process. These samples with polished surfaces were used for X-ray diffraction (XRD), scanning electron microscopy (SEM), and CE tests.

The other as-remelted samples were cut along the laser progressive direction (**Fig. 3.2**). Some as-sprayed and as-sintered samples were also sliced. The cross-section of these samples was grounded and polished as per the same procedures demonstrated above. These samples with polished cross-sections were used for SEM, electron backscattered diffraction (EBSD), and microhardness test. The polished cross-section of the cold-sprayed samples and the LSM cold-sprayed Ni-WC samples was also examined by nanoindentation test. Some thin films were milled and cut from the cross-section of the LSM cold-sprayed Ni-WC samples by

focused ion beam (Auriga, Zeiss, Germany) with liquid Ga⁺ source at 30 kV and 2 nA for transmission electron microscopy (TEM).

In addition, some as-remelted cold-sprayed samples were chemically etched for SEM. The etchant was a mixture of 37 wt.% hydrochloric acid (10 g) and 35 wt.% hydrogen peroxide solution (10 g) in deionised water (30 ml), supplied by Shanghai Aladdin Biochemical Technology, China. The non-coated surface of the specimen was sealed by epoxy resin. Then, the partially sealed specimen was submerged in the etchant for 5 min to completely remove the Ni and fully expose the WC structure.

3.5.2 X-ray diffraction (XRD)

XRD (D8 Advance, Bruker, Germany) was used to identify the phase composition of the samples before and after LSM. The XRD patterns were acquired by the continuous XRD mod at a 2θ rate of 5° per min and specimen spinning at 60 rpm. The copper anode with a curved graphite monochromator was set at 40 kV and 40 mA.

3.5.3 Scanning electron microscopy (SEM)

SEM can produce an image by acquiring and processing the signals from the interaction of a focused beam of electrons and the atoms in a sample. There are various imaging modes depending on which signal is captured,

and the two most frequently used signals are the secondary electron (SE) and backscattered electron (BSE). Generally, the SE signal provides the surface topography since SEs can only escape from the top surface of the sample due to their very low energy and limited mean free path in solid matter. BSEs are reflected from the sample by elastic scattering, and the intensity of the BSE signal is strongly dependent on the atomic number. Therefore, the contrast of BSE images can indicate the compositional distribution of the sample. However, the resolution of BSE images is less than SE images because BSEs are from deep locations.

In this work, field-emission SEM (FESEM, Gemini Sigma 300, Zeiss, Germany) was used to characterise the samples. Unless specified, the SEM characterisation was performed at 20 kV in SE mode since the topography of the samples subjected to CE is very important in this study. In addition, the SE detector in this FESEM can also capture a limited portion of the BSE signal, allowing the SE image to provide compositional information when the surface of the sample is not very rough.

3.5.4 Electron backscattered diffraction (EBSD)

EBSD is a technique for microstructural-crystallographic characterisation based on SEM. In this work, the EBSE detector (e^- Flash^{HD} detector, Bruker, Germany) on the FESEM was used to check whether there is a

preferred crystal orientation in the LSM layer of the sample. Meanwhile, the grain size of the remelted layer was also acquired by processing the EBSD data. Unless specified, the EBSD characterisation in this thesis was performed at 20 kV and 0.5 $\mu\text{m}/\text{step}$.

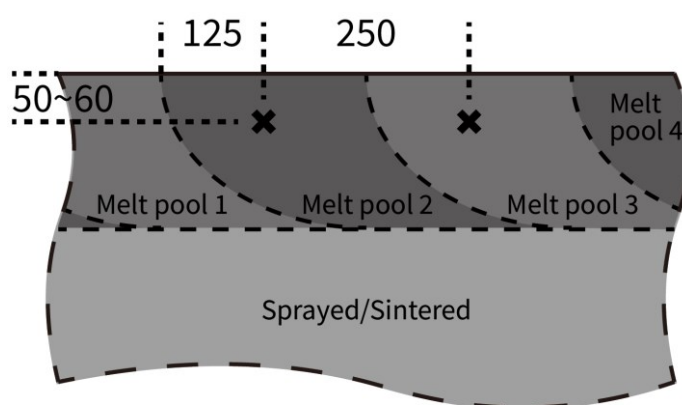
3.5.5 Transmission electron microscopy (TEM)

TEM is a microscopy technique that also acquires and processes the signals from the interaction of the electrons and the atoms in a sample, but the beam of electrons is transmitted through the sample to form an image. TEM images have a significantly high resolution and can provide crystallographic data. In this work, the remelted layer of the LSM cold-sprayed sample treated by a 400-W laser was characterised by TEM (Talos F200x, Thermo Fisher Scientific, USA) at 100 kV.

3.5.6 Microhardness and nanoindentation tests

Vickers microhardness test (Wilson VH3300, Buehler, Germany) was conducted on the polished cross-sections of the samples. An indentation load of 0.2 kgf with a dwell time of 10 s was applied to each test site. The test site was selected at $\sim 60 \mu\text{m}$ beneath the top surface of the samples and the quarter-point of the melt pool, i.e., at the horizontal middle of the half melt pool (since the overlapping ratio was 50%), as demonstrated in

Fig. 3.3. The depth of the test site was at the middle of the remelted region for the LSM samples whose thickness of the remelted region was less than $120\ \mu\text{m}$, the horizontal space of each adjacent test site was at least $200\ \mu\text{m}$ for the as-sprayed and the as-sintered samples. There were 10 sites indented for each sample to obtain the mean value, and the standard deviation was also calculated.



✕ Indented sites Unit: μm

Fig. 3.3 – The indentation sites for the hardness and the nanoindentation tests

Nanoindentation test (Nano Indenter G200, MTS, USA) was performed on the polished cross-section of the as-sprayed and the as-remelted cold-sprayed samples. The selection of the test site was the same as that in the microhardness test, and there were 5 sites indented for each sample. A Berkovich diamond indenter was used, and the maximum displacement into the test site was $2\ \mu\text{m}$ at a strain rate of $0.01\ \mu\text{m/s}$. The load-displacement plot, indentation hardness (H_{IT}), and indentation modulus (E_{IT}) were calculated using the software in the test rig.

3.6 Evaluation of cavitation erosion performance

3.6.1 Cavitation erosion test

The cavitation erosion resistance (CER) of the samples was evaluated by the ultrasonic vibratory apparatus (GBS-SCT 20A, Guobiao Ultrasonic Equipment Ltd., China) as per a modified version of ASTM G32-16(2021)e1 [71] using the indirect cavitation approach (**Fig. 2.12b**). A photograph of the apparatus is shown in **Fig. 3.4**, and the test parameters are given in **Table 3.5**. The heat generated by the transducer during operation is dissipated by the cooling fan and conducted through the sonotrode to the test medium. The temperature of the test medium is monitored by the thermal couple and controlled by the cooling bath. The specimen-to-sonotrode distance can be set precisely by the vertical scale of the liftable platform. The total test time for each sample was 10 h. Before and at each test interval of 1 h, the sample was weighed (ME024E, Mettler Toledo, Switzerland), and the mass loss was recorded. Then, the mean depth of erosion (MDE) and the erosion rate in terms of MDE (MDER) were calculated according to **Eq. 2.3** and **Eq. 2.4** based on the mass loss and the theoretical density (**Table A1** in **Appendix B**), giving the plots of CE and CE rate as per **Fig. 2.13**.

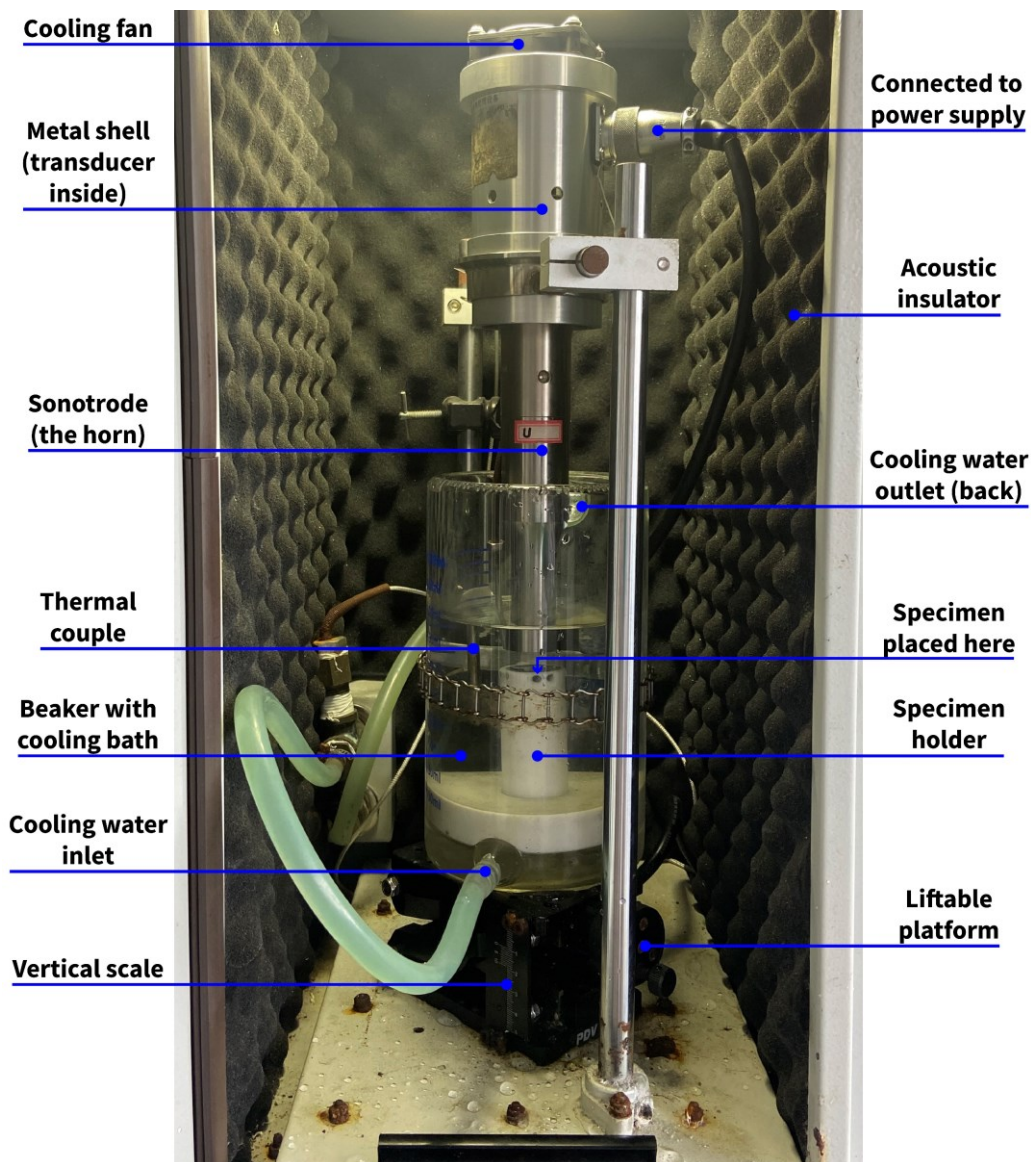


Fig. 3.4 – A photograph of the vibratory cavitation erosion apparatus used in this research.

Table 3.5 – Parameters of cavitation erosion test.

Vibration frequency [kHz]	20
Peak-to-peak amplitude [μm]	50
Depth of the horn below the liquid level [mm]	23 ± 2
Specimen-to-horn distance [mm]	1
Temperature of the test medium [$^{\circ}\text{C}$]	25 ± 2
Test medium	Deionised water

3.6.2 Surface profile

The surface profile of the LSM cold-sprayed samples subjected to CE for 10 h was characterised by a 3D profilometer (Up-Lambda 2, Rtec Instruments, USA) using white-light interferometry, which provided the evaluation of the surface roughness after CE and the depth of the CE pits/craters. The data were collected from three random regions with a dimension of 1.2×1.9 mm and were further analysed by MountainsMap® surface analysis software.

3.6.3 Scanning electron microscopy observation at the same site

The samples before and after exposure to cavitation erosion for 10 h were characterised by SEM. However, the characterisation of the post-mortem samples can only provide limited information. In this work, a series of SEM images were taken from the same positions of the LSM sintered samples after cavitation erosion for 0, 2, 5, and 7 h, respectively, in an attempt to investigate the failure mechanism. This was achieved by indenting a mark on the sample, which provides a reference position to locate the observed region. The approach is referred to as 'SEM observation' for short in this thesis.

Chapter 4

Cavitation erosion of LSM cold-sprayed Ni-WC coating

4.1 Introduction

As reviewed in **Subsection 2.5.3**, the HVOF-sprayed WC-based cermet coatings are still the most extensively adopted in resisting cavitation erosion (CE). However, the adhesion is quite weak at the phase boundaries for the HVOF-sprayed WC-based cermet coatings and other CE-resistant thermal-sprayed cermet coatings. The weak adhesion results in a typical failure mechanism of these coatings during CE: the brittle detachment of the hard ceramic phases followed by the erosion of the exposed metallic binder phases. Moreover, the numerous inter-splat boundaries in the sprayed coatings can block the movement of the dislocations and slips, and thus the cavitation erosion resistance (CER) of the metallic phase in the sprayed coatings may not be as good as the bulk materials. In addition, the inter-splat boundaries formed by the unmelted or partially melted particles are also susceptible to cavitation damage. These issues above can be addressed by post-melting, such as laser surface melting (LSM). The molten metal can wet the ceramic particles, improving the bonding at phase boundaries [145, 260]. Meanwhile, the

inter-splat boundaries are eliminated since the metallic binder phase is remelted.

The work presented in this chapter introduced LSM to the cold-sprayed Ni-WC MMC coatings on the 316L ASS substrates. The original cold-sprayed coatings were denoted as CS-0, and the cold-sprayed Ni-WC MMC coatings treated by the laser with a power of 300, 400, and 500 W were denoted as CS-300, CS-400, and CS-500, respectively. The coatings processed by the 200-W laser were not melted, and those processed by the 600-W laser were seriously damaged. Hence, these coatings were not investigated. A nearly full-scope examination for evaluating the CER of the LSM cold-sprayed Ni-WC MMC coatings was conducted. The microstructure of the coatings was characterised by SEM, TEM, and EBSD, and the mechanical properties were investigated by microhardness and nanoindentation tests. The coatings were subjected to the CE test as per ASTM G32, and their cumulative erosion and the erosion rate were measured. The eroded coatings after 10-h CE were examined by SEM and white-light interferometry. The results in this chapter suggested that the CER of the LSM cold-sprayed Ni-WC MMC coatings was dominated by microstructure but not mechanical properties.

4.2 Characterisation of the cold-sprayed Ni-WC coating

The SEM images in **Fig. 4.1** present the polished cross-section and the polished surface of the cold-sprayed Ni-WC coating, where the bright particles and the dark matrix were WC and Ni, respectively. A thick layer of Ni-WC was successfully deposited onto the 316L ASS substrate without any large defect (**Fig. 4.1a**). However, many small defects were observed. For instance, small pores were inside the coating (highlighted by the red arrows in **Fig. 4.1b**). Meanwhile, the cracks at the Ni-WC phase boundaries (highlighted by the blue arrows in **Fig. 4.1b**) indicated the poor bonding between the Ni and the WC phases. In addition, the WC grains in the coating also exhibited some internal cracks (highlighted by the green arrows in **Fig. 4.1b**), probably caused by the high impact velocity of WC particles to the surface during cold spraying. The image processing

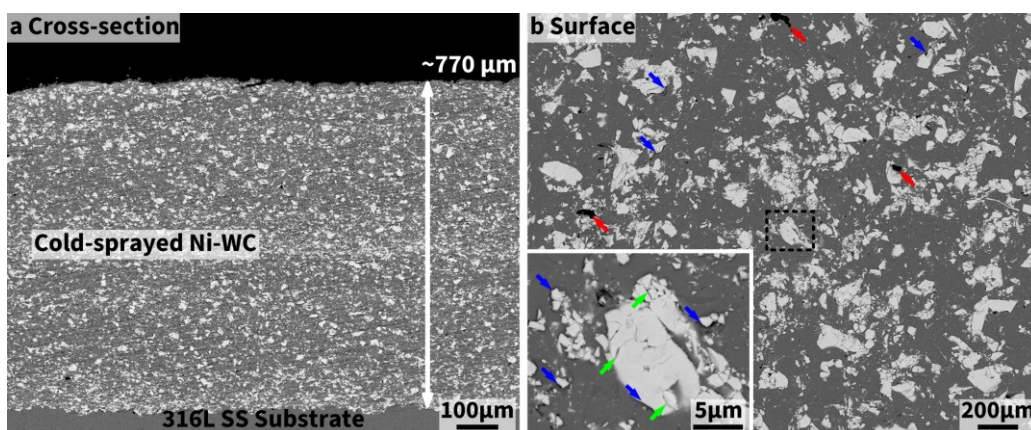


Fig. 4.1 – SEM images showing the cross-section of the cold-sprayed Ni-WC coating on the 316L ASS substrate. a, Polished cross-section; b, Surface. Red arrows: Pores; Green arrows: Cracks on the cold-sprayed WC particle; Blue arrows: cracks at the Ni-WC phase boundaries.

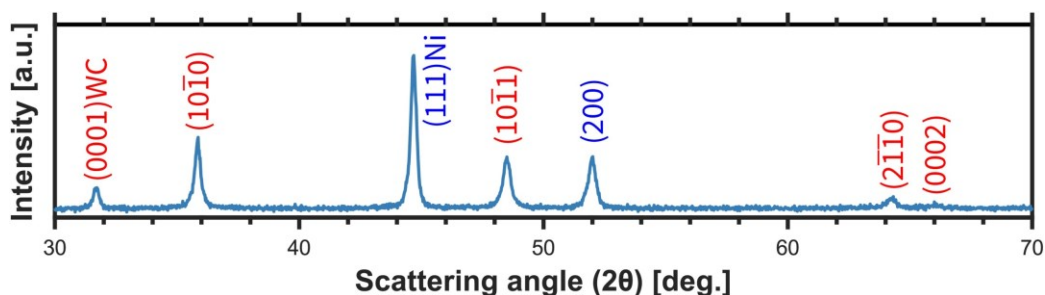


Fig. 4.2 – XRD spectrum of the cold-sprayed Ni-WC coating.

software (Adobe Photoshop) indicated that the content of the WC was about 25.4 ± 4.6 vol.% after analysing 10 random SEM images of the cross-section, and the porosity of the coating was about $0.5 \pm 0.2\%$.

The polished surface of the cold-sprayed coating was examined by XRD to check the phase and chemical composition. The XRD pattern in **Fig. 4.2** shows the peaks of face-centred cubic (FCC) Ni and hexagonal close-packed (HCP) WC.

The EBSD mapping in **Fig. 4.3b** indicated that Ni grain size was very small, about $0.55 \pm 0.28 \mu\text{m}$. It is also worth mentioning that the Ni grains beneath and directly contacting the large WC grains had even smaller grains size (highlighted by the black arrows **Fig. 4.3b**), which was

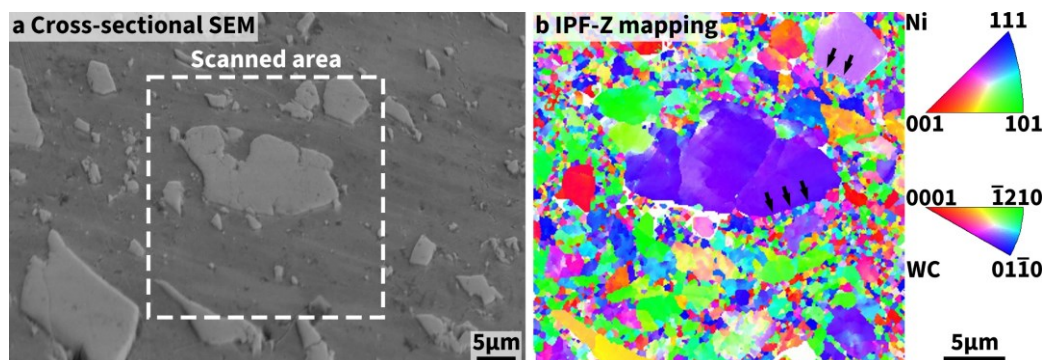


Fig. 4.3 – EBSD mapping of the cold-sprayed Ni-WC coating. **a**, SEM image of the cross-section of the cold-sprayed Ni-WC coating, where the; **b**, The inverse pole figure mapping (z-axis, perpendicular to the image) with a step size of $0.1 \mu\text{m}$, where the refined Ni grains beneath the WC grains are highlighted by the black arrows.

attributed to the stress-driven grain refinery by the impact of the WC particles during the spraying process.

4.3 Microstructure characterisation of the LSM cold-sprayed Ni-WC coatings

4.3.1 XRD results

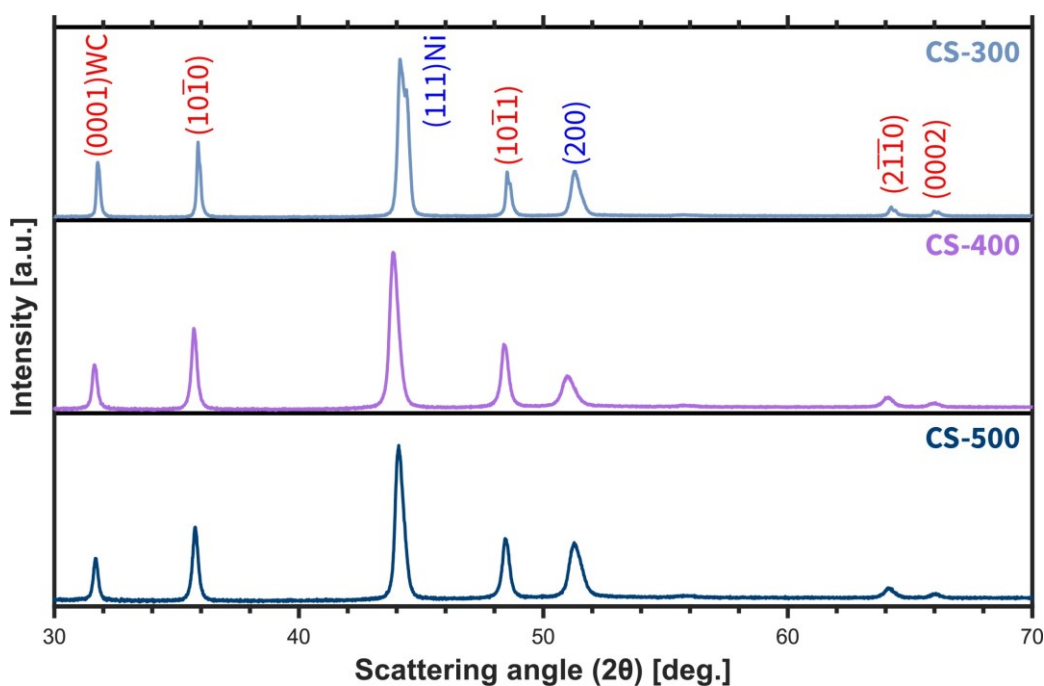


Fig. 4.4 – XRD spectra of the cold-sprayed and the LSM Ni-WC coatings.

The polished surface of the LSM cold-sprayed Ni-WC coatings was characterised by XRD. According to **Fig. 4.4**, all the coatings exhibited almost identical XRD spectra, consisting of FCC Ni and HCP WC only. This indicates that the LSM process did not introduce any new phase, or the contents of WC_x , Ni_4W , and Ni_xW_yC were extremely low.

4.3.2 SEM results

However, the microstructure of the LSM layers was changed significantly. The cross-sections and the etched surfaces of the LSM coatings are presented in **Fig. 4.5** and **Fig. 4.6**. The thickness of the LSM layer was positively correlated to the laser power, and the LSM layer in the CS-500 sample was the thickest which was about 270 μm (**Fig. 4.5a1-c1**). The bands composed of large WC grains were observed in all the LSM layers (highlighted by the horizontal white arrows in **Fig. 4.5a1-c1**), and the distance between two adjacent bands was about 0.25 mm, which was equal to the space between two adjacent traces of the laser (**Fig. 3.2**). The formation of these bands was possibly attributed to the micro-segregation during the solidification.

The LSM layers of all the samples exhibited a very similar microstructure that presented a network of the eutectic Ni-WC composed of the WC lamellae and the Ni binder (**Fig. 4.5a2-c2**), and the differences lay in the defects and the thickness of the eutectic Ni-WC network. Unmelted and partially melted WC particles were found in the LSM layer of the CS-300 sample (highlighted by the blue arrows in **Fig. 4.5a**), which was attributed to the insufficient heat input of the relatively low laser power. The incomplete melting of the WC particles caused the low concentration of the WC as the solute in the molten alloy during LSM, and therefore the

Cavitation erosion of LSM cold-sprayed Ni-WC coating

amount of the precipitated WC was low, resulting in the thinner eutectic Ni-WC network in the CS-300 sample, compared to the CS-400 and the CS-500 samples (Fig. 4.5a2-c2). In other words, there were fewer WC

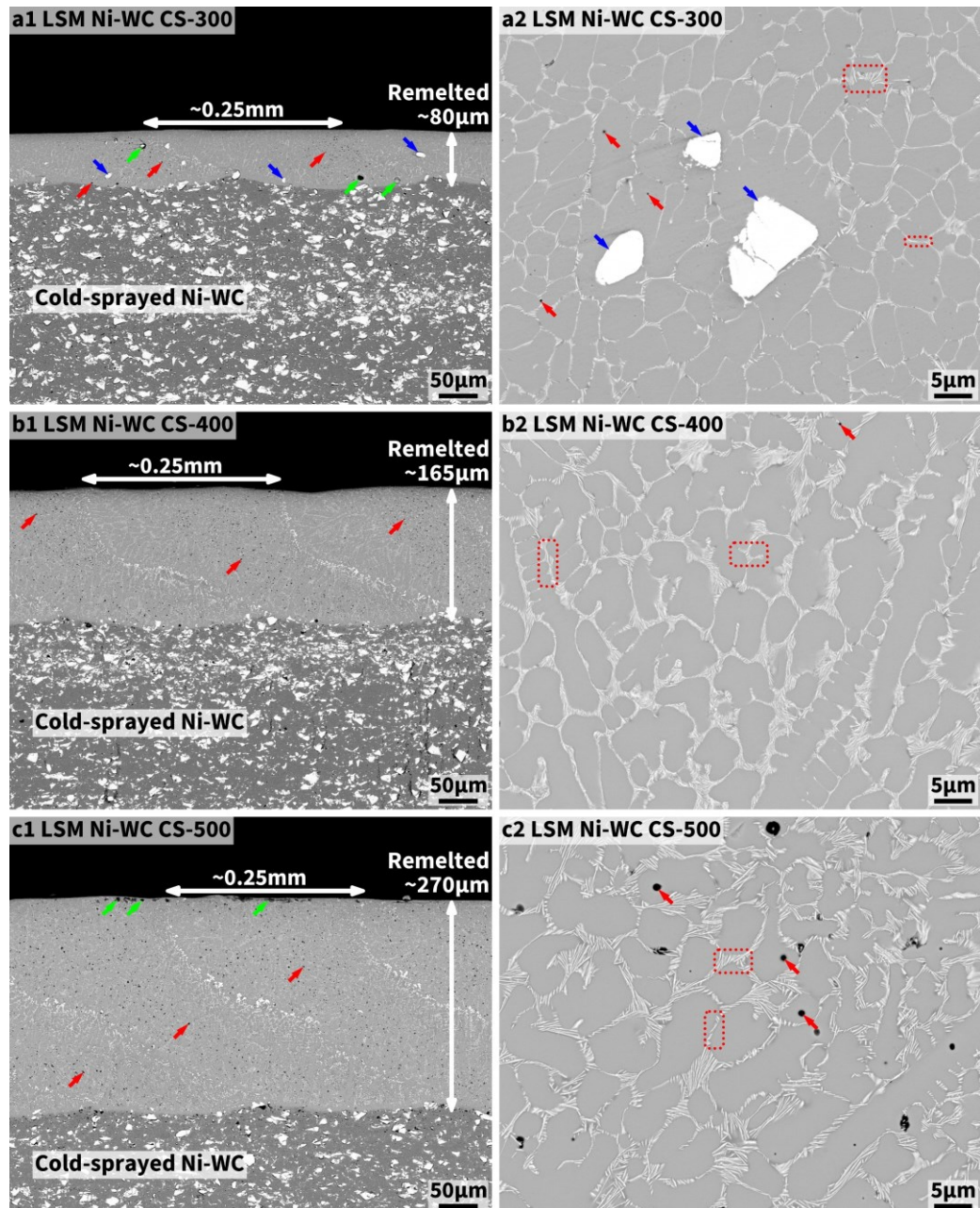


Fig. 4.5 – SEM images showing the cross-sections of the LSM Ni-WC coatings treated by different laser powers. a-c, Specimens treated by 300-, 400-, and 500-W lasers, respectively; 1, Low magnification; 2, High magnification. Arrows: Remelted zone (vertical, white), space of two adjacent bands of large WC grains (horizontal, white), small pores (red), large pores (green), and unmelted (or partially melted) WC particles (blue); Dotted rectangles in a2-c2: Eutectic Ni-WC.

Cavitation erosion of LSM cold-sprayed Ni-WC coating

lamellae in the eutectic Ni-WC network of the CS-300 sample. The LSM layer of the CS-300 sample also had some large pores (highlighted by the green arrows in **Fig. 4.5a1**), which could result from the detachment of the unmelted and partially melted WC particles during the grinding and

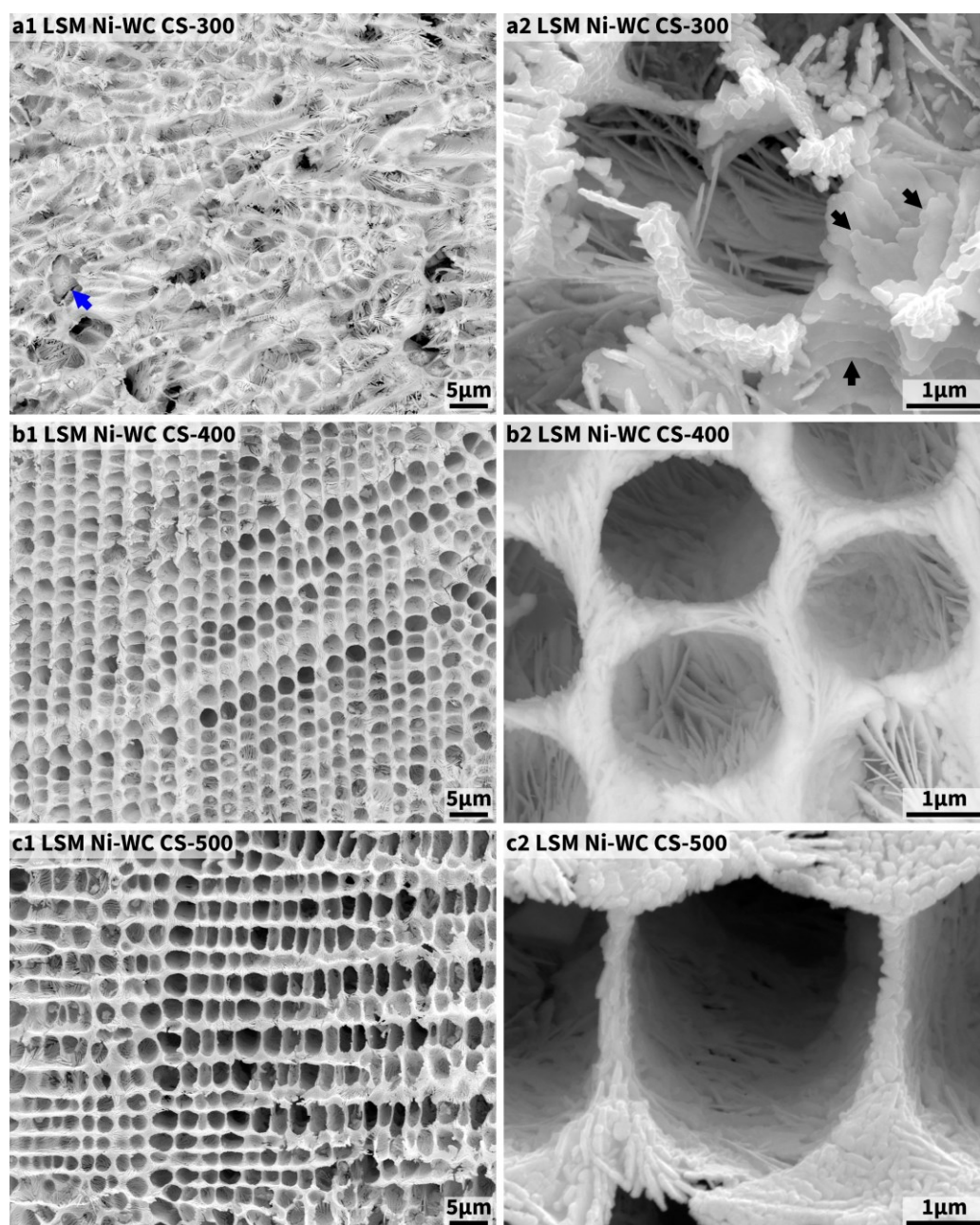


Fig. 4.6 – SEM images showing the etched surfaces of the as-LSM Ni-WC coatings. The Ni at the observed regions was completely removed, showing the structure formed by WC laminae. **a**, The WC skeletons collapsed in the CS-300 sample; **b-c**, The WC skeletons were still rigid in the CS-400 and the CS-500 samples. Arrows: Unmelted WC particle (blue) and WC laminae (black).

polishing process. Small pores were found in the LSM layers of all the samples (highlighted by the red arrows in **Fig. 4.5**), but the size and the amount of the small pores in the CS-500 sample were the largest (**Fig. 4.5c**). The porosity of the CS-300, CS-400, CS-500 samples was $0.9\pm 0.3\%$, $0.4\pm 0.2\%$, and $1.9\pm 0.4\%$, respectively. Meanwhile, large pores were formed at the top of the LSM layer of the CS-500 sample (highlighted by the green arrows in **Fig. 4.5c1**), which could be attributed to the severe convection near the surface of the molten pool since the laser power was relatively high. Apart from these small defects, the LSM layer was more homogeneous and had much fewer defects compared to the original cold-sprayed coating.

The etched surfaces of the as-LSM samples provide a straightforward demonstration of the WC skeleton in the eutectic Ni-WC network (**Fig. 4.6**). The WC skeleton of the CS-300 sample collapsed after etching since the WC lamellae were not quantitatively sufficient to support the skeleton without Ni. (**Fig. 4.6a**). An unmelted (or partially melted) WC particle was also observed from the etched CS-300 sample (highlighted by the blue arrow in **Fig. 4.6a1**). The collapsed WC skeleton also confirmed the lamellar structure of the WC in the eutectic Ni-WC network (highlighted by the black arrows in **Fig. 4.6a2**). The WC skeleton in the CS-400 and the CS-500 samples was almost intact after etching due to the pile-up of

numerous lamellar WC precipitates (Fig. 4.6b-c). Meanwhile, the top surface of the WC skeleton of the CS-400 and the CS-500 samples exhibited a series of ordered and uniformly sized cells enclosed by the WC lamellae.

4.3.3 EBSD results and grain size

The EBSD results of the cross-section of the LSM samples are shown in Fig. 4.7. All the LSM layers exhibited the columnar grains that are commonly found in the laser-additive-manufactured alloys, and preferred orientation was not observed (Fig. 4.7).

The average grain size of the LSM samples was obtained by processing the map in Fig. 4.7 plus another four maps with the same scale for each sample. The statistics of the grain size are presented in Fig. 4.8, indicating that the grain size was positively correlated to the power of the laser.

The surface of the LSM samples was also characterised by EBSD (Fig. 4.9). According to the SEM images and the corresponding grain boundary maps in Fig. 4.9, most of the WC grains were located inside the Ni grains, suggesting that the eutectic growth of the Ni-WC was in-between the Ni dendrite arms during the solidification process, or the high cooling rate during the LSM caused the incompletely developed textures of Ni grains.

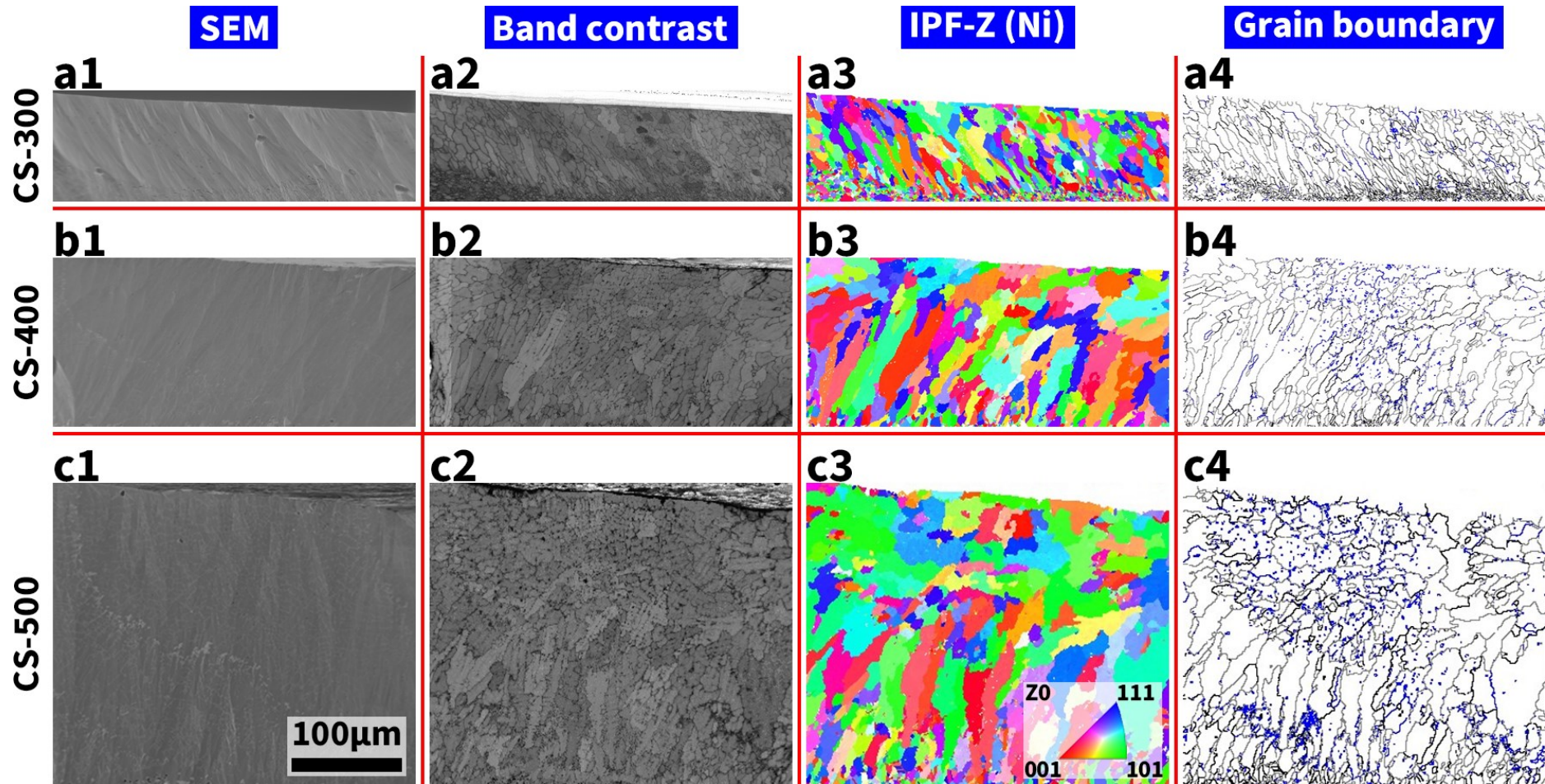


Fig. 4.7 – EBSD results of the cross-section of the LSM Ni-WC coatings. The blue, grey, and black lines in **a4-c4** represent the misorientations $<15^\circ$, $15^\circ-49^\circ$, and $>49^\circ$, respectively. All the images share the same scale bar.

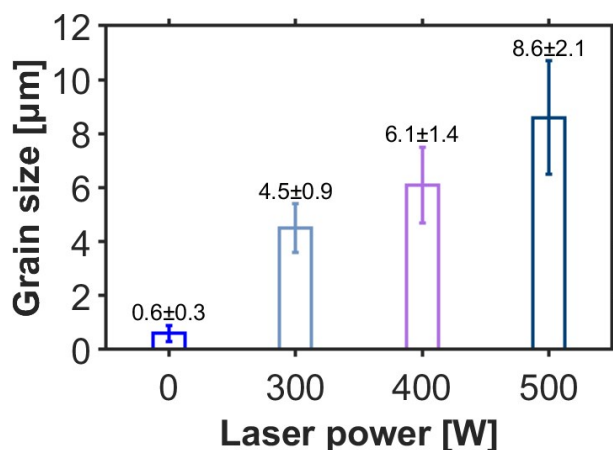


Fig. 4.8 – Grain size of the cold-sprayed and the LSM samples.

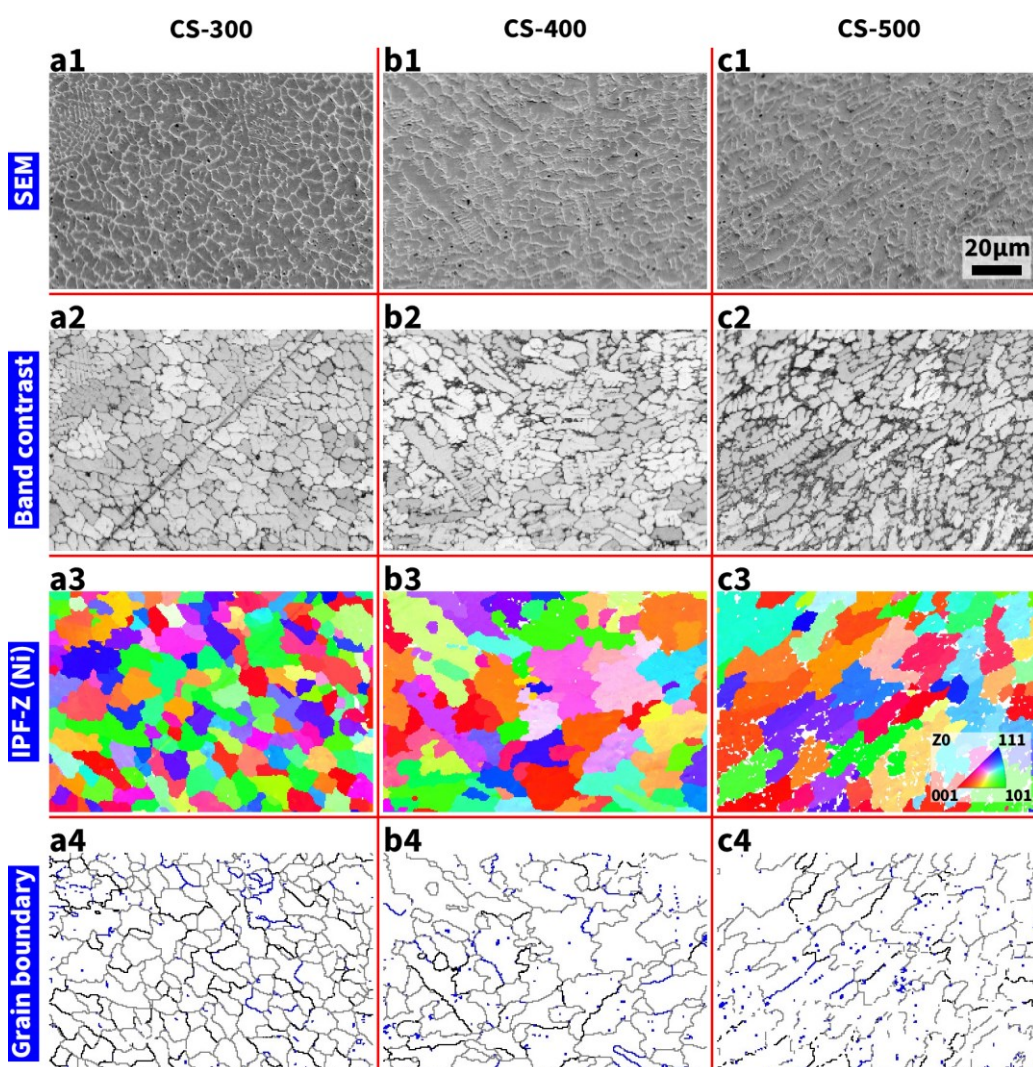


Fig. 4.9 – EBSD results of the surface of the LSM Ni-WC coatings. The blue, grey, and black lines in **a4-c4** represent the misorientations $<15^\circ$, $15^\circ-49^\circ$, and $>49^\circ$, respectively. The comparison of the images in **1** and **4** clearly shows that the WC grains were inside the Ni grains. All the images share the same scale bar.

4.3.4 TEM results

The CS-400 sample was processed by focused ion beam (an SEM image during the process is given in **Appendix C**) and further characterised by TEM. The scanning TEM (STEM) image in **Fig. 4.10a** shows that the WC lamellae were firmly embedded in the Ni matrix. The high-angle annular dark field (HAADF) image with the corresponding energy dispersive X-ray spectroscopy (EDX) mapping in **Fig. 4.10b** presents that very limited W and C diffused into the nearby Ni matrix.

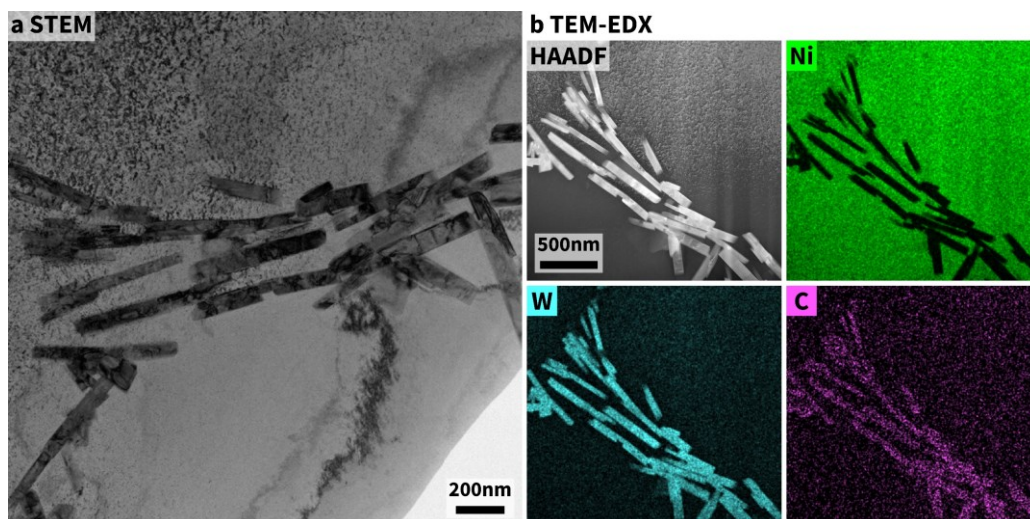


Fig. 4.10 – STEM characterisation of the CS-400 sample and the corresponding TEM-EDX results. **a**, STEM image of the CS-400 sample; **b**, HAADF image and the corresponding TEM-EDX mappings.

The high-resolution TEM (HRTEM) images and the corresponding selected area electron diffraction (SAED) patterns are shown in **Fig. 4.11**. According to the sudden contrast change in **Fig. 4.11a1-b1**, stacking faults were found in the Ni and the WC grains, and there was a thin bright band at the Ni/WC interface confirmed as the complexion of WC_x in the magnified HRTEM image (**Fig. 4.11b3**). The SAED patterns (**Fig. 4.11a2-**

b2) and the magnified HRTEM images (Fig. 4.11a3-b3) with the annotated d-spacing also evidenced that the precipitates and the matrix in the LSM layer were the HCP WC and the FCC. Ni, respectively, which was consistent with the XRD results (Fig. 4.4). The complexion of WC_x were distributed at the WC(0001)/Ni interface, and there were about 2~5 atomic layers (Fig. 4.11b3). The complexion of WC_x was also common in

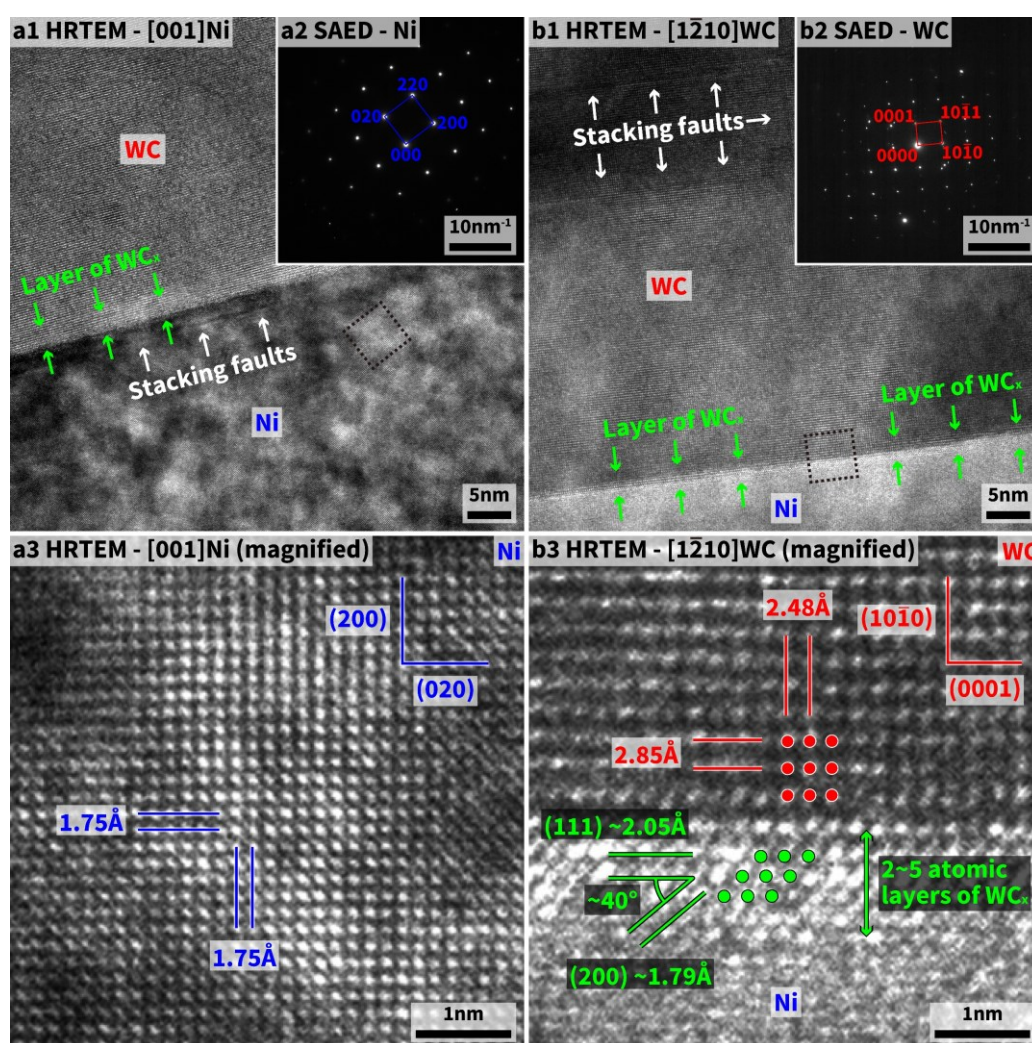


Fig. 4.11 – HRTEM images and SAED patterns of the CS-400 sample. **a**, The images along the zone axis of $[0\ 0\ 1]$ Ni; **b**, The images along the zone axis of $[1\ -2\ 1\ 0]$ WC; **1**, The HRTEM images along the corresponding zone axis; **2**, The SAED patterns along the corresponding zone axis; **3**, The magnified HRTEM images of the areas enclosed by the black dotted squares in **1**. According to the contracts of the HRTEM images, the complexions of WC_x (about 2~5 atomic layers) are observed.

the other types of WC-based cemented MMCs [282, 283].

4.4 Mechanical properties

4.4.1 Microhardness results

The microhardness test and the nanoindentation test were performed on the cold-sprayed coating, the LSM coatings, and the 316L ASS as the reference sample. The results of the microhardness test are given in **Fig. 4.12** and **Fig. 4.13**. The microhardness of the CS-400 sample was higher than that of the cold-sprayed sample (**Fig. 4.12**), which could be attributed to the dense distribution of the eutectic Ni-WC network (**Fig. 4.13c**) and the enhanced adhesion between the Ni and the WC phases by the wetting during the LSM process. However, the microhardness of the CS-300 and the CS-500 samples was slightly reduced. The volume of the precipitated WC grains in the CS-300 sample was less than that of the WC particles in the original cold-sprayed sample and the precipitated WC lamellae in

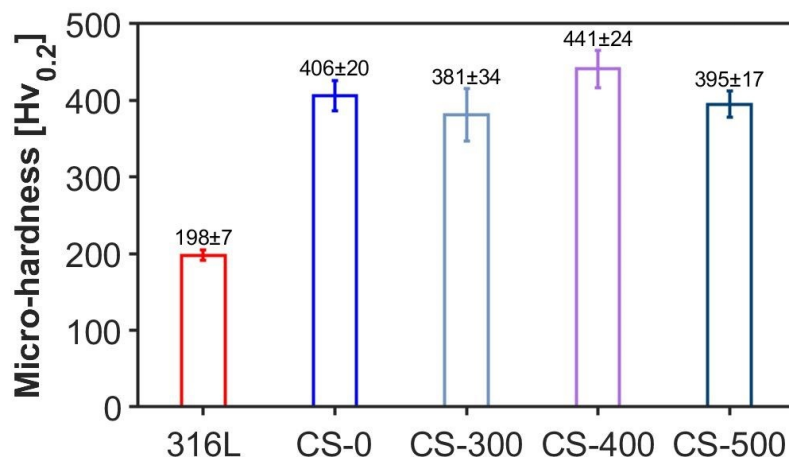


Fig. 4.12 – Microhardness of 316L ASS, cold-sprayed coating, and LSM coatings.

the LSM layer of the CS-400 sample (Fig. 4.5a2 and Fig. 4.13b), and thus the microhardness of the CS-300 sample was lower than that of the cold-sprayed and the CS-400 samples. For the CS-500 sample, the relatively high grain size (Fig. 4.8) and the pores in the LSM layer caused the reduced microhardness (Fig. 4.5a2 and Fig. 4.13c). In addition, there were large cracks at the indented edge and inside the indentation site of the cold-sprayed samples (Fig. 4.13a) but were not found in the LSM sample, suggesting that the cold-sprayed sample may not be resistant to the shear stress and have low fracture toughness.

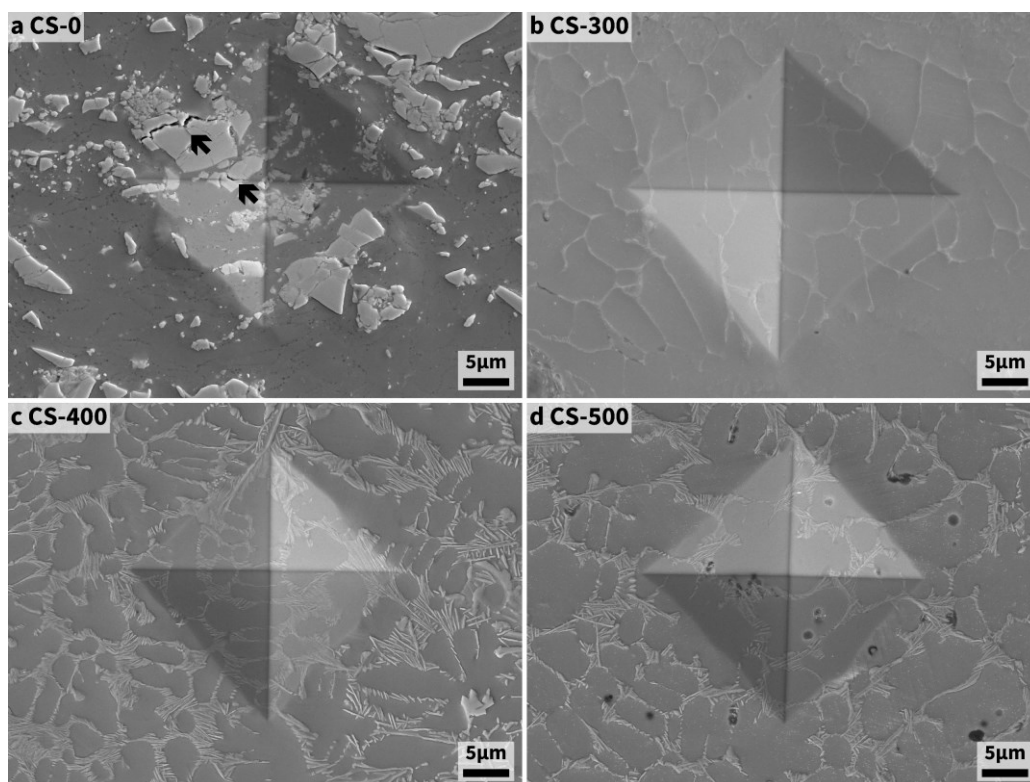


Fig. 4.13 – SEM images of the indented cross-section of the cold-sprayed and the LSM coatings subjected to the microhardness test. Black arrows in a: The large cracks at the indented edge and inside the indentation site.

4.4.2 Nanoindentation results

The results of the nanoindentation test are presented in **Fig. 4.14** and **Fig. 4.15**. The numerical results obtained from the nanoindentation test are the load-displacement curve (**Fig. 4.14a**), the indentation hardness (H_{IT} , **Fig. 4.14b**), and the indentation modulus (E_{IT} , **Fig. 4.14c**). Many studies also discussed the CE performance and other wear behaviours of hard coatings in terms of the ratios of hardness (H) to elastic modulus (E), H^2/E ,

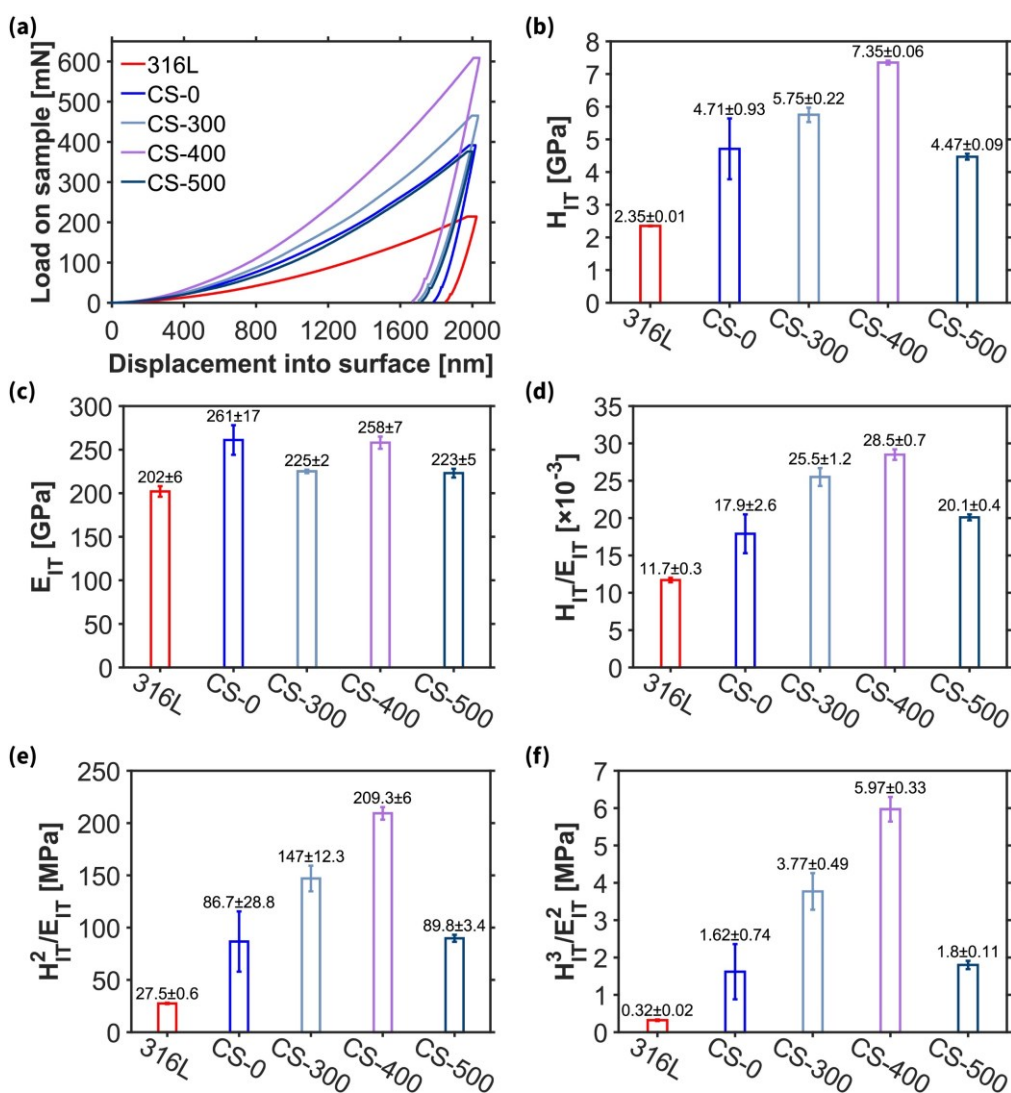


Fig. 4.14 – Nanoindentation results of the 316L ASS, the cold-sprayed coating, and the LSM coatings. a, The load-displacement curves; **b,** The indentation hardness (H_{IT}); **c,** The indentation modulus (E_{IT}); **d,** The H_{IT}/E_{IT} ratio; **e,** The H_{IT}^2/E_{IT} ratio; **f,** The H_{IT}^3/E_{IT}^2 ratio.

and H^3/E^2 [201, 284-289]. Since cavitation applies a heavy load to a very small area on the surface, which is similar to the nanoindentation process [290], the ratios of H_{IT}/E_{IT} , H_{IT}^2/E_{IT} , and H_{IT}^3/E_{IT}^2 obtained from the nanoindentation test are also applicable [285-288], and these ratios of the samples in this work are given in **Fig. 4.14d-f**. The H/E ratio is known as the 'plasticity index' and describes the elastic behaviour limit of a contact surface, which indicates the resistance to contact damage caused by stress pulse attack [284]. The H^2/E ratio expresses the surface resilience level, which is the capacity to absorb elastic deformation energy [291]. The H^3/E^2 ratio indicates the resistance to plastic deformation [284].

According to **Fig. 4.14a**, the CS-400 sample took the heaviest load with the greatest strain recovery and had the greatest H_{IT}/E_{IT} , H_{IT}^2/E_{IT} , and H_{IT}^3/E_{IT}^2 ratios, followed by the CS-300 and the CS-500 samples in descending order. Thus, the ranking of the CER of these LSM samples is supposed to be in the same order. It should be noted that the test results of the cold-sprayed coating may not be reliable. The area of the indented site was very small (**Fig. 4.15a**), and the distribution of the WC particles in the cold-sprayed coating was not very homogeneous in a small scale (**Fig. 4.1**). Hence, the difference in the results obtained from a WC-rich site and a Ni-rich site was significant, which was evidenced by the large deviation in the results of the cold-sprayed coating in **Fig. 4.14b-e**. On the

other hand, the deviation in the results of the LSM samples was narrow, as the indented sites always covered a relatively constant volume of the eutectic Ni-WC for the LSM samples (**Fig. 4.15b-d**). Therefore, the nanoindentation results of the LSM samples are reliable.

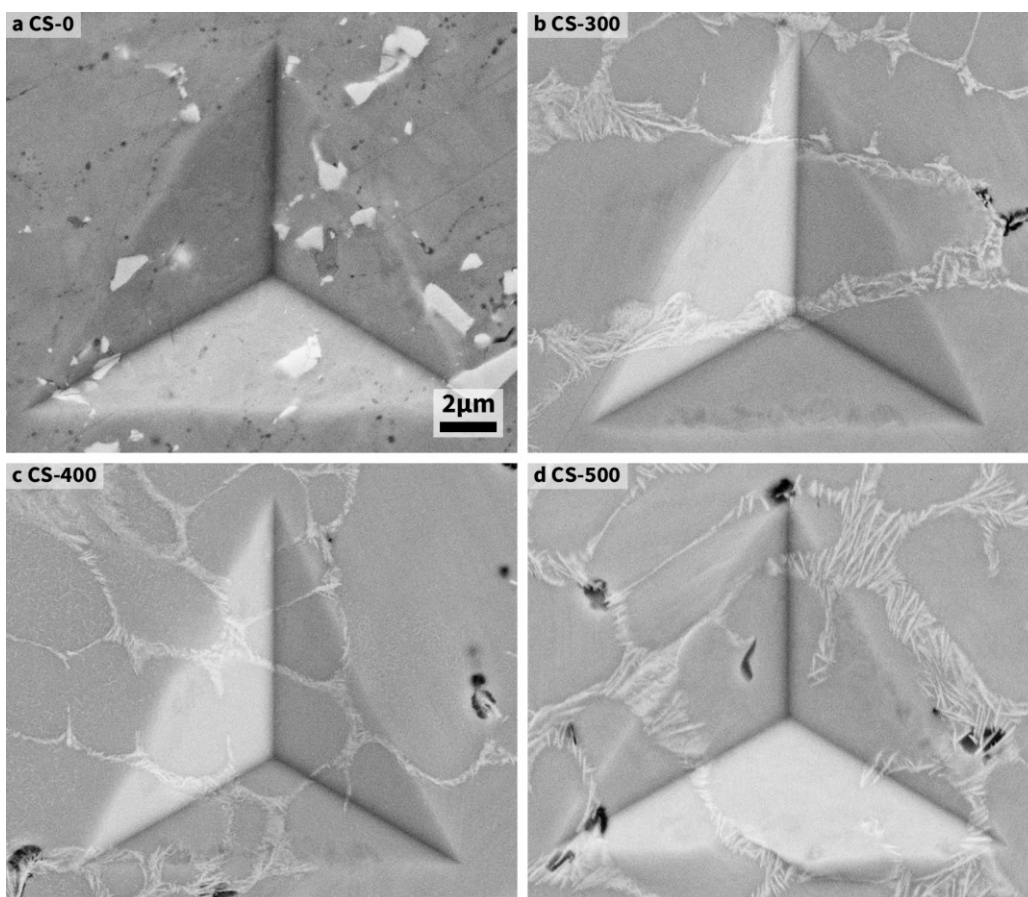


Fig. 4.15 – SEM images of the indented cross-section of the cold-sprayed and the LSM coatings subjected to the nanoindentation test.

4.5 Cavitation erosion performance

4.5.1 Cavitation erosion and erosion rate

The cumulative erosion and the erosion rate of the cold-sprayed coating, the LSM coatings, and the 316LASS in terms of the mean depth of erosion (MDE) and the MDE rate (MDER) are presented in **Fig. 4.16**. The total CE

loss after a 10-h CE test is shown in Fig. 4.17a. The average CE rate from the 8th hour to the 10th hour is considered as the steady-state CE rate, since all the samples entered the steady-state period after the 8th h (Fig. 4.16b), and the results are given in Fig. 4.17b.

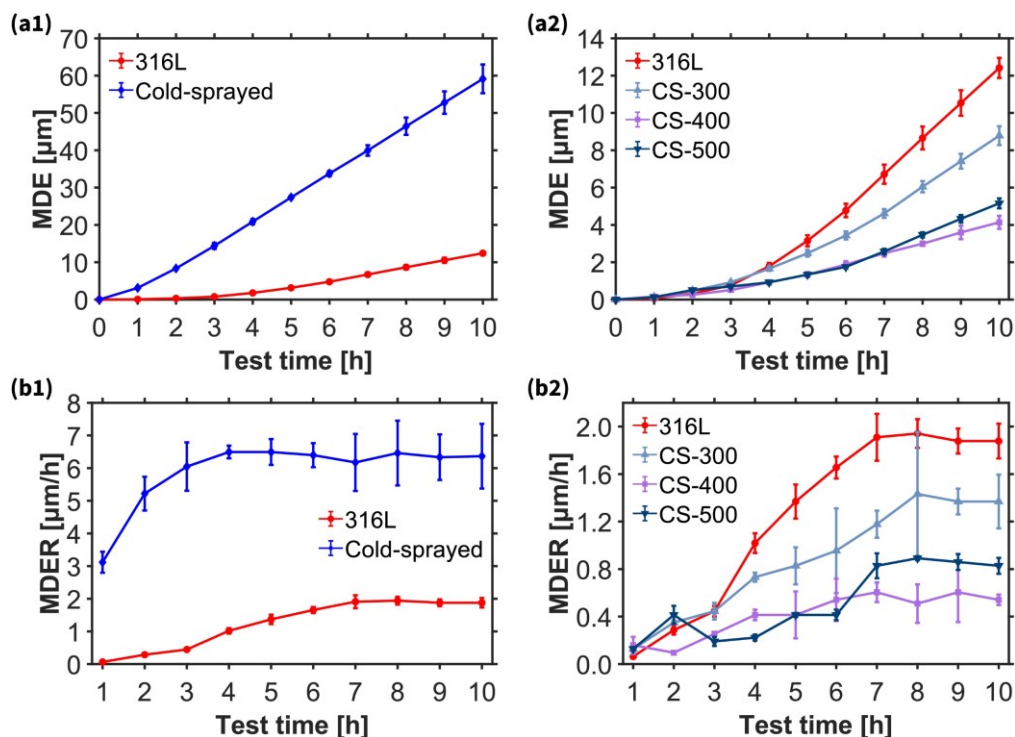


Fig. 4.16 – Cavitation erosion results of the 316L ASS, the cold-sprayed coating, and the LSM coatings. a, Cumulative erosion in terms of MDE; b, Erosion rate in terms of MDER; 1, The results of the cold-sprayed coating and the 316L ASS; 2, The results of the LSM samples and the 316L ASS.

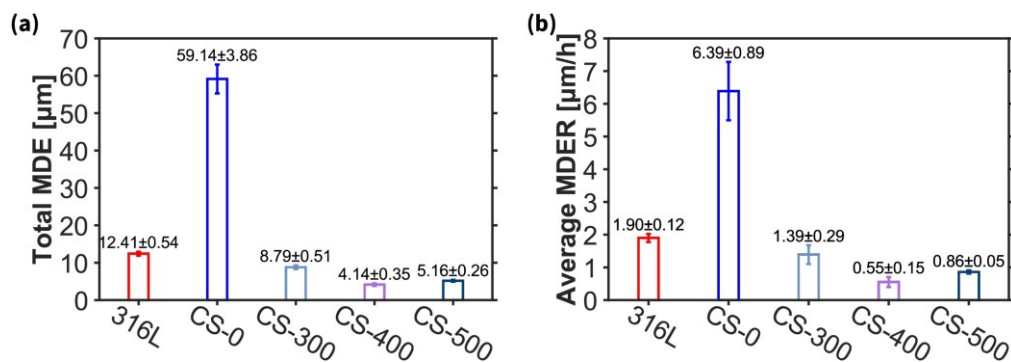


Fig. 4.17 – Erosion and the average erosion rate of the 316L ASS, the cold-sprayed coating, and the LSM coatings. a, Erosion after 10-h cavitation erosion in terms of MDE; b, Average erosion rate during the steady state period (from the 8th to the 10th h) in terms of MDER.

Cavitation erosion of LSM cold-sprayed Ni-WC coating

The samples arranged in the ascending order of the total MDE and the MDER are the CS-400, the CS-500, the CS-300, the 316L ASS, and the CS-0 (Fig. 4.17). All the LSM samples had much lower MDE and MDER compared to the cold-sprayed sample. The lowest total MDE was achieved by the CS-400 sample, which was 7.0% and 33.3% that of the cold-sprayed coating and the 316L ASS, respectively. The CS-400 sample also exhibited the lowest MDER, which was only 8.6% and 28.9% that of the cold-sprayed coating and the 316L ASS, respectively. The results of the CE test indicated that the CS-400 had the best CER, and the LSM could effectively enhance the CER of the cold-sprayed Ni-WC coating.

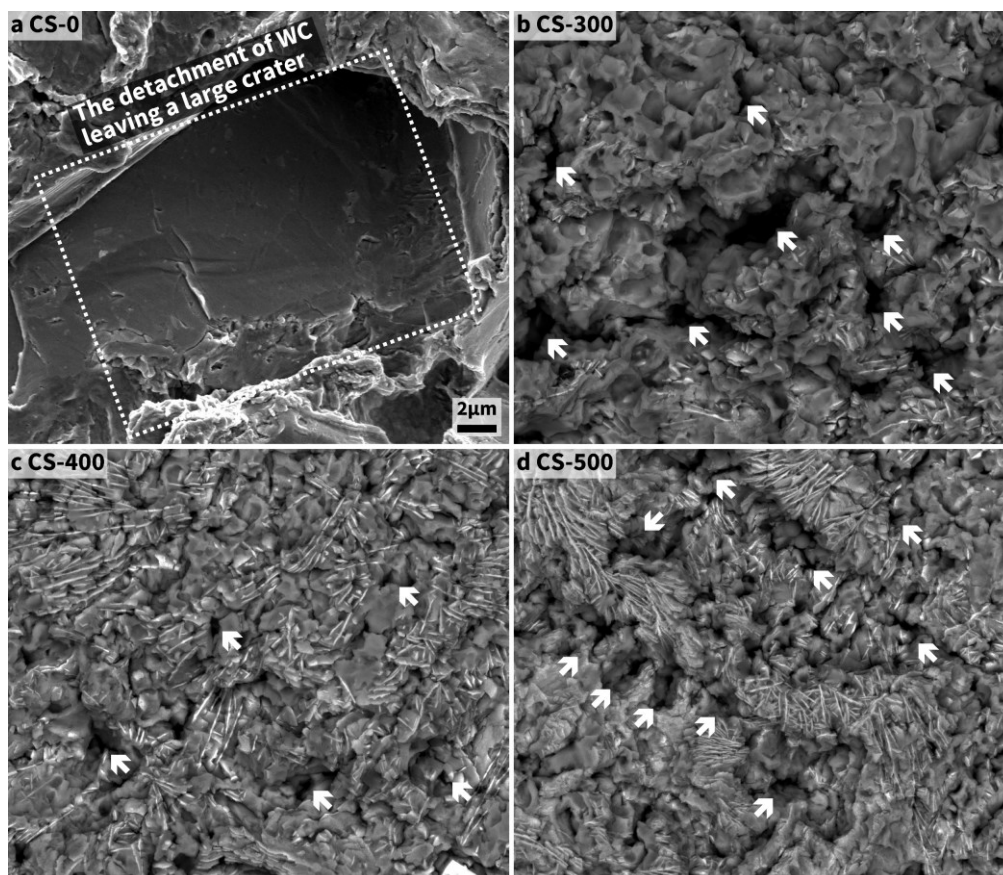


Fig. 4.18 – SEM images showing the surface of the cold-sprayed and the LSM samples after the exposure to cavitation for 10 h. White arrows in b-d: Cavitation erosion pits and microcracks.

4.5.2 SEM characterisation of the eroded samples

The eroded surface and cross-section of the LSM and the cold-sprayed coatings exposed to the 10-h CE test are presented in **Fig. 4.18** and **Fig. 4.19**, respectively. For the cold-sprayed coating, a large cavitation crater (**Fig. 4.18a**) and an exposed WC particle (**Fig. 4.19a**) were observed. The profile of the crater was very smooth, indicating a WC particle just detached recently during the CE test (**Fig. 4.18a**). The exposed WC particle (**Fig. 4.19a**) is supposed to be removed soon and leave a similar large smooth crater on the surface if the sample is exposed to CE further.

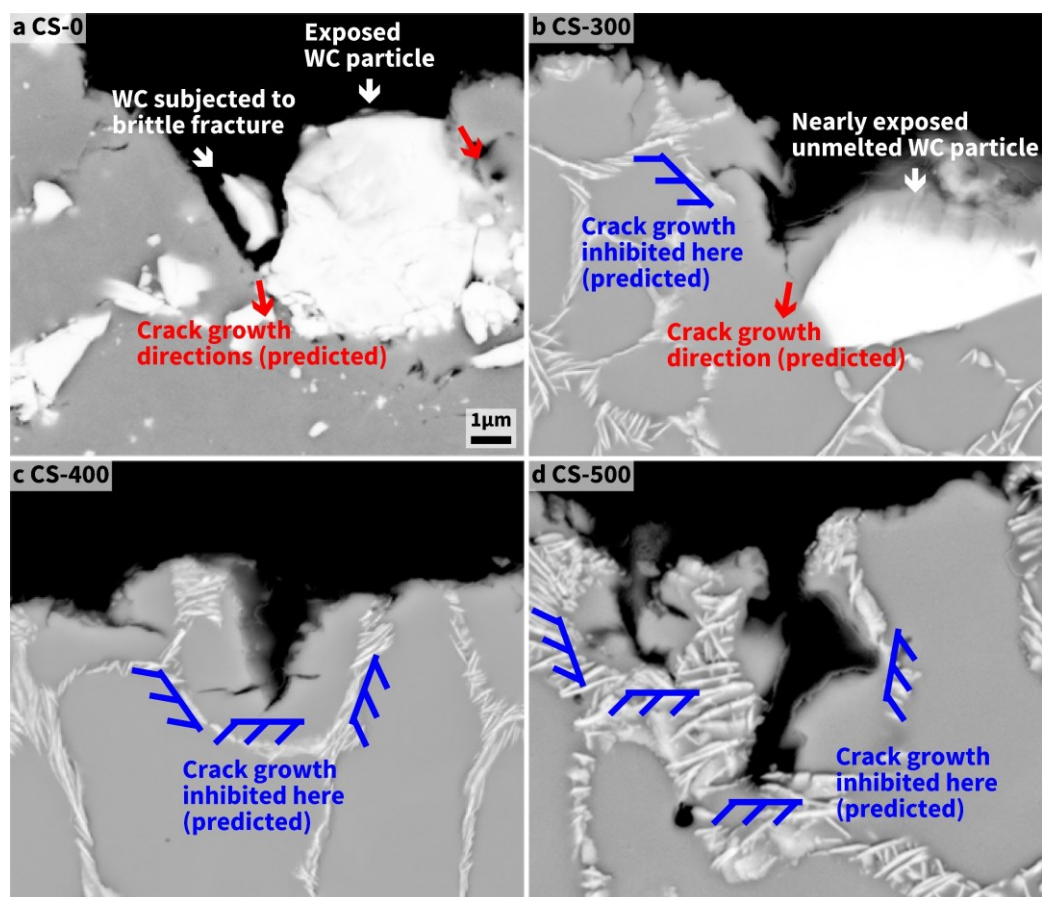


Fig. 4.19 – SEM images showing the cross-section near the surface of the cold-sprayed and the LSM samples after the exposure to cavitation for 10 h.

For the LSM samples, small cavitation pits and micro-cracks were found on the eroded surface (**Fig. 4.18b-d**), and the pits and micro-cracks tended to be located in the Ni-rich region. The preferential erosion of Ni in the LSM samples was also confirmed by the cross-section of the eroded samples. The SEM images in **Fig. 4.19b-d** suggested that the eutectic Ni-WC network may inhibit the growth of the cavitation pits and micro-cracks.

4.5.3 Profilometry of the eroded samples

The surface and linear profiles of the LSM and the cold-sprayed samples subjected to the 10-hour CE test are shown in **Fig. 4.20**. The surfaces ranging from rough to smooth are the cold-sprayed, the CS-300, the CS-500, and the CS-400 samples. The dimension of the cavitation pits in the eroded LSM samples was much smaller than that of the cavitation craters in the eroded cold-sprayed samples. The profile of the eroded cold-sprayed samples showed that the cavitation craters were ~ 250 μm in diameter and ~ 90 μm in depth, suggesting that the cold-sprayed sample had very poor CER. The pits in the eroded CS-300 sample were ~ 150 μm in diameter and ~ 30 μm in maximum depth. The surface of the CS-400 and the CS-500 coatings were relatively smooth after the exposure to CE for 10 h, and the depth of the pits was only ~ 8 μm and ~ 12 μm .

The statistics of the depth distribution based on the surface profile of the

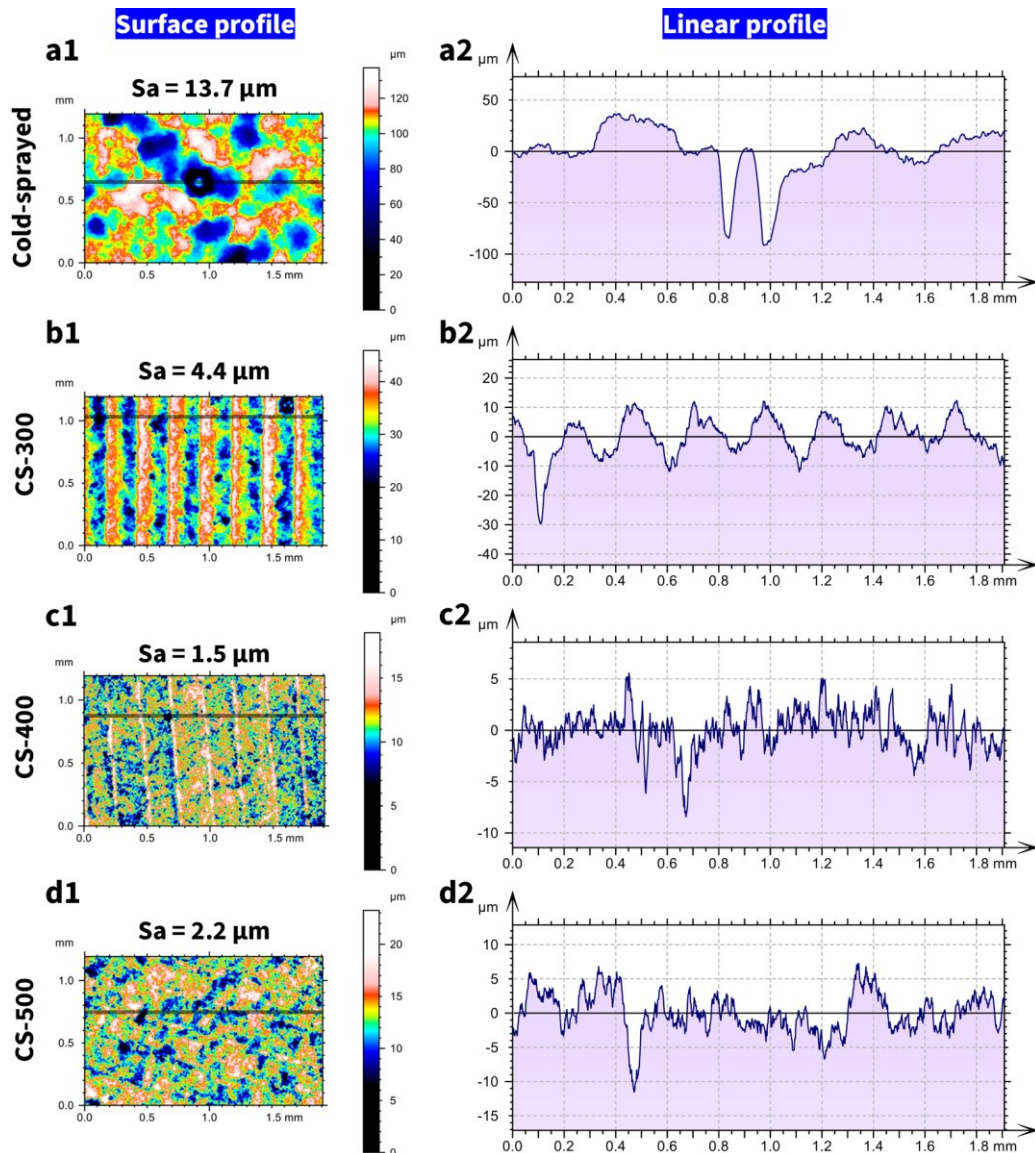


Fig. 4.20 – Surface and linear profiles of the cold-sprayed and the LSM samples after the exposure to cavitation for 10 h. The linear profile is corresponding to the dark horizontal line in the contour of the surface profile.

eroded samples (Fig. 4.20) are presented in Fig. 4.21, which also showed that the eroded surface of the CS-400 and the CS-500 samples was much smoother than that of the cold-sprayed sample. These results (Fig. 4.20 and Fig. 4.21) also confirmed that the LSM samples had much better CER than the cold-sprayed sample.

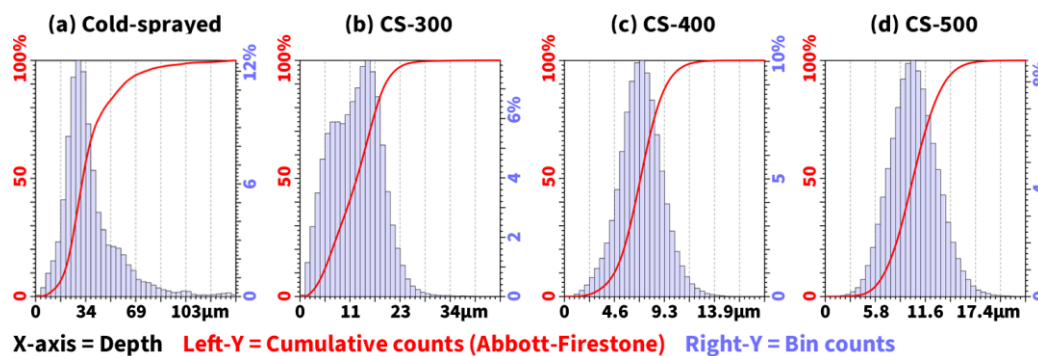


Fig. 4.21 – The depth distribution of the craters/pits of the cold-sprayed and the LSM samples after the exposure to cavitation for 10 h. These plots are based on the surface profiles in Fig. 4.20.

4.6 Discussion

4.6.1 Effects of LSM on cold-sprayed Ni-WC coating

The original intention of using LSM as a post-treatment was to improve the adhesion at the Ni-WC interface by wetting the WC with molten Ni. Meanwhile, the inter-splat boundaries were eliminated. Hence, the improved phase boundary cohesion may slow down the detachment of the WC grains, and the remelted metal matrix may have a good work-hardening ability, which were similar to other post-melted WC-based coatings reported in the literature (**Fig. 2.27**) [201]. According to the SEM (**Fig. 4.5**) and the STEM images (**Fig. 4.10a**), the precipitated WC lamellar grains were firmly bonded to the Ni matrix. The EBSD results (**Fig. 4.7** and **Fig. 4.9**) also evidenced that there were not any inter-splat boundaries within the Ni matrix. Therefore, the expected effects of using LSM as a post-treatment were realised.

4.6.2 Possible reasons for the formation of lamellar WC

However, the LSM process also altered the original microstructure of the cold-sprayed Ni-WC coating into a completely different one. The altered microstructure was composed of the Ni matrix and the eutectic Ni-WC network between the dendrite arms of the Ni grains. Nevertheless, many studies that applied post-melting or laser processing techniques to the Ni-WC-based materials did not achieve a similar microstructure. Some studies found a considerable amount of the undissolved WC particles in the laser-processed layer [27, 218, 292-296]. This is because these studies used a fast scanning speed, a large laser spot, or an impulse laser. As a result, these specific processing parameters could only provide very low energy input, and thus the molten pool could not dissolve the WC particles. The result in this work (**Fig. 4.5a2**) also suggests that sufficient heat input was required.

On the other hand, the cooling condition can affect the morphology of the precipitated WC grains as well. The WC grains in the cast Ni-WC (WC = 25 vol.%) were not lamellar, while WC lamellae were found in the LSM cast Ni-WC treated by the 400 W-laser (**Fig. 4.22**), which suggested that the microstructure of the precipitated WC grains is highly correlated to the cooling condition. The volume of the molten pool was very low during the LSM process because the laser spot size was small. Therefore, the

cooling rate of the molten pool was very high during the solidification process, which may improve the eutectic growth of Ni-WC. In addition, other alloying elements can also affect the microstructure of the LSM layers. For example, the laser-processed Ni-WC-based layers in these studies also exhibited multiple phases, but the precipitated carbides in the matrix and the eutectic region were not lamellar [218, 221, 293-301]. In summary, the high energy input, the fast-cooling rate, and the appropriate chemical composition may contribute to the laminated arrangement of the WC grains in the LSM samples.

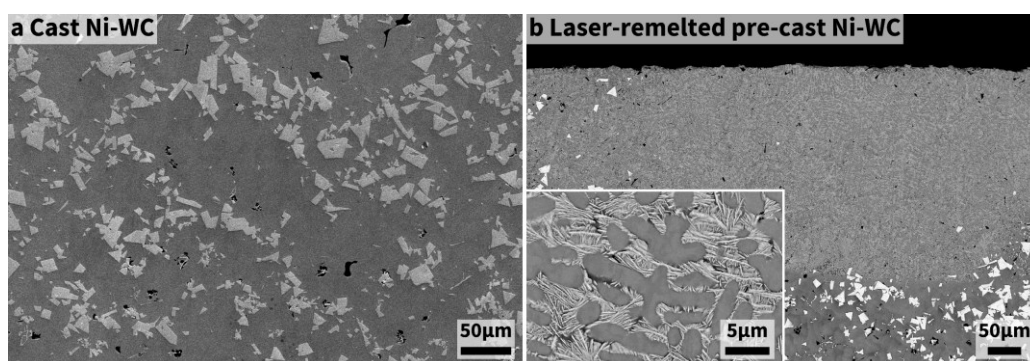


Fig. 4.22 – SEM images of the cast Ni-WC ingot before and after laser surface melted by 400 W laser. a, Original cast Ni-WC ingot; b, The cross-section of the laser surface melted cast Ni-WC.

4.6.3 Mechanical properties and cavitation erosion resistance

The CS-400 sample in this work exhibited the lowest MDER of 0.55 µm/h, and the value was 28.9% that of the 316L ASS, while the conventional HVOF-sprayed WC-10Cr-4Cr coating has a CE rate that is similar to the 316L ASS [302]. Therefore, the CS-400 sample significantly outperformed

the conventional HVOF-sprayed WC-10Cr-4Cr coating in CER, showing its great potential in the application of resisting CE. As mentioned earlier, some studies suggested that the CER was positively correlated to microhardness. Nevertheless, the microhardness of the HVOF-sprayed WC-10Cr-4Cr coating can range from 1000 to 1500 Hv [191, 194, 198, 208], which is 2 to 3 times higher than that of the LSM Ni-WC coating, but the LSM Ni-WC coatings also had much better CER. Moreover, the LSM coatings had similar microhardness as the cold-sprayed coating, but the CER of the LSM coatings was much superior. Hence, microhardness is not a reliable indicator for the CER of the materials with different microstructures, even if the materials have the same chemical composition. Furthermore, other mechanical properties, including H_{IT} , E_{IT} , H_{IT}/E_{IT} , H_{IT}^2/E_{IT} , and H_{IT}^3/E_{IT}^2 (**Fig. 4.14**), could not give a reliable prediction on the CER of the materials either, since the ranking of the CER (**Fig. 4.17**) did not match the ranking of these mechanical properties (**Fig. 4.14**). In addition, other literature also suggests that good mechanical properties modulus may not be associated with good CER [237].

4.6.4 Microstructure and cavitation erosion resistance

As it was claimed that the enhanced CER of the LSM Ni-WC samples was not closely correlated to the improved mechanical properties, the altered

microstructure of the LSM Ni-WC samples can be the only remained factor contributing to the enhanced CER.

The microstructure of the cold-sprayed Ni-WC sample was very similar to that of the conventional sprayed cermet coating. Thus, the cold-sprayed Ni-WC were also subject to the sudden brittle detachment of the hard WC particles, for example, the large smooth crater in **Fig. 4.18a**. Meanwhile, the exposed WC particle shown in **Fig. 4.19a** were supposed to be removed soon if the surrounding Ni matrix were eroded. On the other hand, the bonding between the Ni matrix and the WC particles was very weak because the cold-spraying process can only provide mechanical interlocking [303, 304], which results in the cold-sprayed Ni-WC coating being much more susceptible to cavitation impacts compared to the HVOF-sprayed cermet coating. As a result, the cold-sprayed Ni-WC coatings exhibited very poor CER. In addition, the large deviation in the CE results of the cold-sprayed Ni-WC was also due to the sudden detachment of the WC particles (**Fig. 4.16a1-b1**).

For the LSM Ni-WC coatings, the two microstructural features may be responsible for the remarkable CER, which are the WC lamellae and the eutectic Ni-WC network. As shown in **Fig. 4.19b-d**, microcracks had a minimal chance in forming or propagating inside the eutectic Ni-WC with the hierarchically layered and interlocked WC lamellae. Therefore, the

eutectic Ni-WC network act as a barrier that inhibited crack propagation. However, the hard cermet particles in the conventional HVOF-sprayed cermet coatings in the literature and the cold-sprayed Ni-WC coating in this work can also resist crack propagation, but these coatings did not exhibit excellent CER. This is because there was a large region of metal matrix that was not covered by the cermet particles, and the uncovered matrix could be easily eroded during CE. Furthermore, the propagation of the microcracks tended to bypass the cermet particles instead of being stopped. When multiple cracks reach a confluence, severe material losses can occur. Nevertheless, the eutectic Ni-WC network in the LSM Ni-WC coatings divided the Ni matrix into many individual cells with closed-looped boundaries. As a result, the microcracks were confined within the individual cell and could not bypass or penetrate the eutectic Ni-WC network (**Fig. 4.19b-c**), providing a damage-controlling effect. The inhibition of the crack growth in the LSM Ni-WC coatings was also confirmed by the profilometry results (**Fig. 4.20** and **Fig. 4.21**), showing that the cavitation craters of the LSM coatings were much shallower than those of the cold-sprayed coatings.

In addition, the improved adhesion at the Ni-WC phase boundaries also minimised the chance of the sudden detachment of the WC lamellae. According to **Fig. 4.5a2-c2** and **Fig. 4.10a**, the WC lamellae are closely

bound to the surrounding Ni matrix. After indentation, microcracks were found at the Ni-WC boundaries and within the large WC particles in the cold-sprayed coating (**Fig. 4.13a**) but did not form in the LSM Ni-WC coatings (**Fig. 4.13b-d**), suggesting the enhanced boundary adhesion by the LSM process. Furthermore, the complexions (**Fig. 4.11**) at the Ni-WC phase boundaries could contribute to the improved interface strength as well [283]. As a result, the sudden detachment of the WC lamellae was less likely to occur in the LSM Ni-WC coatings, and hence the deviation of the erosion rate was very small compared to the cold-sprayed Ni-WC coatings (**Fig. 4.16b**).

4.6.5 Defects and cavitation erosion resistance

Despite of the enhanced CER, the LSM Ni-WC coatings processed by different laser power exhibited different defects. For the CS-300 sample, the relatively low heat input resulted in the insufficient melting or dissolving of the WC particles, leaving the unmelted or partially melted WC particles in the remelted Ni matrix (**Fig. 4.5a**). These WC particles could still be subjected to the sudden detachment during CE when the surrounding Ni matrix was eroded (**Fig. 4.19b**). Therefore, the erosion rate of the CS-300 sample had a relatively larger deviation compared to the other LSM coatings (**Fig. 4.16b2**). Meanwhile, the thin eutectic Ni-WC network in the

CS-300 sample due to incomplete melting of the WC particles also resulted in the lower CER of the CS-300 samples compared to the other LSM coatings. According to **Fig. 4.18b-d**, **Fig. 4.20**, and **Fig. 4.21**, the CE pits in the CS-300 sample were deeper and broader than the other LSM coatings. For the CS-500 sample, many small pores were found in the LSM layer (**Fig. 4.5c2**), and these pores were susceptible to cavitation impacts and could compromise the CER. As a result, the CS-500 sample had lower CER (**Fig. 4.16b2**) and exhibited more cavitation pits (**Fig. 4.18d**) compared to the CS-400 sample. It is also worth mentioning that the differences in the mechanical properties of the LSM coatings (**Fig. 4.12** and **Fig. 4.14**) may be attributed to the differences in the type and the number of these defects.

4.6.6 Cavitation erosion and fatigue failure

As the phenomenon of cavitation erosion can be viewed as a form of local surface fatigue induced by repetitive cavitation impacts, it is pertinent to explore the relationship between cavitation erosion and fatigue through estimations and assumptions.

If a micro jet at a velocity, v , is discharged from a cavitation bubble having a diameter, d_b , and the volume of the micro jet is assumed to be equal to the cavitation bubble volume, the momentum of the micro jet, P , is given

by **Eq. 4.1**:

$$P = mv = \frac{1}{6}\pi d_b^3 \rho v \quad \text{Eq. 4.1}$$

Here, m denotes the mass of the micro jet, and ρ is density of water.

Assuming that the momentum of the micro jet is entirely transmitted to an area, the resulting applied load, F , is given by **Eq. 4.3**:

$$\frac{1}{6}\pi d_b^3 \rho v = Ft \quad \text{Eq. 4.2}$$

$$F = \frac{1}{6}\pi d_b^3 \rho v / t \quad \text{Eq. 4.3}$$

Here, t is the duration of the load applied to the area.

If the impacted area is a circle with a diameter, d , the stress applied to this area (δ) can be found:

$$\delta = F \cdot \frac{4}{\pi d^2} = \frac{2d_b^3 \rho v}{3td^2} \quad \text{Eq. 4.4}$$

As the size of the impacted area is generally considered 1/10 of the bubble size [1], the stress applied to the area (δ) is:

$$\delta = \frac{200d_b \rho v}{3t} \quad \text{Eq. 4.5}$$

According to the literature, the size of a theoretical resonance cavitation bubble is about 150 μm at 20 kHz [305], the duration of the load applied to the surface is about 20 μs [1], and the velocity of the micro jet is assumed to be 1000m/s [43, 44]. Then, the stress applied to the area (δ) can be determined from **Eq. 4.5**, which is about 500 MPa.

Assuming there is a random site with d_{rd} diameter and its distance to the sample edge is at least greater than the diameter of the impacted area,

d , the probability of a micro jet hit this site, $P(A)$, is:

$$P(A) = \frac{(2d - d_{rd})^2}{D^2} \quad \text{Eq. 4.6}$$

Where D is the diameter of the sample, which is 20 mm. According to **Fig. 4.18**, the size of cavitation erosion pits was about 1-2 μm . Thus, assuming d_{rd} is 1 μm , $P(A)$ equals 1.05×10^{-8} .

At 20 kHz, there are about 10^4 cavitation bubbles per 1 cm^3 in aqueous media [306]. The diameter of the sample in this work was 20 mm, and the distance of the sample surface to the ultrasonic horn was 1 mm. Thus, the number of the cavitation bubbles above the sample surface is about 3140. Then, assuming the lifetime of these cavitation bubbles is 20 μs , the number of the cavitation bubbles (\dot{N}) is about $1.57 \times 10^8/\text{s}$. Hence, the number of the impacts applied to a random site in one second, \dot{n} , is:

$$\dot{n} = P(A) \cdot \dot{N} = 1.65/\text{s} \quad \text{Eq. 4.7}$$

Therefore, the mathematical expectation of the times for a random site being impacted by micro jets is about 100/min.

According to **Fig. 4.16** the erosion rate of the Ni-WC samples reached maximum and was stabilised at about 7 h. At 7 h, 4.2×10^4 times of loads about 500 MPa are supposed to have applied on the sample. Study reported that Ni microbeams under 500 MPa cyclic bending corresponded to about 10^4 - 10^5 fatigue cycles [307]. Hence it is suggested that there is a strong correlation between CER and fatigue failure.

4.7 Summary

- 1) The cold-sprayed Ni-WC composite coatings were post-treated by LSM using the lasers with 300, 400, and 500 W power, respectively. After the LSM process, the adhesion at the phase boundaries was improved, and the inter-splat boundaries were eliminated in the LSM layer of the Ni-WC composite coatings.
- 2) The microstructure of the LSM coatings was very different from that of the cold-sprayed coatings. The LSM layer exhibited a eutectic Ni-WC network that divided the Ni matrix into many small individual cells. The WC grains in the eutectic Ni-WC were lamellar and showed a hierarchically layered structure. Some of the WC lamellae were interlocked with each other.
- 3) The CER of the LSM coatings was exceptionally enhanced and significantly outperformed that of the conventional HVOF-sprayed WC-based cermet coatings and the 316L ASS. The best CER was achieved by the sample processed by the 400-W laser. The erosion rate of the sample was only 8.6% and 28.9% of the cold-sprayed coating and the 316L ASS.
- 4) The experimental results in this chapter suggest that the mechanical properties were not closely correlated to the CER. However, the microstructure could play the most dominant role in resisting CE. The

Cavitation erosion of LSM cold-sprayed Ni-WC coating

SEM and the profilometry results suggested that the eutectic Ni-WC network had a damage-controlling property that could effectively inhibit microcrack growth and cavitation pits during CE.

- 5) CER may be correlated to the fatigue property of materials. However, further exploration is needed to understand the relationship between CER and fatigue.

Chapter 5

Cavitation erosion of sintered Ni-WC MMCs treated by LSM

5.1 Introduction

In **Chapter 4**, it was found that mechanical properties did not always associate with the resistance to CE, while microstructure could play a dominant role in CER. Despite **Chapter 4** having provided a nearly full-scope analysis on the CER of the samples, the study on the effects of the microstructure on the CER was based on the post-mortem results, and the understanding of the microstructural evolution of the sample in response to cavitation impacts is still absent. On the other hand, it was challenging to precisely control the composition of the materials in the coatings by using the spraying techniques, resulting in difficulties in the material-based optimisation for achieving enhanced CER.

In this chapter, Ni-WC metal matrix composites (MMCs) are post-treated by LSM. The original MMCs are prepared by vacuum hot-pressing sintering (VHS). The microstructure and the CER of the sintered MMCs post-treated by LSM are evaluated to check whether the sintering is a feasible pre-depositing method that can be substituted for the spraying prior to LSM. More importantly, SEM observation is conducted on the

eroded LSM Ni-WC MMCs exposed to cavitation at different test intervals, demonstrating the microstructural evolution of these LSM MMCs at the same site during CE. In addition, numerical simulations are also performed to further study the role of the WC lamellae in resisting CE. The original sintered Ni-WC MMC is denoted as S0-0 sample, and the LSM-treated sintered Ni-WC MMCs by the lasers of 300, 400, and 500 W are denoted as S0-300, S0-400, and S0-500 samples, respectively.

5.2 Characterisation of sintered Ni-WC

The sintered Ni-WC MMC was prepared by VHS, and the feedstock was composed of the 75 vol.% Ni and the 25 vol.% WC powders. The SEM images in **Fig. 5.1** present the polished cross-section of the sintered MMC, showing bright WC particles and dark Ni matrix.

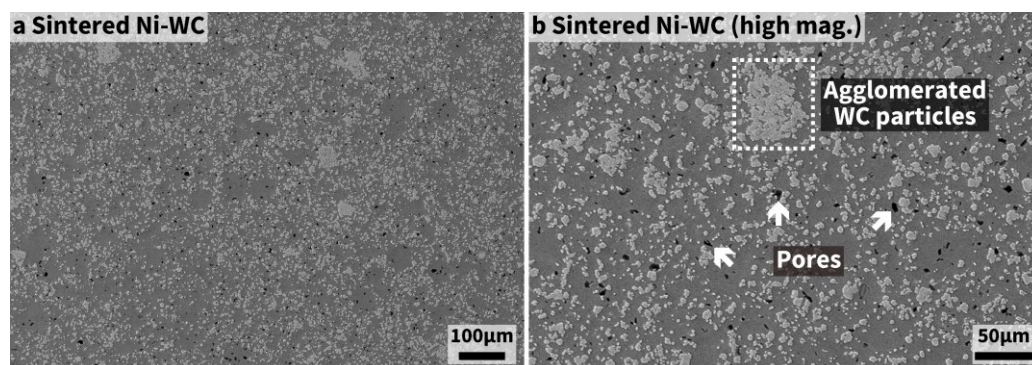


Fig. 5.1 – SEM images of the cross-section of the sintered Ni-WC MMC.

The volumetric content of the WC in the MMC was verified by analysing the SEM image in **Fig. 5.1a** and another nine with the same scale, finding that the content of the WC in the MMC was 24.5 ± 1.6 vol.%, which is

consistent with the initial WC proportion in the feedstock. The porosity of the sintered MMC was $2.1 \pm 0.3\%$, which was higher than the cold-sprayed coating (**Fig. 4.1**). Despite some clusters of agglomerated WC particles in the sintered MMC (**Fig. 5.1b**), the distribution of the WC in the sintered MMC was more homogeneous than that in the cold-sprayed coating (**Fig. 4.1**).

The XRD spectrum of the sintered Ni-WC MMC is presented in **Fig. 5.2**, which shows the peaks of FCC Ni and HCP WC. Meanwhile, no peak corresponds to oxide was found in the XRD spectrum.

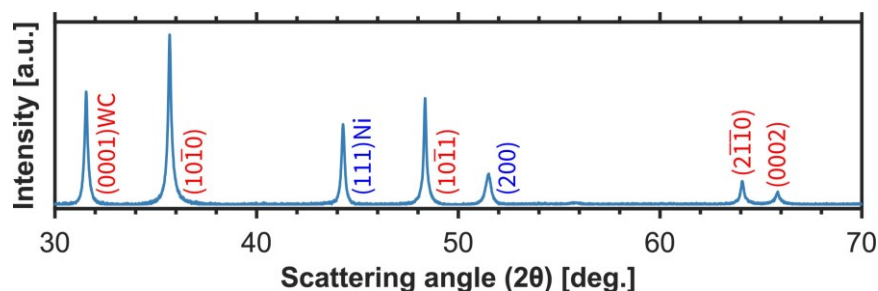


Fig. 5.2 – XRD spectrum of the sintered Ni-WC MMC.

5.3 Characterisation of LSM sintered Ni-WC

5.3.1 XRD results

The polished surface of the LSM sintered Ni-WC MMCs was characterised by XRD. According to **Fig. 5.3**, the XRD spectra of all the LSM MMCs only show the peaks of FCC Ni and HCP WC, indicating that the LSM process did not introduce any new phase or the contents of WC_x , Ni_4W , and Ni_xW_yC were extremely low. It is worth noting that the S0-300

sample had relatively narrower and sharper WC peaks compared to the other two LSM MMCs, suggesting microstrain may develop in the S0-300 sample.

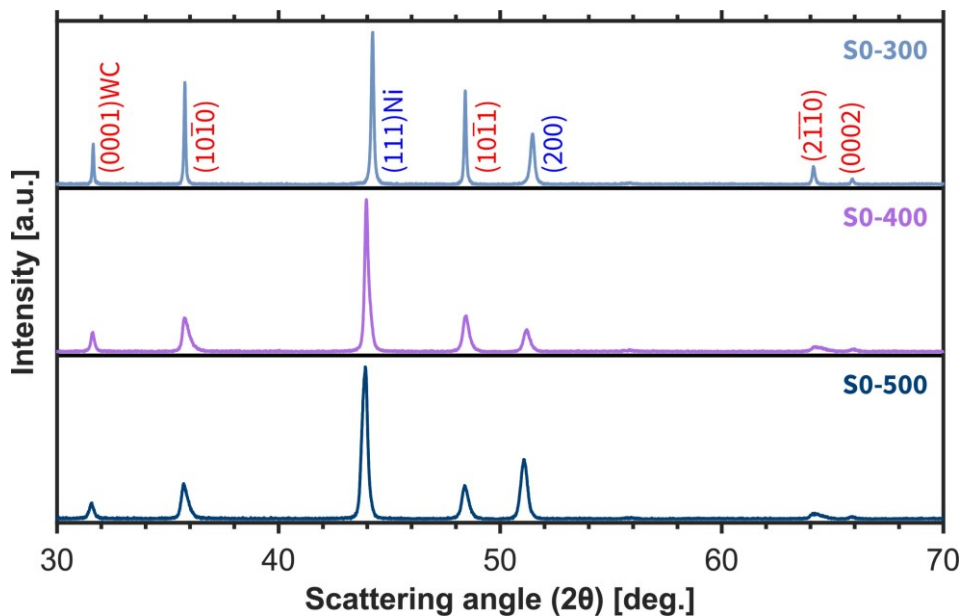


Fig. 5.3 – XRD spectra of the LSM sintered Ni-WC MMC.

5.3.2 SEM results

The SEM images of the polished cross-sections of the LSM sintered Ni-WC MMCs are shown in **Fig. 5.4**. The remelted layer was slightly thicker in the LSM sintered MMC (**Fig. 5.4a1-c1**) than that in the LSM cold-sprayed coating (**Fig. 4.5a1-c1**) when the laser power was the same. The remelted layer in the LSM sintered MMC (**Fig. 5.4a2-c2**) exhibited a microstructure similar to the LSM cold-sprayed coating (**Fig. 4.5a2-c2**), where the eutectic Ni-WC with the hierarchical layered and interlocked WC lamellae divided the Ni matrix into many small cells. Bands of large

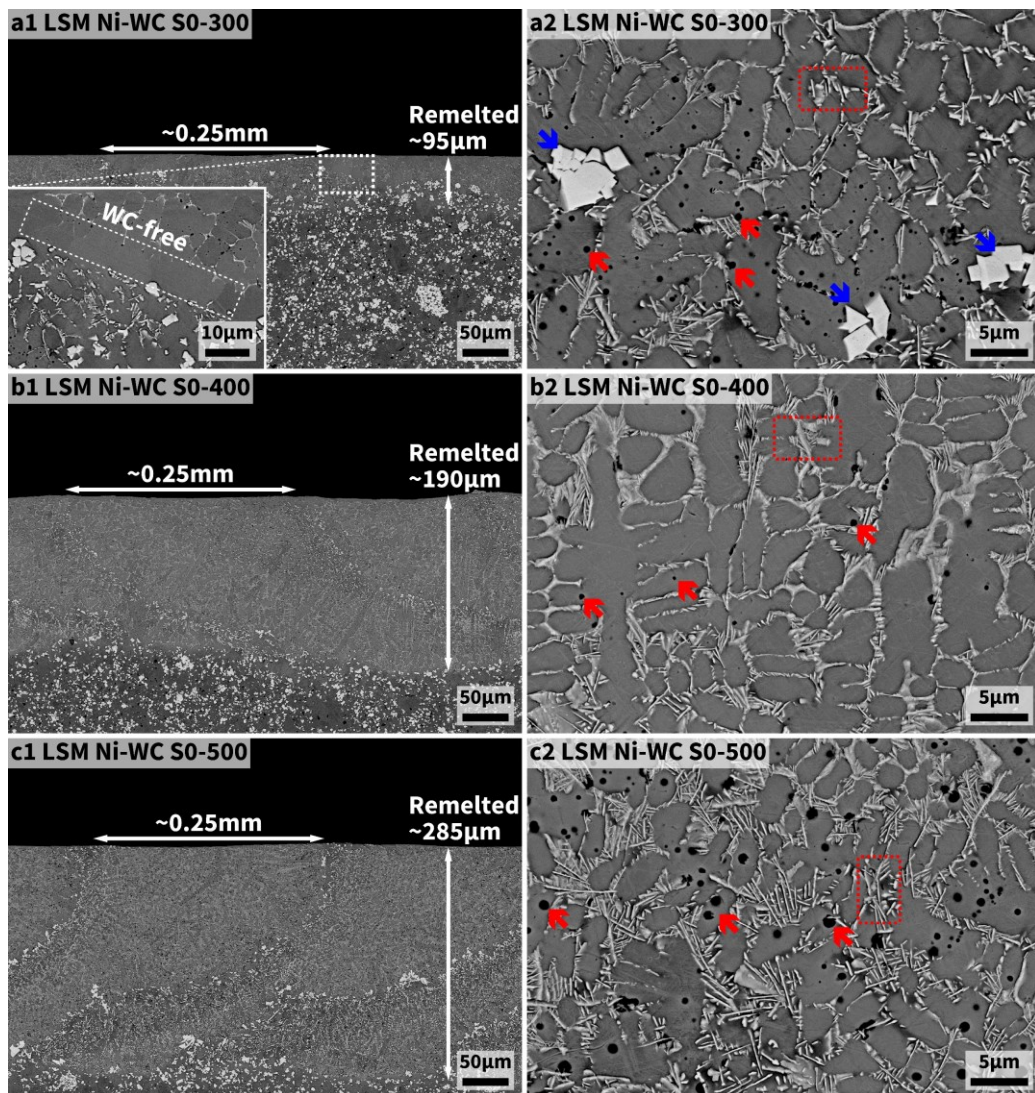


Fig. 5.4 – SEM images showing the cross-sections of the LSM Ni-WC MMCs treated by different laser powers. a-c, Specimens treated by 300-, 400-, and 500-W lasers, respectively; 1, Low magnification; 2, High magnification. Arrows: Remelted zone (vertical, white), space of two adjacent bands of Ni-rich zone or large WC grains (horizontal, white), pores (red), and large WC grains in the LSM layer of the S0-400 sample (blue); Dotted rectangles in a2-c2: Eutectic Ni-WC.

WC grains were also observed in the LSM sintered MMCs treated by 400- and 500-W lasers (highlighted by the horizontal white arrows in **Fig. 5.4b2-c2**), and the distance between two adjacent bands was about 0.25 mm, which was equal to the space between two adjacent traces of the laser (**Fig. 3.2**). These bands located at the edges of the molten pools. Although very large WC grains were also found from the LSM sintered

MMC treated by the 300-W laser, these large WC grains were dispersed and did not form a band (**Fig. 5.4a1**). Instead, bands which were nearly WC-free divided the remelted layer of the S0-300 sample (the magnified image in **Fig. 5.4a1**), and the distance of two adjacent bands was also about 0.25 mm.

Although the LSM sintered MMCs and the LSM cold-sprayed coatings had a similar microstructure, the differences were obvious. The LSM sintered MMCs treated by 300- and 500-W lasers exhibited more pores in the LSM layer compared to the LSM cold-sprayed coatings (**Fig. 5.4a2-c2** and **Fig. 4.5a2-c2**), but the LSM sintered MMC treated by the 400-W laser had the lowest porosity (**Fig. 5.4b2**). The porosity of the S0-300, S0-400, and S0-500 was $1.0\pm 0.3\%$, $0.3\pm 0.2\%$, and $2.1\pm 0.6\%$, respectively. In addition, the large WC grains at the edge of the molten pool were very few (**Fig. 5.4a1**), but many of them were distributed inside the molten pool of the LSM sintered MMC treated by the 300-W laser (**Fig. 5.4a2**). These large WC grains were suspected to be precipitated rather than incompletely melted because the morphology of these WC grains in the remelted layer (**Fig. 5.4a2**) was different from that of the WC particles in the sintered MMC (**Fig. 5.1b**). In addition, it is also worth mentioning that the morphology of these large WC grains in the S0-300 sample (**Fig. 5.4a2**) was very similar to that of the WC grains in the cast Ni-WC ingot (**Fig. 4.22a**).

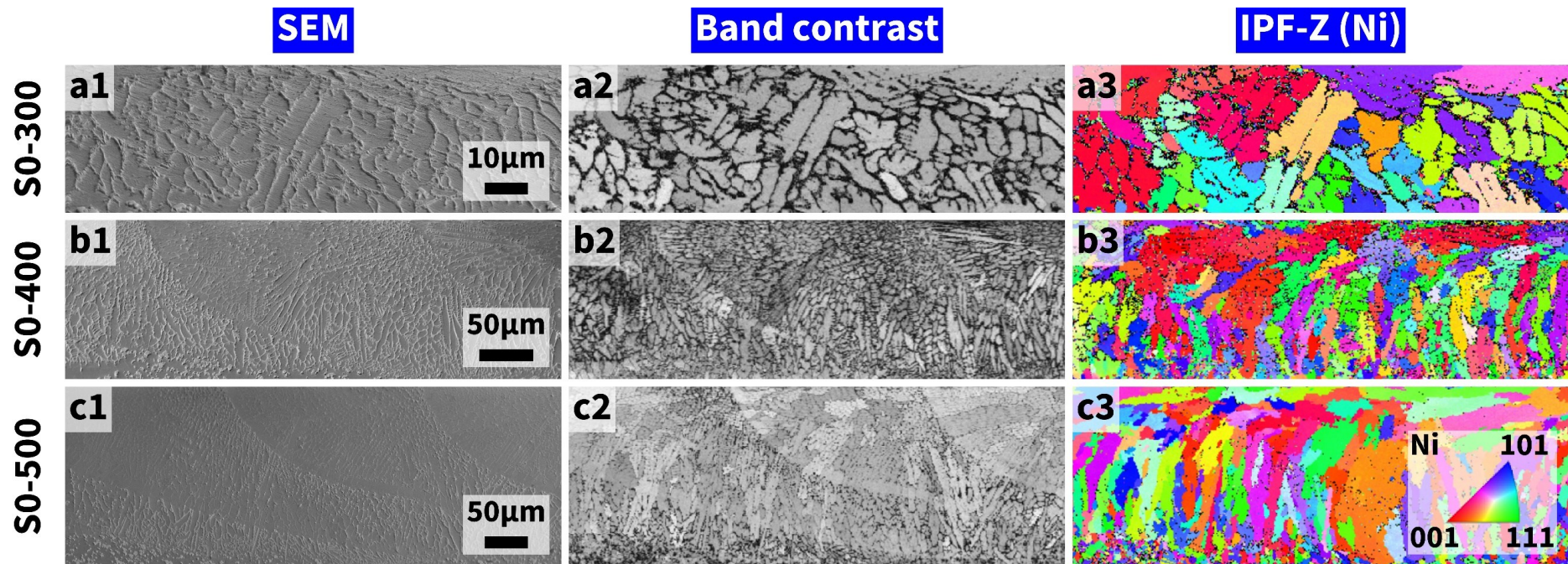


Fig. 5.5 – EBSD results of the cross-section of the LSM Ni-WC MMCs.

5.3.3 EBSD results and grain size

The EBSD results of the LSM sintered Ni-WC MMCs are shown in **Fig. 5.5**. Similar to the LSM cold-sprayed coatings (**Fig. 4.7 a3-c3**), the melted layer of the LSM sintered MMCs also exhibited the columnar grains without any preferred orientation (**Fig. 5.5a3-c3**), and the Ni grain size was positively correlated to the power of the laser (**Fig. 5.6**). For the samples treated by the same laser power, the grain size of the LSM sintered sample was slightly higher than the LSM cold-sprayed samples (**Fig. 4.8** and **Fig. 5.6**).

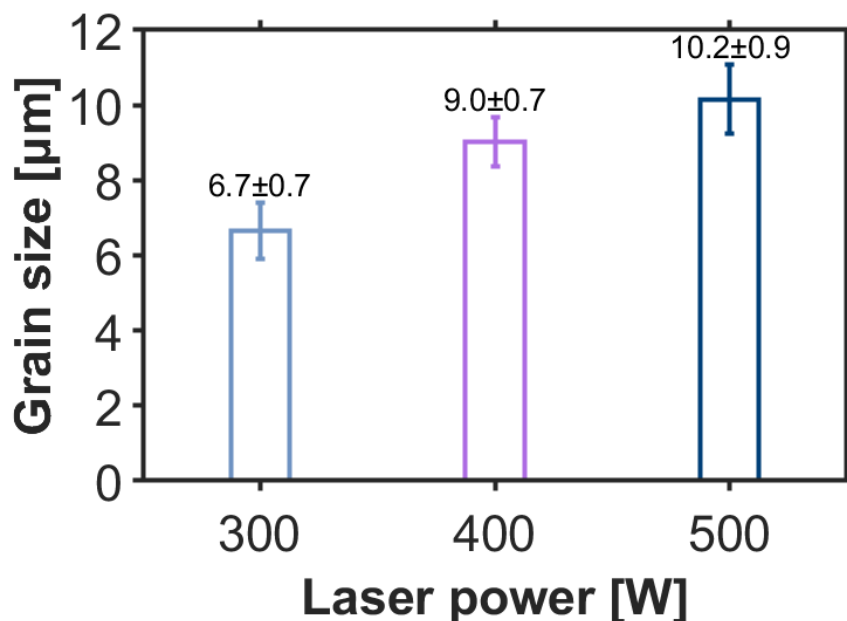


Fig. 5.6 – Grain size of the LSM sintered MMCs.

5.3.4 Microhardness

Although it may not be correlated to CER according to **Chapter 4**, microhardness is a commonly used indicator of the quality of coatings or

overlays. As shown in **Fig. 5.7**, the S0-300 and the S0-500 MMCs had lower microhardness than the S0-400 MMC, because the S0-300 sample had relatively fewer WC lamellae in the Ni-WC eutectic (**Fig. 5.4a2**) and the S0-500 sample had more pores (**Fig. 5.4c2**) compared to the S0-400 sample.

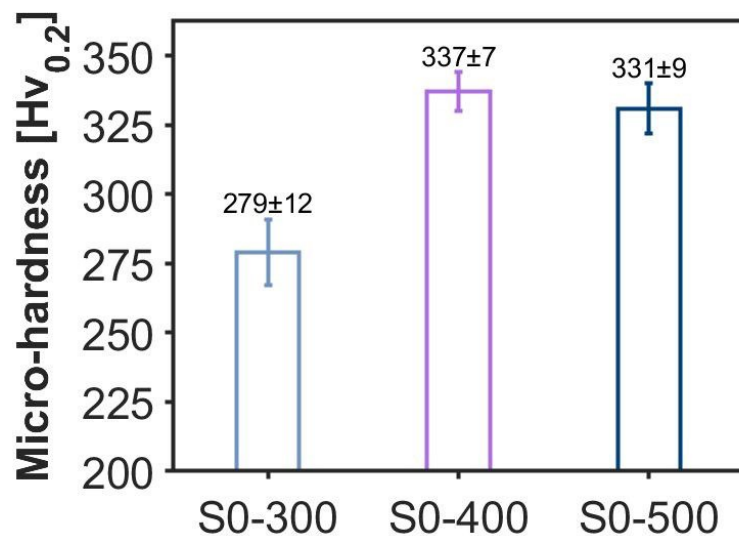


Fig. 5.7 – Microhardness of the LSM sintered MMCs.

5.4 Cavitation erosion and erosion rate

The cumulative erosion and the erosion rate of the LSM sintered Ni-WC MMCs in terms of MDE and MDER are presented in **Fig. 5.8**. The total CE loss after the 10-h CE test is shown in **Fig. 5.9a**. The average CE rate from the 8th h to the 10th h is considered the steady-state CE rate, since all the samples entered the steady-state period after the 8th h (**Fig. 5.8b**), and the results are given in **Fig. 5.9b**. The ranking in the erosion rate of these LSM sintered Ni-WC MMCs was also the same as the LSM cold-

sprayed Ni-WC coatings (**Fig. 4.17b**). The MMC treated by the 400-W laser exhibited the lowest cumulative erosion and erosion rate.

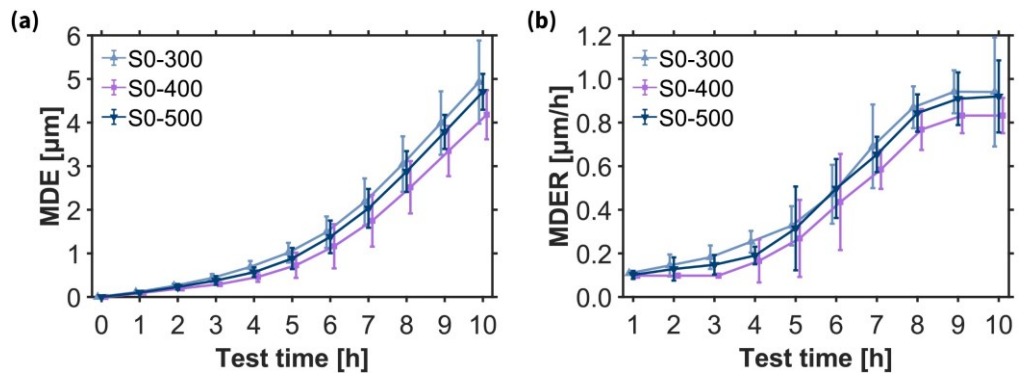


Fig. 5.8 – Cavitation erosion results of the LSM sintered MMCs. a, Cumulative erosion in terms of MDE; **b,** Erosion rate in terms of MDER.

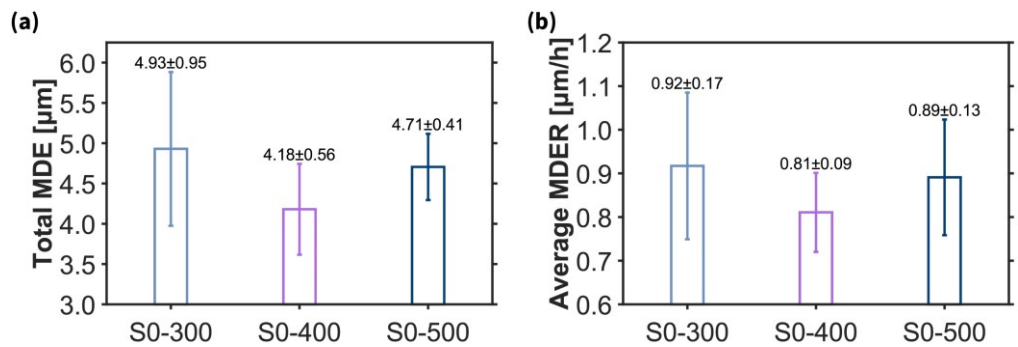


Fig. 5.9 – Total erosion and the average erosion rate of the LSM sintered MMCs. a, Total erosion after 10-h cavitation erosion test in terms of MDE; **b,** Average erosion rate during the steady-state period (from the 8th to the 10th h) in terms of MDER.

5.5 SEM observation of the samples exposed to cavitation erosion at different test intervals

5.5.1 Ni matrix and Ni-WC eutectic in Ni-WC hypoeutectic

The microstructural evolution of the hypoeutectic Ni-WC with lamellar WC in the LSM sintered Ni-WC MMCs subjected to cavitation is demonstrated in **Fig. 5.10**, **Fig. 5.11**, and **Fig. 5.12** in corresponding to S0-300, S0-400, and S0-500 samples, respectively. Slip bands were formed within the

primary Ni grains of the hypoeutectic Ni-WC (highlighted by the white dotted rectangle) as a result of stress accumulation caused by the repetitive cavitation impacts of microjets and shock waves. Meanwhile, preferential erosion was found at the primary Ni grains at the interface of the primary Ni grain and eutectic Ni-WC network (highlighted by the white arrows). The preferential erosion was attributed to the stress concentration at the interface since the hard WC lamellae in the eutectic Ni-WC network could block stress flow.

Then, further exposure to cavitation could result in two failure modes. In most cases, erosion was almost strictly confined within each cell, indicating that the surrounding eutectic Ni-WC with the hierarchically structured WC lamellae provided a damage-controlling effect. On the other hand, material removal also frequently occurred to the eutectic Ni-WC when most of the adjacent Ni in the primary Ni grains was eroded. It should be noted that the eutectic Ni-WC with a low thickness was less resistant to erosion because there were not sufficient WC lamellae to form a hierarchically interlocking structure.

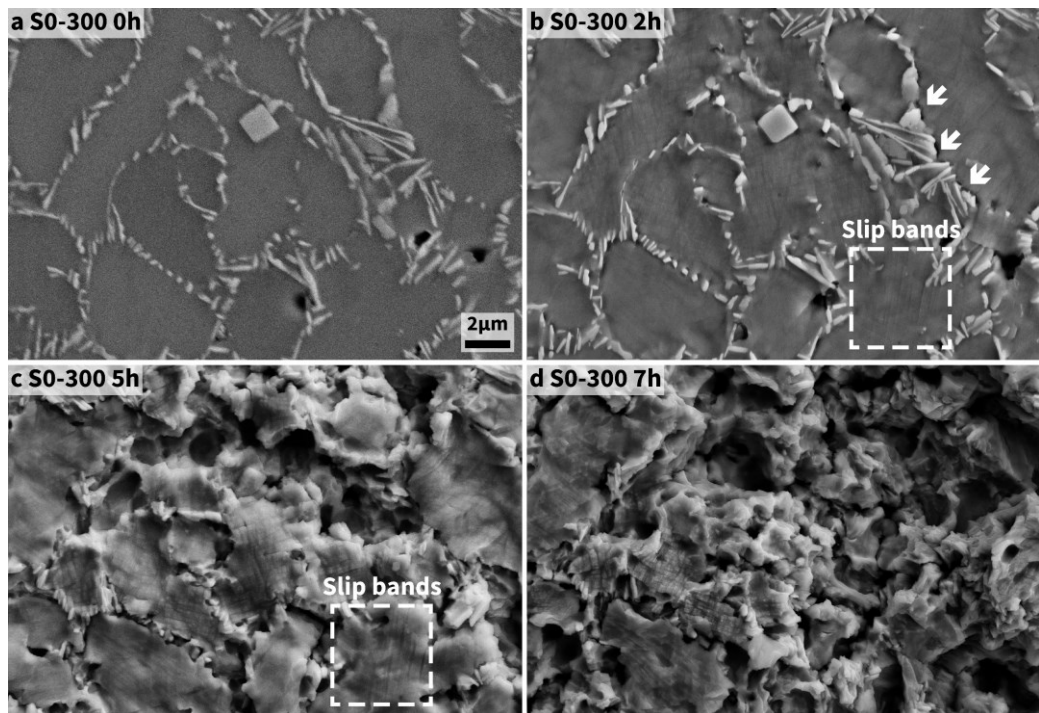


Fig. 5.10 – Microstructural evolution of hypoeutectic Ni-WC in S0-300 sample during cavitation erosion. White arrows: The erosion of the primary Ni at the interface of primary Ni and eutectic Ni-WC.

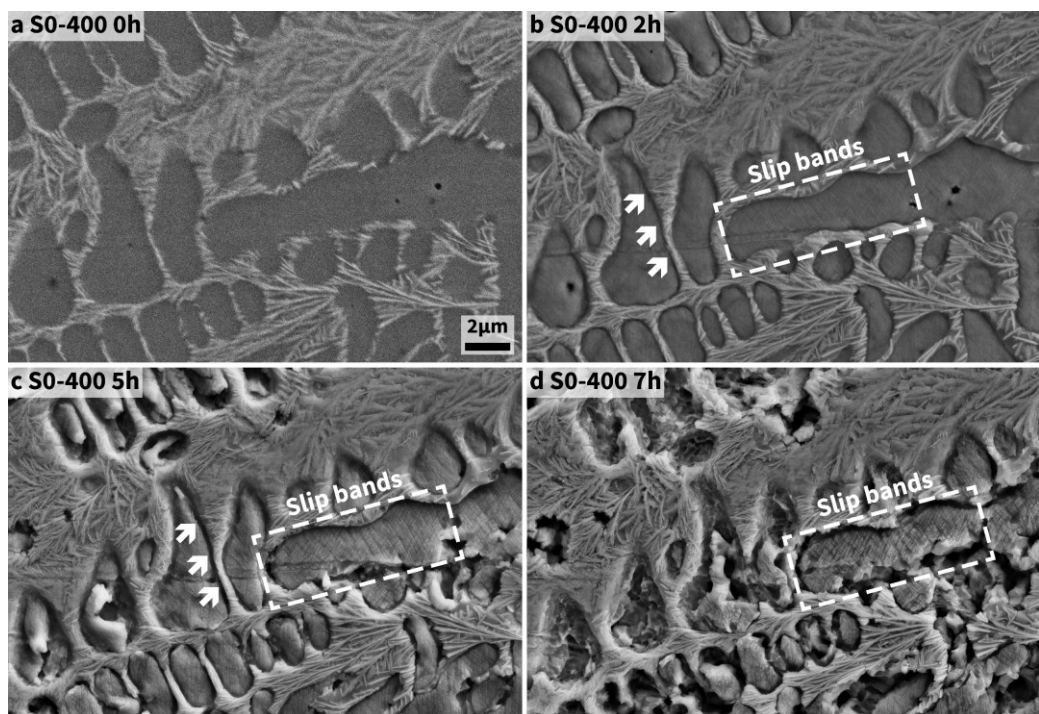


Fig. 5.11 – Microstructural evolution of hypoeutectic Ni-WC in S0-400 sample during cavitation erosion. White arrows: The erosion of the primary Ni at the interface of primary Ni and eutectic Ni-WC.

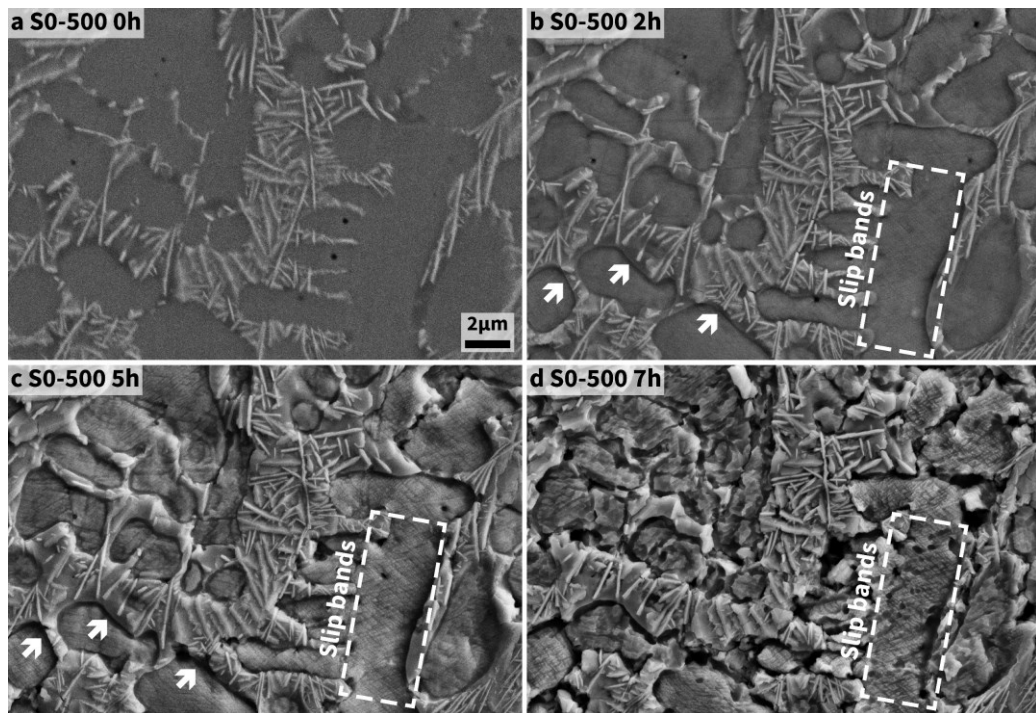


Fig. 5.12 – Microstructural evolution of hypoeutectic Ni-WC in S0-500 sample during cavitation erosion. White arrows: The erosion of the primary Ni at the interface of primary Ni and eutectic Ni-WC.

5.5.2 Other microstructural features

Despite exhibiting a eutectic Ni-WC network with hierarchically layered WC lamellae, these LSM Ni-WC MMCs showed different CER, which could be attributed to the minor differences in the microstructure. Specifically, more pores were found in the S0-300 and the S0-500 samples compared to the S0-400 sample, and the S0-300 sample had large granular WC grains and WC-free regions (**Fig. 5.4**).

Ni without WC lamellae

The microstructural evolution of a WC-free region in response to cavitation

is presented in **Fig. 5.13**. At the early stage of CE, erosion was barely observed, but the repetitive cavitation impacts resulted in the movement and deformation of Ni grains (**Fig. 5.13a-b**). As the planar movement and deformation were blocked by the grain boundaries, the Ni grains tended to be sheared at the grain boundaries, and some of them were extruded (**Fig. 5.13b**). Then, the deformed Ni grains would ultimately reach the plastic limit after further exposure to cavitation, causing sudden failure and significant erosion (**Fig. 5.13c-d**). The CE behaviour of the WC-free region also indicated the effectiveness of the hierarchically layered WC grains in resisting CE.

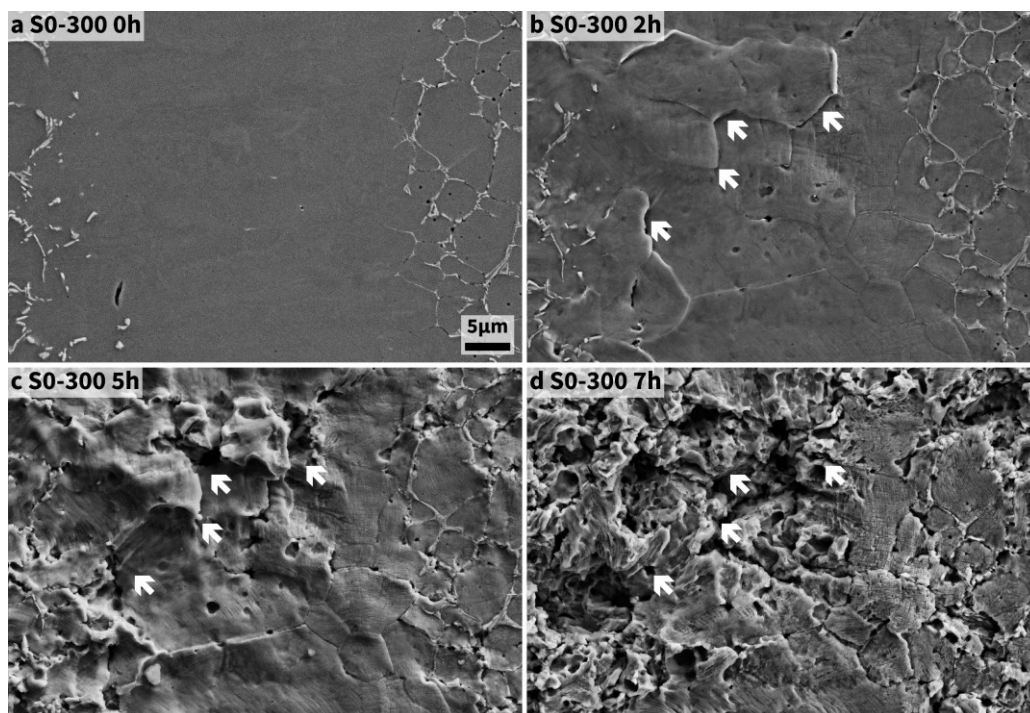


Fig. 5.13 – Microstructural evolution of a WC-free region in S0-300 sample during cavitation erosion. White arrows: Shearing (b-c) and erosion (d) at Ni grain boundaries.

Pre-existing pores

Most of the pre-existing pores got expanded when exposed to cavitation, while some pores could get shrunk at the early stage of CE (**Fig. 5.14a-b**). The shrinkage of pores on the material surface exposed to cavitation impacts was also reported in other literature [80]. Regardless of the extension or the shrinkage of pre-existing pores, the local material was severely eroded after further exposure to cavitation (**Fig. 5.14b-d**), suggesting that pre-existing pores were susceptible to CE.

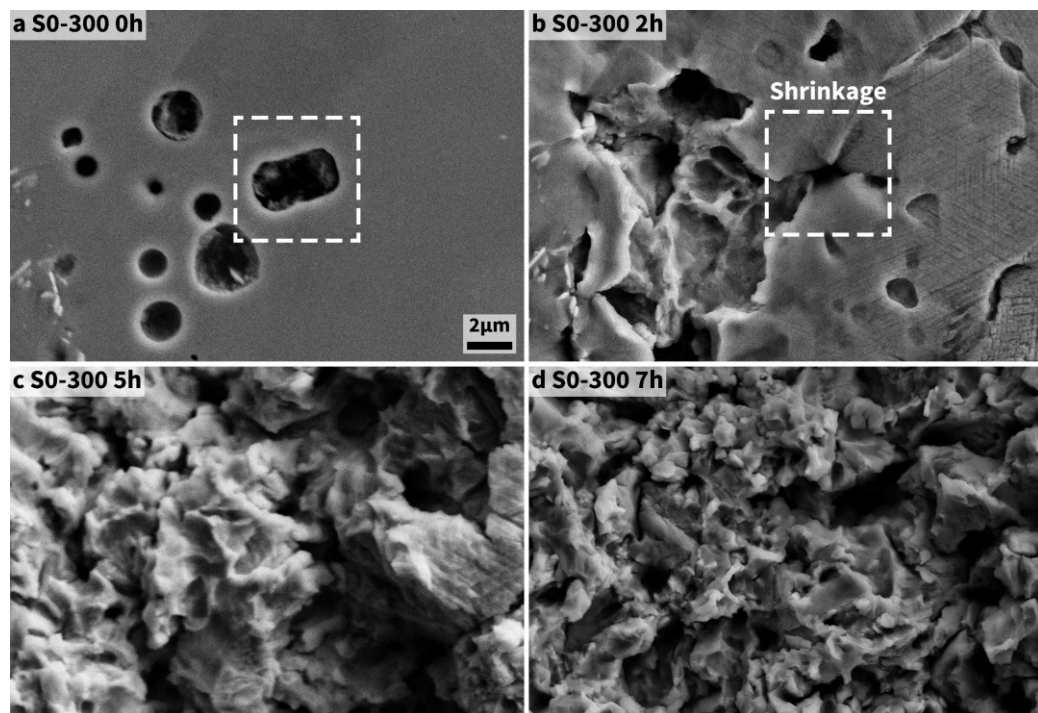


Fig. 5.14 – Microstructural evolution of pre-existing pores in S0-300 sample during cavitation erosion. White dotted square: The shrinkage of a pore.

Granular WC grains

Although the granular WC grains in the S0-300 sample were precipitated

during the solidification process, the failure mechanism of these granular WC grains in response to cavitation impacts was similar to that of the HVOF-sprayed cermet coatings [193, 194, 202]. The granular WC grains were easily detached during CE, leaving the Ni matrix unprotected (**Fig. 5.15a-c**). As a result, the Ni matrix eroded severely after further exposure to cavitation impacts (**Fig. 5.15c-d**).

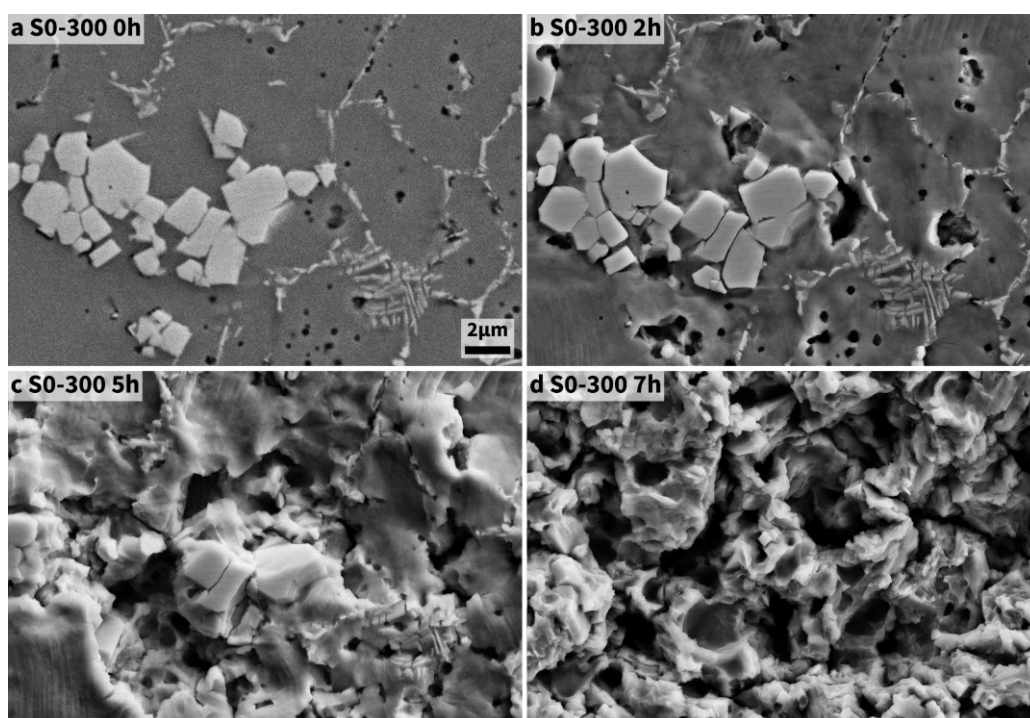


Fig. 5.15 – Microstructural evolution of granular WC grains in S0-300 sample during cavitation erosion.

5.6 Numerical simulation

5.6.1 Model establishment

Numerical simulation was conducted by Ansys LS-DYNA Multiphysics Solver to analyse the dynamic compressive mechanical behaviours of the LSM Ni-WC MMCs. There were two models constructed: one was a pure

Ni structure, and the other was a Ni-WC structure (**Fig. 5.16a-b**). For the Ni-WC model, only two parallel WC lamellae with a width of 200 nm were placed to save computational costs (**Fig. 5.16b**). The thickness of and the distance between WC lamellae were set to be 50 and 100 nm, according to the STEM image (**Fig. 5.16c**). The Ni below the bottommost WC lamella had a large thickness (450 nm) to simulate the large Ni matrix enveloped by the Ni-WC network.

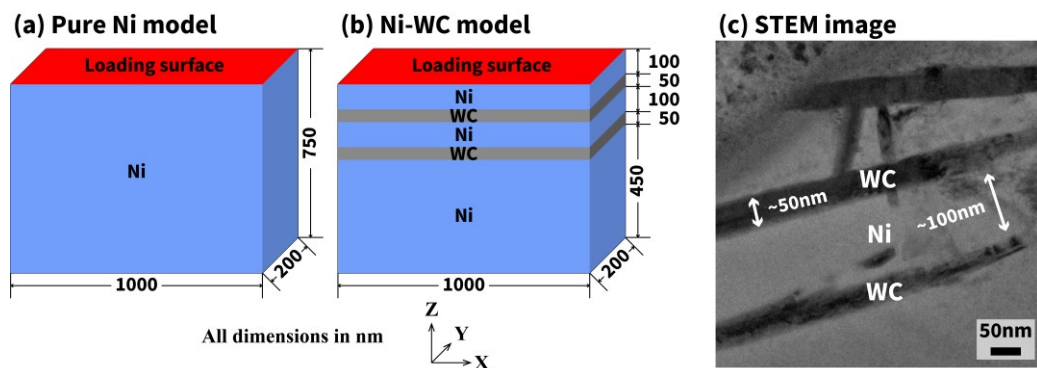


Fig. 5.16 – Numerical models of pure Ni and Ni-WC structures and STEM image of Ni-WC structure.

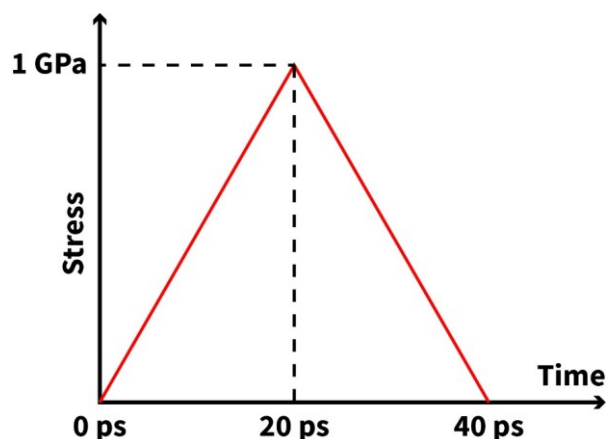


Fig. 5.17 – Impact applied during numerical simulation.

The models were meshed with 960, 000 elements. The elements at 0-400 nm below the loading surface had a size of 5×5×5 nm, and the rest of the elements were in 5×5×10 nm. The top surface of the model was subjected

to a perpendicular impact. According to the reviewed literature [41, 47, 48, 290], the impact was set to have a peak value of 1 GPa and last 40 ps (**Fig. 5.17**). The physical parameters of Ni and WC for modelling were tabulated in **Table 5.1**.

Table 5.1 – Physical parameters of Ni and WC for numerical simulation. The parameters are based on the literature [308, 309], where ρ is density, μ is Poisson's ratio, E_{elastic} is elastic modulus, σ_y is yield stress, E_{plastic} is plastic modulus, σ_f is ultimate stress, and ϵ_f is ultimate strain.

Material	ρ [g/cm³]	μ	E_{elastic} [GPa]	σ_y [MPa]	E_{plastic} [GPa]	σ_f [MPa]	ϵ_f
Ni	8.88	0.31	207	59	0.86	N/A	0.3
WC	15.72	0.24	720	N/A	N/A	2680	N/A

5.6.2 Simulation results

The stress evolution of the pure Ni and the Ni-WC structures are demonstrated in **Fig. 5.18**, where only a quarter of the structures are shown as the models are symmetrical. Meanwhile, the stress above, in between, and beneath the WC lamellae is monitored (**Fig. 5.19a-c**), and the total kinetic energy of the models is recorded (**Fig. 5.19d**).

According to the results (**Fig. 5.18** and **Fig. 5.19a**), great compressive stress initiates at the top of the two structures at about 0-40 ps due to the impulse, and tensile stress brought by the transverse inertia effect appears at about 40-50 ps. The maximum tensile stress at 50 nm beneath the loading surface comes later and is lower in the Ni-WC structure than in the pure Ni structure, which can be attributed to the high density and

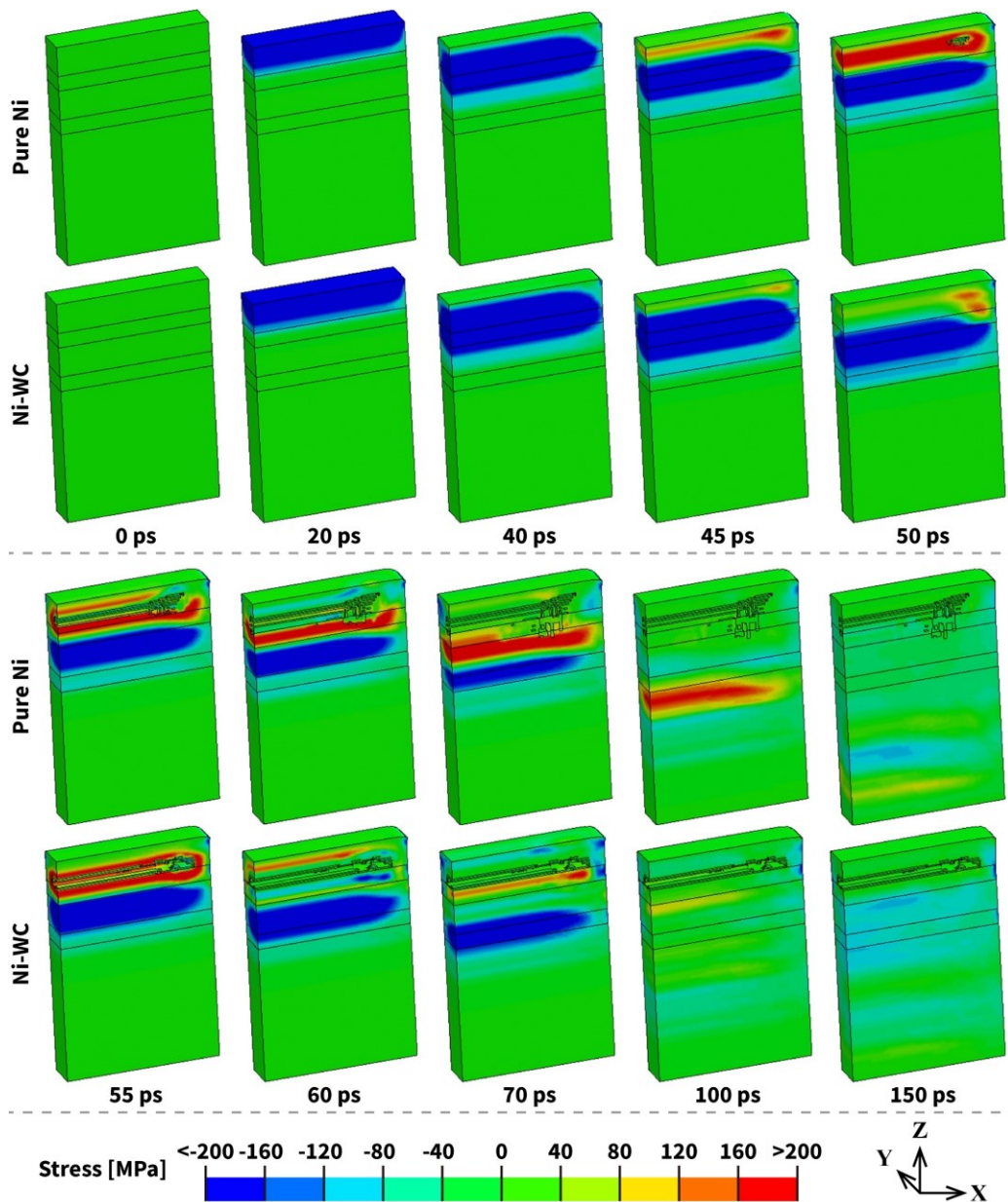


Fig. 5.18 – Stress evolution of the pure Ni and the Ni-WC structures elastic modulus of WC and the transverse inertia effect [310]. The stress at 50 nm beneath the loading surface in the Ni structure is almost in equilibrium after 60 ps, while that in the Ni-WC structure still fluctuates with a small amplitude, indicating that stress waves rebound from the WC lamella.

The rebound of stress by WC lamellae is evidenced by the monitored

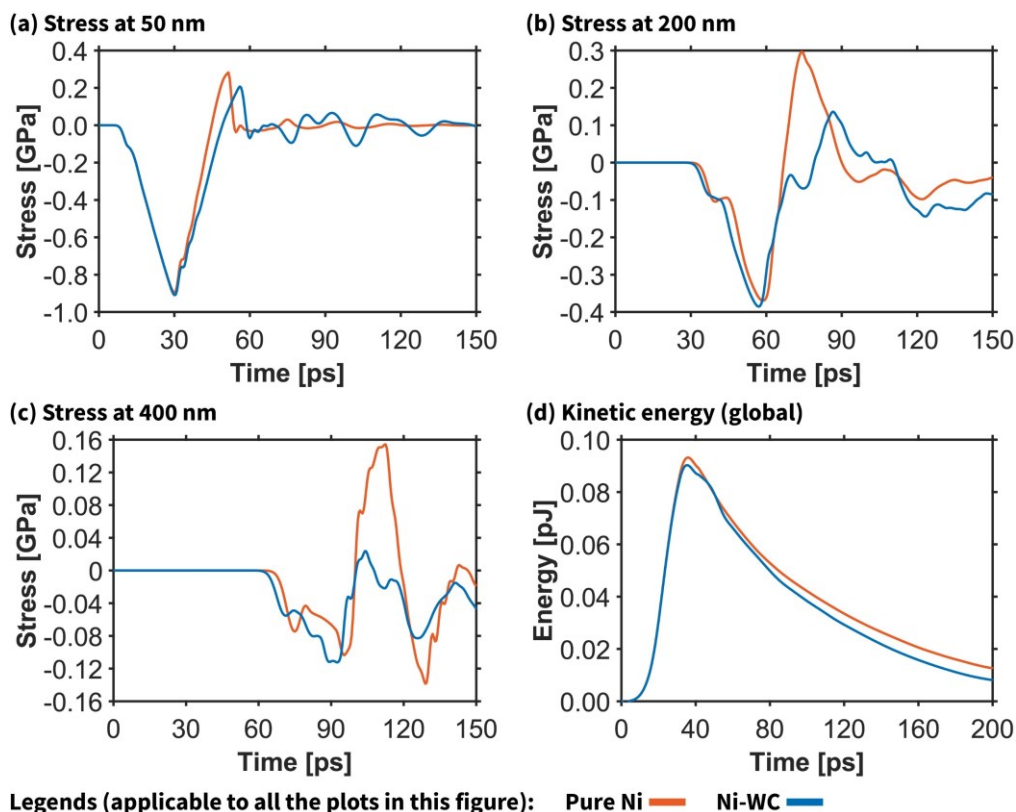


Fig. 5.19 – Stress and kinetic energy of the pure Ni structure and the Ni-WC structure. a-c, Stress (Z-axis) at 50, 200, and 400 nm beneath the loading surface, respectively; d, Kinetic energy in the whole model.

stress at 200 nm beneath the loading surface (in between the two WC lamellae) presented in **Fig. 5.19b**. The maximum tensile stress in the Ni-WC structure is much lower than that in the pure Ni structure, as the first WC lamella reflects a portion of the stress waves. Meanwhile, the fluctuation of the stress in the Ni-WC structure also indicates the rebound of stress waves by the second WC lamella. Hence, the transmitted stress in the Ni-WC structure is very low, and the maximum tensile stress at 400 nm in the Ni-WC structure is 15.3% of the pure Ni structure (**Fig. 5.18** and **Fig. 5.19c**), because most of the stress waves are trapped and re-echo in between the two WC lamellae.

In addition, the WC lamellae can also dissipate the impact energy via the

re-echo of the stress waves. As shown in **Fig. 5.19d**, the kinetic energy of the two structures is almost the same at the beginning. When the first compressive stress peak transmitted through 50 nm (the top surface of the first WC lamella) at about 50-55 ps (**Fig. 5.18**), the difference in the kinetic energy starts to become distinct (**Fig. 5.19d**). At 200 ps, the kinetic energy in the Ni-WC structure is about 36.5% lower than the pure Ni structure, suggesting that the two WC lamellae facilitate energy dissipation.

Apart from stress and energy, the failure of elements in the models are also investigated, and the results are given in **Fig. 5.20**. The element failure penetrates at a depth of 160 nm in the pure Ni structure, while it is not found below the first WC lamella in the Ni-WC structure. Meanwhile,

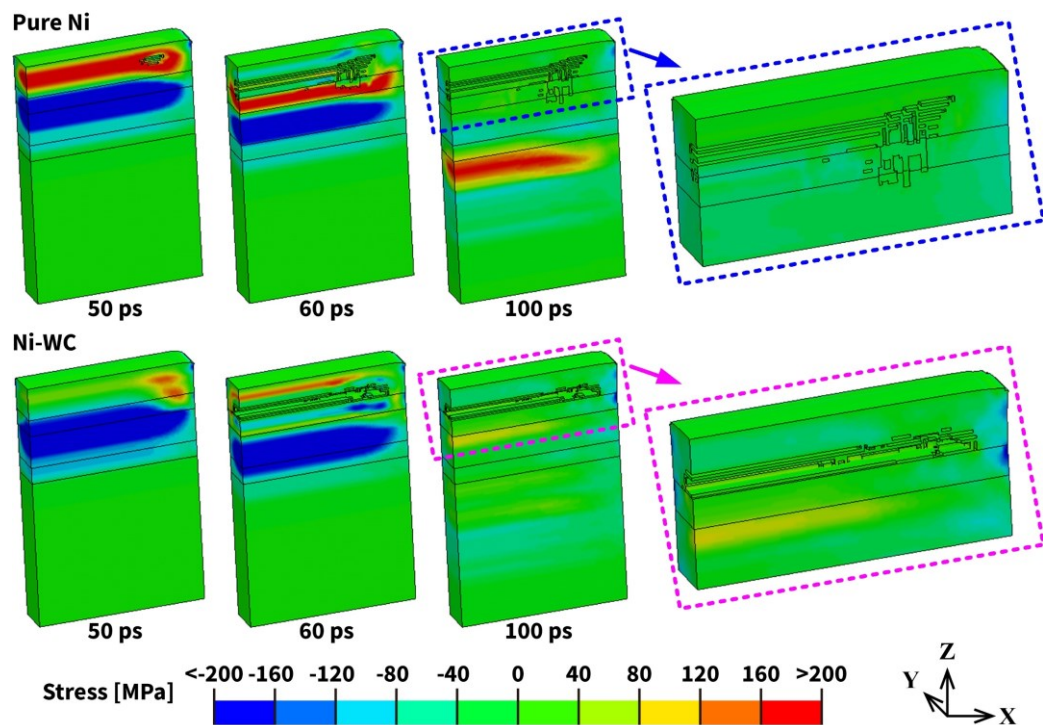


Fig. 5.20 – Element failure of the pure Ni and the Ni-WC structures.

the number of the failed elements in the pure Ni structure is more than that in the Ni-WC structure. In addition, it is worth mentioning that most of the failed elements are located near the top surface of the first WC lamella in the Ni-WC structure, which is in consistency with the SEM observation (**Fig. 5.11** and **Fig. 5.12**).

5.7 Discussion

5.7.1 Sintering as an alternative to spraying for pre-deposition

The work in this chapter attempted to use sintering as an alternative to spraying for the pre-deposition of Ni-WC composite before LSM. The SEM images of the cross-section (**Fig. 4.5** and **Fig. 5.4**) showed that the LSM layers in the sprayed and the sintered Ni-WC MMCs exhibited almost identical eutectic Ni-WC structure regardless of the pre-deposition techniques. Furthermore, the CE performance of the LSM cold-sprayed and the LSM sintered Ni-WC MMCs was also similar (**Fig. 4.16** and **Fig. 5.8**): the samples treated by the 400-W and the 300-W lasers exhibited the best and the worst CER, respectively. The above results suggested that sintering can be a feasible alternative to spraying for the pre-deposition of Ni-WC before LSM when preparing CE-resistant LSM MMCs.

In addition, it is worth noting that the Ni grain size of the LSM cold-sprayed

sample was a bit smaller than that of the LSM sintered sample (**Fig. 4.8** and **Fig. 5.6**). During the spraying process, the inflight particles with a high velocity eventually hit and adhered to the substrate. Thus, the splats in the sprayed coating exhibited a high plastic strain. The highly deformed splats exhibited many dislocations which act as high energy sites. During recrystallisation, new grain boundaries preferentially formed at these high energy sites, resulting in refined Ni grains.

5.7.2 Effect of eutectic Ni-WC on cavitation erosion resistance

In **Chapter 4**, it was suggested that the eutectic Ni-WC network with the hierarchically layered WC lamellae mainly contributed to the excellent CER of the LSM Ni-WC coatings because the eutectic Ni-WC network could inhibit the growth of microcracks (**Fig. 4.19**). In this chapter, solid evidence was provided by the SEM observation, showing that the erosion of the Ni could be confined within each cell divided by the Ni-WC network with the WC lamellae (**Fig. 5.11** and **Fig. 5.12**). Different from the Stellite 6 weld overlay with a similar microstructure (**Fig. 2.25d-e**) [165], only if the Ni in the cell was almost eroded, the eutectic Ni-WC network started to fall off, resulting in subsequent erosion. The severe erosion in the region which were not protected by the eutectic Ni-WC network with the WC lamellae (**Fig. 5.13**) also indicated the effectiveness of the eutectic Ni-WC

network in resisting CE. In microscale, the microstructure of this hypoeutectic Ni-WC could be considered as an imitation of cuttlebone, which exhibits a network structure and fails in a layer-by-layer behaviour when subjected to repeated impacts [311-313].

Numerical modelling also found that the presence of the WC lamellae could stop the failure of the elements penetrating (**Fig. 5.20**), which was consistent with the SEM observation (**Fig. 5.11** and **Fig. 5.12**) as mentioned previously. Furthermore, the numerical modelling showed that the eutectic Ni-WC network with the hierarchically layered WC lamellae could effectively reduce the tensile stress amplitude when the model was subjected to an impact (**Fig. 5.18** and **Fig. 5.19**). This impact-resistant effect could be attributed to the reflection and overlapping of the stress waves by the hierarchically layered WC lamellae. The re-echo of the stress waves also resulted in the effective dissipation of the impact energy (**Fig. 5.19d**), which could be considered as an imitation of nacre (**Appendix D** presented the results of the CE tests on abalone shells) [314-316].

As a result, the excellent CER of the LSM Ni-WC MMCs was facilitated by the imitation of cuttlebone providing the damage-controlling effect and the imitation of nacre providing effective dissipation of stress and energy.

5.7.3 Behaviour of primary Ni phase in response to cavitation

The Ni phase in the LSM Ni-WC layer had an FCC structure (**Fig. 5.3**) that was expected to have low stacking fault energy (SFE). As mentioned in the literature review, the materials with low SFE tend to exhibit good CER. This is because the materials with low SEF have low strain rate sensitivity that provides good ductility, and dislocation and slip can easily form when the materials took the impacts from cavitation, which is beneficial to resisting CE [103, 269]. In addition, the recombination of partial dislocations is less likely to occur in the materials with low SFE, and thus the cross-slipping of dislocations is inhibited, offering improved work hardening ability and good CER [137, 138]. As shown in **Fig. 5.10-Fig. 5.12**, most of the Ni grains were almost intact and exhibited slip bands after 7-h CE. However, it should be noted that pure Ni could not effectively resist CE without the support of the eutectic Ni-WC network (**Fig. 5.13**).

5.7.4 Defects and cavitation erosion resistance

Pre-existing pores and granular WC grains were found in the LSM Ni-WC layer (**Fig. 5.4**), and they were not resistant to CE according to the SEM observation (**Fig. 5.14** and **Fig. 5.15**). Therefore, the pre-existing pores and the granular WC grains were considered as defects in the LSM Ni-WC MMCs.

Some studies attributed the severe erosion at pre-existing pores during CE to the sudden change of local geometry that affected the flow. As a result, the formation of cavitation bubbles near the pre-existing pores was enhanced, and thus these pores were preferentially eroded [234, 317]. Other studies suggest that pores could alter the stress flow and cause stress concentration nearby, resulting in severe erosion at the pores [318, 319]. In this present study, the extrusion of the Ni matrix and the shrinkage of the pre-existing pore (**Fig. 5.13a-b** and **Fig. 5.14a-b**) indicated that the planar deformation and movement of the Ni matrix occurred more easily at the pores than at the defect-free zone, possibly attributed to less obstruction at pores than at grain boundaries. Therefore, the preferential erosion at the pre-existing pores is more likely attributed to the stress concentration.

As for the cluster of granular WC grains (**Fig. 5.15**), the CE failure mechanism was very similar to the HVOF-sprayed WC-based cermet coatings (**Fig. 2.26c**): the sudden detachment of the WC grains leaving the metallic binder phases beneath unprotected, which causes the accelerated erosion due to the unprotected metallic binder phases being severely eroded [193, 197, 198]. As mentioned before, the sudden detachment of the hard phase in the sprayed coatings during CE was mainly attributed to the poor adhesion at the phase boundaries.

Nevertheless, these granular WC grains were precipitated during the solidification process and firmly bonded to the surrounding Ni matrix. However, the granular WC grains were easily removed during CE. This suggests that improving the adhesion at the phase boundaries could provide limited effect on improving the CER for the cermet coatings.

5.8 Summary

- 1) The sintered Ni-WC MMCs were post-treated by LSM using the lasers with 300, 400, and 500 W power, respectively. The LSM sintered Ni-WC MMCs exhibited an almost identical microstructure and very similar CER compared to the LSM cold-sprayed Ni-WC coatings, suggesting that sintering could be a feasible alternative to spraying for the pre-deposition of Ni-WC composites to be treated by LSM.
- 2) The microstructure evolution of the LSM sintered MMCs in response to cavitation impacts was recorded by taking SEM images at the same damaged site in different test intervals. The SEM observation evidenced that the eutectic Ni-WC network could effectively confine the erosion and provide a damage-controlling effect.
- 3) Numerical simulation results suggested that the eutectic Ni-WC with hierarchically layered WC lamellae could effectively reduce the stress and dissipate kinetic energy when subjected to a cavitation impact.

Chapter 6

Effects of CeO₂ addition on cavitation erosion of LSM Ni-WC-CeO₂ MMCs

6.1 Introduction

In the previous two chapters, LSM process introduced the hypoeutectic structure with hierarchically interlocked WC lamellae in the eutectic Ni-WC to the cold-sprayed and the sintered Ni-WC MMCs. Although the hypoeutectic structure provided these LSM Ni-WC with excellent CER, a further enhancement of the CER is worth investigating. As reviewed, a feasible enhancing approach is adding other alloying elements to the material system.

This chapter investigates the effect of rare earth element addition on the microstructure and CER of the LSM sintered Ni-WC MMC. According to the literature, the addition of CeO₂ could refine the microstructure and improve the wear resistance of laser-cladded Ni-based coating and arc-cladded Ni-based WC layer [275-277, 320]. Therefore, CeO₂ was selected to be the additive in this chapter.

The sintered Ni-WC-CeO₂ MMCs with 3 different CeO₂ contents were prepared and processed by LSM. Material characterisations showed that

the addition of CeO₂ altered the microstructure of the LSM Ni-WC-CeO₂ MMCs. The microstructural evolution of these LSM Ni-WC-CeO₂ MMCs in response to cavitation impacts was investigated by SEM. Besides, numerical simulations demonstrated the effect of the differences in microstructure on the CE behaviour of the LSM MMCs.

6.2 Sample information

The sintered Ni-WC-CeO₂ MMCs have the ascending contents of CeO₂, which are 0.9, 1.8, and 2.7 wt.%. A constant volumetric ratio of Ni and WC is held, which is 3:1. The sintered Ni-WC-CeO₂ MMCs were post-treated by LSM with different laser powers of 300, 400, and 500 W, respectively.

Table 6.1 below summarises the information of these samples, and the samples are quoted as the index provided in the table.

Table 6.1 – Chemical composition and process parameters of Ni-WC-CeO₂ MMCs.

Index	Composition (vol.%)			Composition (wt.%)			Process
	Ni	WC	CeO ₂	Ni	WC	CeO ₂	
SA1	74.0	24.7	1.3	62.6	36.5	0.9	Sintered
SA2	73.0	24.4	2.6	62.0	36.2	1.8	
SA3	72.1	24.0	3.9	61.4	35.9	2.7	
SA1-300	74.0	24.7	1.3	62.6	36.5	0.9	Sintered and remelted by 300W laser
SA2-300	73.0	24.4	2.6	62.0	36.2	1.8	
SA3-300	72.1	24.0	3.9	61.4	35.9	2.7	
SA1-400	74.0	24.7	1.3	62.6	36.5	0.9	Sintered and remelted by 400W laser
SA2-400	73.0	24.4	2.6	62.0	36.2	1.8	
SA3-400	72.1	24.0	3.9	61.4	35.9	2.7	
SA1-500	74.0	24.7	1.3	62.6	36.5	0.9	Sintered and remelted by 500W laser
SA2-500	73.0	24.4	2.6	62.0	36.2	1.8	
SA3-500	72.1	24.0	3.9	61.4	35.9	2.7	

6.3 Characterisation of the sintered Ni-WC-CeO₂

The polished cross-sections of the sintered Ni-WC-CeO₂ MMCs are shown in **Fig. 6.1b-d**. Except for the CeO₂ particles in light grey, the cross-sections of the sintered Ni-WC-CeO₂ MMCs are similar to the CeO₂-free sintered MMC (**Fig. 6.1a**), showing bright WC particles and dark Ni matrix. The XRD spectrum of the sintered Ni-WC MMC is presented in **Fig. 6.2**, which shows the peaks of FCC Ni and HCP WC. The peaks corresponding to oxides or Ce-based chemicals were not found, possibly attributed to the low concentration.

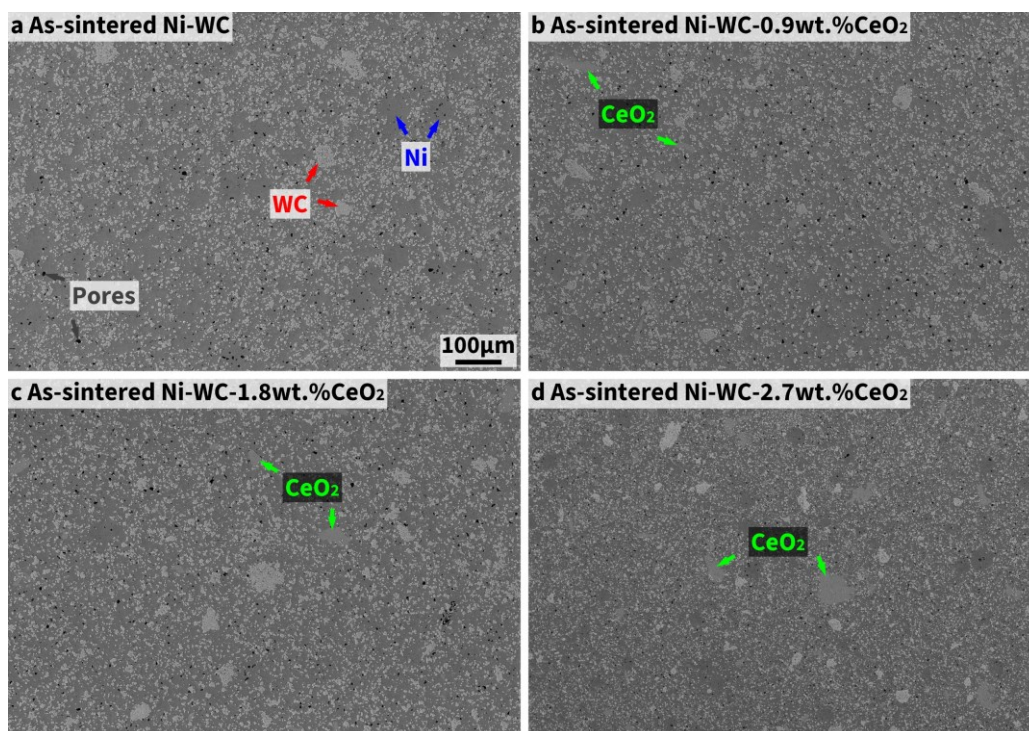


Fig. 6.1 – SEM images of the cross-section of the sintered Ni-WC-(CeO₂) MMCs. a, As-sintered Ni-WC for comparison; **b-d**, As-sintered Ni-WC-CeO₂ with 0.9, 1.8, and 2.7 wt.% CeO₂, respectively.

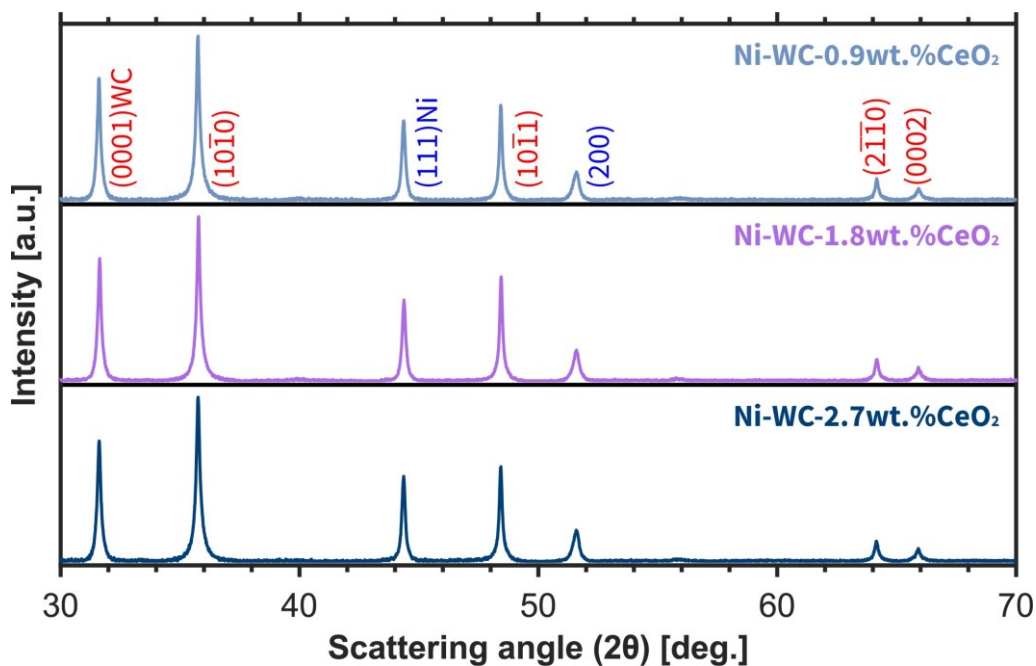


Fig. 6.2 – XRD spectra of the sintered Ni-WC-CeO₂ MMCs.

6.4 Characterisation of LSM sintered Ni-WC-CeO₂

6.4.1 XRD results

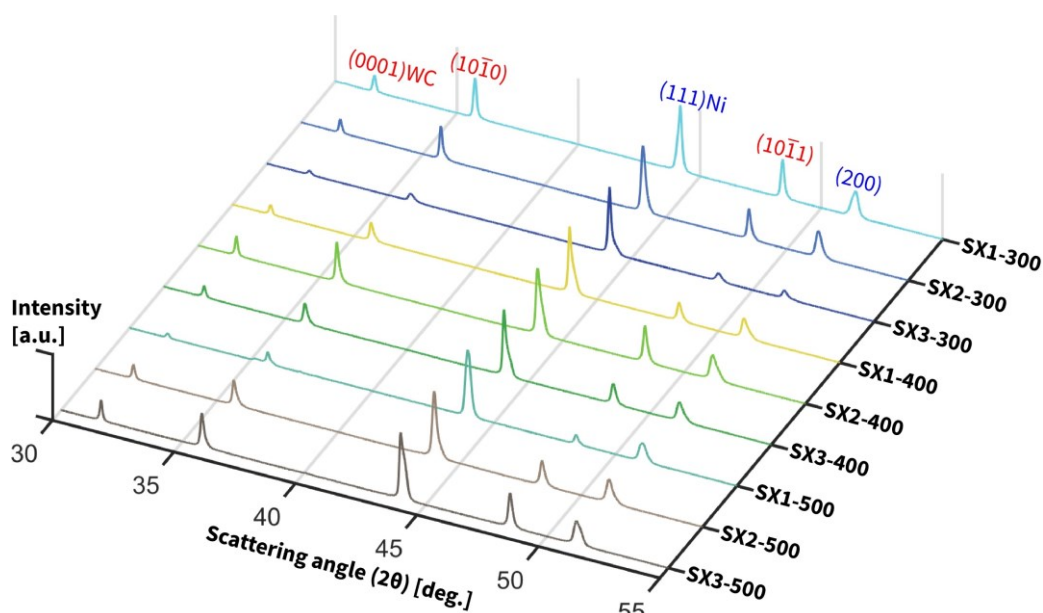


Fig. 6.3 – XRD spectra of the LSM sintered Ni-WC MMC.

After LSM, the phases in the LSM sintered Ni-WC-CeO₂ MMCs were still the same according to the XRD spectra (Fig. 6.3), showing the peaks of

FCC Ni and HCP WC only. The absence of other phases could be attributed to their low concentration.

6.4.2 SEM results

The cross-sections of these LSM sintered Ni-WC-CeO₂ MMCs are characterised by SEM, and the results are shown in **Fig. 6.4**, **Fig. 6.5**, and **Fig. 6.6** for the MMCs with 0.9, 1.8, and 2.7 wt.% CeO₂, respectively.

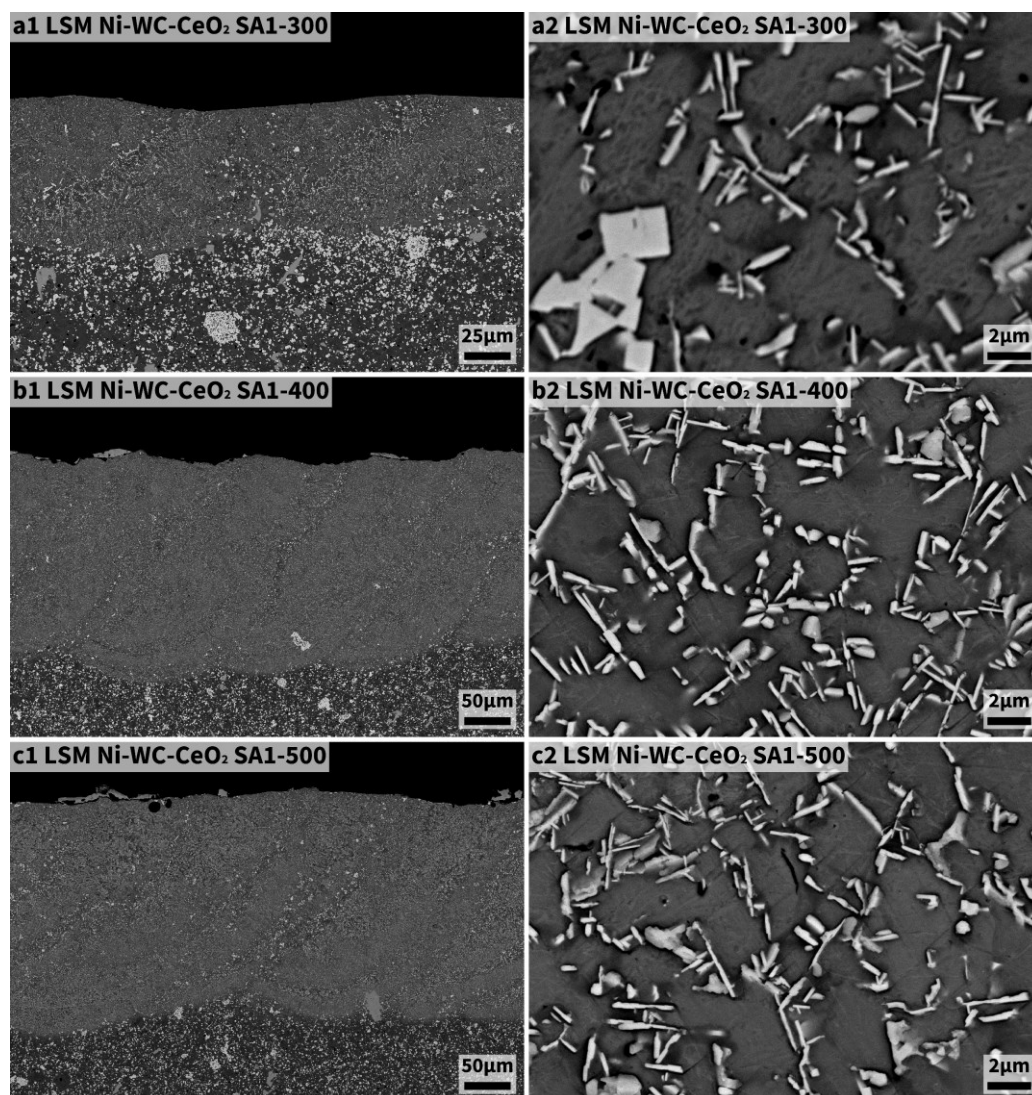


Fig. 6.4 – Cross-sections of the LSM Ni-WC-1.8wt.%CeO₂ MMCs treated by different laser powers. a-c, Specimens treated by 300-, 400-, and 500-W lasers, respectively; 1, Low magnification; 2, High magnification.

Compared to the LSM sintered Ni- WC MMCs (Fig. 5.4), the WC phases in the LSM sintered Ni-WC-CeO₂ MMCs had different morphology and distribution. For the LSM MMCs with 0.9 wt.% CeO₂, eutectic Ni-WC network was found in the LSM layer (Fig. 6.4). However, the WC lamellae were fewer but thicker in the LSM Ni-WC-0.9CeO₂ MMCs than in the CeO₂-free LSM MMCs (Fig. 5.4). Meanwhile, some WC lamellae were no longer interlocked with each other, and other WC lamellae did not connect

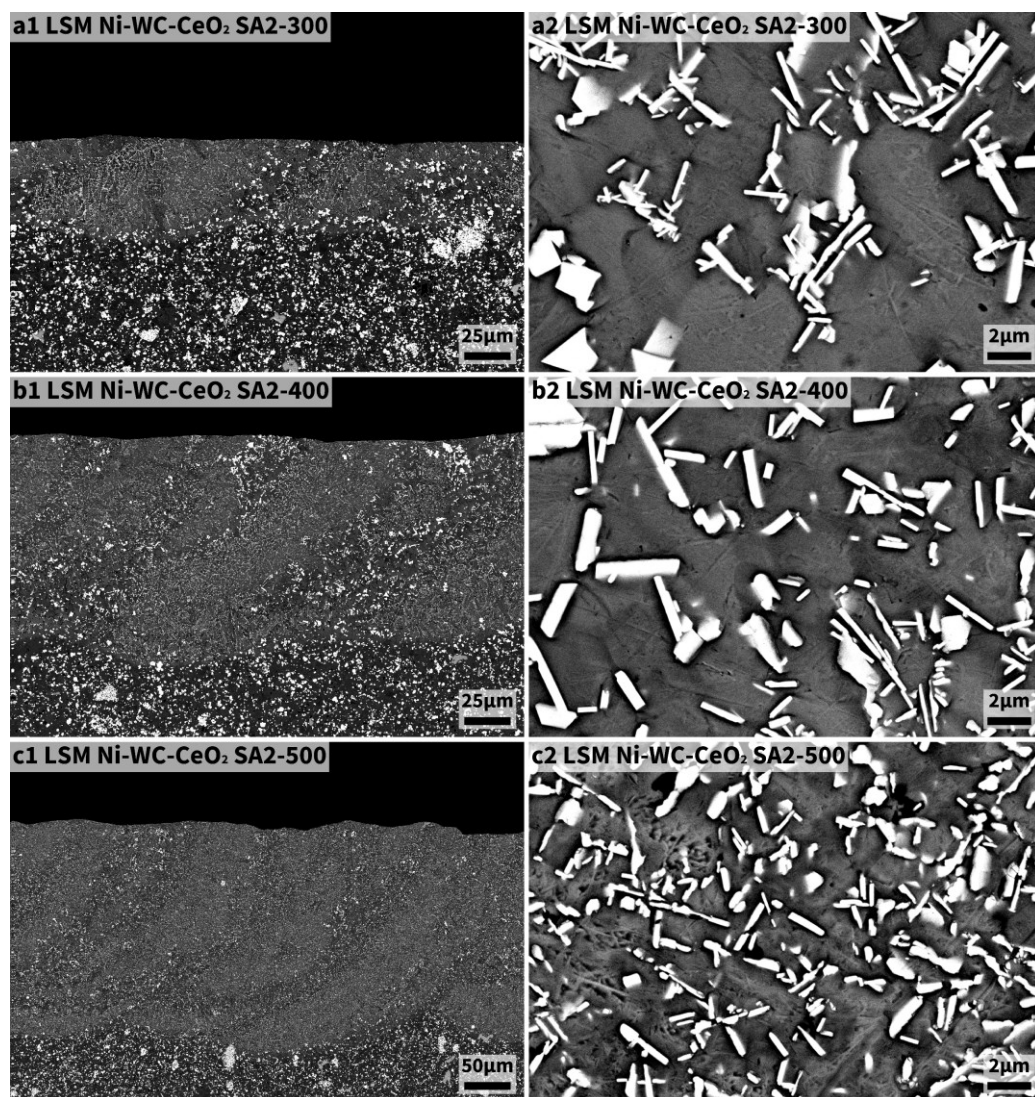


Fig. 6.5 – Cross-sections of the LSM Ni-WC-1.8wt.%CeO₂ MMCs treated by different laser powers. a-c, Specimens treated by 300-, 400-, and 500-W lasers, respectively; 1, Low magnification; 2, High magnification.

to the eutectic network but homogeneously distributed in the Ni matrix. The WC lamellae grew even thicker when the CeO₂ content increased to 1.8 wt.% (Fig. 6.5). Most of the WC lamellae did not hierarchically interlock with each other to form a network but were homogeneously distributed in the Ni matrix. In addition, the microstructure of the LSM sintered Ni-WC-CeO₂ MMCs with 0.9 and 1.8 wt.% CeO₂ seemed to be less dependent on the laser power (Fig. 6.4 and Fig. 6.5).

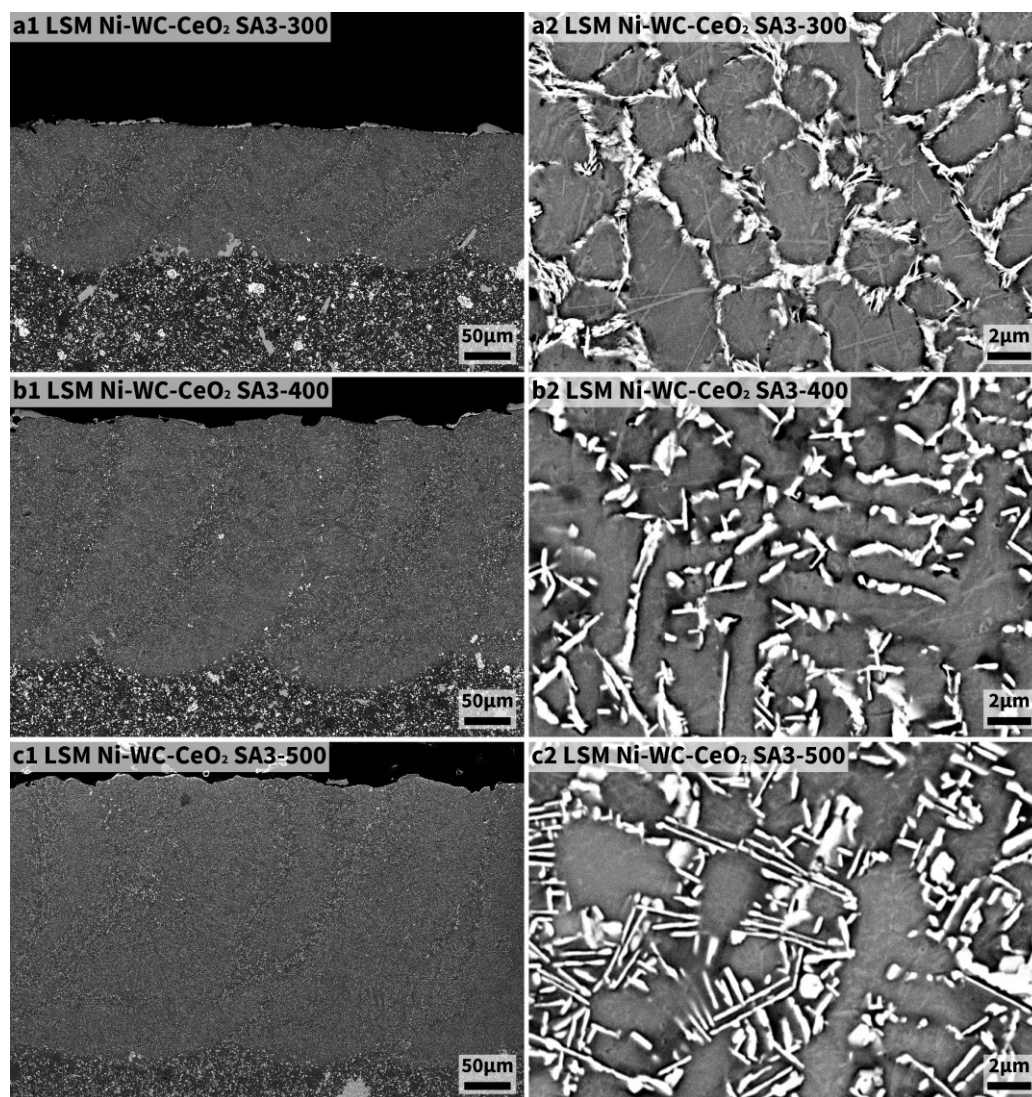
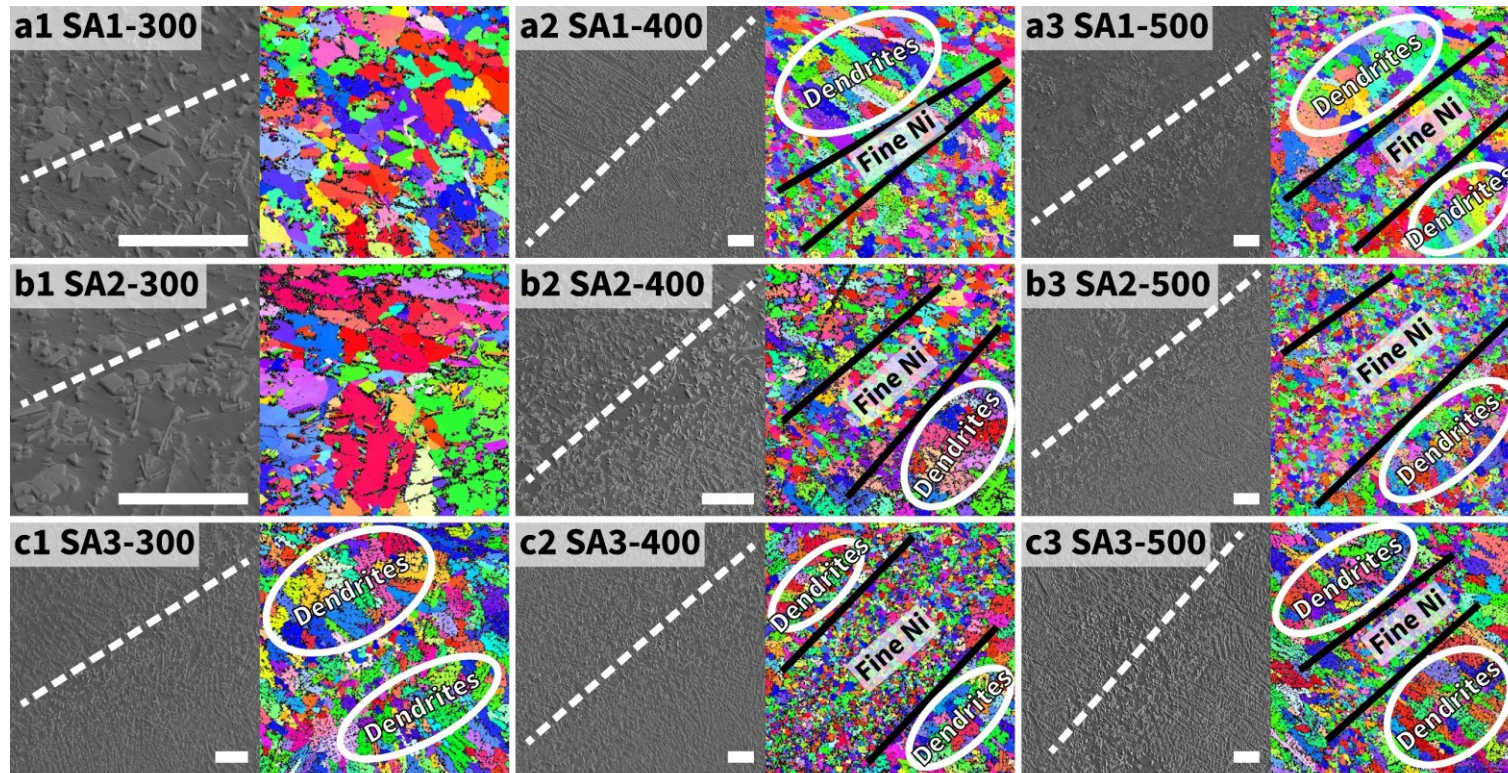


Fig. 6.6 – Cross-sections of the LSM Ni-WC-2.7wt.%CeO₂ MMCs treated by different laser powers. a-c, Specimens treated by 300-, 400-, and 500-W lasers, respectively; 1, Low magnification; 2, High magnification.

When the content of CeO₂ increased to 2.7 wt.%, the microstructure of the LSM Ni-WC-CeO₂ MMCs changed again and was affected by the laser power (**Fig. 6.6**). Generally, the networks of Ni-WC were found in the LSM layers in the MMCs with 2.7 wt.% CeO₂ again, but there were differences in the WC lamellae. Compared to the LSM sintered Ni-WC MMCs, the WC lamellae in the SA3-300 sample were much thinner, while those in the SA3-500 sample were thicker. On the other hand, the WC lamellae in the SA-400 sample had a similar distribution as the LSM MMCs with 1.8 wt.% CeO₂.

6.4.3 EBSD results

The LSM layers in the Ni-WC-CeO₂ MMCs were further characterised by EBSD (**Fig. 6.7**). Preferred orientation was not found from the mappings. For the MMCs treated by a 300-W laser (**Fig. 6.7a1-c1**), the addition of CeO₂ by 0.9 and 1.8 wt.% did not alter the morphology of the Ni grains (**Fig. 6.7a1-b1**). However, dendrites were found from the MMC with 2.7 wt.% CeO₂ treated by a 300-W laser, (**Fig. 6.7c1**). For the MMCs treated by 400- and 500-W lasers, a band of fine Ni grains was found near the molten pool edge, and dendrites were aside from the band (**Fig. 6.7a2-c3**).



All the scale bars = 20 μ m

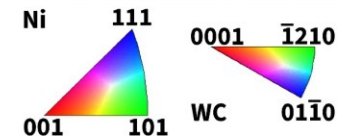


Fig. 6.7 – EBSD results of the cross-section of the LSM Ni-WC-CeO₂ MMCs. a-c, Specimens with 0.9, 1.8, and 2.7wt.% CeO₂, respectively; 1-3, Specimens treated by 300-, 400-, and 500-W lasers, respectively. White dotted lines: Edge of the molten pool.

6.4.4 Grain size and microhardness

According to the EBSD mappings (**Fig. 6.7**), the Ni grain size in the LSM sintered Ni-WC-CeO₂ MMCs was affected by the content of the CeO₂. The Ni grain size was measured to provide a quantitative comparison among these LSM MMCs with different CeO₂ content, and the result is given in **Fig. 6.8a**. Generally, the Ni grain size was positively correlated to the laser power for the LSM MMCs with the same CeO₂ content (**Fig. 6.8a1**). However, the exceptions were the LSM MMCs with 1.8 wt.% CeO₂, among which the MMC treated by a laser of 400 W exhibited the most refined Ni

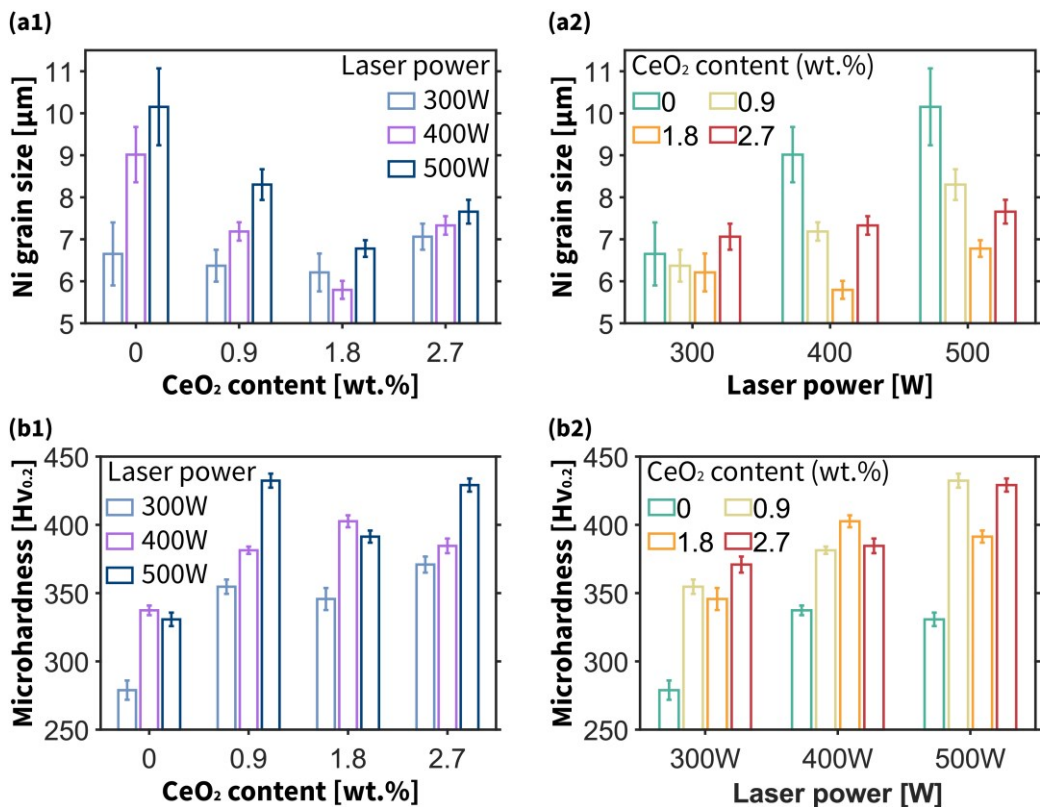


Fig. 6.8 – Ni grain size and microhardness of the LSM Ni-WC-CeO₂ MMCs. a, Ni grain size; b, Microhardness. The results are grouped according to CeO₂ contents (1) and laser powers (2), allowing the comparison based on different laser powers and CeO₂ contents, respectively. The results of the LSM sintered Ni-WC are also given as references.

grain. On the other hand, the Ni grain size could be effectively reduced by the increase of CeO₂ content until the CeO₂ content exceeded 1.8 wt.% (**Fig. 6.8a2**). Nevertheless, the Ni grains became coarser when the CeO₂ content increased to 2.7 wt.%. For the LSM MMCs treated by a laser of 300 W, the Ni grain size of the MMC with 2.7 wt.% CeO₂ was even greater than that of the CeO₂-free MMC. In addition, it is worth noticing that the deviation of the Ni grain size of the MMCs with CeO₂ was less than that of the CeO₂-free MMCs.

The microhardness of the LSM sintered Ni-WC-CeO₂ MMCs was summarised in (**Fig. 6.8b**). Compared to the CeO₂-free MMCs, the microhardness of the Ni-WC-CeO₂ MMCs was significantly increased, which may be attributed to the refined Ni grain size. However, a further decrease in the Ni grain size did not always result in the improved microhardness for the Ni-WC-CeO₂ MMCs. For example, the MMCs treated by 300- and 400-W lasers exhibited the lowest microhardness when the CeO₂ content was 1.8 wt.% but they had the smallest Ni grain size (**Fig. 6.8b2**). The results indicated that the microhardness of the MMCs may be predominated by the morphology of the WC lamellae, as the change in microhardness was not strongly correlated to the Ni grain size or the CeO₂ content.

6.5 Cavitation erosion and erosion rate

The erosion at the 10th h in terms of MDE is shown in **Fig. 6.9**, and the CE rate of the LSM sintered Ni-WC-CeO₂ MMCs in terms of MDER is presented in **Fig. 6.10**. The average CE rate from the 8th to the 10th h is considered as the steady-state CE rate, since all the samples entered the steady-state period after the 8th h (**Fig. 6.10**), and the results are given in (**Fig. 6.11**). According to **Fig. 6.10d**, all the LSM Ni-WC-CeO₂ MMCs exhibited the CE rate that was much lower compared to the 316L ASS. Surprisingly, most of the LSM MMCs with CeO₂ had lower resistance to CE than the LSM MMCs without CeO₂. The exception was the MMC with 2.7 wt.% CeO₂ treated by a laser of 300 W, which exhibited the lowest erosion rate among all the LSM MMCs with and without CeO₂ (**Fig. 6.10d** and **Fig. 6.11**).

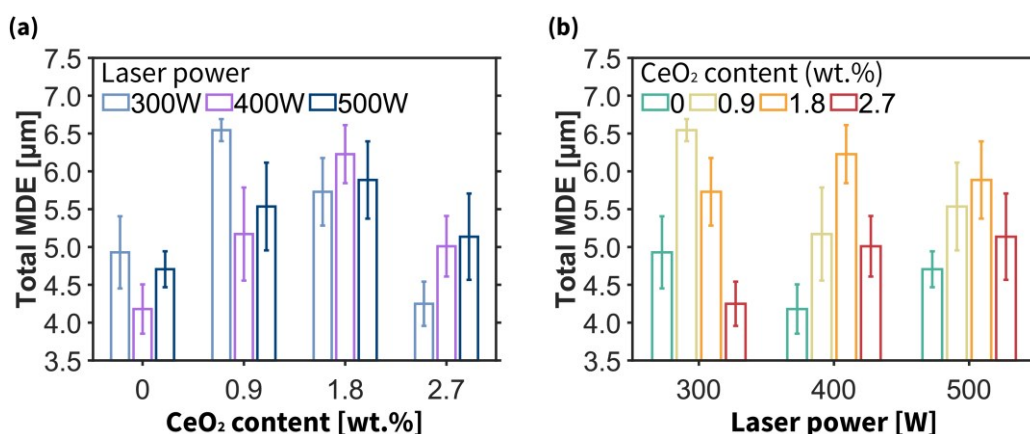


Fig. 6.9 – Erosion of the LSM Ni-WC-CeO₂ MMCs after 10-hour cavitation erosion test. The results are in terms of MDE and at the 10th h; The results are grouped according to CeO₂ contents (a) and laser powers (b), allowing the comparison based on different laser powers and CeO₂ contents, respectively. The results of the LSM sintered Ni-WC are also given as references.

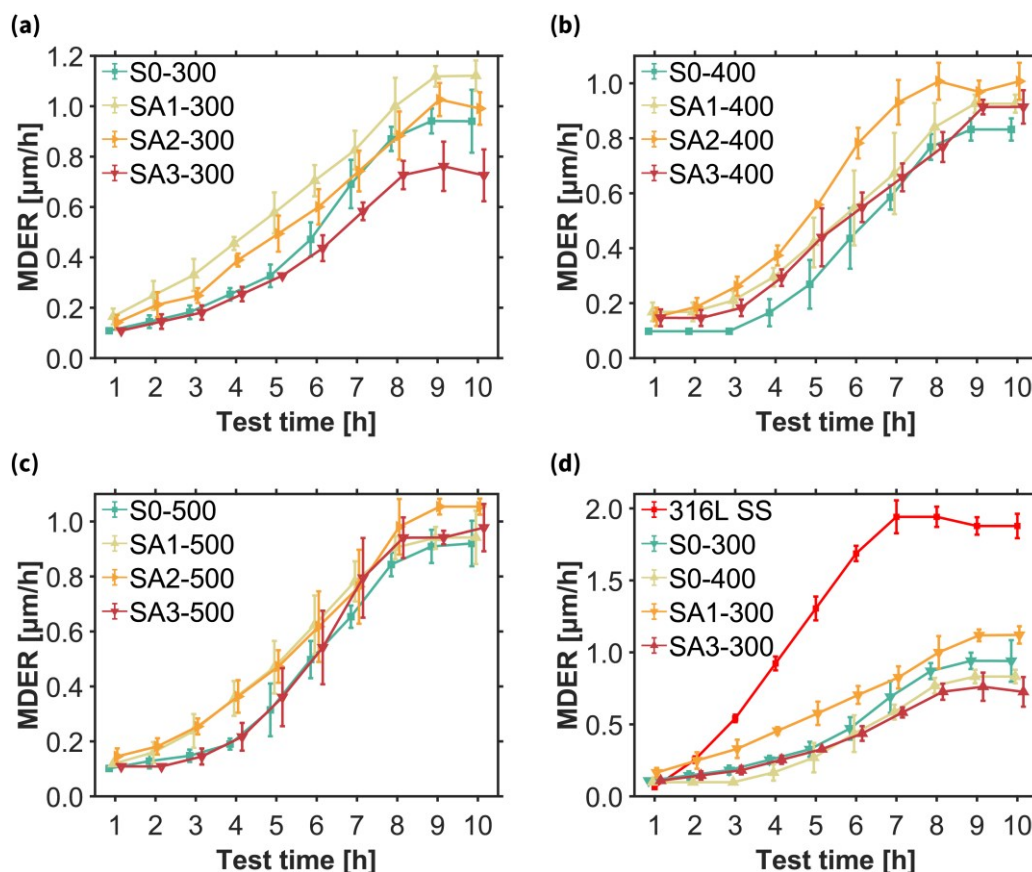


Fig. 6.10 – Erosion rate of the LSM Ni-WC-CeO₂ MMCs in terms of MDER. a-c, The results are grouped according to laser powers (300, 400, and 500 W, respectively) allowing the comparison based on different CeO₂ contents, and the results of the LSM sintered Ni-WC are also given as references; d, The highest and lowest erosion rates of the LSM MMCs with and without CeO₂ compared to 316L ASS.

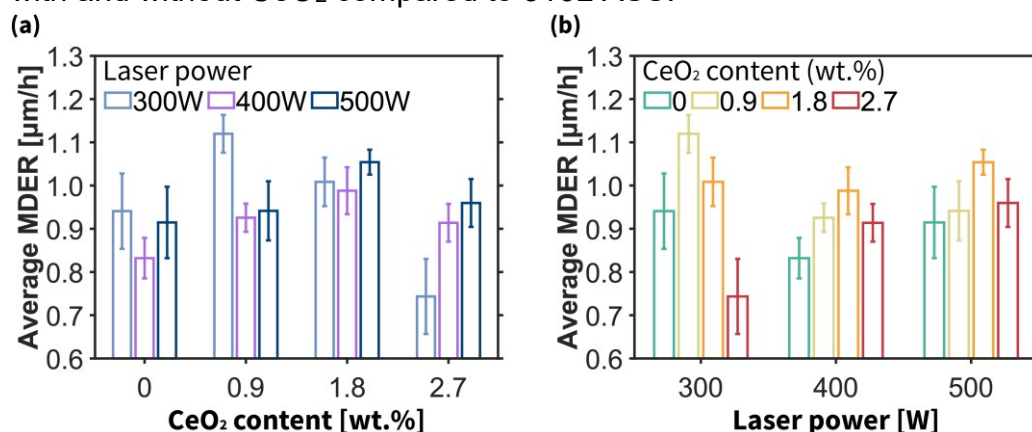


Fig. 6.11 – Cavitation erosion rate of the LSM Ni-WC-CeO₂ MMCs. The results are the average erosion rates during the steady state period (from the 8th to the 10th h) in terms of MDER; The results are grouped according to CeO₂ contents (a) and laser powers (b), allowing the comparison based on different laser powers and CeO₂ contents, respectively. The results of the LSM sintered Ni-WC are also given as references.

6.6 SEM observation of the samples exposed to cavitation erosion at different test intervals

6.6.1 Specimens with 0.9wt.% CeO₂

The microstructural behaviours of the LSM Ni-WC-CeO₂ MMCs with 0.9 wt.% CeO₂ in response to cavitation are shown in **Fig. 6.12**. These MMCs have a very similar microstructure regardless of being processed by different laser powers, and thus they also showed a similar failure

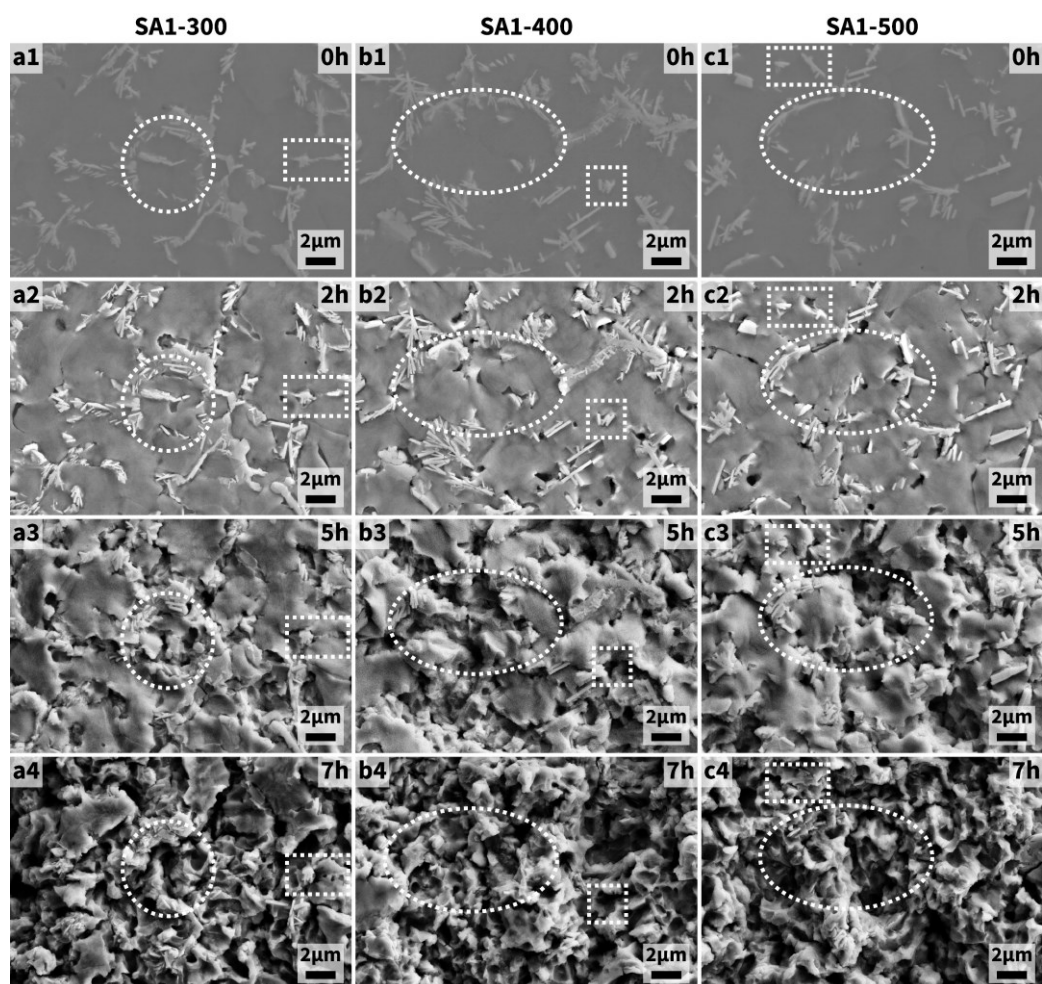


Fig. 6.12 – Microstructural evolution of the LSM MMCs with 0.9 wt.% CeO₂ during cavitation erosion. a-c, the MMCs treated by 300-, 400-, and 500-W lasers, respectively; White dotted rectangles: Isolated WC lamellae; White dotted circles/ellipse: Ni grains incompletely enclosed by eutectic Ni-WC.

mechanism when exposed to cavitation. As mentioned previously, the eutectic Ni-WC in the LSM MMCs with 0.9 wt.% CeO₂ had a lower volume and was less continuous compared to the LSM MMCs without CeO₂ (**Fig. 5.11**). A few of isolated WC lamellae (highlighted by the white dotted rectangles in **Fig. 6.12**) were found in the LSM MMCs with 0.9 wt.% CeO₂ and were easily detached when exposed to cavitation, suggesting that the isolated WC could not offer much protection against CE. Meanwhile, the LSM MMCs with 0.9 wt.% CeO₂ could not effectively confine the damage since the Ni grain was not fully enclosed by the eutectic Ni-WC (highlighted by the white dotted circles/ellipse in **Fig. 6.12**).

6.6.2 Specimens with 1.8wt.% CeO₂

The LSM Ni-WC-CeO₂ MMCs with 1.8 wt.% CeO₂ also had a similar microstructure despite being processed by different laser powers. Therefore, these MMCs also showed a similar behaviour when subjected to cavitation, and the results are presented in **Fig. 6.13**. The WC lamellae in these MMCs were very discrete and did not interlock with each other. Thus, many WC lamellae got eroded at the early stage of CE and could not protect the Ni matrix from CE or constrain the damage (**Fig. 6.13a3-c3**). Consequently, these MMCs experienced very severe damage after further exposure to cavitation impacts (**Fig. 6.13a4-c4**).

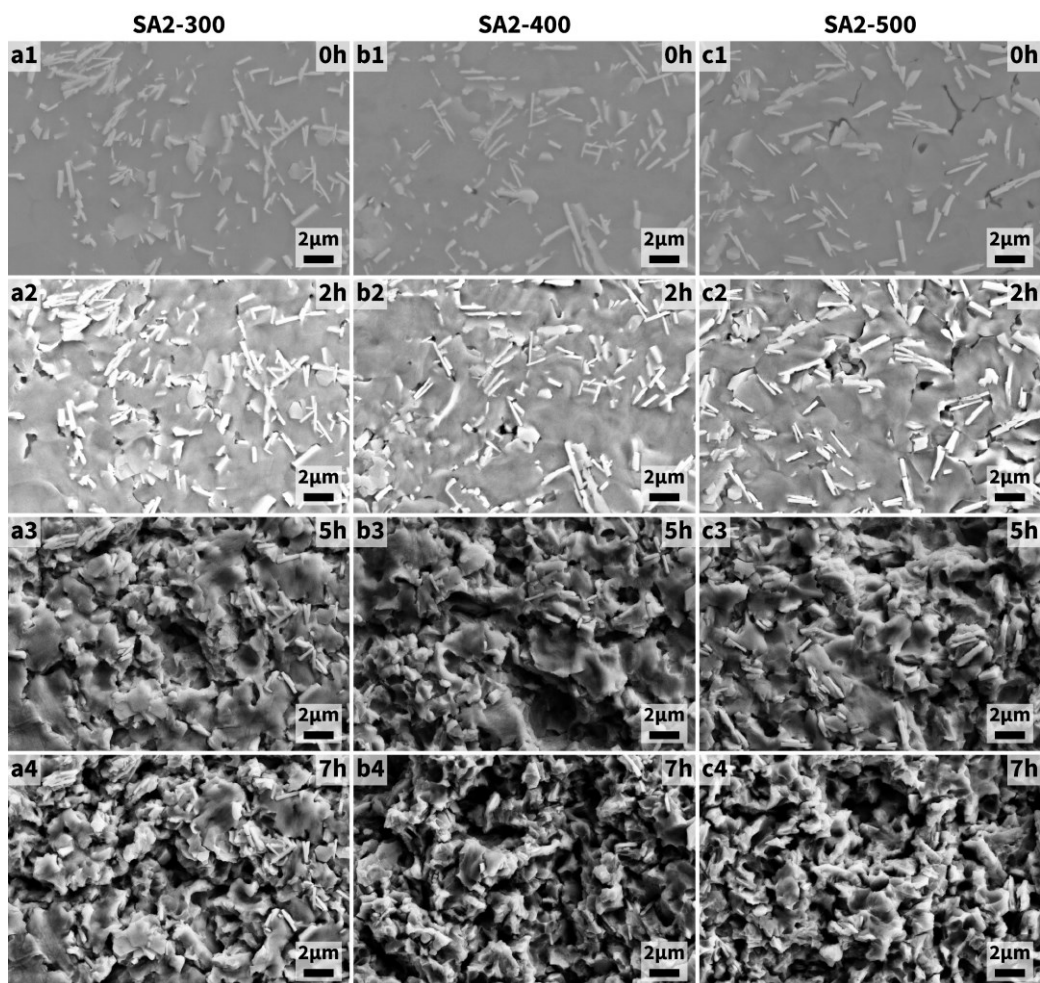


Fig. 6.13 – Microstructural evolution of the LSM MMCs with 1.8 wt.% CeO₂ during cavitation erosion. a-c, the MMCs treated by 300-, 400-, and 500-W lasers, respectively.

6.6.3 Specimens with 2.7wt.% CeO₂

The LSM Ni-WC-CeO₂ MMCs with 2.7 wt.% CeO₂ showed different microstructures depending on the laser power. In the SA3-300 MMC (**Fig. 6.6a2** and **Fig. 6.14a**), the WC lamellae were hierarchically interlocked, but the thickness of the lamellae was reduced. In addition, the number of the WC lamellae was increased, and the space between the WC lamellae was narrowed compared to the LSM MMCs without CeO₂ (**Fig. 5.4**). the

behaviour of the SA3-300 MMC in response to cavitation was very similar to that of the LSM MMCs without CeO₂ (Fig. 6.14). In most cases, the erosion was confined by the enclosed eutectic Ni-WC network.

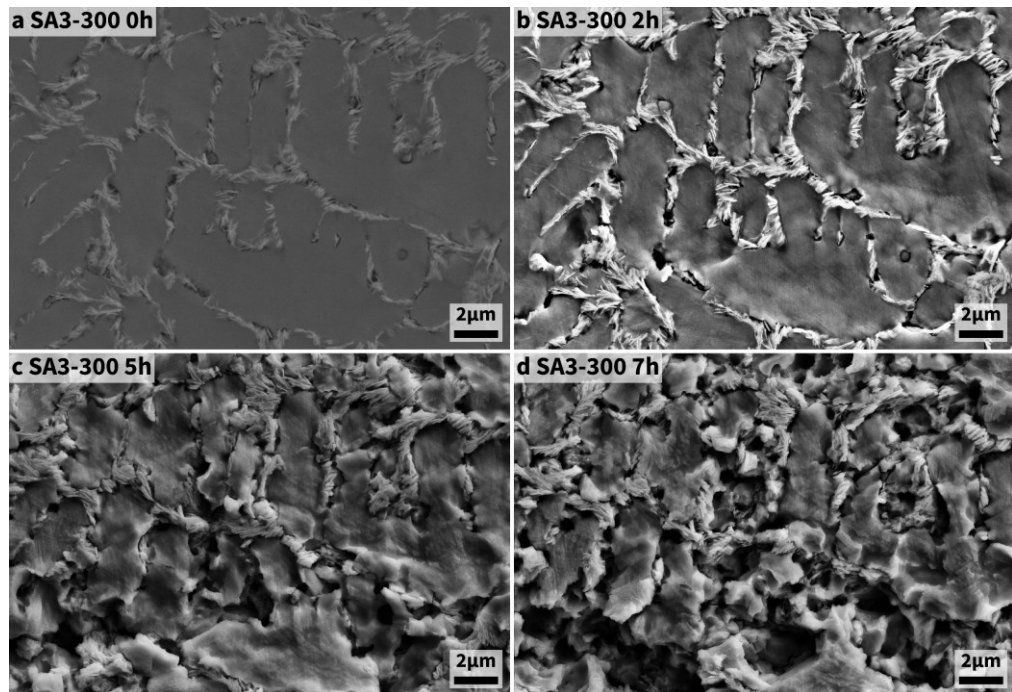


Fig. 6.14 – Microstructural evolution of the LSM MMCs with 2.7 wt.% CeO₂ treated by a laser of 300 W during cavitation erosion.

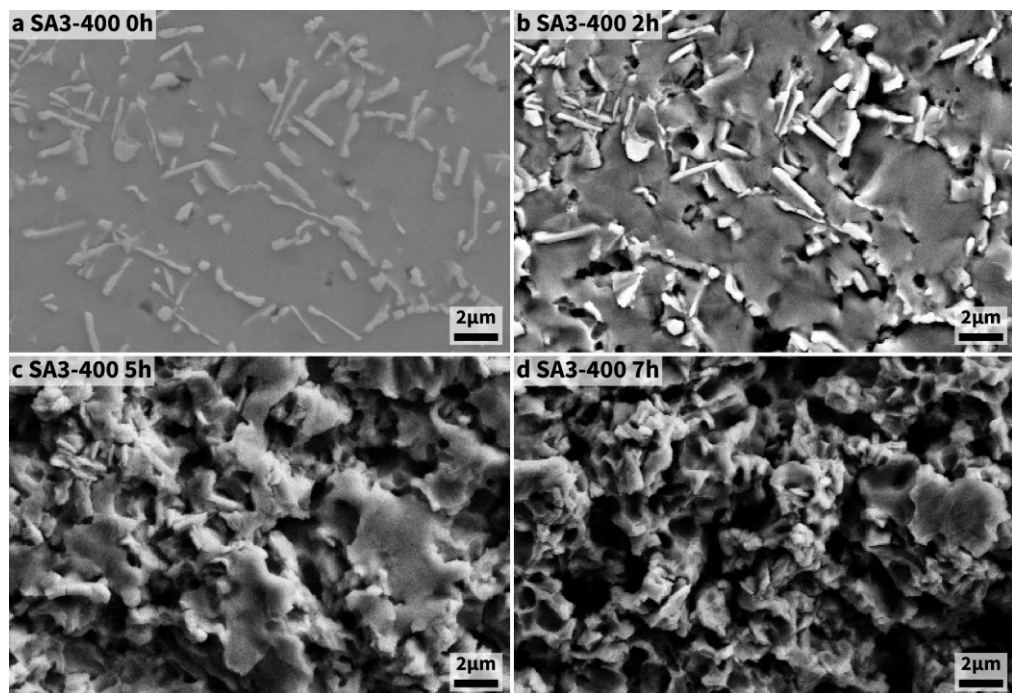


Fig. 6.15 – Microstructural evolution of the LSM MMCs with 2.7 wt.% CeO₂ treated by a laser of 400 W during cavitation erosion.

The WC lamellae in the SA3-400 MMC were very discrete (Fig. 6.6b2) and could not provide effective resistance to CE (Fig. 6.15), which was similar to the LSM MMCs with 1.8 wt.% CeO₂.

The SA3-500 MMC also presented a microstructure with a continuous eutectic Ni-WC network (Fig. 6.6c2 and Fig. 6.16a), but the lamellae were thicker compared to the LSM MMCs without CeO₂ (Fig. 5.4) and the SA3-300 MMC (Fig. 6.6a2). These WC lamellae could provide effective assistance in resisting CE (Fig. 6.16a-c). However, it seemed that the Ni in the eutectic Ni-WC could be preferentially eroded, resulting in the failure of the WC lamellae without the support of the Ni when further exposed to cavitation (Fig. 6.16d).

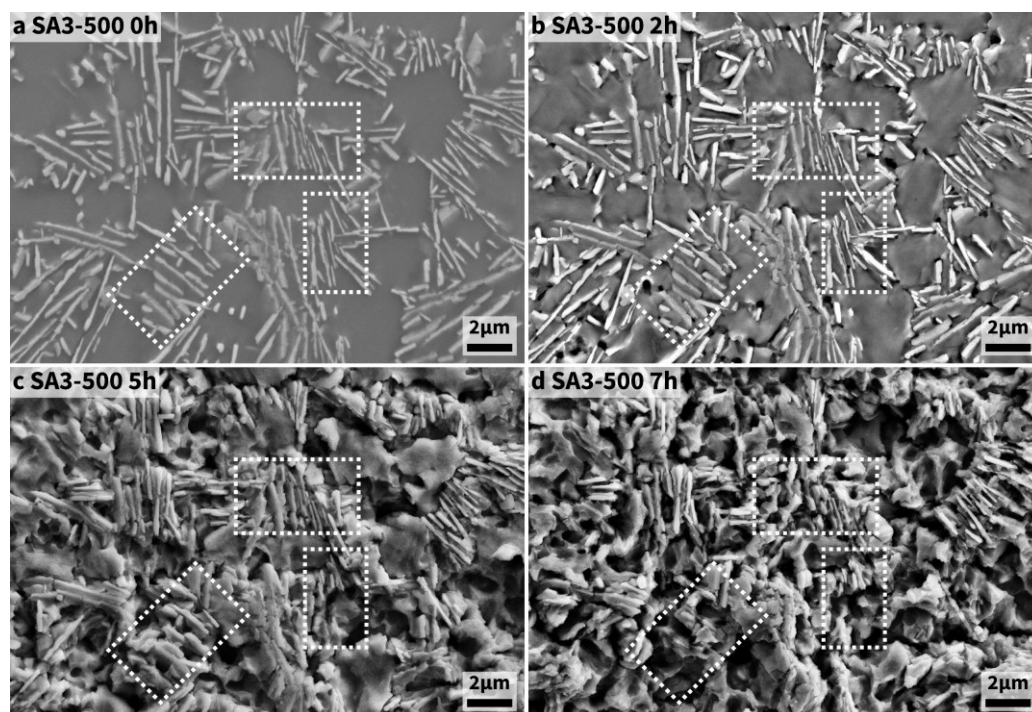


Fig. 6.16 – Microstructural evolution of the LSM MMCs with 2.7 wt.% CeO₂ treated by a laser of 500 W during cavitation erosion. White dotted rectangles: The Ni in between the WC lamellae eroded, resulting in the removal of the WC lamellae during cavitation erosion.

6.7 Numerical simulation

6.7.1 Model establishment

Numerical simulation was conducted by Ansys LS-DYNA Multiphysics Solver to further investigate the Ni-WC structures with different thickness and spacing of WC lamellae when subjected to a cavitation impact. There were five models denoted as Md1 to Md5 (**Fig. 6.17**). The first two models (Md1 and Md5) are similar to what were presented in **Chapter 5**, which are the model of pure Ni (**Fig. 6.17a**) and the model with two WC lamellae (**Fig. 6.17b**). Md3 has an extra WC lamella compared to Md2 (**Fig. 6.17c**). The volume of WC in Md4 (**Fig. 6.17d**) and Md5 (**Fig. 6.17e**) is the same as that in Md3, and the bottom surface of the bottommost WC lamella in Md3, Md4, and Md5 is at the same depth. The differences lie in the thickness of and the space between the WC lamellae, which allows the simulation of the models with different arrangement of WC lamellae. All the models were meshed into 1,280,000 cubic elements with a dimension of 5 nm. The impact was set to have a peak value of 1 GPa and last 40 ps (**Fig. 5.17**). The physical parameters of Ni and WC for modelling were tabulated in **Table 5.1**.

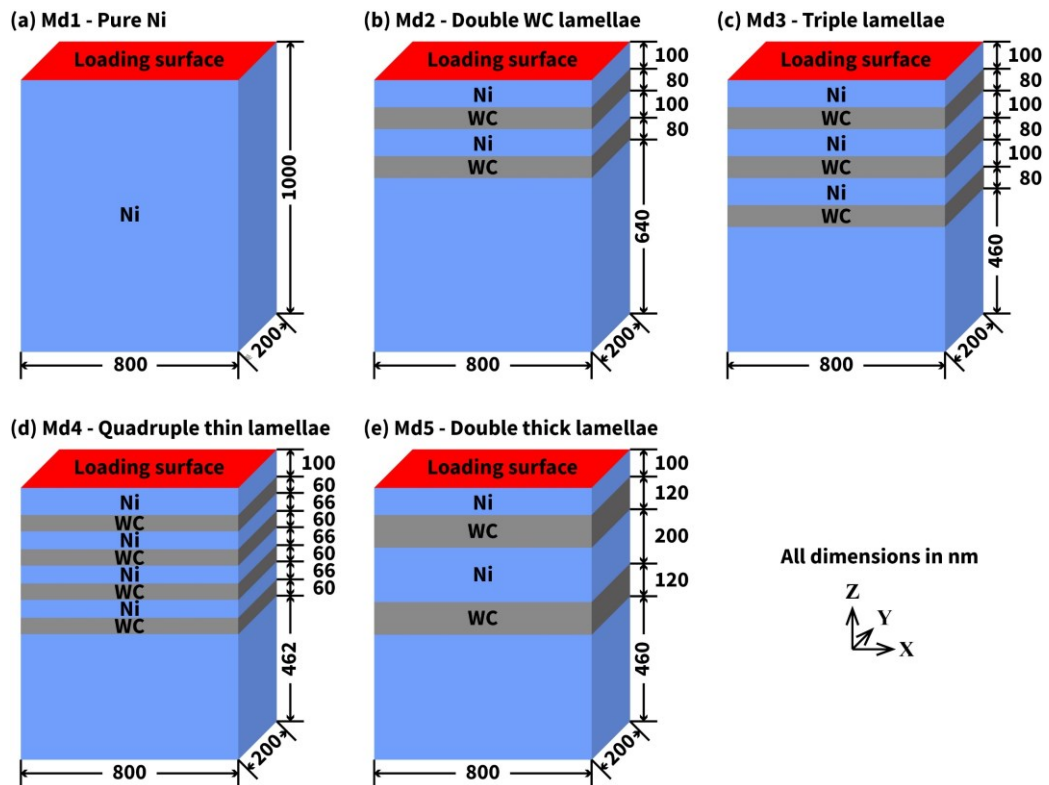


Fig. 6.17 – Numerical models of the pure Ni structure and the Ni-WC structures with different dimensions and distributions of WC lamellae.

6.7.2 Simulation results

The stress evolution of each model is demonstrated in **Fig. 6.18**, where only a quarter of the structures are shown as the models are symmetrical.

The stress at 100 nm depth and 640 nm depth in each model is plotted in **Fig. 6.19a-b**, and the local maximum stress (tensile and compressive) and the overall maximum stress at 640 nm depth are given in **Fig. 6.19c-d**.

Meanwhile, the total kinetic energy and the kinetic energy of the part below 640 nm are presented in **Fig. 6.19e-f**.

For all the models, tensile stress and compressive stress appeared alternately and travelled from the top surface to the bottom after being

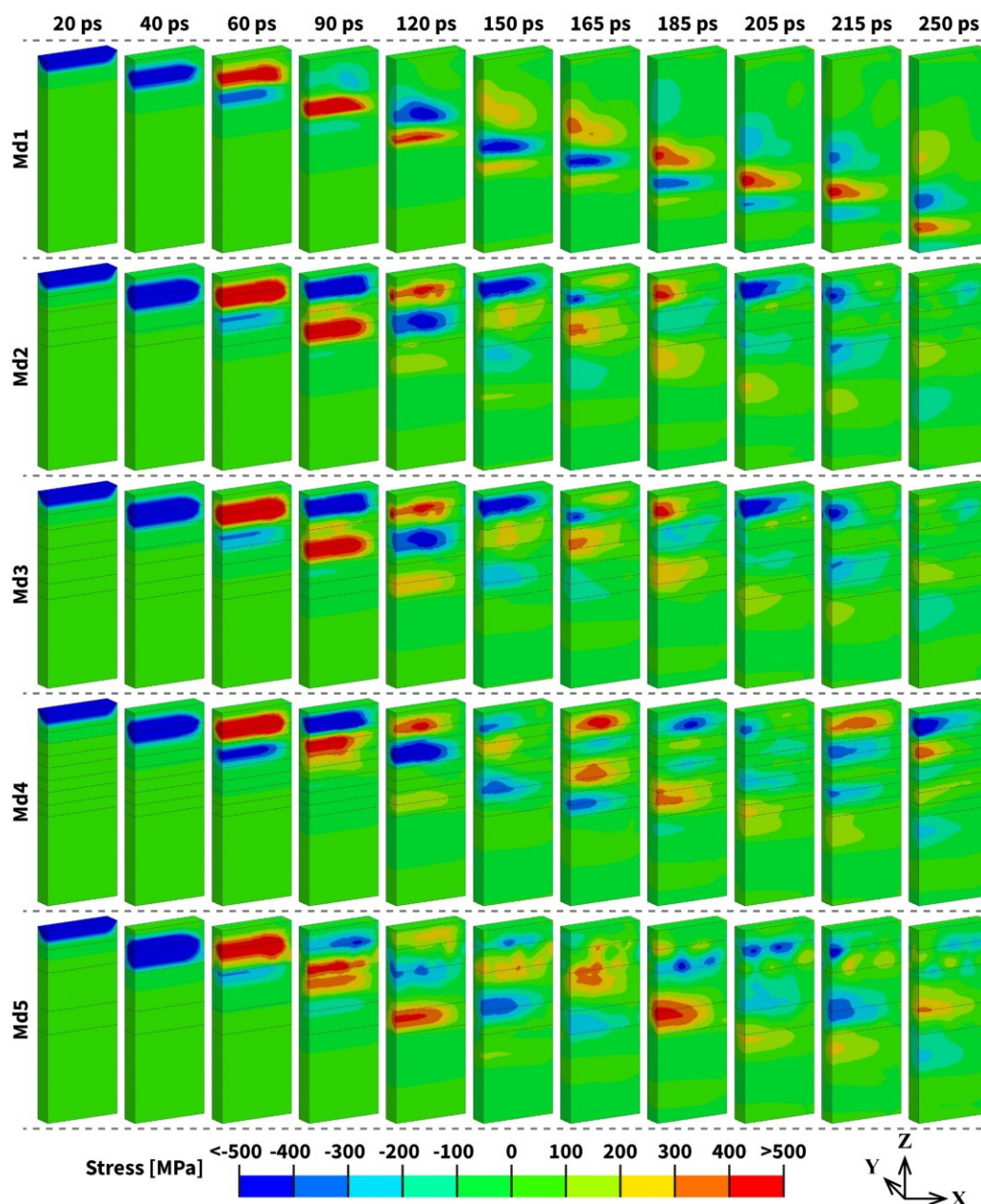


Fig. 6.18 – Stress evolution of the pure Ni structure and the Ni-WC structures with different dimensions and distributions of WC lamellae.

impacted. The stress wave in the pure Ni structure (Md1 in **Fig. 6.18**) was not engaged with any obstruction during its progression. However, the stress wave in the other models bounced between WC lamellae (Md2-Md5 in **Fig. 6.18**), and the stress was significantly reduced after transmitted through WC lamellae (**Fig. 6.18** and **Fig. 6.19a-d**). Meanwhile,

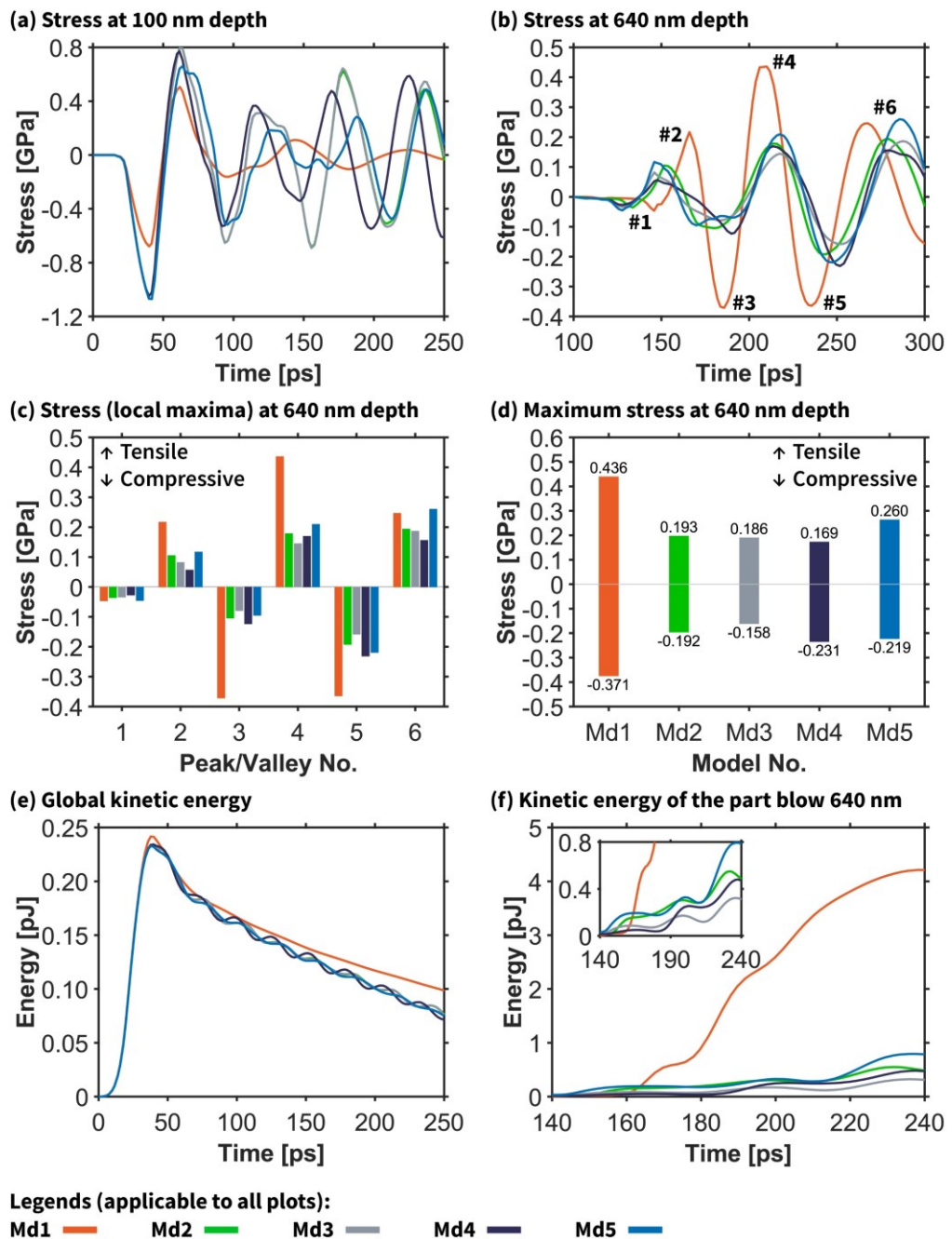


Fig. 6.19 – Stress and kinetic energy of the pure Ni structure and the Ni-WC structures with different dimensions and distributions of WC lamellae. **a**, Stress at 100 nm depth (the curves of Md2 and Md3 overlapped); **b**, Stress at 640 nm depth; The valleys in the stress wave are denoted as #1, #3, and #5, and the peaks in the stress wave are denoted as #2, #4, and #6; **c**, Stress of the peaks and the valleys denoted in **b**; **d**, Maximum stress (tensile and compressive) at 640 nm depth in each model; **e**, Global kinetic energy of each model; **f**, Kinetic energy of the part below 640 nm in each model.

the global kinetic energy in Md2-Md5 decreased faster than that in Md1

(**Fig. 6.19e**), and the kinetic energy of the part below 640 nm in Md2-Md5

was much lower than that in Md1 (**Fig. 6.19f**), suggesting consumption or dissipation of kinetic energy in Md2-Md5. Therefore, the above results indicate that the WC lamellae could mitigate the cavitation impact and facilitate effective CER, which is similar to what has been demonstrated in previous **Section 5.6**.

On the other hand, the Ni-WC models showed slightly different capabilities of stress and energy reduction based on the morphology and arrangement of WC lamellae. The WC lamellae in Md2 was fewer than those in Md3 (**Fig. 6.17**), and Md2 showed greater tensile stress and kinetic energy than Md3 (**Fig. 6.19c-d**).

Md3, Md4, and Md5 had the same WC volume (240 nm thick in total) and the same dimensions of the Ni-WC part (**Fig. 6.17**), but they exhibited the WC lamellae that were different in number, thickness, and spacing. Compared to Md3, an extra WC lamella was in Md4, but the WC lamellae in Md4 had lower thickness and denser distribution (**Fig. 6.17**). According to the simulation result, Md4 exhibited lower tensile stress than Md3 in most cases (**Fig. 6.19c**) and had the lowest tensile stress among all the models (**Fig. 6.19d**). Md5 had WC lamellae that were much thicker and distributed more discretely than Md3 (**Fig. 6.17**). The simulation results show that MD5 exhibited the greatest tensile stress (**Fig. 6.19c-d**) and kinetic energy (**Fig. 6.19f**) among the models with WC lamellae.

6.8 Discussion

6.8.1 Effect of CeO₂ addition on the microstructure of LSM Ni-WC

MMCs

When the content of CeO₂ was less than or equal to 1.8 wt.%, the Ni grain size in the LSM Ni-WC-CeO₂ MMCs was negatively correlated to the CeO₂ content (**Fig. 6.8a**). Meanwhile, the WC lamellae became thicker and more discretely distributed as the CeO₂ content increased to 1.8 wt.% (**Fig. 6.4** and **Fig. 6.5**). Furthermore, the microstructure of the LSM MMCs with 0.9 and 1.8 wt.% CeO₂ seemed to be irrelevant to the laser power (**Fig. 6.4** and **Fig. 6.5**).

The refined Ni grain could be attributed to the increased nucleation sites provided by CeO₂ or other Ce compounds [277, 321]. Then, the increased number of the refined Ni grains could provide more sites for the precipitation of the WC lamellae, resulting in a discrete and uniform distribution of the WC lamellae. On the other hand, a portion of CeO₂ was decomposed by the irradiation of high energy laser and released Ce and O₂ during the LSM process [322]. Ce atoms can affect the grain growth speed. The crystal surface that grows at the greatest speed tends to capture Ce atoms, and the CE atoms can reduce the free energy of the interfaces. Thus, the difference in the surface energy and the grain growth rate of each interface can be reduced [277, 322, 323]. As a result, the

thickness of the WC lamellae was increased in the LSM Ni-WC-CeO₂ MMCs (**Fig. 6.4** and **Fig. 6.5**) because of the inhibited growth speed of the WC lamella in the planar direction.

However, when CeO₂ content increased to 2.7 wt.%, the microstructure of the LSM MMCs would be influenced by the laser power. Nevertheless, other characterisation techniques may be required to explore the causes of the changes on the microstructure of the LSM MMCs with 2.7 wt.% CeO₂.

In addition, it is worth mentioning that the addition of the CeO₂ increased the thickness of the LSM layer in the LSM Ni-WC MMCs. For example, the LSM Ni-WC-2.7CeO₂ MMC treated by a laser of 300 W (**Fig. 6.6a1**) had a LSM layer that was almost as thick as the LSM layer of the CeO₂-free Ni-WC MMC treated by a laser of 500 W (**Fig. 5.4c1**). The increased thickness of the LSM layer was attributed to the decreased melting point by the addition of CeO₂ [274]. Meanwhile, the pre-existing defects in the LSM Ni-WC MMCs were minimised by the CeO₂ addition. Therefore, although it may not enhance the CER of the LSM Ni-WC MMC, the addition of CeO₂ could improve the durability and quality of the LSM layer, which may be beneficial to other applications.

6.8.2 Microstructure and cavitation erosion resistance

According to the cavitation erosion results in **Section 6.5** and the SEM observations in **Section 6.6**, it is confirmed that the eutectic Ni-WC network was crucial to the accomplishment of the effective CER for the LSM Ni-WC-CeO₂ MMCs. Specifically, the eutectic Ni-WC network should exhibit hierarchically interlocked WC lamellae and divide the Ni matrix into the cells that were completely enwrapped.

For the LSM MMCs with 1.8 wt.% CeO₂ (**Fig. 6.13**) and the SA3-400 sample (**Fig. 6.15**), the WC lamellae were very discrete, and most of the WC lamellae were eroded during CE, which could not provide effective protection to the Ni matrix. Therefore, these LSM MMCs had a higher MDER than the other LSM MMCs processed with the same laser power (**Fig. 6.11b**), and the MDER of the MMCs with 1.8 wt.% CeO₂ was almost the highest (**Fig. 6.11a**).

The LSM MMCs with 0.9 wt.% CeO₂ had the eutectic Ni-WC network with hierarchically interlocked WC lamellae. However, the eutectic Ni-WC network did not completely enclose the Ni cells, and thus the erosion at the Ni cells could not be confined (**Fig. 6.12**). Meanwhile, the thickness of the eutectic Ni-WC network Ni-WC network and the number of the WC lamellae were reduced compared to the CeO₂-free MMCs (**Fig. 5.11**). According to the numerical simulation results of Md2 and Md3, one layer

missing of the WC lamellae could cause higher stress amplitude (**Fig. 6.19c-d**) and kinetic energy (**Fig. 6.19f**) penetrating to the deep when being exposed to cavitation impacts. Hence, the MDER of the LSM MMCs with 0.9 wt.% CeO₂ was higher than that of the S0-400 sample (**Fig. 6.11a**).

Nevertheless, the SA1-400 and the SA1-500 samples showed the CER that was similar to that of the S0-300 and the S0-500 samples (**Fig. 6.11a**) because pre-existing pores (**Fig. 5.14**) and the granular WC grains (**Fig. 5.15**) in the latter two were considered being vulnerable to CE. Therefore, minimising the pre-existing defects is as important as having a CE-resistant microstructure in achieving effective CER. In addition, the SA1-300 sample showed the greatest CE since it had discontinuous eutectic Ni-WC network and the granular WC grains (**Fig. 6.4a**) which further compromised the CER.

The remained SA3-300 and SA3-500 samples are the only two that exhibited continuous eutectic Ni-WC network with hierarchically arranged WC lamellae among the LSM Ni-WC-CeO₂ MMCs (**Fig. 6.14** and **Fig. 6.16**). However, the thickness of and the space between the WC lamellae in the SA3-500 sample were much greater compared to the SA3-300 sample and the LSM CeO₂-free MMCs (**Fig. 5.11**). The increased space between the WC lamellae allowed Ni in the eutectic Ni-WC being eroded

during CE (**Fig. 6.16**), and then the WC lamellae were also eroded without the support of the Ni. As a result, the CER of the SA3-500 sample was not as good as that of the LSM CeO₂-free MMCs (**Fig. 6.11a**). The numerical simulation results of the model with the greatest thickness of and the space between the WC lamellae (Md5) exhibited the greatest stress amplitude (**Fig. 6.19c-d**) and kinetic energy (**Fig. 6.19f**), which also implied the less effective CER of the SA3-500 sample compared to the LSM CeO₂-free MMCs.

Among the LSM Ni-WC-CeO₂ MMCs, the SA3-300 sample (**Fig. 6.6a**) had the microstructure that was most similar to the LSM CeO₂-free MMCs (**Fig. 5.4**). Nevertheless, the WC lamellae in the SA3-300 sample was finer and denser than those in the LSM CeO₂-free MMCs. The numerical simulation models, Md4 and Md3, imitated the microstructures of the SA3-300 sample and the LSM CeO₂-free MMC, respectively. Compared to Md3, Md4 had an extra WC lamella, but the thickness of the WC lamellae was reduced (**Fig. 6.17**). The numerical simulation result showed that the transmitted tensile stress in Md4 was lower than that in Md3 when the models were subjected to the cavitation impact in most cases (**Fig. 6.19c**), and the Md4 had the least maximum tensile stress among all the models (**Fig. 6.19d**). Therefore, it is not surprising that the SA3-300 sample outperformed the S0-400 sample in CER (**Fig. 6.11a**) and exhibited the

lowest MDER among all the LSM Ni-WC MMCs with and without CeO₂.

On the other hand, more tolerance could be provided by more WC lamellae that were densely distributed. As mentioned in **Chapter 5**, the Ni at the interface of the primary Ni matrix and the eutectic Ni-WC tended to be preferentially eroded at the early stage of CE (**Fig. 5.11** and **Fig. 5.20**). Thus, the outmost WC lamella in the eutectic Ni-WC could be easily removed from the surface. Furthermore, the numerical simulation results of Md2 and Md3 suggested that reducing WC lamellae could cause increased stress amplitude (**Fig. 6.19c-d**) and kinetic energy (**Fig. 6.19f**) penetrating to the deep due to the reduced eutectic Ni-WC region. Then, if Md3 and Md4 had one WC lamella removed, a similar outcome could be reached, but the WC lamellae and the Ni-WC region in Md4 were still more and thicker than in Md3. Hence, it is reasonable to predict that the remained Ni-WC structure in Mod 04 is more resistant to impact than in M3. Therefore, M4 is more tolerant to the compromise of impact resistance caused by the removal of the outmost WC lamella. This inference is supported by the CE results (**Fig. 6.10d**) that the MDER of the SA3-300 sample was higher than that of the S0-400 sample at the early stage of CE (as the outmost WC lamella was still intact) but was lower at the steady-state period (as the outmost WC lamella was removed).

In addition, although the results in this chapter and **Chapter 5** suggested that the microstructure and distribution of WC lamellae predominated the CER of these LSM Ni-WC MMCs, Ni grain size may also affect the CER. Nevertheless, it is difficult to evaluate the effect of Ni grain size because the microstructure and distribution of WC lamellae changed significantly.

6.9 Summary

- 1) The sintered Ni-WC-CeO₂ MMCs were post-treated by LSM using the 300-, 400-, and 500-W lasers, respectively. The microstructure of the LSM Ni-WC-CeO₂ MMCs depended on the CeO₂ content and the laser power. The morphology and distribution of the WC lamellae were dominated by the CeO₂ content when the CeO₂ content was less than or equal to 1.8 wt.%. For the LSM MMCs with 2.7 wt.% CeO₂, the MMCs treated by different laser power showed different microstructure. Moreover, the addition of CeO₂ could minimise the defects in the LSM layer, improving the quality of the LSM layer.
- 2) Only the LSM Ni-WC-2.7CeO₂ MMCs treated by 300- and 500-W lasers exhibited a microstructure similar to the LSM CeO₂-free MMCs, which showed the continuous eutectic Ni-WC network with hierarchically arranged WC lamellae. The best CER was achieved by the LSM Ni-WC-2.7CeO₂ MMCs treated by a laser of 300 W (SA3-300

sample), which outperformed the LSM MMCs without CeO₂. On the other hand, the other LSM Ni-WC-CeO₂ MMCs showed a much more discrete distribution of WC lamellae. The CE test and the SEM observation demonstrated that the dispersedly distributed WC lamellae could not provide very effective CER.

- 3) SEM observation on the LSM Ni-WC-CeO₂ MMCs with different microstructures during CE test and the numerical simulation of different models with different arrangements of WC lamellae suggested that the CER was predominated by the morphology and distribution of the hard phases. For the Ni-WC MMCs in this study, outstanding CER could be achieved by the following features. Firstly, the pre-existing defects should be minimised as defects are vulnerable to CE. Secondly, the MMCs must exhibit inter-connected eutectic Ni-WC networks with hierarchically interlocked WC lamellae that divide and enclose the primary Ni matrix into many cells. In addition, refining and increasing the WC lamellae in the eutectic Ni-WC network could further improve the CER.

Chapter 7

Effects of Cr addition on cavitation erosion of LSM NiCr-WC MMCs

7.1 Introduction

As reviewed in **Subsection 2.5.3**, customising the ratio and the chemical composition of the metallic binder phase can be a practical approach to improve the CER of the WC-based cermet coatings. Cr is known for its outstanding corrosion resistance and high hardness, which can effectively improve the corrosion and oxidation resistance of coatings when being used as an alloy element [270, 271]. In addition, some studies prepared wear- and CE-resistant coatings by laser cladding WC with Cr and other metals [220, 273]. Hence, it is anticipated that the CER of the LSM Ni-WC MMCs may be enhanced if the Ni in the LSM Ni-WC MMCs is partially replaced by Cr.

In this chapter, a preparatory study reports the CER of the LSM NiCr-WC MMCs. The sintered NiCr-WC MMCs with 3 different Cr contents were prepared and processed by LSM. The effect of Cr addition on the microstructure and CER of the LSM sintered NiCr-WC MMC was investigated. Surprisingly, the LSM NiCr-WC MMCs present extraordinary resistance to CE. The CE of these LSM NiCr-WC MMCs was nearly

negligible after the 10-h CE test, and SEM images showed that the surface was almost intact after the exposure to CE for 7 h.

7.2 Sample information

The sintered NiCr-WC MMCs have a constant volumetric metal-to-ceramic ratio of 3:1. The contents of Cr are ascending, which are 10, 20, and 30 vol.%. The sintered NiCr-WC MMCs were post-treated by LSM with different laser powers of 300, 400, and 500 W, respectively. **Table 7.1** below summarises the information of these samples, and the samples are quoted as the index provided in the table.

Table 7.1 – Chemical composition and process parameters of NiCr-WC MMCs.

Index	Composition (vol.%)			Composition (wt.%)			Process
	Ni	WC	Cr	Ni	WC	Cr	
SB1	65.0	25.0	10.0	55.6	37.5	6.9	Sintered
SB2	55.0	25.0	20.0	47.9	38.1	14.0	
SB3	45.0	25.0	30.0	39.9	38.8	21.3	
SB1-300	65.0	25.0	10.0	55.6	37.5	6.9	Sintered and remelted by 300W laser
SB2-300	55.0	25.0	20.0	47.9	38.1	14.0	
SB3-300	45.0	25.0	30.0	39.9	38.8	21.3	
SB1-400	65.0	25.0	10.0	55.6	37.5	6.9	Sintered and remelted by 400W laser
SB2-400	55.0	25.0	20.0	47.9	38.1	14.0	
SB3-400	45.0	25.0	30.0	39.9	38.8	21.3	
SB1-500	65.0	25.0	10.0	55.6	37.5	6.9	Sintered and remelted by 500W laser
SB2-500	55.0	25.0	20.0	47.9	38.1	14.0	
SB3-500	45.0	25.0	30.0	39.9	38.8	21.3	

7.3 Characterisation of the sintered Ni-WC-Cr

The polished cross-sections of the sintered NiCr-WC MMCs are shown in **Fig. 7.1b-d**. Except for the presence of Cr, the cross-sections of the sintered NiCr-WC MMCs are similar as the sintered Ni-WC MMC (**Fig. 7.1a**), showing bright WC particles and dark Ni matrix. The volumetric contents of the Cr in the MMCs were checked by analysing the SEM image in **Fig. 7.1b-d** and another nine with the same scale for each MMC with different content of Cr, finding that the contents of the Cr in the MMCs were 9.2 ± 1.9 , 18.7 ± 2.4 , 28.4 ± 2.3 vol.%, respectively, which were in agreement with the designed contents.

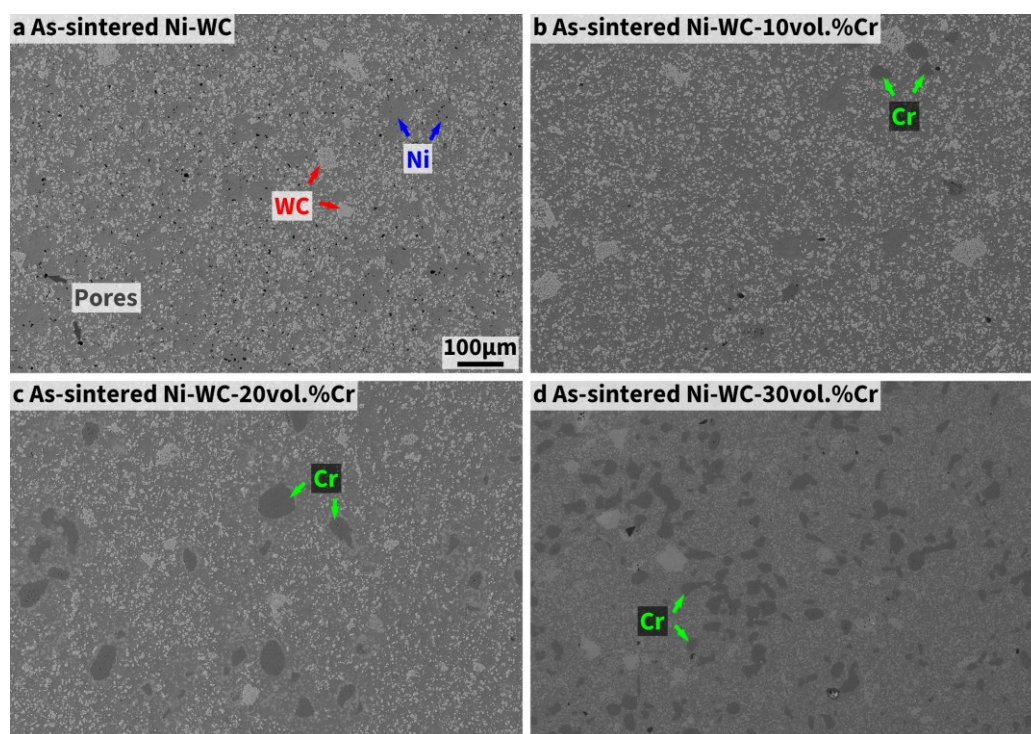


Fig. 7.1 – SEM images of the cross-section of the sintered NiCr-WC MMCs. a, As-sintered Ni-WC for comparison; **b-d**, As-sintered NiCr-WC with 10, 20, and 30 vol.% Cr, respectively.

7.4 Characterisation of LSM NiCr-WC

7.4.1 SEM results

The cross-sections of these LSM sintered NiCr-WC MMCs are characterised by SEM, and the results are shown in **Fig. 7.2**, **Fig. 7.3**, and **Fig. 7.4** for the MMCs with 10, 20, and 30 vol.% Cr, respectively. Compared to the LSM Ni-WC MMCs (**Fig. 5.4**), the microstructures of the LSM sintered NiCr-WC MMCs were quite different.

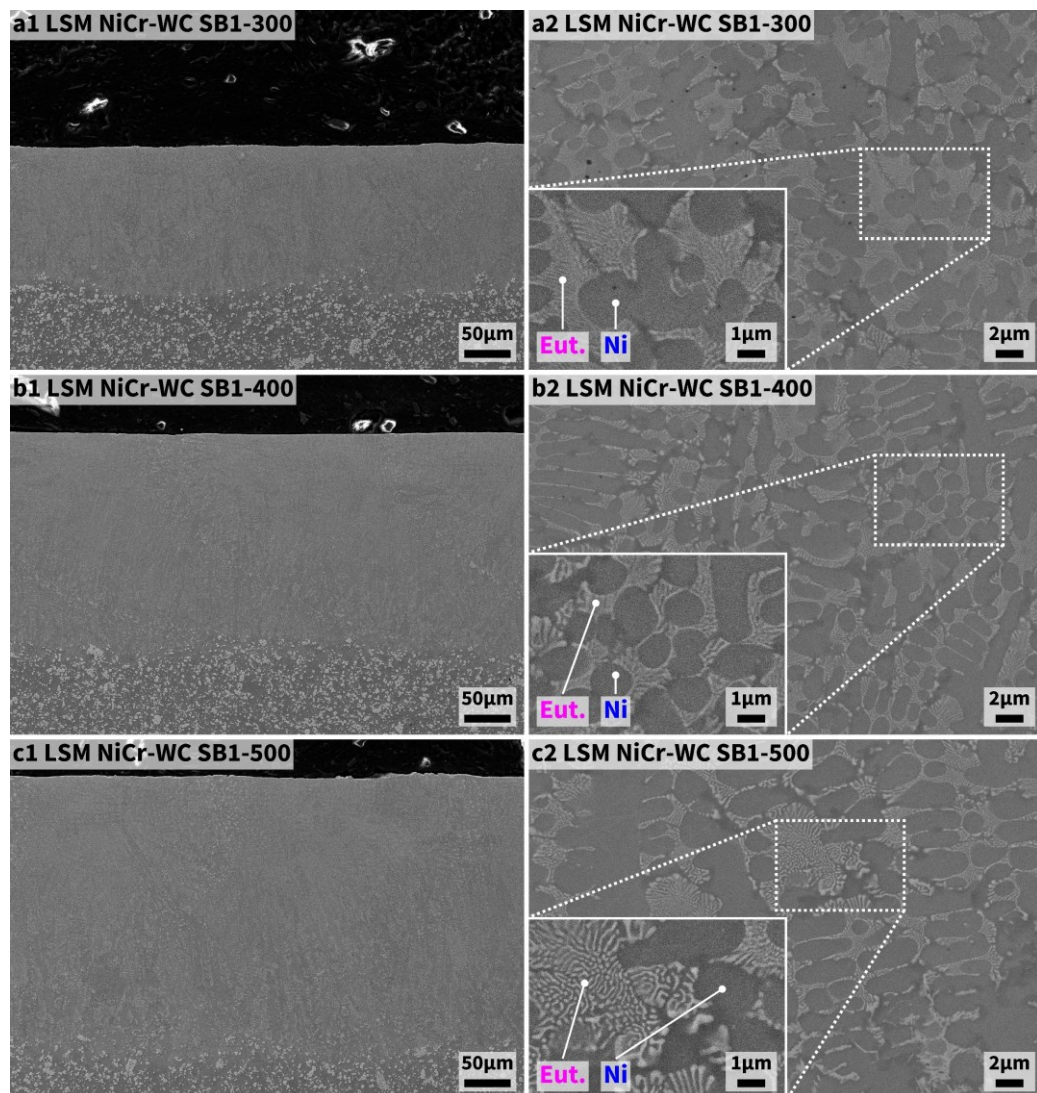


Fig. 7.2 – SEM images showing the cross-sections of the LSM NiCr-WC MMCs (with 10 vol.% of Cr) treated by different laser powers. a-c, Specimens treated by 300-, 400-, and 500-W lasers, respectively; 1-2, Low and high magnifications.

All the LSM Ni-10vol.%Cr-WC MMCs showed the same hypoeutectic microstructure regardless of being treated by the laser with different power (Fig. 7.2). The carbides in the eutectic region of the LSM NiCr-WC MMCs were lamellar.

For the LSM Ni-20vol.%Cr-WC MMCs, the microstructure was affected by the laser power (Fig. 7.3). The SB2-300 sample was filled with the lamellar eutectic that was similar to that of the LSM Ni-10vol.%Cr-WC MMCs (Fig.

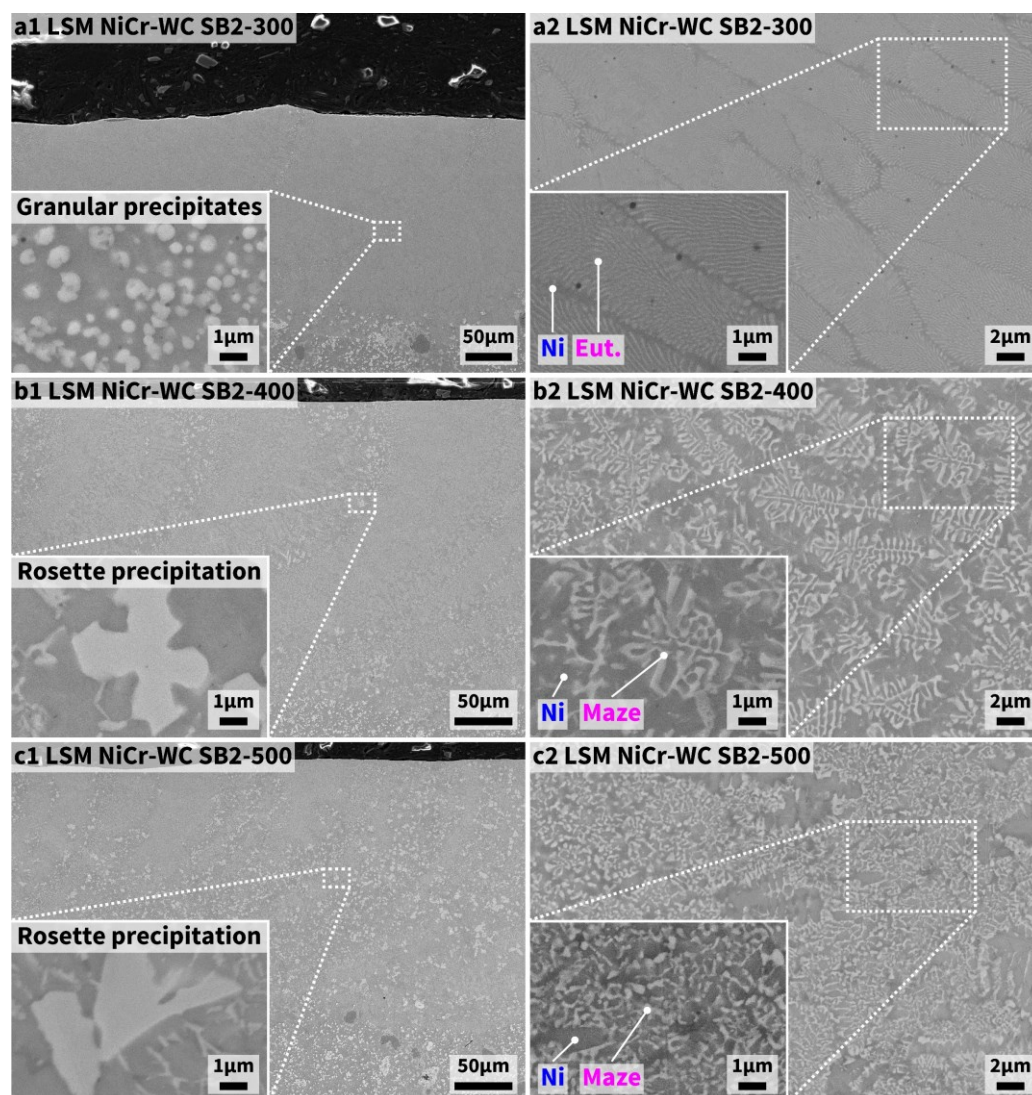


Fig. 7.3 – SEM images showing the cross-sections of the LSM NiCr-WC MMCs (with 20 vol.% of Cr) treated by different laser powers. a-c, Specimens treated by 300-, 400-, and 500-W lasers, respectively; 1-2, Low and high magnifications.

7.3a2), and granular precipitates were found at the edge of the molten pool (Fig. 7.3a1). Meanwhile, there were Ni-rich interfaces that divided the lamellar eutectic region (Fig. 7.3a2). When the sintered MMC was treated by a 400-W laser, most of the carbides became maze-like (Fig. 7.3b2), and large rosette-like precipitates were found at the edge of the molten pool (Fig. 7.3b1). When the laser power reached 500 W, the maze-like carbides became finer (Fig. 7.3c2), and more rosette-like precipitates

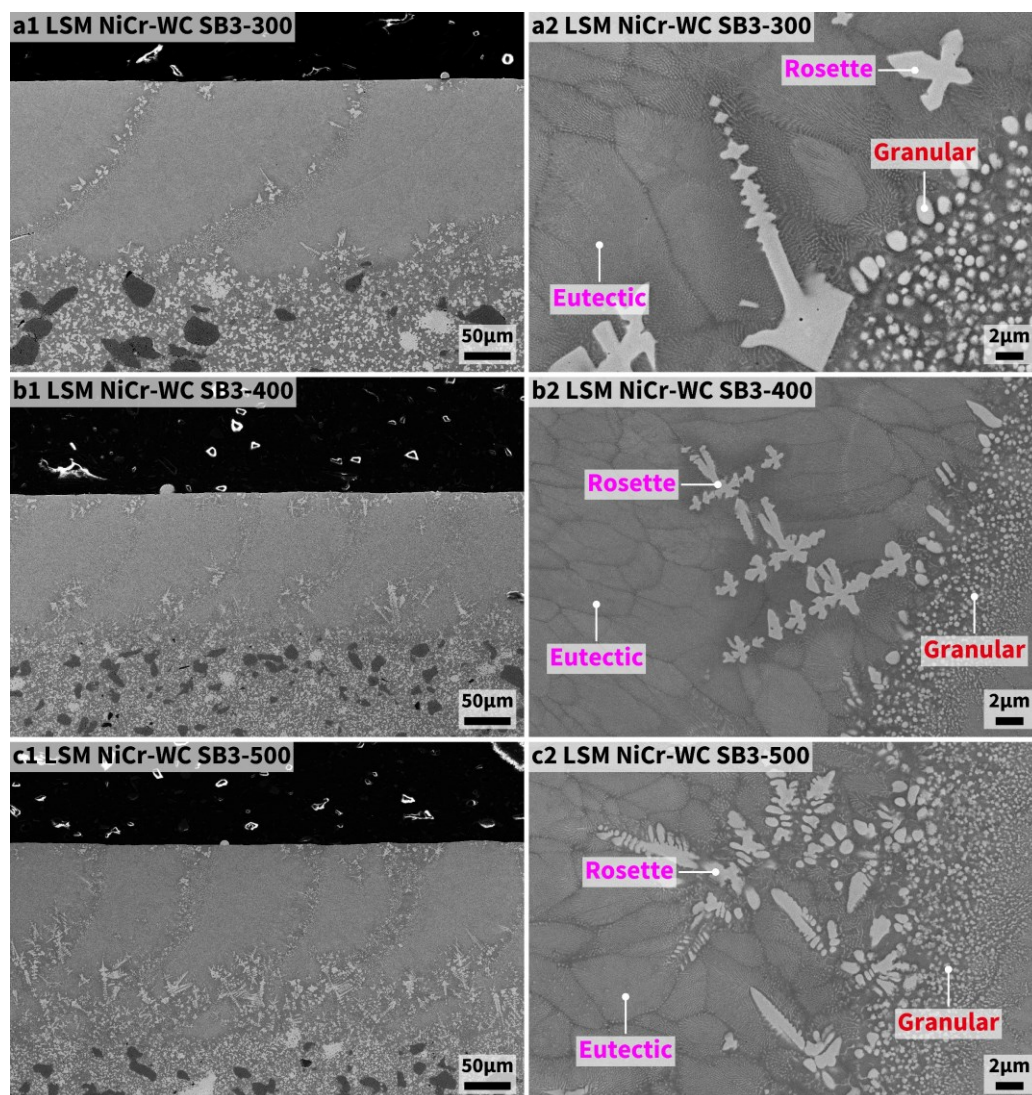


Fig. 7.4 – SEM images showing the cross-sections of the LSM NiCr-WC MMCs (with 30 vol.% of Cr) treated by different laser powers. a-c, Specimens treated by 300-, 400-, and 500-W lasers, respectively; 1-2, Low and high magnifications.

were found (Fig. 7.3c1).

The LSM Ni-30vol.%Cr-WC MMCs exhibited the same microstructural features regardless of the post-treatment by the laser with different power (Fig. 7.4). All these LSM MMCs were mainly composed of the lamellar eutectic and the large rosette-like precipitates, and the small granular precipitates were found at the edge of the molten pool (Fig. 7.4a2-c2). The difference was that the increased laser power would result in more rosette-like precipitates (Fig. 7.4a1-c1).

It is also worth mentioning that large cracks were formed in the LSM layer of the LSM NiCr-WC MMCs with 20 and 30 vol.% Cr (Fig. 7.5, Fig. 7.6, and Appendix E). Meanwhile, microcracks were found in the large

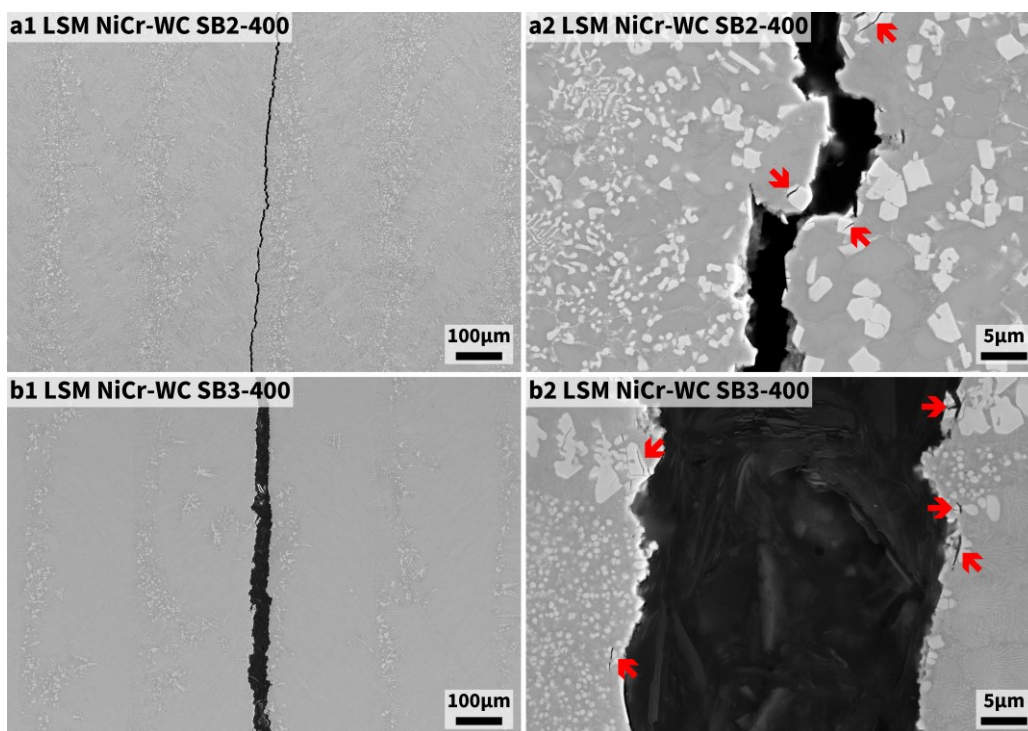


Fig. 7.5 – SEM image showing the large cracks and microcracks on the surface of LSM NiCr-WC MMCs with 20 and 30 vol.% of Cr treated by 400-W laser. Red arrows in a2 and b2: Microcracks formed in carbides.

carbides (**Fig. 7.5a2-b2**). The formation of the cracks may be attributed to the significant thermal shock and the fast solidification of the molten pool during the LSM process. According to the literature [324, 325], tensile stress should be responsible for the crack initiation in the carbides due to the poor fracture toughness. However, microcracks were not observed from the matrix, indicating that the tensile residual stress during the solidification may not be sufficient to initiate cracks in the ductile matrix. Therefore, the initiation of the cracks was from the large carbides.

In addition, the large cracks seemed to grow deeper and wider as the Cr content increase. The LSM Ni-30vol.%Cr-WC MMCs showed that some cracks even penetrated through the LSM layer and propagated into the regions which were not remelted (**Fig. 7.6d-f**). Meanwhile, the LSM layer of the Ni-30vol.%Cr-WC MMC treated by a 500-W laser was almost detached from the MMC (**Appendix E**). According to **Fig. 7.3** and **Fig. 7.4**,

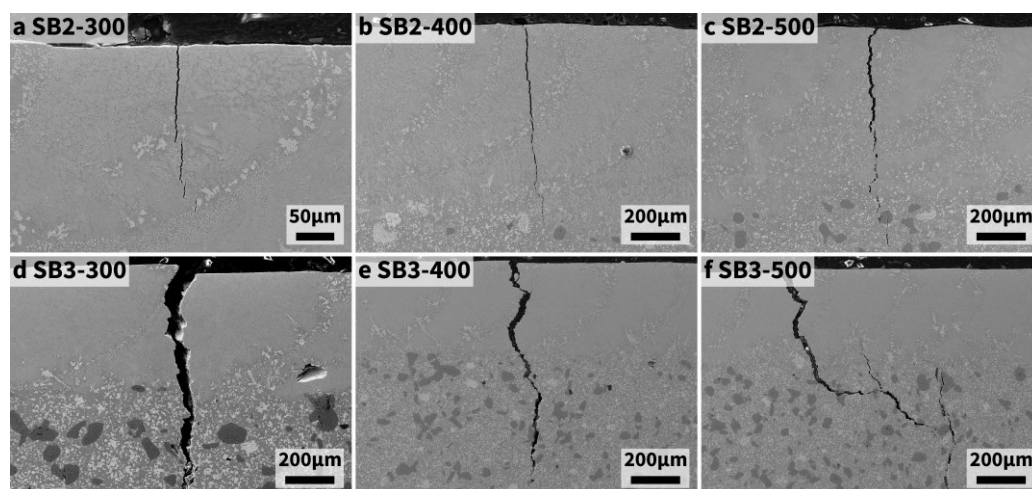


Fig. 7.6 – Cross-sectional SEM image showing the cracks in the LSM NiCr-WC MMCs with 20 and 30 vol.% of Cr. The cutting direction was perpendicular to the laser scanning direction.

the volume and size of rosette-like carbides were increased as the Cr content increased. As cracks tended to initiate at large carbides, more serious cracking happened to the LSM MMCs with a higher Cr content.

7.4.2 SEM-EDX results

SEM-EDX analysis was conducted to investigate the elemental composition of different microstructural features in the LSM NiCr-WC MMCs (Fig. 7.7). However, the chemical composition of the lamellar eutectic and the maze-like carbides could not be identified due to the limitation of resolution.

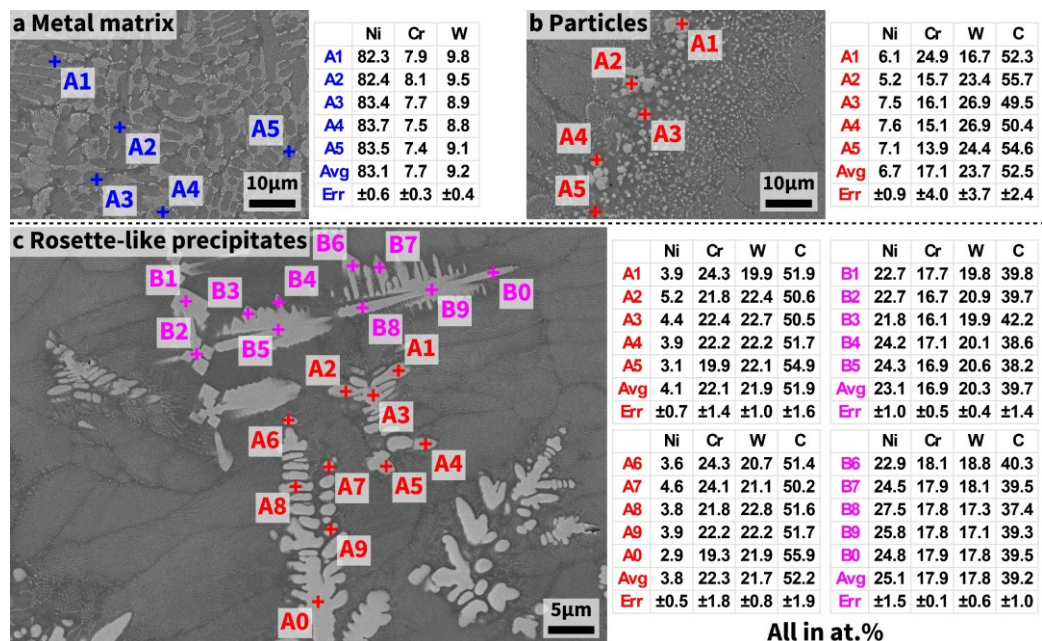


Fig. 7.7 – SEM-EDX results of various microstructure features in the LSM NiCr-WC MMCs.

According to the SEM-EDX results, the primary metallic phase in the hypoeutectic LSM Ni-10vol.%Cr-WC was mainly composed of Ni (Fig. 7.7a). The granular carbides were Cr- and W-rich, and the content of Ni

was negligible (**Fig. 7.7b**). The large rosette-like carbides were sorted into two types based on the elemental composition. Some had a similar elemental content as the granular precipitate (series **A** in **Fig. 7.7c**), while the others showed Ni, Cr, and W, in an almost equivalent ratio (series **B** in **Fig. 7.7c**).

7.4.3 EBSD results

The microstructural features of the LSM NiCr-WC MMCs were further characterised by EBSD (**Fig. 7.7**). According to the results, the LSM MMCs were composed of the FCC Ni-rich metal matrix and two types of precipitated carbides with different crystal structures, which were orthorhombic (ORH) or HCP (**Fig. 7.7a3-f3**). The ratio of the two carbides was not the same in different microstructural features. Most of the carbides in the eutectic matrix of the hypoeutectic LSM Ni-10vol.%Cr-WC MMCs and the granular precipitation showed an HCP structure (**Fig. 7.7a3-b3**), while the maze-like carbide was ORH (**Fig. 7.7d3**). The rosette-like phases could be either HCP or ORH (**Fig. 7.7c3**). However, the phase composition of the fine eutectic matrix in the SB2-300 MMC and the LSM Ni-30vol.%Cr-WC MMCs could not be identified due to the limited resolution, but it could be confirmed that the precipitates near the Ni-rich interfaces were mainly composed of HCP carbides, and the fine lamellar

carbide can be either HCP or ORH (Fig. 7.7e3-f3). Assuming the carbides with the same crystal structure have the same chemical composition, and according to the SEM-EDX and the EBSD results, the carbides in these LSM NiCr-WC MMCs can be sorted into the types summarised in Table 7.2.

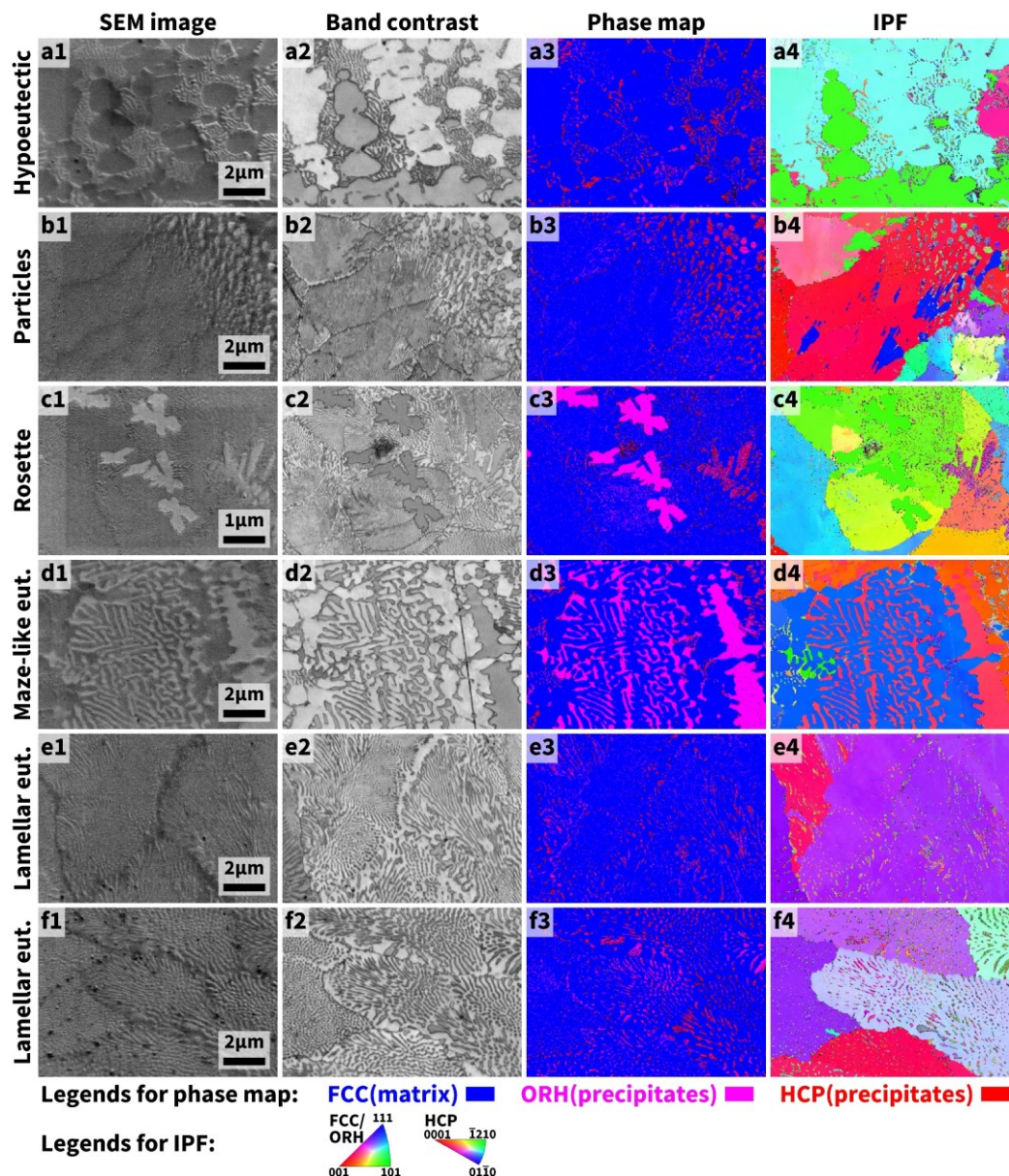


Fig. 7.8 – EBSD results of various microstructure features in the LSM NiCr-WC MMCs. The step size was 0.025 µm.

Table 7.2 – Summary of the carbides in the LSM NiCr-WC.

Carbides	Dominant phases
Lamellar carbides in hypoeutectic LSM Ni-10vol.%Cr-WC (Fig. 7.2)	HCP
Maze-like carbides in LSM Ni-20vol.%Cr-WC (Fig. 7.3b-c)	ORH
Lamellar carbides in eutectic LSM Ni-10/20vol.%Cr-WC (Fig. 7.3a, Fig. 7.4)	HCP/ORH
Rosette-like carbides in LSM Ni-10/20vol.%Cr-WC (Fig. 7.3b-c, Fig. 7.4)	HCP/ORH
Granular carbides at the edge of the molten pool (Fig. 7.4)	HCP

7.5 Cavitation erosion

The LSM NiCr-WC MMCs were subjected to CE test for 10 h, and total erosion after 10 h in terms of MDE is shown in Fig. 7.9. The total CE at the 10th h of these LSM NiCr-WC MMCs was surprisingly low and was about 5~10% that of the LSM Ni-WC MMCs without Cr (Fig. 5.9a). The LSM Ni-10vol.%Cr-WC MMCs exhibited lower CE than the LSM NiCr-WC MMCs with a higher Cr content.

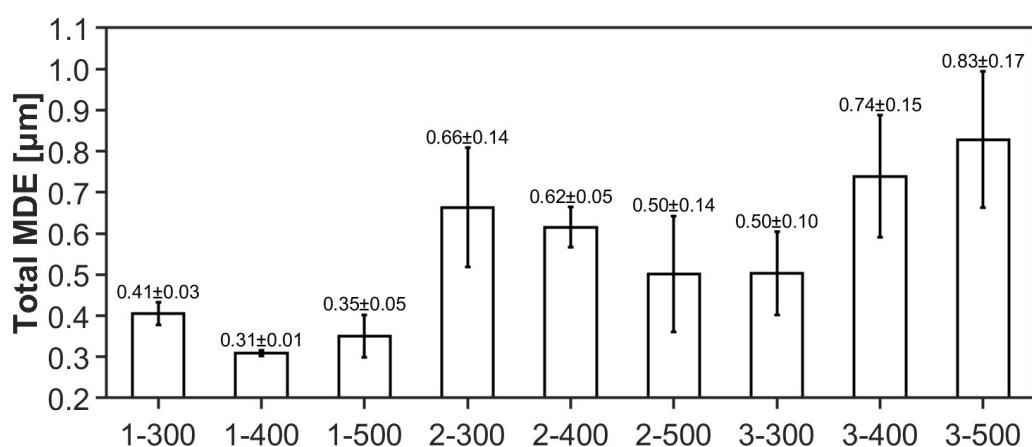


Fig. 7.9 – Erosion of LSM NiCr-WC MMCs after 10-hour cavitation erosion test.

7.6 SEM observation of the samples exposed to cavitation erosion at different test intervals

7.6.1 Specimens with 10 vol.% Cr

The microstructural behaviours of the LSM Ni-10vol.%Cr-WC MMCs in response to cavitation are shown in **Fig. 7.10**. These MMCs had an almost identical microstructure regardless of being processed by different laser powers, and thus their behaviour was the same when exposed to cavitation impacts. As shown in **Fig. 7.10**, the exposure to cavitation

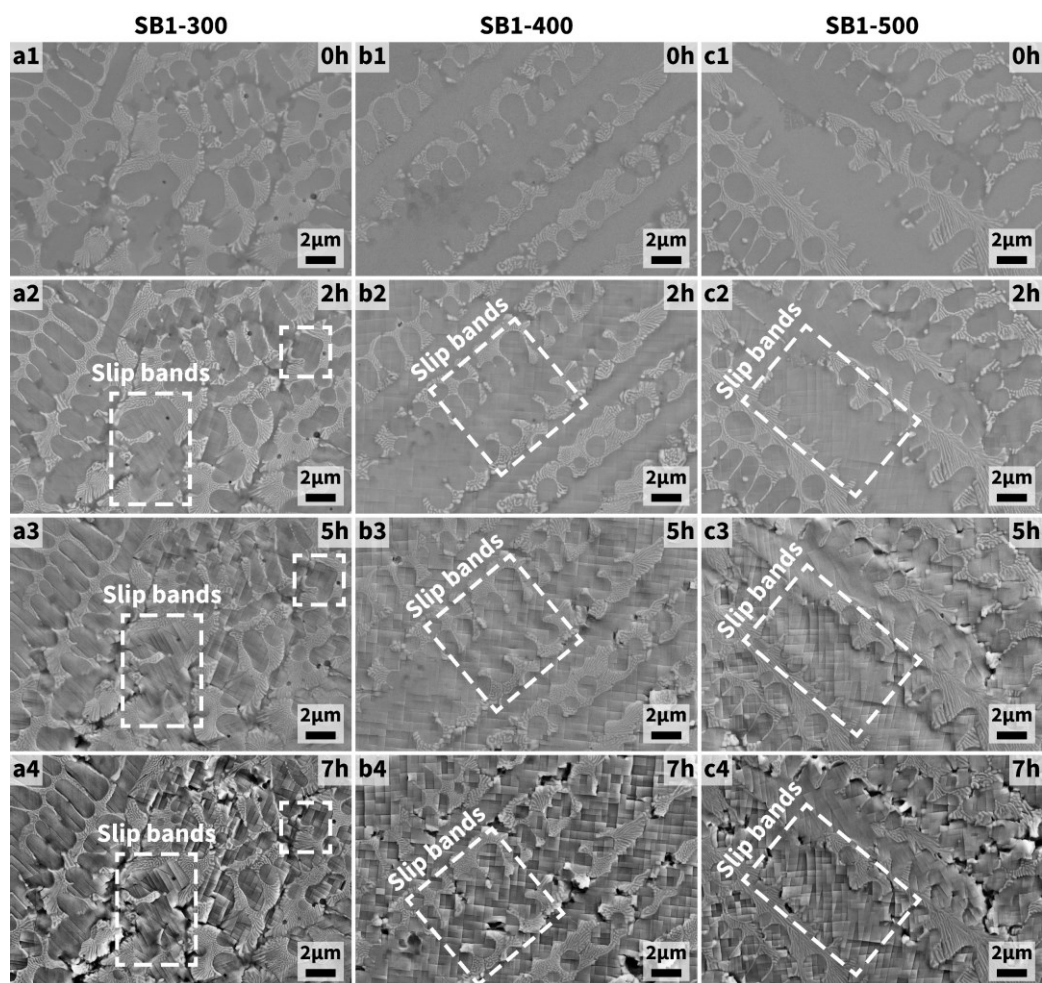


Fig. 7.10 – Microstructural evolution of the LSM MMCs with 10 vol.% Cr during cavitation erosion. a-c, the MMCs treated by 300-, 400-, and 500-W lasers, respectively.

impacts only resulted in the formation of slip bands in the Ni-rich matrix, and little material removal was found. The erosion preferentially occurred to the Ni-rich matrix at the interfaces between the Ni-rich matrix and the lamellar eutectic matrix, while the lamellar eutectic matrix was barely eroded.

7.6.2 Specimens with 20 vol.% Cr

The behaviours of the LSM Ni-20vol.%Cr-WC MMCs in response to

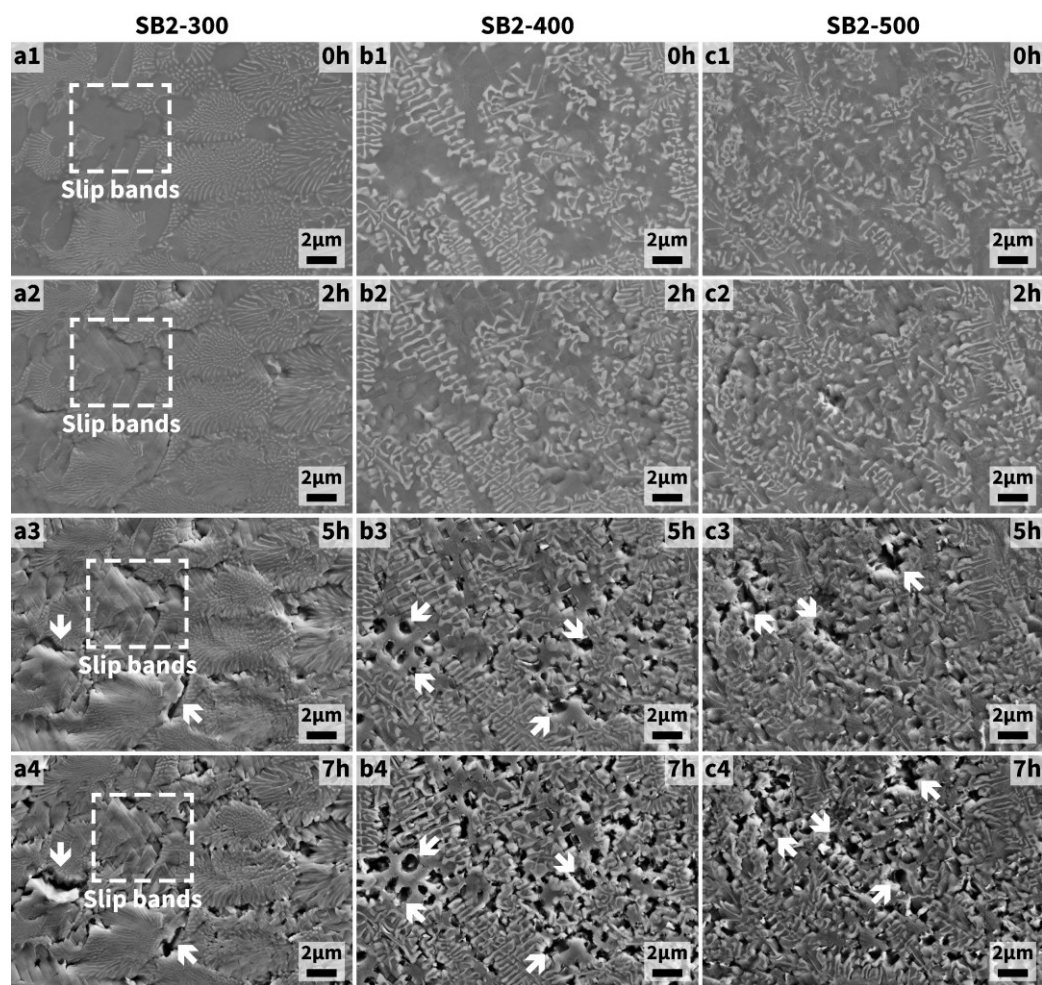


Fig. 7.11 – Microstructural evolution of the LSM MMCs with 20 vol.% Cr during cavitation erosion. a-c, the MMCs treated by 300-, 400-, and 500-W lasers, respectively. White arrows: The erosion of the primary Ni.

cavitation were different as these MMCs had different microstructures depending on the laser power (**Fig. 7.11**). The SB2-300 sample was mostly filled with the lamellar eutectic matrix. The lamellar eutectic matrix was almost free off any damage, and the erosion was only found in the Ni-rich matrix and at the boundary of the adjacent eutectic region (**Fig. 7.11a**). Meanwhile, slip bands were also found in the Ni-rich matrix in the SB2-300 sample. On the other hand, the maze-like structure in the SB2-400 and the SB2-500 samples seemed to be less resistant to CE, and the

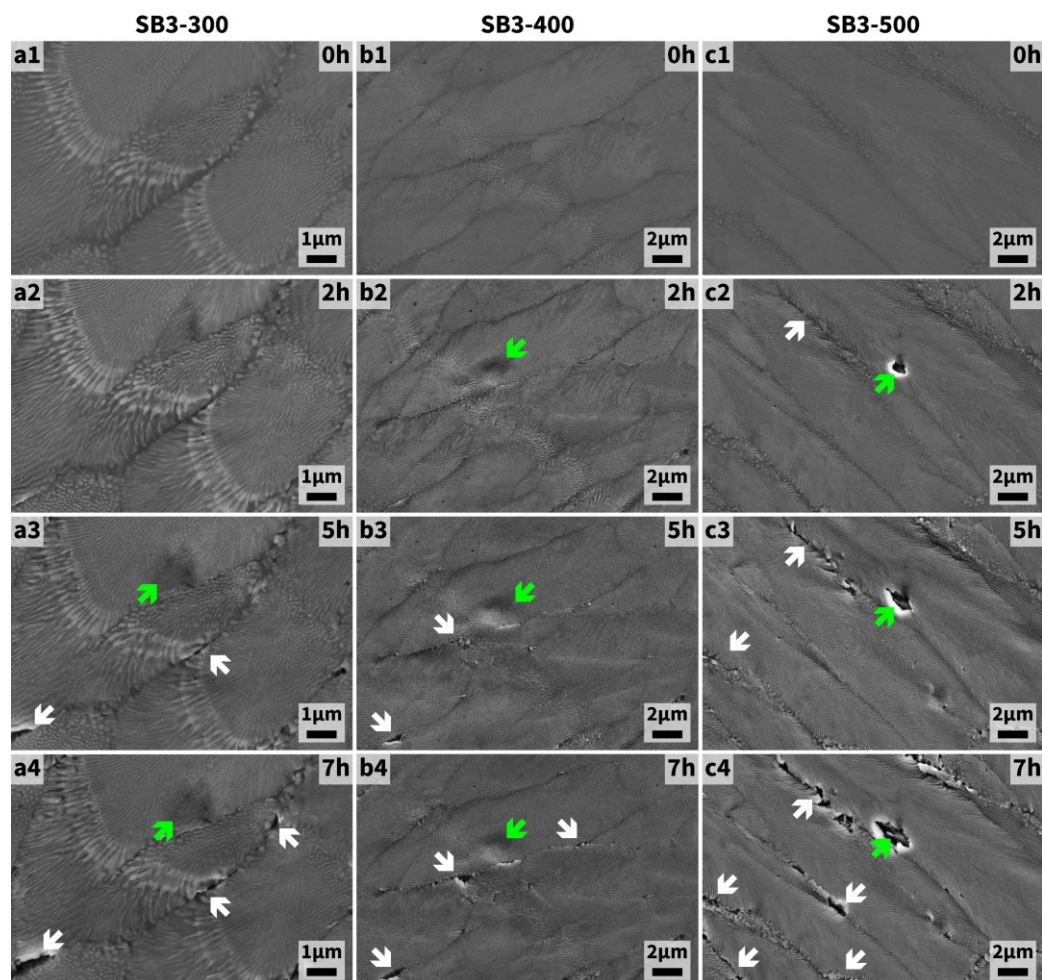


Fig. 7.12 – Microstructural evolution of the LSM MMCs with 30 vol.% Cr during cavitation erosion. a-c, the MMCs treated by 300-, 400-, and 500-W lasers, respectively. White arrows: Erosion at the boundary of the eutectic region; Green arrows: Deformation (a-b) and erosion (c) in the eutectic region.

Ni-rich matrix was eroded much more easily compared to the SB2-300 sample (**Fig. 7.11b3-c4**).

7.6.3 Specimens with 30 vol.% Cr

All the LSM Ni-30vol.%Cr-WC MMCs exhibited a dense distribution of the lamellar eutectic matrix, and the lamellar eutectic matrix was so resistant to cavitation impacts that it was fairly difficult to find the sign of erosion from the surface of these LSM MMCs (**Fig. 7.12**). In most cases, after the 7-h CE test, very slight erosion occurred at the boundary of the adjacent eutectic regions (**Fig. 7.12a-b**). The erosion inside the lamellar eutectic matrix was barely found (**Fig. 7.12c**).

7.6.4 Other microstructural features

The other microstructural features (the granular and the rosette-like precipitates) of the LSM NiCr-WC MMCs in response to cavitation impacts were presented in **Fig. 7.13** and they could not restrict CE effectively. The Ni-rich matrix surrounding the granular carbides could be easily eroded at the early stage of CE (**Fig. 7.13b1-b2**), and then the granular carbides were detached from the surface (**Fig. 7.13b3-b4**), causing severe erosion. For the large rosette-like carbides, many microcracks formed in the carbides at the beginning of CE test (**Fig. 7.13c1-c2**), resulting in the

subsequent erosion when the carbides were further exposed to cavitation impacts (Fig. 7.13c3-c4).

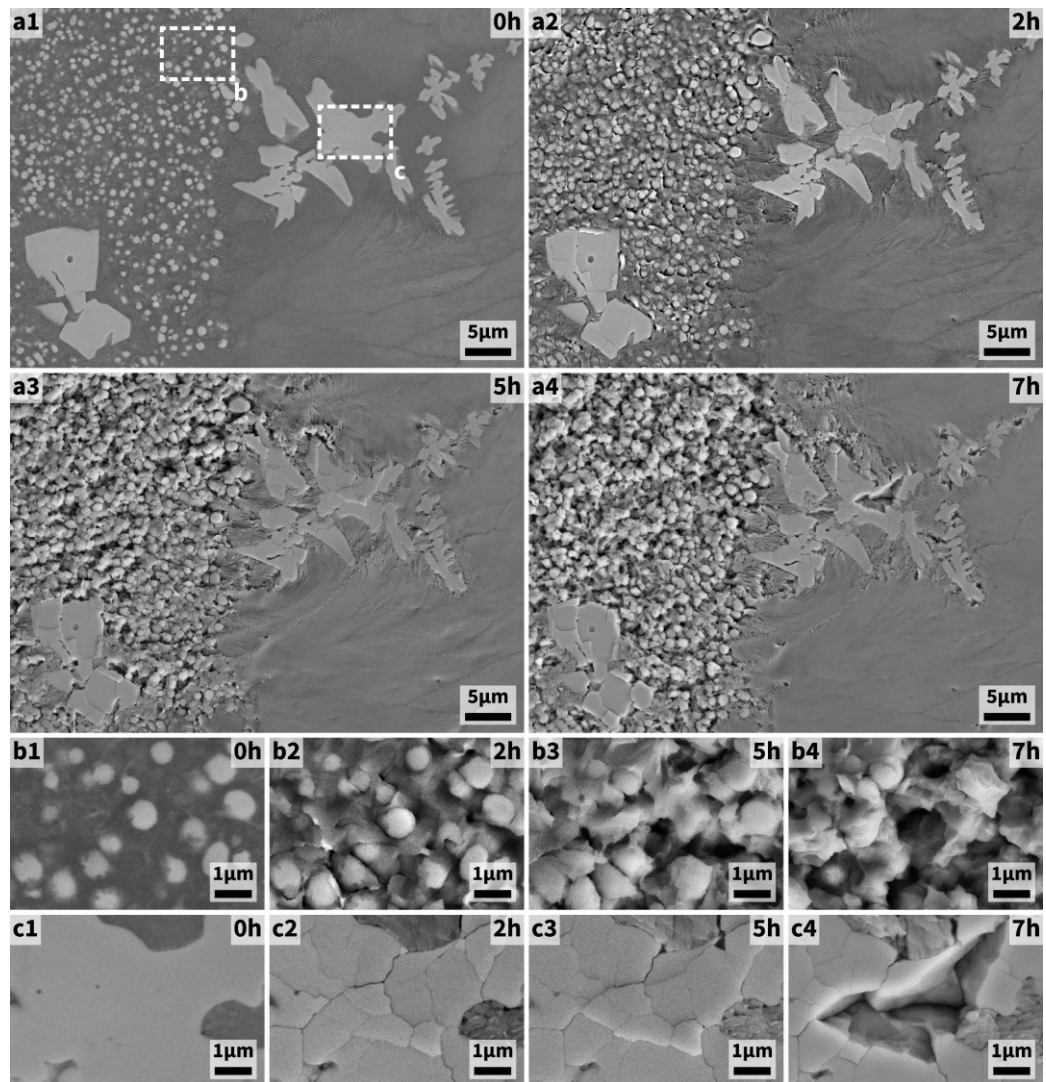


Fig. 7.13 – Microstructural evolution of the other interested features in the LSM NiCr-WC MMCs during cavitation erosion. a, Low-magnified SEM images showing the granular and the large rosette-like precipitates at the edge of the molten pool; **b,** Microstructural evolution of the small granular precipitates; **c,** Microstructural evolution of the large rosette-like precipitates.

7.6.5 Large pre-existing cracks

As mentioned previously, all the LSM NiCr-WC MMCs with 20 and 30 vol.% Cr had large cracks due to thermal shock or fast solidification of the

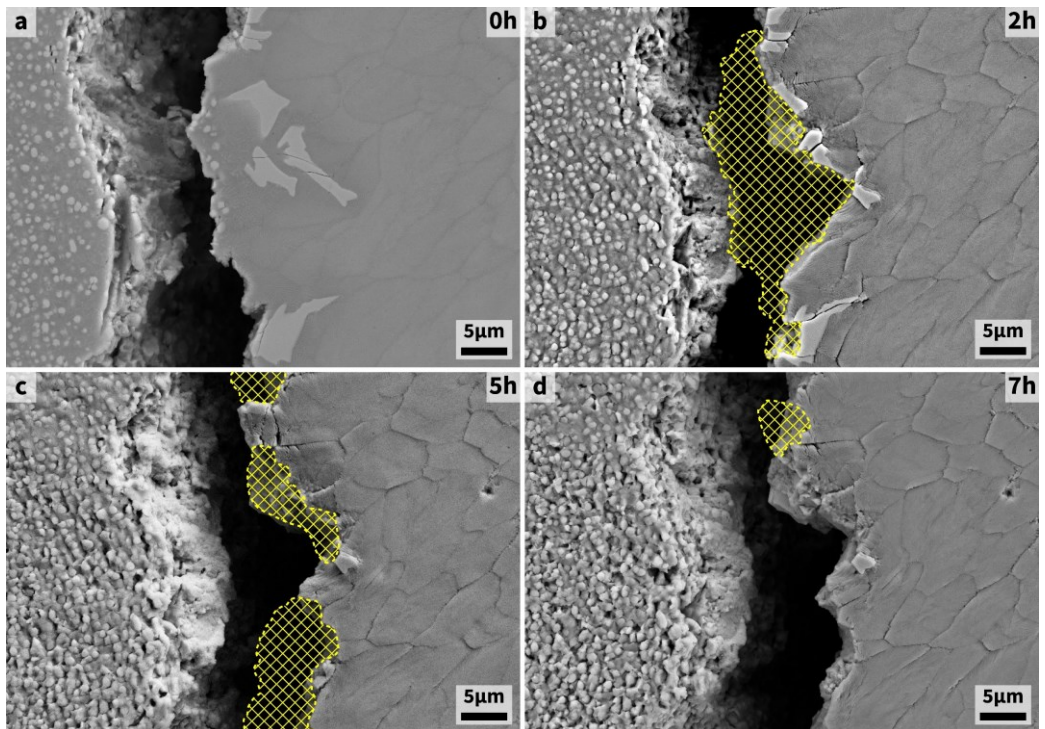


Fig. 7.14 – Microstructural evolution of the crack crossing the edge of the molten pool in the LSM NiCr-WC MMC during cavitation erosion. The yellow shaded regions highlight the eroded pieces.

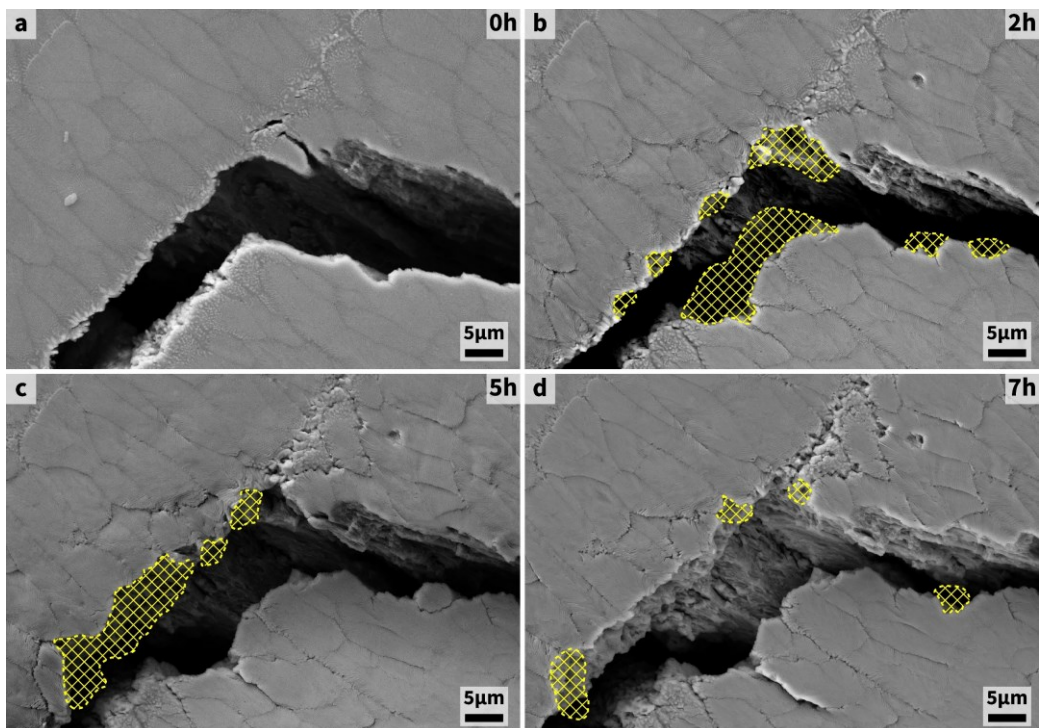


Fig. 7.15 – Microstructural evolution of the crack crossing the eutectic matrix in the LSM NiCr-WC MMC during cavitation erosion. The yellow shaded regions highlight the eroded pieces.

molten pool (**Fig. 7.6**). The material at the edge of the crack was susceptible to cavitation impacts regardless of which site the crack was located (**Fig. 7.14** and **Fig. 7.15**). However, it seemed that severe erosion only occurred at the early stage of CE, and fewer pieces of the materials at the crack eroded when the exposure to cavitation impacts was extended.

7.7 Discussion

7.7.1 Effect of Cr addition on the microstructure of LSM NiCr-WC

MMCs

The crystal structure of transition-metal carbides depends on the atomic structure of the metal [326]. Firstly, transition-metals can be sorted into strong and weak carbide formers based on the metal-carbon affinity determined by the number of the electrons in the d-orbital. Strong carbide formers tend to form a stable and closely packed structure with carbon and yield a metal-carbon ratio of 1:1, such as HCP WC. On the other hand, the binary carbide consisted of a weak carbide former can exhibit a more complex crystalline structure, such as trigonal M_3C formed by Fe, Co, and Ni. In addition, weak carbide formers have very low solubility in the carbides with strong carbide formers.

Secondly, the atomic radius of the transition-metal is related to the crystal

structure of transition-metal carbides. A binary carbide with the ratio of the carbon and the metal atom radii ranging from 0.41 to about 0.59 generally has a closely packed structure. When this ratio is greater than 0.59 (usually for the metal having a small atomic radius), a complex structure can form. For example, although Cr is a strong carbide former, it can form various complex carbides with different stoichiometries, such as Cr_3C_2 , Cr_7C_3 , and Cr_{23}C_6 . Meanwhile, the complex structure of the chromium carbide also allows the substitutional solubility of the weak carbide formers.

For the LSM NiCr-WC MMCs prepared in this work, Ni is the weak carbide former, while W and Cr are the strong carbide formers. However, W has a slightly stronger carbon affinity than Cr. When the Cr content is low, W dominates the crystal structure of the carbide, which is HCP. Nevertheless, Cr is a strong carbide former that can be substitutionally soluble in WC, while Ni cannot. Therefore, the carbides in the LSM Ni-10vol.%Cr-WC MMCs were the HCP with very few Ni and but a roughly equal atomic content of W and Cr. On the other hand, when the Cr content greatly exceeds the W content, Cr dominates and changes the carbide structure, which is ORH in this case. Since weak carbide formers exhibit a good substitutional solubility in the structure dominated by chromium carbide and the Ni content is significantly greater than the Cr and the W

contents in the LSM Ni-20/30vol.%Cr-WC, the ORH carbide was Ni-rich, but the content of Ni cannot exceed the total content of Cr and W.

7.7.2 Microstructure and cavitation erosion resistance

In **Section 7.6**, various microstructures of the LSM NiCr-WC MMCs in response to cavitation impacts were observed by SEM, showing that they had different CER. The hypoeutectic structure in the LSM Ni-10vol.%Cr-WC was very resistant to CE, and slip bands were found in the metal matrix (**Fig. 7.10**), which is similar to the hypoeutectic structure in the LSM Ni-WC MMCs (**Fig. 5.11**). However, the addition of Cr may improve the strength of the metal matrix, and thus severe erosion did not occur, which is different from the LSM Ni-WC MMCs. In addition, the work-hardening ability of the metal matrix may be improved by Cr, which allows the metal matrix taking more cavitation impacts before rupture. Hence, the LSM Ni-10vol.%Cr-WC MMCs had much lower CE (**Fig. 7.9**) than the LSM Ni-WC MMCs (**Fig. 5.9a**), even if they exhibited a similar hypoeutectic microstructure.

The LSM Ni-20vol.%Cr-WC MMCs showed two different microstructures, either the lamellar eutectic or the maze-like eutectic, depending on the laser power, but their CE behaviours were similar. The eutectic regions were free from CE, while the metal matrix outside the eutectic was eroded

(**Fig. 7.11**). The primary metal phase was divided by the eutectic regions, and each divided area was very small but still large enough to be subjected to cavitation impacts. As the volume of the divided primary metal matrix was small, very few dislocations or slip bands could form in the primary metal matrix. Hence, the energy by the cavitation impacts could not be effectively dissipated, resulting in the material ruptured from the primary metal matrix (**Fig. 7.11**).

The LSM Ni-30vol.%Cr-WC MMCs (**Fig. 7.12**) exhibit lamellar eutectic which had better CER than the hypoeutectic of the LSM Ni-10vol.%Cr-WC MMCs (**Fig. 7.10**) according to the SEM observation. However, the CE of the LSM Ni-30vol.%Cr-WC MMCs was higher than the LSM Ni-10vol.%Cr-WC MMCs (**Fig. 7.9**) because the granular and the rosette-like precipitates in the LSM Ni-30vol.%Cr-WC MMCs were not resistant to CE (**Fig. 7.13**). On the other hand, the cracks in the LSM Ni-30vol.%Cr-WC MMCs were susceptible to cavitation impacts, compromising the CER.

7.7.3 Ideal microstructure for resisting cavitation erosion

As mentioned before, the primary Ni-rich matrix in the LSM Ni-10vol.%Cr-WC MMCs (**Fig. 7.9**) was more resistant to CE compared to the primary Ni matrix in the LSM Ni-WC MMCs (**Fig. 5.9a**). However, it is predicted that the primary Ni-rich matrix will be eroded ultimately when it is exposed

to cavitation impacts for a sufficient time. Although the previous chapters suggested that the hierarchically layered carbide lamellae could confine the erosion of the metal matrix during CE and provide effective CER, the CER can be improved if the erosion of the metal matrix is minimised. This can be achieved by the lamellar eutectic structure in the LSM Ni-30vol.%Cr-WC MMCs (**Fig. 7.12**). Compared to the Ni-WC eutectic in the previous LSM Ni-WC MMCs, the Ni-carbide eutectic in the LSM NiCr-WC MMCs had much finer and more densely distributed carbide lamellae. As mentioned in **Chapter 6**, a dense distribution of fine carbide lamellae could further mitigate the transmitted tensile stress, providing good CER. Meanwhile, the addition of Cr may also enhance the strength of the metal matrix in the eutectic region. Therefore, the lamellar Ni-carbide eutectic in the LSM Ni-30vol.%Cr-WC MMCs is believed to be the most ideal microstructure for resisting CE among the others shown in this thesis. Nevertheless, there are two significant issues remained. Firstly, the Cr content needs to be optimised to minimise the large rosette-like carbides. Secondly, the cracks caused by the thermal shock and the fast solidification of the molten pool during the LSM process has to be controlled, which may be achieved by introducing other suitable alloying elements, changing the processing parameters of the LSM, or pre-heating the substrate to reduce the thermal stress in the LSM layer. In addition, it

seemed that the erosion preferentially occurred at the boundary of the adjacent lamellar eutectic regions. Eliminating these boundaries may also help improve CER.

7.8 Summary

- 1) The sintered NiCr-WC MMCs were post-treated by LSM using the lasers with 300, 400, and 500 W power, respectively. The microstructure of the LSM NiCr-WC MMCs depended on the content of Cr and the power of laser. The LSM Ni-10vol.%Cr-WC MMCs showed a hypoeutectic microstructure with hierarchically layered carbide lamellae that was similar to the LSM Ni-WC MMCs. The Ni-30vol.%Cr-WC MMCs exhibited lamellar Ni-carbide eutectic, and the lamellar carbides were much finer and more densely distributed compared to the WC lamellae in the LSM Ni-WC MMCs. The LSM Ni-20vol.%Cr-WC MMC treated by a 300-W laser also showed lamellar eutectic, while the LSM Ni-20vol.%Cr-WC MMCs treated by a laser with higher power had a maze-like eutectic.
- 2) The Cr content could affect the crystal structure of the carbides in the LSM NiCr-WC MMCs. At a low Cr content, the carbides were HCP consisted of W and Cr with roughly equal atomic content and very little Ni. When the Cr content increased, a portion of the carbides became

ORH composed of Ni, W, and Cr in a ratio of about 1:1:1 with a slightly higher Ni content. An exceeded Cr content could allow the formation of large rosette-like HCP/ORH carbides. In addition, the increasing Cr content could result in large cracks caused by thermal shock during the LSM process.

- 3) The lowest CE was found in the LSM Ni-10vol.%Cr-WC MMCs. However, SEM observation found that the lamellar metal-carbide eutectic in the LSM Ni-30vol.%Cr-WC MMCs was barely eroded. The higher CE of the LSM Ni-30vol.%Cr-WC MMCs was attributed to the large rosette-like carbides and the cracks. If these large rosette-like carbides and the cracks were minimised, the LSM Ni-30vol.%Cr-WC MMCs were expected to have the best CER. Meanwhile, the lamellar metal-carbide eutectic in the LSM Ni-30vol.%Cr-WC MMCs is believed to be the most ideal microstructure for resisting CE among the others presented in this thesis.

Chapter 8

Conclusions

In this thesis, several combinations of laser-surface-melted (LSM) WC-based metal matrix composites (MMCs) were successfully prepared, and these LSM MMCs remarkably outperformed the conventional thermal-sprayed WC-based coatings and 316L austenitic stainless steels (ASS) on cavitation erosion resistance (CER). **Appendix F** also provides a benchmark against other materials. Meanwhile, the behaviours of the microstructural features in these LSM MMCs were investigated by SEM observation, and the lamellar metal-carbide eutectic structure was considered the ideal microstructure for resisting cavitation erosion (CE). According to the results presented previously, the main conclusions are listed below.

- 1) **Effect of LSM process on the microstructure of the Ni-WC composites:** The LSM process changed the microstructure of the cold-sprayed Ni-WC coatings and the sintered Ni-WC MMCs into a hypoeutectic structure, which was consisted of primary Ni matrix and lamellar Ni-WC eutectic. The laminated arrangement of the WC grains in the LSM Ni-WC samples was likely attributed to the high energy input and the fast-cooling rate during the LSM process.

- 2) **CER of the LSM Ni-WC composites and its correlation to microstructure and mechanical properties:** The LSM Ni-WC samples showed outstanding CER which was much superior to 316L ASS and the conventional thermal-sprayed WC-based coatings. However, the experimental results in **Chapter 4** suggested that it was the microstructure rather than the mechanical properties responsible for the outstanding CER. The eutectic Ni-WC network with hierarchically interlocked WC lamellae could effectively inhibit the growth of microcracks and cavitation pits and confine the erosion of the primary metal matrix, providing a damage-controlling effect.
- 3) **Numerical simulations of the lamellar metal-carbide eutectic structure:** In **Sections 5.6** and **6.7**, numerical simulations were carried out to investigate the behaviour of the lamellar metal-carbide eutectic structure in response to a cavitation impact. Results showed that the lamellar metal-carbide eutectic structure could effectively reduce the stress and dissipate kinetic energy when being subjected to the cavitation impact. Furthermore, the eutectic structure with finer and more densely distributed lamellar carbides tended to have lower tensile stress.
- 4) **Effect of CeO₂ addition on the microstructure and the CER of the LSM Ni-WC-CeO₂ MMCs:** The addition of CeO₂ changed the

microstructure, refined the Ni grains, and enhanced the microhardness of the LSM Ni-WC-CeO₂ MMCs. However, the CeO₂ addition could not guarantee the improvement of CER. Despite of the enhanced microhardness, most of the LSM Ni-WC-CeO₂ MMCs had dispersedly distributed WC lamellae that could not provide effective resistance to CE. Only the Ni-WC-2.7wt.%CeO₂ treated by a 300-W laser (SA3-300 sample) exhibited the hypoeutectic structure with the lamellar metal-carbide eutectic. Meanwhile, the carbide lamellae were much finer and densely distributed in the SA3-300 sample, and the CER of the SA3-300 sample was better than the LSM CeO₂-free Ni-WC MMCs, which was in an agreement with the numerical simulation results.

- 5) **Effect of Cr addition on the microstructure and the CER of the LSM NiCr-WC MMCs:** The addition of Cr could change the crystal structure of the carbides of the LSM NiCr-WC MMCs. The volume of the carbide increased with the Cr content, which also affect the microstructure of the LSM NiCr-WC MMCs. The LSM NiCr-WC MMCs exhibited either a hypoeutectic structure similar to the LSM Ni-WC MMCs or a fully eutectic structure depending on the Cr content. Meanwhile, the addition of Cr significantly enhanced the CER of the LSM NiCr-WC MMCs, which was about 5-10 times higher than the LSM Ni-WC MMCs. The SEM observation suggested that the lamellar

eutectic with fine and densely distributed carbide lamellae, which was achieved by the LSM MMCs with the highest Cr content, maybe the most ideal microstructure for resisting CE among the others presented in this work. Nevertheless, high Cr content could result in the formation of the cracks by hot tearing and the large rosette-like carbides by the exceeded volume of the carbide forming element (Cr), which were susceptible to CE.

Chapter 9

Future work

- 1) The excellent CER of the LSM Ni-WC MMCs was mainly attributed to their microstructure: the eutectic Ni-WC networks with hierarchically interlocked WC lamellae. However, the microstructure was different from the laser-treated WC-based composites by a large laser spot reported in the literature. Therefore, it is necessary to investigate the solidification progress of the molten Ni-WC during the LSM process and find what conditions are required to achieve the microstructure.
- 2) The effect of the microstructure and distribution of WC lamellae on the CER of LSM Ni-WC-CeO₂ MMCs was investigated in this work. However, it is difficult to evaluate the effect of the Ni grain size based on the current results because the WC lamellae exhibited significant changes due to the addition of CeO₂. A lower content of CeO₂ (less than 0.5 wt.%) may refine the Ni grain without significantly changing the microstructure and distribution of WC lamellae, which may allow the evaluation of Ni grain size on the CER.
- 3) The lamellar metal-carbide eutectic in the LSM NiCr-WC MMCs showed even better CER than the LSM Ni-WC MMCs. However, the large rosette-like carbides and the cracks in the LSM NiCr-WC were

susceptible to CE. Hence, it can be very rewarding to eliminate these unwanted microstructural features. In addition, there is still some characterisation to be conducted on the LSM NiCr-WC. For example, the microstructure of the fine lamellar carbide needs to be characterised by transmission electron microscopy or transmission Kikuchi diffraction, obtaining more accurate and precise results.

- 4) Laser processing techniques may not be the most feasible techniques to process large-scaled components considering the cost and schedule. Hence, if the conditions to achieve the eutectic Ni-WC network presented in this study were confirmed, the exploration of other possible low-cost processing techniques would be beneficial. For example, either using large area electron beam surface melting or designing a series of heat-treatment processes could be applicable.
- 5) In corrosive environments, such as seawater and sewerage, the synergistic attack of CE and corrosion is one of the greatest concerns. Thus, it is worthwhile to evaluate the corrosion resistance of the LSM Ni(Cr)-WC-(CeO₂) MMCs presented in this work in the cavitating condition.
- 6) The LSM Ni(Cr)-WC-(CeO₂) MMCs may exhibit other promising properties. For example, they may have good fatigue resistance as some studies suggested there is a correlation between CE and fatigue

failure. Therefore, the other properties of the LSM Ni-WC MMCs are worthy of exploration, which may expand the potential application.

- 7) The addition of CeO₂ changed the microstructure of the LSM Ni-WC MMCs. Nevertheless, a further investigation on the mechanism may be required. For example, how the Ce atoms with different concentrations affect the solidification progress of Ni-WC and influence the morphology of the WC grains.
- 8) The LSM Ni(Cr)-WC-(CeO₂) MMCs presented in this study showed excellent CER. However, Ni and WC are quite costly compared to other engineering metals and ceramics. Hence, it is meaningful to seek low-cost substitutes for either or both.

References

- [1] G.L. Chahine, J.-P. Franc, A. Karimi, Cavitation and cavitation Erosion, in: K.-H. Kim, G. Chahine, J.-P. Franc, A. Karimi (Eds.), *Advanced Experimental and Numerical Techniques for Cavitation Erosion Prediction*, Springer Netherlands, Dordrecht, 2014, pp. 3-20.
- [2] C.E. Brennen, *Cavitation and Bubble Dynamics*, Cambridge University Press, Cambridge, 2013.
- [3] J.-P. Franc, J.-M. Michel, *Fundamentals of Cavitation*, Springer, Dordrecht, 2005.
- [4] University of Cambridge, *The Examinations for the Degree of Bachelor of Arts, Cambridge, January, 1847*, George Bell, London, 1847.
- [5] W.H. Besant, *A Treatise on Hydrostatics and Hydrodynamics*, Bell and Daldy, London, 1859.
- [6] O. Reynolds, Experiments showing the boiling of water in an open tube at ordinary temperatures, *Report of the Sixty-fourth Meeting of the British Association for the Advancement of Science Held at Oxford in August 1894* (1894) p. 564.
- [7] O. Reynolds, Experiments showing the boiling of water in an open tube at ordinary temperatures, in: *Papers on Mechanical and Physical Subjects*, Cambridge University Press, Cambridge, 1901, pp. 578-587.
- [8] J.I. Thornycroft, S.W. Barnaby, Torpedo-boat destroyers, *Minutes of Proceedings of the Institution of Civil Engineers* 122 (1895), pp. 51-69.
<https://doi.org/10.1680/imotp.1895.19695>
- [9] G. Cravotto, P. Cintas, Introduction to sonochemistry: A historical and conceptual overview, in: D. Chen, S.K. Sharma, A. Mudhoo (Eds.), *Handbook on Applications of Ultrasound: Sonochemistry for Sustainability*, CRC Press, Boca Raton, Florida, 2011, pp. 23-40.
- [10] Lord Rayleigh O.M. F.R.S., VIII. On the pressure developed in a liquid during the collapse of a spherical cavity, *The London, Edinburgh, and Dublin Philosophical Magazine and Journal of Science* 34(200) (1917), pp. 94-98.
<https://doi.org/10.1080/14786440808635681>
- [11] S.S. Cook, Erosion by water-hammer, *Proceedings of the Royal Society A: Mathematical, Physical and Engineering Sciences* 119(783) (1928) pp. 481-488.
<https://doi.org/10.1098/rspa.1928.0107>
- [12] M. Harrison, An experimental study of single bubble cavitation noise, *The Journal of the Acoustical Society of America* 24(6) (1952), pp. 776-782.
<https://doi.org/10.1121/1.1906978>
- [13] W. Güth, Zur Entstehung der Stoßwellen bet der Kavitation, *Acta*

- Acustica united with Acustica* 6(6) (1956), pp. 526-531.
- [14] M. Kornfeld, L. Suvorov, On the destructive action of cavitation, *Journal of Applied Physics* 15(6) (1944), pp. 495-506.
<https://doi.org/10.1063/1.1707461>
- [15] S.E. Shipilov, V.P. Yakubov, History of technical protection. 60 years in science: to the jubilee of Prof. V.F. Minin, *IOP Conference Series: Materials Science and Engineering* 363 (2018), Article 012033.
<https://doi.org/10.1088/1757-899x/363/1/012033>
- [16] M. Rattray, Jr., *Perturbation Effects in Cavitation Bubble Dynamics*, Ph.D. thesis, California Institute of Technology, 1951.
- [17] C.F. Naude', A.T. Ellis, On the mechanism of cavitation damage by nonhemispherical cavities collapsing in contact with a solid boundary, *Journal of Basic Engineering* 83(4) (1961), pp. 648-656.
<https://doi.org/10.1115/1.3662286>
- [18] P.P. Gohil, R.P. Saini, Coalesced effect of cavitation and silt erosion in hydro turbines – A review, *Renewable & Sustainable Energy Reviews* 33 (2014), pp. 280-289.
<https://doi.org/10.1016/j.rser.2014.01.075>
- [19] X. Liu, Y.Y. Luo, Z.W. Wang, A review on fatigue damage mechanism in hydro turbines, *Renewable and Sustainable Energy Reviews* 54 (2016), pp. 1-14.
<https://doi.org/10.1016/j.rser.2015.09.025>
- [20] B.K. Sreedhar, S.K. Albert, A.B. Pandit, Cavitation damage: Theory and measurements - A review, *Wear* 372 (2017), pp. 177-196.
<https://doi.org/10.1016/j.wear.2016.12.009>
- [21] A.A. Noon, M.H. Kim, Sediment and cavitation erosion in Francis turbines - Review of latest experimental and numerical techniques, *Energies* 14(6) (2021), Article 1516.
<https://doi.org/10.3390/en14061516>
- [22] R.E. Bensow, Numerical prediction of cavitation and related nuisances in marine propulsion systems, in: P. Koukouvini, M. Gavaises (Eds.), *Cavitation and Bubble Dynamics: Fundamentals and Applications*, Academic Press, 2021, pp. 111-132.
- [23] Brijkishore, R. Khare, V. Prasad, Prediction of cavitation and its mitigation techniques in hydraulic turbines – A review, *Ocean Engineering* 221 (2021), Article 108512.
<https://doi.org/10.1016/j.oceaneng.2020.108512>
- [24] *Hydropower Special Market Report*, International Energy Agency, 2021.
- [25] *International Energy Outlook 2016*, U.S. Energy Information Administration, 2016.
- [26] *Third IMO GHG Study 2014*, International Maritime Organization,

2015.

[27] S.W. Huang, M. Samandi, A. Brandt, Abrasive wear performance and microstructure of laser clad WC/Ni layers, *Wear* 256(11-12) (2004), pp. 1095-1105.

[https://doi.org/10.1016/s0043-1648\(03\)00526-x](https://doi.org/10.1016/s0043-1648(03)00526-x)

[28] Y. Iwabuchi, S. Sawada, Metallurgical characteristics of a large hydraulic runner casting of type 13Cr-Ni stainless steel, in: V.G. Behal, A.S. Melilli (Eds.), *ASTM STP-756 Stainless Steel Castings*, American Society for Testing and Materials, Philadelphia, Pennsylvania, 1982, pp. 332-354.

[29] A. Kjølle, *Hydropower in Norway*, 2001.

[30] R. Singh, S.K. Tiwari, S.K. Mishra, Cavitation erosion in hydraulic turbine components and mitigation by coatings: current status and future needs, *Journal of Materials Engineering and Performance* 21(7) (2012), pp. 1539-1551.

<https://doi.org/10.1007/s11665-011-0051-9>

[31] R.K. Kumar, S. Seetharamu, M. Kamaraj, Quantitative evaluation of 3D surface roughness parameters during cavitation exposure of 16Cr–5Ni hydro turbine steel, *Wear* 320 (2014), pp. 16-24.

<https://doi.org/10.1016/j.wear.2014.07.015>

[32] W.L. Williams, Aluminum bronzes for marine applications, *Journal of the American Society for Naval Engineers* 69(3) (1957), pp. 453-461.

<https://doi.org/10.1111/j.1559-3584.1957.tb03218.x>

[33] J.N. Bradley, Recent developments in copper-base alloys for naval marine applications, *International Metallurgical Reviews* 17(1) (1972), pp. 81-99.

<https://doi.org/10.1179/imt1r.1972.17.1.81>

[34] T. Yoshikawa, C. Schneider, Anti-erosion materials for hydroturbine (A research report at the Three-Gorges Dam hydropower plant), *Turbomachinery* 28(10) (2000), pp. 577-581.

<https://doi.org/10.11458/tsj1973.28.577>

[35] G. Prashar, H. Vasudev, L. Thakur, Performance of different coating materials against slurry erosion failure in hydrodynamic turbines: A review, *Engineering Failure Analysis* 115 (2020), Article 104622.

<https://doi.org/10.1016/j.engfailanal.2020.104622>

[36] GlobleCore, Hydrodynamic cavitation and its application in the fuel industry (2019). [Online] (Accessed on Dec. 16, 2021)

<https://globecore.co.za/hydrodynamic-cavitation-and-its-application-in-the-fuel-industry/>

[37] O. Supponen, P. Kobel, D. Obreschkow, M. Farhat, The inner world of a collapsing bubble, *Physics of Fluids* 27(9) (2015), Article 091113.

<https://doi.org/10.1063/1.4931098>

- [38] T.J. Mason, J.P. Lorimer, *Applied Sonochemistry: Uses of Power Ultrasound in Chemistry and Processing*, Wiley-VCH, Weinheim, 2002.
- [39] Y.T. Shah, A.B. Pandit, V.S. Moholkar, Sources and types of cavitation, in: *Cavitation Reaction Engineering*, Springer, Boston, MA, 1999, pp. 1-14.
- [40] A.V. Mahulkar, P.S. Bapat, A.B. Pandit, F.M. Lewis, Steam bubble cavitation, *AIChE Journal* 54(7) (2008), pp. 1711-1724.
<https://doi.org/10.1002/aic.11509>
- [41] M.M. Grant, P.A. Lush, Liquid impact on a bilinear elastic-plastic solid and its role in cavitation erosion, *Journal of Fluid Mechanics* 176 (1987), pp. 237-252.
<https://doi.org/10.1017/S0022112087000648>
- [42] G.M. Wood, L.K. Knudsen, F.G. Hammitt, Cavitation damage studies with rotating disk in water, *Journal of Basic Engineering* 89(1) (1967), pp. 98-109.
<https://doi.org/10.1115/1.3609577>
- [43] H.S. Chen, J.D. Wang, Y.J. Li, D.R. Chen, Effect of hydrodynamic pressures near solid surfaces in the incubation stage of cavitation erosion, *Proceedings of the Institution of Mechanical Engineers Part J-Journal of Engineering Tribology* 222(J4) (2008), pp. 523-531.
<https://doi.org/10.1243/13506501jet384>
- [44] I. Tzanakis, D.G. Eskin, A. Georgoulas, D.K. Fytanidis, Incubation pit analysis and calculation of the hydrodynamic impact pressure from the implosion of an acoustic cavitation bubble, *Ultrasonics Sonochemistry* 21(2) (2014), pp. 866-878.
<https://doi.org/10.1016/j.ultsonch.2013.10.003>
- [45] F. Reuter, C.-D. Ohl, Nonspherical collapse of single bubbles near boundaries and in confined spaces, in: P. Koukouvinis, M. Gavaises (Eds.), *Cavitation and Bubble Dynamics: Fundamentals and Applications*, Academic Press, 2021, pp. 37-72.
- [46] E.B. Flint, K.S. Suslick, The temperature of cavitation, *Science* 253(5026) (1991), pp. 1397-1399.
<https://doi.org/10.1126/science.253.5026.1397>
- [47] C. Haosheng, L. Yongjian, C. Darong, W. Jiadao, Experimental and numerical investigations on development of cavitation erosion pits on solid surface, *Tribology Letters* 26(2) (2007), pp. 153-159.
<https://doi.org/10.1007/s11249-006-9188-3>
- [48] D. Heath, B. Širok, M. Hocevar, B. Pečnik, The use of the cavitation effect in the mitigation of CaCO₃ deposits, *2013* 59(4) (2013), pp. 203-215.
<https://doi.org/10.5545/sv-jme.2012.732>
- [49] C.E. Brennen, Bubble dynamics, damage and noise, in:

Hydrodynamics of Pumps, Cambridge University Press, New York, 2011, pp. 78-88.

[50] E. Axdahl, Cavitation Propeller Damage.JPG --- Wikimedia Commons, the free media repository (2006). [Online] (Accessed on Mar. 8, 2022)

https://commons.wikimedia.org/w/index.php?title=File:Cavitation_Propeller_Damage.JPG&oldid=491576019

[51] PES Solutions, PES-201: Boat Propeller Cavitation And Repair (2014). [Online] (Accessed on Mar. 8, 2022)

<http://blog.pes-solutions.com/boat-propeller-cavitation-and-repair-pes-201/>

[52] Y. Utturkar, S. Thakur, W. Shyy, Computational modeling of thermodynamic effects in cryogenic cavitation, at: *43rd AIAA Aerospace Sciences Meeting and Exhibit* (2005). <https://doi.org/10.2514/6.2005-1286>

[53] J. Casciani-Wood, An introduction to propeller cavitation (2015). [Online] (Accessed on Dec. 16, 2021)

<https://www.iims.org.uk/introduction-propeller-cavitation/>

[54] Maritime Research Institute Netherlands, Marine Cavitation (2017). [Online] (Accessed on Mar. 9, 2022)

<https://www.youtube.com/watch?v=gRNVZva6doM>

[55] CNU FINCL, Cavitation on a hydrofoil (2020). [Online] (Accessed on Mar. 9, 2022)

<https://www.youtube.com/watch?v=i6HRMILBtiU>

[56] The Maritime Executive, Moving ahead powerfully with cutting-edge simulation (2017). [Online] (Accessed on Mar. 9, 2022)

<https://www.maritime-executive.com/features/moving-ahead-powerfully-with-cutting-edge-simulation>

[57] T.J.C. van Terwisga, M. van Rijsbergen, E. van Wijngaarden, J. Bosschers, S. Schenke, T. Melissaris, Cavitation nuisance in ship propulsion: A review of developments, in: P. Koukouvini, M. Gavaises (Eds.), *Cavitation and Bubble Dynamics: Fundamentals and Applications*, Academic Press, 2021, pp. 73-109.

[58] G. Bark, R.E. Bensow, Hydrodynamic Processes Controlling Cavitation Erosion, in: K.-H. Kim, G. Chahine, J.-P. Franc, A. Karimi (Eds.), *Advanced Experimental and Numerical Techniques for Cavitation Erosion Prediction*, Springer Netherlands, Dordrecht, 2014, pp. 185-220.

[59] P.F. Pelz, T. Keil, G. Ludwig, On the Kinematics of Sheet and Cloud Cavitation and Related Erosion, in: K.-H. Kim, G. Chahine, J.-P. Franc, A. Karimi (Eds.), *Advanced Experimental and Numerical Techniques for Cavitation Erosion Prediction*, Springer Netherlands, Dordrecht, 2014, pp. 221-237.

[60] H.J. Amarendra, G.P. Chaudhari, S.K. Nath, Synergy of cavitation and

slurry erosion in the slurry pot tester, *Wear* 290 (2012), pp. 25-31.

<https://doi.org/10.1016/j.wear.2012.05.025>

[61] J.J. Lian, W.J. Gou, H.P. Li, H. Zhang, Effect of sediment size on damage caused by cavitation erosion and abrasive wear in sediment-water mixture, *Wear* 398 (2018), pp. 201-208.

<https://doi.org/10.1016/j.wear.2017.12.010>

[62] J. Basumatary, M. Nie, R.J.K. Wood, The synergistic effects of cavitation erosion–corrosion in ship propeller materials, *Journal of Bio-and Tribo-Corrosion* 1 (2015), Article 12.

<https://doi.org/10.1007/s40735-015-0012-1>

[63] J. Basumatary, R.J.K. Wood, Synergistic effects of cavitation erosion and corrosion for nickel aluminium bronze with oxide film in 3.5% NaCl solution, *Wear* 376 (2017), pp. 1286-1297.

<https://doi.org/10.1016/j.wear.2017.01.047>

[64] J. Basumatary, R.J.K. Wood, Different methods of measuring synergy between cavitation erosion and corrosion for nickel aluminium bronze in 3.5% NaCl solution, *Tribology International* 147 (2017), Article 104843.

<https://doi.org/10.1016/j.triboint.2017.08.006>

[65] J. Ryl, K. Darowicki, P. Slepski, Evaluation of cavitation erosion-corrosion degradation of mild steel by means of dynamic impedance spectroscopy in galvanostatic mode, *Corrosion Science* 53(5) (2011), pp. 1873-1879.

<https://doi.org/10.1016/j.corsci.2011.02.004>

[66] D.M. Garcia-Garcia, J. Garcia-Anton, A. Igual-Munoz, E. Blasco-Tamarit, Effect of cavitation on the corrosion behaviour of welded and non-welded duplex stainless steel in aqueous LiBr solutions, *Corrosion Science* 48(9) (2006), pp. 2380-2405.

<https://doi.org/10.1016/j.corsci.2005.09.009>

[67] A.R. Mayer, K. Bertuol, I. Siqueira, A. Chicowski, R.F. Vaz, M.J. de Sousa, A.G.M. Pukasiewicz, Evaluation of cavitation/corrosion synergy of the Cr₃C₂-25NiCr coating deposited by HVOF process, *Ultrasonics Sonochemistry* 69 (2020), Article 105271.

<https://doi.org/10.1016/j.ultsonch.2020.105271>

[68] Q.N. Song, Y. Tong, N. Xu, S.Y. Sun, H.L. Li, Y.F. Bao, Y.F. Jiang, Z.B. Wang, Y.X. Qiao, Synergistic effect between cavitation erosion and corrosion for various copper alloys in sulphide-containing 3.5% NaCl solutions, *Wear* 450-451 (2020), Article 203258.

<https://doi.org/10.1016/j.wear.2020.203258>

[69] J. Yang, Z.B. Wang, Y.X. Qiao, Y.G. Zheng, Synergistic effects of deposits and sulfate reducing bacteria on the corrosion of carbon steel, *Corrosion Science* 199 (2022), Article 110210.

<https://doi.org/10.1016/j.corsci.2022.110210>

- [70] S. Hong, Y.P. Wu, J.F. Zhang, Y.G. Zheng, Y.J. Qin, J.R. Lin, Effect of ultrasonic cavitation erosion on corrosion behavior of high-velocity oxygen-fuel (HVOF) sprayed near-nanostructured WC-10Co-4Cr coating, *Ultrasonics Sonochemistry* 27 (2015), pp. 374-378.
<https://doi.org/10.1016/j.ultsonch.2015.06.006>
- [71] ASTM G32-16(2021)e1, Standard test method for cavitation erosion using vibratory apparatus, American Society for Testing and Materials International, West Conshohocken, Pennsylvania, United States, 2021.
- [72] ASTM G73-10(2017), Standard test method for liquid impingement erosion using rotating apparatus, American Society for Testing and Materials International, West Conshohocken, Pennsylvania, United States, 2017.
- [73] ASTM G134-17, Standard test method for erosion of solid materials by cavitating liquid jet, American Society for Testing and Materials International, West Conshohocken, Pennsylvania, United States, 2017.
- [74] M.S. Plesset, Temperature effects in cavitation damage, *Journal of Basic Engineering* 94(3) (1972), pp. 559-563.
<https://doi.org/10.1115/1.3425484>
- [75] F.G. Hammitt, D.O. Rogers, Effects of pressure and temperature variation in vibratory cavitation damage test, *Journal of Mechanical Engineering Science* 12(6) (1970), pp. 432-439.
https://doi.org/10.1243/jmes_jour_1970_012_072_02
- [76] C.T. Kwok, H.C. Man, L.K. Leung, Effect of temperature, pH and sulphide on the cavitation erosion behaviour of super duplex stainless steel, *Wear* 211(1) (1997), pp. 84-93.
[https://doi.org/10.1016/s0043-1648\(97\)00072-0](https://doi.org/10.1016/s0043-1648(97)00072-0)
- [77] Z. Li, J.S. Han, J.J. Lu, J.S. Zhou, J.M. Chen, Vibratory cavitation erosion behavior of AISI 304 stainless steel in water at elevated temperatures, *Wear* 321 (2014), pp. 33-37.
<https://doi.org/10.1016/j.wear.2014.09.012>
- [78] V. Cojocar, V.C. Campian, D. Frunzaverde, A comparative analysis of the methods used for testing the cavitation erosion resistance on the vibratory devices, *University Politehnica of Bucharest Scientific Bulletin: Series D* 77(4) (2015), pp. 257-262.
- [79] J. Mago, S. Bansal, D. Gupta, V. Jain, Investigation of erosion and pressure for direct and indirect acoustic cavitation testing, *Journal of Emerging Technologies and Innovative Research* 6(5) (2019), pp. 468-476.
- [80] Y. Tian, H. Zhao, R. Yang, X. Liu, X. Chen, J. Qin, A. McDonald, H. Li, *In-situ* SEM investigation on stress-induced microstructure evolution of austenitic stainless steels subjected to cavitation erosion and cavitation erosion-corrosion, *Materials & Design* 213 (2022), Article 110314.

<https://doi.org/10.1016/j.matdes.2021.110314>

[81] H. Soyama, C.R. Chighizola, M.R. Hill, Effect of compressive residual stress introduced by cavitation peening and shot peening on the improvement of fatigue strength of stainless steel, *Journal of Materials Processing Technology* 288 (2021), Article 116877.

<https://doi.org/10.1016/j.jmatprotec.2020.116877>

[82] H. Soyama, Comparison between the improvements made to the fatigue strength of stainless steel by cavitation peening, water jet peening, shot peening and laser peening, *Journal of Materials Processing Technology* 269 (2019), pp. 65-78.

<https://doi.org/10.1016/j.jmatprotec.2019.01.030>

[83] K. Takahashi, H. Osedo, T. Suzuki, S. Fukuda, Fatigue strength improvement of an aluminum alloy with a crack-like surface defect using shot peening and cavitation peening, *Engineering Fracture Mechanics* 193 (2018), pp. 151-161.

<https://doi.org/10.1016/j.engfracmech.2018.02.013>

[84] D. Odhiambo, H. Soyama, Cavitation shotless peening for improvement of fatigue strength of carbonized steel, *International Journal of Fatigue* 25(9-11) (2003), pp. 1217-1222.

[https://doi.org/10.1016/s0142-1123\(03\)00121-x](https://doi.org/10.1016/s0142-1123(03)00121-x)

[85] R.F. Patella, J.L. Reboud, A. Archer, Cavitation damage measurement by 3D laser profilometry, *Wear* 246(1-2) (2000), pp. 59-67.

[https://doi.org/10.1016/s0043-1648\(00\)00446-4](https://doi.org/10.1016/s0043-1648(00)00446-4)

[86] A. Jayaprakash, J.K. Choi, G.L. Chahine, F. Martin, M. Donnelly, J.P. Franc, A. Karimi, Scaling study of cavitation pitting from cavitating jets and ultrasonic horns, *Wear* 296(1-2) (2012), pp. 619-629.

<https://doi.org/10.1016/j.wear.2012.07.025>

[87] J.P. Franc, M. Riondet, A. Karimi, G.L. Chahine, Material and velocity effects on cavitation erosion pitting, *Wear* 274 (2012), pp. 248-259.

<https://doi.org/10.1016/j.wear.2011.09.006>

[88] D. Carnelli, A. Karimi, J.P. Franc, Evaluation of the hydrodynamic pressure of cavitation impacts from stress-strain analysis and geometry of individual pits, *Wear* 289 (2012), pp. 104-111.

<https://doi.org/10.1016/j.wear.2012.04.009>

[89] B. Belahadji, J.P. Franc, J.M. Michel, A statistical analysis of cavitation erosion pits, *Journal of Fluids Engineering* 113(4) (1991), pp. 700-706.

<https://doi.org/10.1115/1.2926539>

[90] G.G.A. Fatjo, M. Hadfield, C. Vieillard, J. Sekulic, Early stage cavitation erosion within ceramics-An experimental investigation, *Ceramics International* 35(8) (2009), pp. 3301-3312.

<https://doi.org/10.1016/j.ceramint.2009.05.020>

[91] S.M. Ahmed, K. Hokkirigawa, Y. Ito, R. Oba, Y. Matsudaira, Scanning

electron-microscopy observation on the incubation period of vibratory cavitation erosion, *Wear* 142(2) (1991), pp. 303-314.

[https://doi.org/10.1016/0043-1648\(91\)90171-p](https://doi.org/10.1016/0043-1648(91)90171-p)

[92] J.-P. Franc, G.L. Chahine, A. Karimi, Pitting and Incubation Period, in: K.-H. Kim, G. Chahine, J.-P. Franc, A. Karimi (Eds.), *Advanced Experimental and Numerical Techniques for Cavitation Erosion Prediction*, Springer Netherlands, Dordrecht, 2014, pp. 37-69.

[93] G.L. Chahine, J.-P. Franc, A. Karimi, Mass Loss and Advanced Periods of Erosion, in: K.-H. Kim, G. Chahine, J.-P. Franc, A. Karimi (Eds.), *Advanced Experimental and Numerical Techniques for Cavitation Erosion Prediction*, Springer Netherlands, Dordrecht, 2014, pp. 97-121.

[94] R. Garcia, F.G. Hammitt, Cavitation damage and correlations with material and fluid properties, *Journal of Basic Engineering* 89(4) (1967), pp. 753-763.

<https://doi.org/10.1115/1.3609699>

[95] P.V. Rao, C.S. Martin, B.C.S. Rao, N.S.L. Rao, Estimation of cavitation erosion with incubation periods and material properties, *Journal of Testing and Evaluation* 9(3) (1981), pp. 189-197.

<https://doi.org/10.1520/JTE11555J>

[96] A. Thiruvengadam, S. Waring, Mechanical properties of metals and their cavitation-damage resistance, *Journal of Ship Research* 10(1) (1966), pp. 1-9.

<https://doi.org/10.5957/jsr.1966.10.1.1>

[97] R.H. Richman, W.P. McNaughton, Correlation of cavitation erosion behavior with mechanical-properties of metals, *Wear* 140(1) (1990), pp. 63-82.

[https://doi.org/10.1016/0043-1648\(90\)90122-q](https://doi.org/10.1016/0043-1648(90)90122-q)

[98] S.D. Washko, G. Aggen, Wrought Stainless Steels, in: ASM Handbook Committee (Ed.) *ASM Handbook Volume 1: Properties and Selection: Irons, Steels, and High-Performance Alloys*, ASM International, 1990, pp. 841-907.

[99] M. Mokhtabad Amrei, Y. Verreman, F. Bridier, D. Thibault, P. Bocher, Microstructure characterization of single and multipass 13Cr4Ni steel welded joints, *Metallography, Microstructure, and Analysis* 4(3) (2015), pp. 207-218.

<https://doi.org/10.1007/s13632-015-0202-8>

[100] S. Verma, P. Dubey, A.W. Selokar, D.K. Dwivedi, R. Chandra, Cavitation erosion behavior of nitrogen ion implanted 13Cr4Ni steel, *Transactions of the Indian Institute of Metals* 70(4) (2017), pp. 957-965.

<https://doi.org/10.1007/s12666-016-0887-7>

[101] B. Kishor, G.P. Chaudhari, S.K. Nath, Cavitation erosion of thermomechanically processed 13/4 martensitic stainless steel, *Wear*

319(1-2) (2014), pp. 150-159.

<https://doi.org/10.1016/j.wear.2014.07.024>

[102] Y.Y. Song, D.H. Ping, F.X. Yin, X.Y. Li, Y.Y. Li, Microstructural evolution and low temperature impact toughness of a Fe-13%Cr-4%Ni-Mo martensitic stainless steel, *Materials Science and Engineering: A* 527(3) (2010), pp. 614-618.

<https://doi.org/10.1016/j.msea.2009.08.022>

[103] C.J. Heathcock, B.E. Protheroe, A. Ball, Cavitation erosion of stainless-steels, *Wear* 81(2) (1982), pp. 311-327.

[https://doi.org/10.1016/0043-1648\(82\)90278-2](https://doi.org/10.1016/0043-1648(82)90278-2)

[104] S. Hattori, R. Ishikura, Revision of cavitation erosion database and analysis of stainless steel data, *Wear* 268(1-2) (2010), pp. 109-116.

<https://doi.org/10.1016/j.wear.2009.07.005>

[105] L.L. Santos, R.P. Cardoso, S.F. Brunatto, Direct correlation between martensitic transformation and incubation-acceleration transition in solution-treated AISI 304 austenitic stainless steel cavitation, *Wear* 462 (2020), Article 203522.

<https://doi.org/10.1016/j.wear.2020.203522>

[106] L.M. Zhang, Z.X. Li, J.X. Hu, A.L. Ma, S. Zhang, E.F. Daniel, A.J. Umoh, H.X. Hu, Y.G. Zheng, Understanding the roles of deformation-induced martensite of 304 stainless steel in different stages of cavitation erosion, *Tribology International* 155 (2021), Article 106752.

<https://doi.org/10.1016/j.triboint.2020.106752>

[107] M.C. Park, K.N. Kim, G.S. Shin, S.J. Kim, Effects of strain induced martensitic transformation on the cavitation erosion resistance and incubation time of Fe-Cr-Ni-C alloys, *Wear* 274 (2012), pp. 28-33.

<https://doi.org/10.1016/j.wear.2011.08.011>

[108] G. Gao, Z. Zhang, Cavitation erosion behavior of 316L stainless steel, *Tribology Letters* 67(4) (2019), Article 112.

<https://doi.org/10.1007/s11249-019-1225-0>

[109] M.C. Park, K.N. Kim, G.S. Shin, J.Y. Yun, M.H. Shin, S.J. Kim, Effects of Ni and Mn on the Cavitation Erosion Resistance of Fe-Cr-C-Ni/Mn Austenitic Alloys, *Tribology Letters* 52(3) (2013), pp. 477-484.

<https://doi.org/10.1007/s11249-013-0231-x>

[110] M.C. Park, G.S. Shin, J.Y. Yun, J.H. Heo, D.I. Kim, S.J. Kim, Damage mechanism of cavitation erosion in austenite → martensite phase transformable Fe-Cr-C-Mn/Ni alloys, *Wear* 310(1-2) (2014), pp. 27-32.

<https://doi.org/10.1016/j.wear.2013.12.015>

[111] K.Y. Wang, K.H. Lo, C.T. Kwok, M.M. Wong, I.W. Long, W.J. Ai, The Influences of Martensitic Transformations on Cavitation-Erosion Damage Initiation and Pitting Resistance of a Lean Austenitic Stainless Steel, *Materials Research-Ibero-American Journal of Materials* 19(6) (2016), pp.

1366-1371.

<https://doi.org/10.1590/1980-5373-mr-2015-0409>

[112] Z.X. Li, L.M. Zhang, Udoh, II, A.L. Ma, Y.G. Zheng, Deformation-induced martensite in 304 stainless steel during cavitation erosion: Effect on passive film stability and the interaction between cavitation erosion and corrosion, *Tribology International* 167 (2022), Article 107422.

<https://doi.org/10.1016/j.triboint.2021.107422>

[113] BS EN 10088-1:2014, Stainless steels Part 1: List of stainless steels (British Standard), 2014.

[114] A. Karimi, Cavitation erosion of a duplex stainless-steel, *Materials Science and Engineering* 86 (1987), pp. 191-203.

[https://doi.org/10.1016/0025-5416\(87\)90452-6](https://doi.org/10.1016/0025-5416(87)90452-6)

[115] W. Liu, Y.G. Zheng, C.S. Liu, Z.M. Yao, W. Ke, Cavitation erosion behavior of Cr-Mn-N stainless steels in comparison with 0Cr13Ni5Mo stainless steel, *Wear* 254(7-8) (2003), pp. 713-722.

[https://doi.org/10.1016/s0043-1648\(03\)00128-5](https://doi.org/10.1016/s0043-1648(03)00128-5)

[116] S. Luo, H. Jing, Y. Zheng, Z. Yao, W. Ke, Cavitation-corrosion behavior of CrMnN duplex stainless steel, *Journal of Chinese Society of Corrosion and Protection* 23(5) (2003), pp. 276-281.

[117] J.F. Grubb, T. DeBold, J.D. Fritz, Corrosion of Wrought Stainless Steels, in: S.D. Cramer, B.S. Covino, Jr. (Eds.), *ASM Handbook Volume 13B: Corrosion: Materials*, ASM International, 2005, pp. 54-77.

[118] C.T. Kwok, H.C. Man, F.T. Cheng, Cavitation erosion of duplex and super duplex stainless steels, *Scripta Materialia* 39(9) (1998), pp. 1229-1236.

[https://doi.org/10.1016/s1359-6462\(98\)00308-x](https://doi.org/10.1016/s1359-6462(98)00308-x)

[119] S. Kim, H.-S. Heo, Electrochemical and cavitation-erosion characteristics of duplex stainless steels in seawater environment, *Corrosion Science and Technology* 20(6) (2021), pp. 466-474.

<https://doi.org/10.14773/cst.2021.20.6.466>

[120] A. Al-Hashem, W. Riad, The effect of duplex stainless steel microstructure on its cavitation morphology in seawater, *Materials Characterization* 47(5) (2001), pp. 389-395.

[https://doi.org/10.1016/s1044-5803\(02\)00186-9](https://doi.org/10.1016/s1044-5803(02)00186-9)

[121] S. Saravanan, K. Raghukandan, N. Sivagurumanikandan, Pulsed Nd: YAG laser welding and subsequent post-weld heat treatment on super duplex stainless steel, *Journal of Manufacturing Processes* 25 (2017), pp. 284-289.

<https://doi.org/10.1016/j.jmapro.2016.12.015>

[122] Z.Y. Zhang, H. Zhao, H.Z. Zhang, J. Hu, J.R. Jin, Microstructure evolution and pitting corrosion behavior of UNS S32750 super duplex stainless steel welds after short-time heat treatment, *Corrosion Science*

121 (2017), pp. 22-31.

<https://doi.org/10.1016/j.corsci.2017.02.006>

[123] I. Richardson, *Guide to Nickel Aluminium Bronze for Engineers*, Copper Development Association, 2016.

[124] BS EN 12165:2016, Copper and copper alloys. Wrought and unwrought forging stock (British Standard), 2016.

[125] F. Hasan, A. Jahanafrooz, G.W. Lorimer, N. Ridley, The morphology, crystallography, and chemistry of phases in as-cast nickel-aluminum bronze, *Metallurgical Transactions: A* 13(8) (1982), pp. 1337-1345.

<https://doi.org/10.1007/bf02642870>

[126] E.A. Culpán, G. Rose, Microstructural characterization of cast nickel aluminum bronze, *Journal of Materials Science* 13(8) (1978), pp. 1647-1657.

<https://doi.org/10.1007/bf00548728>

[127] F. Hasan, J. Iqbal, N. Ridley, Microstructure of as-cast aluminium bronze containing iron, *Materials Science and Technology* 1(4) (1985), pp. 312-315.

<https://doi.org/10.1179/mst.1985.1.4.312>

[128] G.W. Lorimer, F. Hasan, J. Iqbal, N. Ridley, Observation of microstructure and corrosion behaviour of some aluminium bronzes, *British Corrosion Journal* 21(4) (1986), pp. 244-248.

<https://doi.org/10.1179/000705986798272046>

[129] R.S. Oakley, J.C. Galsworthy, G.S. Fox, K.R. Stokes, Long-term and accelerated corrosion testing methods for cast nickel–aluminium bronzes in seawater, in: D. Féron (Ed.) *Corrosion Behaviour and Protection of Copper and Aluminium Alloys in Seawater*, Woodhead Publishing, 2007, pp. 119-127.

[130] A. Al-Hashem, P.G. Caceres, W.T. Riad, H.M. Shalaby, Cavitation corrosion behavior of cast nickel-aluminum bronze in seawater, *Corrosion* 51(5) (1995), pp. 331-342.

<https://doi.org/10.5006/1.3293598>

[131] A. Al-Hashem, W. Riad, The role of microstructure of nickel-aluminium-bronze alloy on its cavitation corrosion behavior in natural seawater, *Materials Characterization* 48(1) (2002), pp. 37-41.

[https://doi.org/10.1016/s1044-5803\(02\)00196-1](https://doi.org/10.1016/s1044-5803(02)00196-1)

[132] D. Nakhaie, A. Davoodi, A. Imani, The role of constituent phases on corrosion initiation of NiAl bronze in acidic media studied by SEM-EDS, AFM and SKPFM, *Corrosion Science* 80 (2014), pp. 104-110.

<https://doi.org/10.1016/j.corsci.2013.11.017>

[133] Q.N. Song, Y.G. Zheng, D.R. Ni, Z.Y. Ma, Studies of the nobility of phases using scanning Kelvin probe microscopy and its relationship to corrosion behaviour of Ni-Al bronze in chloride media, *Corrosion Science*

92 (2015), pp. 95-103.

<https://doi.org/10.1016/j.corsci.2014.11.039>

[134] Q.N. Song, N. Xu, Y.F. Bao, Y.F. Jiang, W. Gu, Y.G. Zheng, Y.X. Qiao, Corrosion and cavitation erosion behaviors of two marine propeller materials in clean and sulfide-polluted 3.5% NaCl solutions, *Acta Metallurgica Sinica-English Letters* 30(8) (2017), pp. 712-720.

<https://doi.org/10.1007/s40195-017-0602-7>

[135] L.M. Zhang, A.L. Ma, H. Yu, A.J. Umoh, Y.G. Zheng, Correlation of microstructure with cavitation erosion behaviour of a nickel-aluminum bronze in simulated seawater, *Tribology International* 136 (2019), pp. 250-258.

<https://doi.org/10.1016/j.triboint.2019.03.071>

[136] C.D.S. Tuck, C.A. Powell, J. Nuttall, Corrosion of copper and its alloys, in: B. Cottis, M. Graham, R. Lindsay, S. Lyon, T. Richardson, D. Scantlebury, H. Stott (Eds.), *Shreir's Corrosion*, Elsevier, Oxford, 2010, pp. 1937-1973.

[137] J. Hucinska, M. Glowacka, Cavitation erosion of copper and copper-based alloys, *Metallurgical and Materials Transactions: A* 32(6) (2001), pp. 1325-1333.

<https://doi.org/10.1007/s11661-001-0223-6>

[138] A. Karimi, M. Maamouri, J.L. Martin, Cavitation-erosion-induced microstructures in copper single-crystals, *Materials Science and Engineering: A* 113 (1989), pp. 287-296.

[https://doi.org/10.1016/0921-5093\(89\)90317-1](https://doi.org/10.1016/0921-5093(89)90317-1)

[139] Z.B. Qin, Q. Zhang, Q. Luo, Z. Wu, B. Shen, L. Liu, W.B. Hu, Microstructure design to improve the corrosion and cavitation corrosion resistance of a nickel-aluminum bronze, *Corrosion Science* 139 (2018), pp. 255-266.

<https://doi.org/10.1016/j.corsci.2018.04.043>

[140] L. Pawlowski, Thermal spraying techniques, in: *The Science and Engineering of Thermal Spray Coatings*, John Wiley & Sons, 2008, pp. 67-113.

[141] T.C. Hanson, C.M. Hackett, G.S. Settles, Independent control of HVOF particle velocity and temperature, *Journal of Thermal Spray Technology* 11(1) (2002), pp. 75-85.

<https://doi.org/10.1361/105996302770349005>

[142] Flame Spray Technologies B.V., HVOF - High Velocity Oxygen Fuel. [Online] (Accessed on Oct. 24, 2022)

<https://www.fst.nl/thermal-spray-equipment/modular-thermal-spray-systems/hvof-spray-systems/hvof-high-velocity-oxygen-fuel.html>

[143] Flame Spray Technologies B.V., Cold Gas Spray. [Online] (Accessed on Oct. 24, 2022)

<https://www.fst.nl/thermal-spray-equipment/modular-thermal-spray-systems/cold-gas-spray-systems/cold-gas-spray.html>

[144] M.F. Smith, Comparing cold spray with thermal spray coating technologies, in: V.K. Champagne (Ed.) *The Cold Spray Materials Deposition Process*, Woodhead Publishing, 2007, pp. 43-61.

[145] C.T. Kwok, H.C. Man, F.T. Cheng, K.H. Lo, Developments in laser-based surface engineering processes: with particular reference to protection against cavitation erosion, *Surface & Coatings Technology* 291 (2016), pp. 189-204.

<https://doi.org/10.1016/j.surfcoat.2016.02.019>

[146] R. Cottam, V. Luzin, H. Moody, D. Edwards, A. Majumdar, Y.C. Wong, J. Wang, M. Brandt, The role of microstructural characteristics in the cavitation erosion behaviour of laser melted and laser processed Nickel–Aluminium Bronze, *Wear* 317(1-2) (2014), pp. 56-63.

<https://doi.org/10.1016/j.wear.2014.05.002>

[147] Q.N. Song, Y. Tong, H.L. Li, H.N. Zhang, N. Xu, G.Y. Zhang, Y.F. Bao, W. Liu, Z.G. Liu, Y.X. Qiao, Corrosion and cavitation erosion resistance enhancement of cast Ni-Al bronze by laser surface melting, *Journal of Iron and Steel Research International* 29(2) (2022), pp. 359-369.

<https://doi.org/10.1007/s42243-021-00674-3>

[148] C.H. Tang, F.T. Cheng, H.C. Man, Effect of laser surface melting on the corrosion and cavitation erosion behaviors of a manganese-nickel-aluminium bronze, *Materials Science and Engineering: A* 373(1-2) (2004), pp. 195-203.

<https://doi.org/10.1016/j.msea.2004.01.016>

[149] C.H. Tang, F.T. Cheng, H.C. Man, Improvement in cavitation erosion resistance of a copper-based propeller alloy by laser surface melting, *Surface & Coatings Technology* 182(2-3) (2004), pp. 300-307.

<https://doi.org/10.1016/j.surfcoat.2003.08.048>

[150] Z.G. Li, Q.G. Zheng, J. Li, W.G. Hu, H.S. Wang, H. Tian, Laser surface-treatment of high-phosphorus cast-iron, *Journal of Applied Physics* 58(10) (1985), pp. 3860-3864.

<https://doi.org/10.1063/1.335603>

[151] C.T. Kwok, H.C. Man, F.T. Cheng, Cavitation erosion and pitting corrosion of laser surface melted stainless steels, *Surface & Coatings Technology* 99(3) (1998), pp. 295-304.

[https://doi.org/10.1016/s0257-8972\(97\)00624-5](https://doi.org/10.1016/s0257-8972(97)00624-5)

[152] C.T. Kwok, H.C. Man, F.T. Cheng, Cavitation erosion and pitting corrosion behaviour of laser surface-melted martensitic stainless steel UNSS42000, *Surface & Coatings Technology* 126(2-3) (2000), pp. 238-255.

[https://doi.org/10.1016/s0257-8972\(00\)00533-8](https://doi.org/10.1016/s0257-8972(00)00533-8)

[153] R. Clinktan, V. Senthil, K.R. Ramkumar, S. Sivasankaran, F.A. Al-Mufadi, Influence of B₄C nanoparticles on mechanical behaviour of Silicon brass nanocomposite through mechanical alloying and hot pressing, *Ceramics International* 45(15) (2019), pp. 18691-18700.

<https://doi.org/10.1016/j.ceramint.2019.06.094>

[154] R. Simoneau, Austenitic stainless steel with high cavitation erosion resistance, 1988, U.S. Patent, US4751046A.

[155] G.Y. Koga, W. Wolf, R. Schulz, S. Savoie, C. Bolfarini, C.S. Kiminami, W.J. Botta, Corrosion and wear properties of FeCrMnCoSi HVOF coatings, *Surface & Coatings Technology* 357 (2019), pp. 993-1003.

<https://doi.org/10.1016/j.surfcoat.2018.10.101>

[156] A. Kumar, J. Boy, R. Zatorski, L.D. Stephenson, Thermal spray and weld repair alloys for the repair of cavitation damage in turbines and pumps: A technical note, *Journal of Thermal Spray Technology* 14(2) (2005), pp. 177-182.

<https://doi.org/10.1361/10599630523737>

[157] C.R. Will, A.R. Capra, A.G.M. Pukasiewicz, J.d.G. Chandelier, R.S.C. Paredes, Comparative study of three austenitic alloy with cobalt resistant to cavitation deposited by plasma welding, *Welding International* 26(2) (2012), pp. 96-103.

<https://doi.org/10.1080/09507116.2010.527487>

[158] P. Rudolf, M. Julis, L. Klakurkova, P. Gejdos, M. Hudec, Iop, Cavitation erosion testing of different cavitation-resistant materials and coatings using the cavitating jet method, *29th IAHR Symposium on Hydraulic Machinery and Systems (IAHR)* 240 (2018).

<https://doi.org/10.1088/1755-1315/240/6/062057>

[159] S. Lavigne, F. Pougoum, S. Savoie, L. Martinu, J.E. Klemberg Sapieha, R. Schulz, Cavitation erosion behavior of HVOF CaviTec coatings, *Wear* 386-387 (2017), pp. 90-98.

<https://doi.org/10.1016/j.wear.2017.06.003>

[160] M. Riddihough, Stellite as a wear-resistant material, *Tribology* 3(4) (1970), pp. 211-215.

[https://doi.org/10.1016/0041-2678\(70\)90058-8](https://doi.org/10.1016/0041-2678(70)90058-8)

[161] D.A. Woodford, Cavitation-erosion-induced phase transformations in alloys, *Metallurgical Transactions* 3 (1972), pp. 1137-1145.

<https://doi.org/10.1007/bf02642445>

[162] C.J. Heathcock, A. Ball, B.E. Protheroe, Cavitation erosion of cobalt-based Stellite[®] alloys, cemented carbides and surface-treated low alloy steels, *Wear* 74(1) (1981), pp. 11-26.

[https://doi.org/10.1016/0043-1648\(81\)90191-5](https://doi.org/10.1016/0043-1648(81)90191-5)

- [163] H.G. Feller, Y. Kharrazi, Cavitation erosion of metals and alloys, *Wear* 93(3) (1984), pp. 249-260.
[https://doi.org/10.1016/0043-1648\(84\)90199-6](https://doi.org/10.1016/0043-1648(84)90199-6)
- [164] M.K. Lee, W.W. Kim, C.K. Rhee, W.J. Lee, Investigation of liquid impact erosion for 12Cr steel and Stellite 6B, *Journal of Nuclear Materials* 257(2) (1998), pp. 134-144.
[https://doi.org/10.1016/s0022-3115\(98\)00440-1](https://doi.org/10.1016/s0022-3115(98)00440-1)
- [165] S. Hattori, N. Mikami, Cavitation erosion resistance of stellite alloy weld overlays, *Wear* 267(11) (2009), pp. 1954-1960.
<https://doi.org/10.1016/j.wear.2009.05.007>
- [166] S.A. Romo, J.F. Santa, J.E. Giraldo, A. Toro, Cavitation and high-velocity slurry erosion resistance of welded Stellite 6 alloy, *Tribology International* 47 (2012), pp. 16-24.
<https://doi.org/10.1016/j.triboint.2011.10.003>
- [167] R. Singh, D. Kumar, S.K. Mishra, S.K. Tiwari, Laser cladding of Stellite 6 on stainless steel to enhance solid particle erosion and cavitation resistance, *Surface & Coatings Technology* 251 (2014), pp. 87-97.
<https://doi.org/10.1016/j.surfcoat.2014.04.008>
- [168] Y.P. Ding, J.H. Yao, R. Liu, L. Wang, Q.L. Zhang, J.J. Sheng, C.G. Xue, Effects of surface treatment on the cavitation erosion-corrosion performance of 17-4PH stainless steel in sodium chloride solution, *Journal of Materials Engineering and Performance* 29(4) (2020), pp. 2687-2696.
<https://doi.org/10.1007/s11665-020-04773-2>
- [169] Q.L. Zhang, L.J. Wu, H.S. Zou, B. Li, G. Zhang, J.Y. Sun, J.J. Wang, J.H. Yao, Correlation between microstructural characteristics and cavitation resistance of Stellite-6 coatings on 17-4 PH stainless steel prepared with supersonic laser deposition and laser cladding, *Journal of Alloys and Compounds* 860 (2021), Article 158417.
<https://doi.org/10.1016/j.jallcom.2020.158417>
- [170] Y.P. Ding, R. Liu, J.H. Yao, Q.L. Zhang, L. Wang, Stellite alloy mixture hardfacing via laser cladding for control valve seat sealing surfaces, *Surface & Coatings Technology* 329 (2017), pp. 97-108.
<https://doi.org/10.1016/j.surfcoat.2017.09.018>
- [171] H.R. Silva, V.A. Ferraresi, Effect of cobalt alloy addition in erosive wear and cavitation of coatings welds, *Wear* 426 (2019), pp. 302-313.
<https://doi.org/10.1016/j.wear.2019.01.120>
- [172] B.K. Sreedhar, S.K. Albert, A.B. Pandit, Improving cavitation erosion resistance of austenitic stainless steel in liquid sodium by hardfacing - comparison of Ni and Co based deposits, *Wear* 342 (2015), pp. 92-99.
<https://doi.org/10.1016/j.wear.2015.08.009>
- [173] V. Shankar, K.B.S. Rao, S.L. Mannan, Microstructure and mechanical properties of Inconel 625 superalloy, *Journal of Nuclear*

Materials 288(2-3) (2001), pp. 222-232.

[https://doi.org/10.1016/s0022-3115\(00\)00723-6](https://doi.org/10.1016/s0022-3115(00)00723-6)

[174] G.A. Rao, M. Kumar, M. Srinivas, D.S. Sarma, Effect of standard heat treatment on the microstructure and mechanical properties of hot isostatically pressed superalloy Inconel 718, *Materials Science and Engineering: A* 355(1-2) (2003), pp. 114-125.

[https://doi.org/10.1016/s0921-5093\(03\)00079-0](https://doi.org/10.1016/s0921-5093(03)00079-0)

[175] H.X. Hu, Y.G. Zheng, C.P. Qin, Comparison of Inconel 625 and Inconel 600 in resistance to cavitation erosion and jet impingement erosion, *Nuclear Engineering and Design* 240(10) (2010), pp. 2721-2730.

<https://doi.org/10.1016/j.nucengdes.2010.07.021>

[176] H.H. Chen, W.T. Wu, Cavitation erosion behavior of Inconel 690 alloy, *Materials Science and Engineering: A* 489(1-2) (2008), pp. 451-456.

<https://doi.org/10.1016/j.msea.2007.12.007>

[177] Z. Li, J.S. Zhou, J.S. Han, J.M. Chen, Formation of cavitation-induced nanosize precipitates on the eroded surface for Inconel 718 alloy, *Materials Letters* 164 (2016), pp. 267-269.

<https://doi.org/10.1016/j.matlet.2015.10.122>

[178] H.Y. Al-Fadhli, J. Stokes, M.S.J. Hashmi, B.S. Yilbas, The erosion-corrosion behaviour of high velocity oxy-fuel (HVOF) thermally sprayed Inconel-625 coatings on different metallic surfaces, *Surface & Coatings Technology* 200(20-21) (2006), pp. 5782-5788.

<https://doi.org/10.1016/j.surfcoat.2005.08.143>

[179] Q.B. Jia, D.D. Gu, Selective laser melting additive manufacturing of Inconel 718 superalloy parts: Densification, microstructure and properties, *Journal of Alloys and Compounds* 585 (2014), pp. 713-721.

<https://doi.org/10.1016/j.jallcom.2013.09.171>

[180] T.E. Abioye, D.G. McCartney, A.T. Clare, Laser cladding of Inconel 625 wire for corrosion protection, *Journal of Materials Processing Technology* 217 (2015), pp. 232-240.

<https://doi.org/10.1016/j.jmatprotec.2014.10.024>

[181] S.S. Sandhu, A.S. Shahi, Metallurgical, wear and fatigue performance of Inconel 625 weld claddings, *Journal of Materials Processing Technology* 233 (2016), pp. 1-8.

<https://doi.org/10.1016/j.jmatprotec.2016.02.010>

[182] X. Yuan, H. Qiu, F. Zeng, W. Luo, H. Li, X. Wang, N. Guan, F. Cui, Microstructural evolution and mechanical properties of Inconel 625 superalloy fabricated by pulsed microplasma rapid additive manufacturing, *Journal of Manufacturing Processes* 77 (2022), pp. 63-74.

<https://doi.org/10.1016/j.jmapro.2022.03.008>

[183] X.J. Jiang, N. Overman, C. Smith, K. Ross, Microstructure, hardness and cavitation erosion resistance of different cold spray coatings on

stainless steel 316 for hydropower applications, *Materials Today Communications* 25 (2020), Article 101305.

<https://doi.org/10.1016/j.mtcomm.2020.101305>

[184] M. Kazasidis, S. Yin, J. Cassidy, T. Volkov-Husovic, M. Vlahovic, S. Martinovic, E. Kyriakopoulou, R. Lupoi, Microstructure and cavitation erosion performance of nickel-Inconel 718 composite coatings produced with cold spray, *Surface & Coatings Technology* 382 (2020), Article 125195.

<https://doi.org/10.1016/j.surfcoat.2019.125195>

[185] G. Taillon, K. Miyagawa, Cavitation erosion of Ni-based superalloys manufactured by forging and additive manufacturing, *Journal of Failure Analysis and Prevention* 21(5) (2021), pp. 1902-1917.

<https://doi.org/10.1007/s11668-021-01241-4>

[186] B. Wang, Y.D. Wang, Z.H. Zhang, WC-M coating to improve resistance of hydraulic turbines to cavitation erosion and abrasion, *Transactions of Nonferrous Metals Society of China* 13(4) (2003), pp. 893-897.

[187] Y. Gao, C. Li, W. Guo, Application of HVOF technology in anti-abrasion for hydraulic turbine in Liujiaxia hydropower station, *Shaanxi Electric Power* 36(5) (2008), pp. 51-53.

[188] Z. Wang, J. Chen, Compound metal layer with cavitation erosion and abrasion resistance and its application in hydraulic turbine, *Proceedings of the Thirteenth National Welding Conference of China*(2) (2009), pp. 38-46.

[189] H. Kumar, C. Chittosiya, V.N. Shukla, HVOF sprayed WC based cermet coating for mitigation of cavitation, erosion & abrasion in hydro turbine blade, *7th International Conference of Materials Processing and Characterization (ICMPC)* 5 (2017) pp. 6413-6420.

<https://doi.org/10.1016/j.matpr.2017.12.253>

[190] S. Hong, Y.P. Wu, J.H. Wu, Y.Q. Zhang, Y. Zheng, J.H. Li, J.R. Lin, Microstructure and cavitation erosion behavior of HVOF sprayed ceramic-metal composite coatings for application in hydro-turbines, *Renewable Energy* 164 (2021), pp. 1089-1099.

<https://doi.org/10.1016/j.renene.2020.08.099>

[191] J. Liu, T. Chen, C. Yuan, X. Bai, Performance analysis of cavitation erosion resistance and corrosion behavior of HVOF-sprayed WC-10Co-4Cr, WC-12Co, and Cr₃C₂-NiCr coatings, *Journal of Thermal Spray Technology* 29(4) (2020), pp. 798-810.

<https://doi.org/10.1007/s11666-020-00994-y>

[192] R. Piola, A.S.M. Ang, M. Leigh, S.A. Wade, A comparison of the antifouling performance of air plasma spray (APS) ceramic and high velocity oxygen fuel (HVOF) coatings for use in marine hydraulic

- applications, *Biofouling* 34(5) (2018), pp. 479-491.
<https://doi.org/10.1080/08927014.2018.1465052>
- [193] S. Hong, Y.P. Wu, J.F. Zhang, Y.G. Zheng, Y.J. Qin, W.W. Gao, G.Y. Li, Cavitation erosion behavior and mechanism of HVOF sprayed WC-10Co-4Cr coating in 3.5 wt% NaCl solution, *Transactions of the Indian Institute of Metals* 68(1) (2015), pp. 151-159.
<https://doi.org/10.1007/s12666-014-0440-5>
- [194] X. Ding, Y. Huang, C. Yuan, Z. Ding, Deposition and cavitation erosion behavior of multimodal WC-10Co4Cr coatings sprayed by HVOF, *Surface and Coatings Technology* 392 (2020), Article 125757.
<https://doi.org/10.1016/j.surfcoat.2020.125757>
- [195] S. Hong, Y.P. Wu, J.F. Zhang, Y.G. Zheng, Y. Zheng, J.R. Lin, Synergistic effect of ultrasonic cavitation erosion and corrosion of WC-CoCr and FeCrSiBMn coatings prepared by HVOF spraying, *Ultrasonics Sonochemistry* 31 (2016), pp. 563-569.
<https://doi.org/10.1016/j.ultsonch.2016.02.011>
- [196] X.B. Liu, J.J. Kang, W. Yue, G.Z. Ma, Z.Q. Fu, L.N. Zhu, D.S. She, J. Liang, W. Weng, H.D. Wang, C.B. Wang, Cavitation erosion behavior of HVOF sprayed WC-10Co4Cr cermet coatings in simulated sea water, *Ocean Engineering* 190 (2019), Article 106449.
<https://doi.org/10.1016/j.oceaneng.2019.106449>
- [197] Y.P. Wu, S. Hong, J.F. Zhang, Z.H. He, W.M. Guo, Q. Wang, G.Y. Li, Microstructure and cavitation erosion behavior of WC-Co-Cr coating on 1Cr18Ni9Ti stainless steel by HVOF thermal spraying, *International Journal of Refractory Metals & Hard Materials* 32 (2012), pp. 21-26.
<https://doi.org/10.1016/j.ijrmhm.2012.01.002>
- [198] S. Hong, Y.P. Wu, J.F. Zhang, Y.G. Zheng, Y.J. Qin, J.R. Lin, Ultrasonic cavitation erosion of high-velocity oxygen-fuel (HVOF) sprayed near-nanostructured WC-10Co-4Cr coating in NaCl solution, *Ultrasonics Sonochemistry* 26 (2015), pp. 87-92.
<https://doi.org/10.1016/j.ultsonch.2015.01.012>
- [199] H.J. Zhang, X.Y. Chen, Y.F. Gong, Y. Tian, A. McDonald, H. Li, *In-situ* SEM observations of ultrasonic cavitation erosion behavior of HVOF-sprayed coatings, *Ultrasonics Sonochemistry* 60 (2020), Article 104760.
<https://doi.org/10.1016/j.ultsonch.2019.104760>
- [200] J.R. Lin, S. Hong, Y. Zheng, W. Sun, M. Kang, X.Q. Fu, Cavitation erosion resistance in NaCl medium of HVOF sprayed WC-based cermet coatings at various flow velocities: A comparative study on the effect of Ni and CoCr binder phases, *International Journal of Refractory Metals & Hard Materials* 94 (2021), Article 105407.
<https://doi.org/10.1016/j.ijrmhm.2020.105407>
- [201] M.M. Lima, C. Godoy, P.J. Modenesi, J.C. Avelar-Batista, A.

Davison, A. Matthews, Coating fracture toughness determined by Vickers indentation: an important parameter in cavitation erosion resistance of WC-Co thermally sprayed coatings, *Surface & Coatings Technology* 177 (2004), pp. 489-496.

[https://doi.org/10.1016/s0257-8972\(03\)00917-4](https://doi.org/10.1016/s0257-8972(03)00917-4)

[202] T. Varis, T. Suhonen, A. Ghabchi, A. Valarezo, S. Sampath, X. Liu, S.P. Hannula, Formation mechanisms, structure, and properties of HVOF-sprayed WC-CoCr coatings: An approach toward process maps, *Journal of Thermal Spray Technology* 23(6) (2014), pp. 1009-1018.

<https://doi.org/10.1007/s11666-014-0110-5>

[203] X. Ding, X.D. Cheng, C.Q. Yuan, J. Shi, Z.X. Ding, Structure of micro-nano WC-10Co4Cr coating and cavitation erosion resistance in NaCl solution, *Chinese Journal of Mechanical Engineering* 30(5) (2017), pp. 1239-1247.

<https://doi.org/10.1007/s10033-017-0162-9>

[204] X. Ding, X.D. Cheng, X. Yu, C. Li, C.Q. Yuan, Z.X. Ding, Structure and cavitation erosion behavior of HVOF sprayed multi-dimensional WC-10Co4Cr coating, *Transactions of Nonferrous Metals Society of China* 28(3) (2018), pp. 487-494.

[https://doi.org/10.1016/s1003-6326\(18\)64681-3](https://doi.org/10.1016/s1003-6326(18)64681-3)

[205] X. Ding, D. Ke, C.Q. Yuan, Z.X. Ding, X.D. Cheng, Microstructure and cavitation erosion resistance of HVOF deposited WC-Co coatings with different sized WC, *Coatings* 8(9) (2018), Article 307.

<https://doi.org/10.3390/coatings8090307>

[206] M.S. Lamana, A.G.M. Pukasiewicz, S. Sampath, Influence of cobalt content and HVOF deposition process on the cavitation erosion resistance of WC-Co coatings, *Wear* 398 (2018), pp. 209-219.

<https://doi.org/10.1016/j.wear.2017.12.009>

[207] A. Kanno, K. Takagi, M. Arai, Influence of chemical composition, grain size, and spray condition on cavitation erosion resistance of high-velocity oxygen fuel thermal-sprayed WC cermet coatings, *Surface & Coatings Technology* 394 (2020), Article 125881.

<https://doi.org/10.1016/j.surfcoat.2020.125881>

[208] Q. Wang, Z. Tang, L. Cha, Cavitation and sand slurry erosion resistances of WC-10Co-4Cr coatings, *Journal of Materials Engineering and Performance* 24(6) (2015), pp. 2435-2443.

<https://doi.org/10.1007/s11665-015-1496-z>

[209] J. Du, J. Zhang, C. Zhang, Effect of heat treatment on the cavitation erosion performance of WC-12Co coatings, *Coatings* 9(10) (2019), Article 690.

<https://doi.org/10.3390/coatings9100690>

[210] A. Becker, K. Bertoul, A.G.M. Pukasiewicz, I.B.A.F. Siqueira, A.

Chicoski, F. Caliari, R.F. Vaz, M.J.d. Sousa, Influence of fuel/oxygen ratio on coating properties and cavitation resistance of WC and Cr₃C₂ cermet coatings deposited by HVOF, *International Thermal Spray Conference 2021 Thermal Spray 2021: Proceedings from the International Thermal Spray Conference* (2021) pp. 716-721.

<https://doi.org/10.31399/asm.cp.itsc2021p0716>

[211] T. Varis, T. Suhonen, J. Laakso, M. Jokipii, P. Vuoristo, Evaluation of residual stresses and their influence on cavitation erosion resistance of high kinetic HVOF and HVOF-sprayed WC-CoCr coatings, *Journal of Thermal Spray Technology* 29(6) (2020), pp. 1365-1381.

<https://doi.org/10.1007/s11666-020-01037-2>

[212] Z.X. Ding, W. Chen, Q. Wang, Resistance of cavitation erosion of multimodal WC-12Co coatings sprayed by HVOF, *Transactions of Nonferrous Metals Society of China* 21(10) (2011), pp. 2231-2236.

[https://doi.org/10.1016/s1003-6326\(11\)61000-5](https://doi.org/10.1016/s1003-6326(11)61000-5)

[213] Z. Ding, Y. Hu, H. Zhao, Structures and resistance of cavitation erosion micro-nanostructured WC-12Co coatings sprayed by HVOF, *Tribology* 33(5) (2013), pp. 429-435.

[214] S. Hong, Y.P. Wu, J.H. Wu, Y. Zheng, Y.Q. Zhang, J.B. Cheng, J.H. Li, J.R. Lin, Effect of flow velocity on cavitation erosion behavior of HVOF sprayed WC-10Ni and WC-20Cr₃C₂-7Ni coatings, *International Journal of Refractory Metals & Hard Materials* 92 (2020), Article 105330.

<https://doi.org/10.1016/j.ijrmhm.2020.105330>

[215] Y. Korobov, H. Alwan, N. Soboleva, A. Makarov, N. Lezhnin, V. Shumyakov, M. Antonov, M. Deviatarov, Cavitation resistance of WC-10Co4Cr and WC-20CrC-7Ni HVOF coatings, *Journal of Thermal Spray Technology* 31(1-2) (2022), pp. 234-246.

<https://doi.org/10.1007/s11666-021-01242-7>

[216] L. Thakur, N. Arora, A study of processing and slurry erosion behaviour of multi-walled carbon nanotubes modified HVOF sprayed nano-WC-10Co-4Cr coating, *Surface & Coatings Technology* 309 (2017), pp. 860-871.

<https://doi.org/10.1016/j.surfcoat.2016.10.073>

[217] F.T. Cheng, C.T. Kwok, H.C. Man, Cavitation erosion resistance of stainless steel laser-clad with WC-reinforced MMC, *Materials Letters* 57(4) (2002), pp. 969-974.

[https://doi.org/10.1016/s0167-577x\(02\)00907-2](https://doi.org/10.1016/s0167-577x(02)00907-2)

[218] K.H. Lo, F.T. Cheng, H.C. Man, Cavitation erosion mechanism of S31600 stainless steel laser surface-modified with unclad WC, *Materials Science and Engineering: A* 357(1-2) (2003), pp. 168-180.

[https://doi.org/10.1016/s0921-5093\(03\)00216-8](https://doi.org/10.1016/s0921-5093(03)00216-8)

[219] K.H. Lo, F.T. Cheng, C.T. Kwok, H.C. Man, Improvement of

cavitation erosion resistance of AISI 316 stainless steel by laser surface alloying using fine WC powder, *Surface & Coatings Technology* 165(3) (2003), pp. 258-267.

[https://doi.org/10.1016/s0257-8972\(02\)00739-9](https://doi.org/10.1016/s0257-8972(02)00739-9)

[220] K.F. Tam, F.T. Cheng, H.C. Man, Cavitation erosion behavior of laser-clad Ni-Cr-Fe-WC on brass, *Materials Research Bulletin* 37(7) (2002), pp. 1341-1351.

[https://doi.org/10.1016/s0025-5408\(02\)00766-3](https://doi.org/10.1016/s0025-5408(02)00766-3)

[221] M. Duraiselvam, R. Galun, V. Wesling, B.L. Mordike, Laser clad WC reinforced Ni-based intermetallic-matrix composites to improve cavitation erosion resistance, *Journal of Laser Applications* 18(4) (2006), pp. 297-304.

<https://doi.org/10.2351/1.2355521>

[222] X.B. Zhang, C.S. Liu, X.D. Liu, J. Dong, B. Yu, Cavitation erosion behavior of WC coatings on CrNiMo stainless steel by laser alloying, *International Journal of Minerals Metallurgy and Materials* 16(2) (2009), pp. 203-207.

[https://doi.org/10.1016/s1674-4799\(09\)60034-0](https://doi.org/10.1016/s1674-4799(09)60034-0)

[223] Y.F. Bao, L.P. Guo, C.H. Zhong, Q.N. Song, K. Yang, Y.F. Jiang, Z.R. Wang, Effects of WC on the cavitation erosion resistance of FeCoCrNiB_{0.2} high entropy alloy coating prepared by laser cladding, *Materials Today Communications* 26 (2021), Article 102154.

<https://doi.org/10.1016/j.mtcomm.2021.102154>

[224] D. Ma, T.J. Harvey, Y.N. Zhuk, R.G. Wellman, R.J.K. Wood, Cavitation erosion performance of CVD W/WC coatings, *Wear* 452 (2020), Article 203276.

<https://doi.org/10.1016/j.wear.2020.203276>

[225] A. Babu, H.S. Arora, H.S. Grewal, Development of cavitation erosion-resistant microwave processed WC-based cladding, *Tribology Transactions* 64(6) (2021), pp. 1118-1126.

<https://doi.org/10.1080/10402004.2021.1976891>

[226] W.M. Guo, Y.P. Wu, J.F. Zhang, S. Hong, G.Y. Li, G.B. Ying, J. Guo, Y.J. Qin, Fabrication and characterization of thermal-sprayed Fe-based amorphous/nanocrystalline composite coatings: An overview, *Journal of Thermal Spray Technology* 23(7) (2014), pp. 1157-1180.

<https://doi.org/10.1007/s11666-014-0096-z>

[227] C.A.C. Souza, D.V. Ribeiro, C.S. Kiminami, Corrosion resistance of Fe-Cr-based amorphous alloys: An overview, *Journal of Non-Crystalline Solids* 442 (2016), pp. 56-66.

<https://doi.org/10.1016/j.jnoncrysol.2016.04.009>

[228] B. Huang, C. Zhang, G. Zhang, H.L. Liao, Wear and corrosion resistant performance of thermal-sprayed Fe-based amorphous coatings:

A review, *Surface & Coatings Technology* 377 (2019), Article 124896.

<https://doi.org/10.1016/j.surfcoat.2019.124896>

[229] R.F. Vaz, A.G.M. Pukasiewicz, I.B.A.F. Siqueira, G.B. Sucharski, A. Chicowski, R. Tristante, Thermal spraying of FeMnCrSi alloys: An overview, *International Thermal Spray Conference 2021 Thermal Spray 2021: Proceedings from the International Thermal Spray Conference (2021)* pp. 431-439.

<https://doi.org/10.31399/asm.cp.itsc2021p0431>

[230] Z.B. Zheng, Y.G. Zheng, W.H. Sun, J.Q. Wang, Effect of heat treatment on the structure, cavitation erosion and erosion-corrosion behavior of Fe-based amorphous coatings, *Tribology International* 90 (2015), pp. 393-403.

<https://doi.org/10.1016/j.triboint.2015.04.039>

[231] G. Hou, X. Zhao, H. Zhou, J. Lu, Y. An, J. Chen, J. Yang, Cavitation erosion of several oxy-fuel sprayed coatings tested in deionized water and artificial seawater, *Wear* 311(1-2) (2014), pp. 81-92.

<https://doi.org/10.1016/j.wear.2013.12.026>

[232] Y.P. Wu, P.H. Lin, C.L. Chu, Z.H. Wang, M. Cao, J.H. Hu, Cavitation erosion characteristics of a Fe-Cr-Si-B-Mn coating fabricated by high velocity oxy-fuel (HVOF) thermal spray, *Materials Letters* 61(8-9) (2007), pp. 1867-1872.

<https://doi.org/10.1016/j.matlet.2006.07.147>

[233] Z. Wang, X. Zhang, J. Cheng, J. Lin, Z. Zhou, Cavitation erosion resistance of Fe-based amorphous/nanocrystal coatings prepared by high-velocity arc spraying, *Journal of Thermal Spray Technology* 23(4) (2014), pp. 742-749.

<https://doi.org/10.1007/s11666-014-0074-5>

[234] Y.J. Kim, J.W. Jang, D.W. Lee, S. Yi, Porosity effects of a Fe-based amorphous/nanocrystals coating prepared by a commercial high velocity oxy-fuel process on cavitation erosion behaviors, *Metals and Materials International* 21(4) (2015), pp. 673-677.

<https://doi.org/10.1007/s12540-015-4580-x>

[235] L. Qiao, Y. Wu, S. Hong, J. Zhang, W. Shi, Y. Zheng, Relationships between spray parameters, microstructures and ultrasonic cavitation erosion behavior of HVOF sprayed Fe-based amorphous/nanocrystalline coatings, *Ultrasonics Sonochemistry* 39 (2017), pp. 39-46.

<https://doi.org/10.1016/j.ultsonch.2017.04.011>

[236] L. Qiao, Y.P. Wu, S. Hong, J. Cheng, Ultrasonic cavitation erosion mechanism and mathematical model of HVOF sprayed Fe-based amorphous/nanocrystalline coatings, *Ultrasonics Sonochemistry* 52 (2019), pp. 142-149.

<https://doi.org/10.1016/j.ultsonch.2018.11.010>

- [237] G. Taillon, F. Pougoum, S. Lavigne, L. Ton-That, R. Schulz, E. Bousser, S. Savoie, L. Martinu, J.E. Klemberg-Sapieha, Cavitation erosion mechanisms in stainless steels and in composite metal-ceramic HVOF coatings, *Wear* 364 (2016), pp. 201-210.
<https://doi.org/10.1016/j.wear.2016.07.015>
- [238] X. Yang, J. Zhang, G. Li, Cavitation erosion behaviour and mechanism of HVOF-sprayed NiCrBSi-(Cr₃C₂-NiCr) composite coatings, *Surface Engineering* 34(3) (2018), pp. 211-219.
<https://doi.org/10.1080/02670844.2016.1258770>
- [239] V. Matikainen, H. Koivuluoto, P. Vuoristo, J. Schubert, S. Houdkova, Effect of nozzle geometry on the microstructure and properties of HVOF-sprayed WC-10Co4Cr and Cr₃C₂-25NiCr coatings, *Journal of Thermal Spray Technology* 27(4) (2018), pp. 680-694.
<https://doi.org/10.1007/s11666-018-0717-z>
- [240] V. Matikainen, H. Koivuluoto, P. Vuoristo, A study of Cr₃C₂-based HVOF- and HVOF-sprayed coatings: Abrasion, dry particle erosion and cavitation erosion resistance, *Wear* 446 (2020), Article 203188.
<https://doi.org/10.1016/j.wear.2020.203188>
- [241] L.A. Luiz, J. de Andrade, C.M. Pesqueira, I. Siqueira, G.B. Sucharski, M.J. de Sousa, Corrosion behavior and galvanic corrosion resistance of WC and Cr₃C₂ cermet coatings in Madeira River water, *Journal of Thermal Spray Technology* 30(1-2) (2021), pp. 205-221.
<https://doi.org/10.1007/s11666-021-01152-8>
- [242] S. Hong, Y.P. Wu, Q. Wang, G.B. Ying, G.Y. Li, W.W. Gao, B. Wang, W.M. Guo, Microstructure and cavitation-silt erosion behavior of high-velocity oxygen-fuel (HVOF) sprayed Cr₃C₂-NiCr coating, *Surface & Coatings Technology* 225 (2013), pp. 85-91.
<https://doi.org/10.1016/j.surfcoat.2013.03.020>
- [243] J. Stella, T. Poirier, M. Pohl, Cavitation-erosion of 3Y-TZPs obtained at different sintering temperatures, *Wear* 300(1-2) (2013), pp. 163-168.
<https://doi.org/10.1016/j.wear.2013.01.104>
- [244] Y. Wang, G. Darut, T. Poirier, J. Stella, H.L. Liao, M.P. Planche, Cavitation erosion of plasma sprayed YSZ coatings produced by feedstocks with different initial sizes, *Tribology International* 111 (2017), pp. 226-233.
<https://doi.org/10.1016/j.triboint.2017.03.019>
- [245] Y. Wang, J. Stella, G. Darut, T. Poirier, H.L. Liao, M.P. Planche, APS prepared NiCrBSi-YSZ composite coatings for protection against cavitation erosion, *Journal of Alloys and Compounds* 699 (2017), pp. 1095-1103.
<https://doi.org/10.1016/j.jallcom.2017.01.034>
- [246] W. Deng, Y.L. An, G.L. Hou, S.J. Li, H.D. Zhou, J.M. Chen, Effect of

substrate preheating treatment on the microstructure and ultrasonic cavitation erosion behavior of plasma-sprayed YSZ coatings, *Ultrasonics Sonochemistry* 46 (2018), pp. 1-9.

<https://doi.org/10.1016/j.ultsonch.2018.04.004>

[247] Y. Wang, B. Lebon, I. Tzanakis, Y.L. Zhao, K.S. Wang, J. Stella, T. Poirier, G. Darut, H.L. Liao, M.P. Planche, Experimental and numerical investigation of cavitation-induced erosion in thermal sprayed single splats, *Ultrasonics Sonochemistry* 52 (2019), pp. 336-343.

<https://doi.org/10.1016/j.ultsonch.2018.12.008>

[248] S. Yilmaz, M. Ipek, G.F. Celebi, C. Bindal, The effect of bond coat on mechanical properties of plasma-sprayed Al₂O₃ and Al₂O₃-13 wt% TiO₂ coatings on AISI 316L stainless steel, *Vacuum* 77(3) (2005), pp. 315-321.

<https://doi.org/10.1016/j.vacuum.2004.11.004>

[249] R. Yilmaz, A.O. Kurt, A. Demir, Z. Tatli, Effects of TiO₂ on the mechanical properties of the Al₂O₃-TiO₂ plasma sprayed coating, *Journal of the European Ceramic Society* 27(2-3) (2007), pp. 1319-1323.

<https://doi.org/10.1016/j.jeurceramsoc.2006.04.099>

[250] J. Porter, L. Suhl, Anti-fouling coating process, 1992, U.S. Patent, US5080926A.

[251] I. Gosteva, Y. Morgalev, T. Morgaleva, S. Morgalev, Effect of Al₂O₃ and TiO₂ nanoparticles on aquatic organisms, *3rd International Youth Conference on Interdisciplinary Problems of Nanotechnology, Biomedicine and Nanotoxicology (Nanobiotech)* 98 (2015).

<https://doi.org/10.1088/1757-899x/98/1/012007>

[252] K. Jafarzadeh, Z. Valefi, B. Ghavidel, The effect of plasma spray parameters on the cavitation erosion of Al₂O₃-TiO₂ coatings, *Surface & Coatings Technology* 205(7) (2010), pp. 1850-1855.

<https://doi.org/10.1016/j.surfcoat.2010.08.044>

[253] H.X. Hu, S.L. Jiang, Y.S. Tao, T.Y. Xiong, Y.G. Zheng, Cavitation erosion and jet impingement erosion mechanism of cold sprayed Ni-Al₂O₃ coating, *Nuclear Engineering and Design* 241(12) (2011), pp. 4929-4937.

<https://doi.org/10.1016/j.nucengdes.2011.09.038>

[254] L. Latka, M. Szala, M. Michalak, T. Palka, Impact of atmospheric plasma spray parameters on cavitation erosion resistance of Al₂O₃-13% TiO₂ coatings, *Acta Physica Polonica A* 136(2) (2019), pp. 342-347.

<https://doi.org/10.12693/APhysPolA.136.342>

[255] M. Szala, L. Latka, M. Walczak, M. Winnicki, Comparative study on the cavitation erosion and sliding wear of cold-sprayed Al/Al₂O₃ and Cu/Al₂O₃ coatings, and stainless steel, aluminium alloy, copper and brass, *Metals* 10(7) (2020), Article 856.

<https://doi.org/10.3390/met10070856>

- [256] M. Szala, L. Latka, M. Awtoniuk, M. Winnicki, M. Michalak, Neural modelling of APS thermal spray process parameters for optimizing the hardness, porosity and cavitation erosion resistance of Al₂O₃-13 wt% TiO₂ Coatings, *Processes* 8(12) (2020), Article 1544.
<https://doi.org/10.3390/pr8121544>
- [257] M. Szala, T. Hejwowski, Cavitation erosion resistance and wear mechanism model of flame-sprayed Al₂O₃-40%TiO₂/NiMoAl cermet coatings, *Coatings* 8(7) (2018), Article 254.
<https://doi.org/10.3390/coatings8070254>
- [258] S. Pandey, A. Bansal, A. Omer, A.K. Singla, D.K. Goyal, J. Singh, M.K. Gupta, Effect of fuel pressure, feed rate, and spray distance on cavitation erosion of Rodojet sprayed Al₂O₃+50%TiO₂ coated AISI410 steel, *Surface & Coatings Technology* 410 (2021), Article 126961.
<https://doi.org/10.1016/j.surfcoat.2021.126961>
- [259] J. Kiilakoski, J. Puranen, E. Heinonen, H. Koivuluoto, P. Vuoristo, Characterization of powder-precursor HVOF-sprayed Al₂O₃-YSZ/ZrO₂ coatings, *Journal of Thermal Spray Technology* 28(1-2) (2019), pp. 98-107.
<https://doi.org/10.1007/s11666-018-0816-x>
- [260] F.T. Cheng, C.T. Kwok, H.C. Man, Laser surfacing of S31603 stainless steel with engineering ceramics for cavitation erosion resistance, *Surface & Coatings Technology* 139(1) (2001), pp. 14-24.
[https://doi.org/10.1016/s0257-8972\(00\)01103-8](https://doi.org/10.1016/s0257-8972(00)01103-8)
- [261] F.T. Cheng, P. Shi, H.C. Man, Cavitation erosion resistance of heat-treated NiTi, *Materials Science and Engineering: A* 339(1-2) (2003), pp. 312-317.
[https://doi.org/10.1016/s0921-5093\(02\)00162-4](https://doi.org/10.1016/s0921-5093(02)00162-4)
- [262] Z. Wu, Y.F. Cheng, L. Liu, W.J. Lv, W.B. Hu, Effect of heat treatment on microstructure evolution and erosion-corrosion behavior of a nickel-aluminum bronze alloy in chloride solution, *Corrosion Science* 98 (2015), pp. 260-270.
<https://doi.org/10.1016/j.corsci.2015.05.037>
- [263] Q.N. Song, Y.G. Zheng, S.L. Jiang, D.R. Ni, Z.Y. Ma, Comparison of corrosion and cavitation erosion behaviors between the as-cast and friction-stir-processed nickel aluminum bronze, *Corrosion* 69(11) (2013), pp. 1111-1121.
<https://doi.org/10.5006/0984>
- [264] Y. Li, Y. Lian, Y.J. Sun, Cavitation erosion behavior of friction stir processed nickel aluminum bronze, *Journal of Alloys and Compounds* 795 (2019), pp. 233-240.
<https://doi.org/10.1016/j.jallcom.2019.04.302>
- [265] Y. Li, Y. Lian, Y.J. Sun, Synergistic effect between cavitation erosion

and corrosion for friction stir processed NiAl bronze in artificial seawater, *Metals and Materials International* 27(12) (2021), pp. 5082-5094.

<https://doi.org/10.1007/s12540-020-00916-1>

[266] Y. Li, Y. Lian, Y.J. Sun, Comparison of cavitation erosion behaviors between the as-cast and friction stir processed Ni-Al bronze in distilled water and artificial seawater, *Journal of Materials Research and Technology* 13 (2021), pp. 906-918.

<https://doi.org/10.1016/j.jmrt.2021.05.015>

[267] X.F. Zhang, L. Fang, The effect of stacking fault energy on the cavitation erosion resistance of α -phase aluminum bronzes, *Wear* 253(11-12) (2002), pp. 1105-1110.

[https://doi.org/10.1016/s0043-1648\(02\)00168-0](https://doi.org/10.1016/s0043-1648(02)00168-0)

[268] M. Szala, D. Chocyk, A. Skic, M. Kaminski, W. Macek, M. Turek, Effect of nitrogen ion implantation on the cavitation erosion resistance and cobalt-based solid solution phase transformations of HIPed Stellite 6, *Materials* 14(9) (2021), Article 2324.

<https://doi.org/10.3390/ma14092324>

[269] B.C.S. Rao, D.H. Buckley, Deformation and erosion of f.c.c. metals and alloys under cavitation attack, *Materials Science and Engineering* 67(1) (1984), pp. 55-67.

[https://doi.org/10.1016/0025-5416\(84\)90031-4](https://doi.org/10.1016/0025-5416(84)90031-4)

[270] T.H. Zhang, J.D. Xie, C.Z. Ji, J. Chen, H. Xu, J. Li, G.R. Sun, H.X. Zhang, Influence of the structure of implanted steel with Y, Y+C and Y+Cr on the behaviors of wear, oxidation and corrosion-resistance, *Surface & Coatings Technology* 72(1-2) (1995), pp. 93-98.

[https://doi.org/10.1016/0257-8972\(94\)02337-9](https://doi.org/10.1016/0257-8972(94)02337-9)

[271] L. Lin, G.L. Li, H.D. Wang, J.J. Kang, Z.L. Xu, H.J. Wang, Structure and wear behavior of NiCr-Cr₃C₂ coatings sprayed by supersonic plasma spraying and high velocity oxy-fuel technologies, *Applied Surface Science* 356 (2015), pp. 383-390.

<https://doi.org/10.1016/j.apsusc.2015.08.019>

[272] I. Bordeasu, I. Mitelea, Cavitation erosion behaviour of stainless steels with constant nickel and variable chromium content, *Materials Testing* 54(1) (2012), pp. 53-58.

<https://doi.org/10.3139/120.110297>

[273] L. St-Georges, Development and characterization of composite Ni-Cr+WC laser cladding, *Wear* 263(1) (2007), pp. 562-566.

<https://doi.org/10.1016/j.wear.2007.02.023>

[274] L.Y. Chen, Y. Zhao, C. Guan, T.B.A. Yu, Effects of CeO₂ addition on microstructure and properties of ceramics reinforced Fe-based coatings by laser cladding, *International Journal of Advanced Manufacturing Technology* 115(7-8) (2021), pp. 2581-2593.

<https://doi.org/10.1007/s00170-021-07297-8>

[275] K.L. Wang, Q.B. Zhang, M.L. Sun, X.G. Wei, Y.M. Zhu, Microstructure and corrosion resistance of laser clad coatings with rare earth elements, *Corrosion Science* 43(2) (2001), pp. 255-267.

[https://doi.org/10.1016/s0010-938x\(00\)00081-0](https://doi.org/10.1016/s0010-938x(00)00081-0)

[276] K.L. Wang, Q.B. Zhang, M.L. Sun, X.G. Wei, Y.M. Zhu, Rare earth elements modification of laser-clad nickel-based alloy coatings, *Applied Surface Science* 174(3-4) (2001), pp. 191-200.

[https://doi.org/10.1016/s0169-4332\(01\)00017-4](https://doi.org/10.1016/s0169-4332(01)00017-4)

[277] K.L. Wang, Q.B. Zhang, M.L. Sun, X.G. Wei, Microstructural characteristics of laser clad coatings with rare earth metal elements, *Journal of Materials Processing Technology* 139(1-3) (2003), pp. 448-452.

[https://doi.org/10.1016/s0924-0136\(03\)00551-x](https://doi.org/10.1016/s0924-0136(03)00551-x)

[278] S.I. Shim, Y.S. Park, S.T. Kim, C.B. Song, Effects of rare earth metal addition on the cavitation erosion-corrosion resistance of super duplex stainless steels, *Metals and Materials International* 8(3) (2002), pp. 301-307.

<https://doi.org/10.1007/bf03186100>

[279] D. Li, S. Song, D. Chen, P. Liang, Effects of Ce, Sm and Yb on cavitation erosion of NAB alloy in 3.5% NaCl solution, *Ultrasonics Sonochemistry* 88 (2022), Article 106093.

<https://doi.org/10.1016/j.ultsonch.2022.106093>

[280] J. Liu, T.Z. Chen, H.T. Duan, C.Q. Yuan, X.Q. Bai, Mechanical properties and cavitation erosion behavior of CeO₂-modified dual-scale WC-10Co-4Cr coating prepared by HVOF, *Journal of Thermal Spray Technology* (2022).

<https://doi.org/10.1007/s11666-022-01442-9>

[281] N.M. Melendez, A.G. McDonald, Development of WC-based metal matrix composite coatings using low-pressure cold gas dynamic spraying, *Surface and Coatings Technology* 214 (2013), pp. 101-109.

<https://doi.org/10.1016/j.surfcoat.2012.11.010>

[282] X.X. Liu, X. Song, H. Wang, X.X. Liu, F. Tang, H. Lu, Complexions in WC-Co cemented carbides, *Acta Materialia* 149 (2018), pp. 164-178.

<https://doi.org/10.1016/j.actamat.2018.02.018>

[283] I. Konyashin, A. Sologubenko, T. Weirich, B. Ries, Complexion at WC-Co grain boundaries of cemented carbides, *Materials Letters* 187 (2017), pp. 7-10.

<https://doi.org/10.1016/j.matlet.2016.10.055>

[284] A. Leyland, A. Matthews, On the significance of the H/E ratio in wear control: a nanocomposite coating approach to optimised tribological behaviour, *Wear* 246(1-2) (2000), pp. 1-11.

[https://doi.org/10.1016/s0043-1648\(00\)00488-9](https://doi.org/10.1016/s0043-1648(00)00488-9)

- [285] A. Krella, A. Czyzniewski, Investigation concerning the cavitation resistance of TiN coatings deposited on austenitic stainless steel at various temperatures, *Wear* 265(1-2) (2008), pp. 72-80.
<https://doi.org/10.1016/j.wear.2007.08.020>
- [286] A. Krella, The influence of TiN coatings properties on cavitation erosion resistance, *Surface & Coatings Technology* 204(3) (2009), pp. 263-270.
<https://doi.org/10.1016/j.surfcoat.2009.07.014>
- [287] F.D. Severo, C.J. Scheuer, R.P. Cardoso, S.F. Brunatto, Cavitation erosion resistance enhancement of martensitic stainless steel via low-temperature plasma carburizing, *Wear* 428 (2019), pp. 162-166.
<https://doi.org/10.1016/j.wear.2019.03.009>
- [288] J. Xu, S. Peng, Z.Y. Li, S.Y. Jiang, Z.H. Xie, P. Munroe, The influence of semiconducting properties of passive films on the cavitation erosion resistance of a NbN nanoceramic coating, *Ultrasonics Sonochemistry* 71 (2021), Article 105406.
<https://doi.org/10.1016/j.ultsonch.2020.105406>
- [289] G. Hou, Y. Ren, X. Zhang, F. Dong, Y. An, X. Zhao, H. Zhou, J. Chen, Cavitation erosion mechanisms in Co-based coatings exposed to seawater, *Ultrasonics Sonochemistry* 60 (2020), Article 104799.
<https://doi.org/10.1016/j.ultsonch.2019.104799>
- [290] L. Ye, X. Zhu, Y. He, X. Wei, Ultrasonic cavitation damage characteristics of materials and a prediction model of cavitation impact load based on size effect, *Ultrasonics Sonochemistry* 66 (2020), Article 105115.
<https://doi.org/10.1016/j.ultsonch.2020.105115>
- [291] M.L. Oyen, R.R. Cook, A practical guide for analysis of nanoindentation data, *Journal of the Mechanical Behavior of Biomedical Materials* 2(4) (2009), pp. 396-407.
<https://doi.org/10.1016/j.jmbbm.2008.10.002>
- [292] K. Van Acker, D. Vanhoyweghen, R. Persoons, J. Vangrunderbeek, Influence of tungsten carbide particle size and distribution on the wear resistance of laser clad WC/Ni coatings, *Wear* 258(1-4) (2005), pp. 194-202.
<https://doi.org/10.1016/j.wear.2004.09.041>
- [293] C. Guo, J.S. Zhou, J.M. Chen, J.R. Zhao, Y.J. Yu, H.D. Zhou, High temperature wear resistance of laser cladding NiCrBSi and NiCrBSi/WC-Ni composite coatings, *Wear* 270(7-8) (2011), pp. 492-498.
<https://doi.org/10.1016/j.wear.2011.01.003>
- [294] C. Guo, J.M. Chen, J.S. Zhou, J.R. Zhao, L.Q. Wang, Y.J. Yu, H.D. Zhou, Effects of WC-Ni content on microstructure and wear resistance of laser cladding Ni-based alloys coating, *Surface & Coatings Technology*

206(8-9) (2012), pp. 2064-2071.

<https://doi.org/10.1016/j.surfcoat.2011.06.005>

[295] J.S. Xu, X.C. Zhang, F.Z. Xuan, Z.D. Wang, S.T. Tu, Microstructure and sliding wear resistance of laser clad WC/Ni composite coatings with different contents of WC particle, *Journal of Materials Engineering and Performance* 21(9) (2012), pp. 1904-1911.

<https://doi.org/10.1007/s11665-011-0109-8>

[296] Z.K. Weng, A.H. Wang, X.H. Wu, Y.Y. Wang, Z.X. Yang, Wear resistance of diode laser-clad Ni/WC composite coatings at different temperatures, *Surface & Coatings Technology* 304 (2016), pp. 283-292.

<https://doi.org/10.1016/j.surfcoat.2016.06.081>

[297] Z.D. Chen, L.C. Lim, M. Qian, Laser cladding of WC-Ni composite, *Journal of Materials Processing Technology* 62(4) (1996), pp. 321-323.

[298] S.F. Zhou, Y.J. Huang, X.Y. Zeng, Q.W. Hu, Microstructure characteristics of Ni-based WC composite coatings by laser induction hybrid rapid cladding, *Materials Science and Engineering: A* 480(1-2) (2008), pp. 564-572.

<https://doi.org/10.1016/j.msea.2007.07.058>

[299] S.F. Zhou, Y.J. Huang, X.Y. Zeng, A study of Ni-based WC composite coatings by laser induction hybrid rapid cladding with elliptical spot, *Applied Surface Science* 254(10) (2008), pp. 3110-3119.

<https://doi.org/10.1016/j.apsusc.2007.10.062>

[300] S.F. Zhou, X.Y. Zeng, Q.W. Hu, Y.J. Huang, Analysis of crack behavior for Ni-based WC composite coatings by laser cladding and crack-free realization, *Applied Surface Science* 255(5) (2008), pp. 1646-1653.

<https://doi.org/10.1016/j.apsusc.2008.04.003>

[301] P. Farahmand, R. Kovacevic, Corrosion and wear behavior of laser clad Ni-WC coatings, *Surface & Coatings Technology* 276 (2015), pp. 121-135.

<https://doi.org/10.1016/j.surfcoat.2015.06.039>

[302] H.J. Zhang, Y.F. Gong, X.Y. Chen, A. McDonald, H. Li, A comparative study of cavitation erosion resistance of several HVOF-sprayed coatings in deionized water and artificial seawater, *Journal of Thermal Spray Technology* 28(5) (2019), pp. 1060-1071.

<https://doi.org/10.1007/s11666-019-00869-x>

[303] H. Assadi, H. Kreye, F. Gärtner, T. Klassen, Cold spraying – A materials perspective, *Acta Materialia* 116 (2016), pp. 382-407.

<https://doi.org/10.1016/j.actamat.2016.06.034>

[304] J. Lienhard, C. Crook, M.Z. Azar, M. Hassani, D.R. Mumm, D. Veysset, D. Apelian, K.A. Nelson, V. Champagne, A. Nardi, C.A. Schuh,

- L. Valdevit, Surface oxide and hydroxide effects on aluminum microparticle impact bonding, *Acta Materialia* 197 (2020), pp. 28-39.
<https://doi.org/10.1016/j.actamat.2020.07.011>
- [305] M. Ashokkumar, The characterization of acoustic cavitation bubbles - An overview, *Ultrasonics Sonochemistry* 18(4) (2011), pp. 864-872.
<https://doi.org/10.1016/j.ultsonch.2010.11.016>
- [306] D.G. Shchukin, E. Skorb, V. Belova, H. Mohwald, Ultrasonic cavitation at solid surfaces, *Advanced Materials* 23(17) (2011), pp. 1922-1934.
<https://doi.org/10.1002/adma.201004494>
- [307] A. Barrios, E. Kakandar, G. Castelluccio, O.N. Pierron, Comparison of the low and high/very high cycle fatigue behaviors in Ni microbeams under bending, *Journal of Materials Research* 36(11) (2021), pp. 2337-2348.
<https://doi.org/10.1557/s43578-020-00097-y>
- [308] M. Yamamoto, On Elastic constants of nickel crystals, *Physical Review* 77 (1950), pp. 566-566.
<https://doi.org/10.1103/PhysRev.77.566>
- [309] J. Kim, Y.J. Suh, I. Kang, First-principles calculations of the phase stability and the elastic and mechanical properties of η -phases in the WC-Co system, *Journal of Alloys and Compounds* 656 (2016), pp. 213-217.
<https://doi.org/10.1016/j.jallcom.2015.09.214>
- [310] Y. Yu, D. Chen, H. Tan, H. Wang, S. Xie, M. Zhang, Spall investigations for LY12 Al using triangular waves, *International Journal of Impact Engineering* 34 (2007), pp. 395-404.
<https://doi.org/10.1016/j.ijimpeng.2005.11.006>
- [311] J. Cadman, S.W. Zhou, Y.H. Chen, W. Li, R. Appleyard, Q. Li, Characterization of cuttlebone for a biomimetic design of cellular structures, *Acta Mechanica Sinica* 26(1) (2010), pp. 27-35.
<https://doi.org/10.1007/s10409-009-0310-2>
- [312] J. Cadman, S.W. Zhou, Y.H. Chen, Q. Li, Cuttlebone: Characterisation, application and development of biomimetic materials, *Journal of Bionic Engineering* 9(3) (2012), pp. 367-376.
[https://doi.org/10.1016/s1672-6529\(11\)60132-7](https://doi.org/10.1016/s1672-6529(11)60132-7)
- [313] A.R. Mao, N.F. Zhao, Y.H. Liang, H. Bai, Mechanically efficient cellular materials inspired by cuttlebone, *Advanced Materials* 33(15) (2021), Article 2007348.
<https://doi.org/10.1002/adma.202007348>
- [314] J. Sun, B. Bhushan, Hierarchical structure and mechanical properties of nacre: A review, *RSC Advances* 2 (2012), pp. 7617-7632.
<https://doi.org/10.1039/c2ra20218b>
- [315] T. Verho, P. Karppinen, A.H. Groschel, O. Ikkala, Imaging inelastic

fracture processes in biomimetic nanocomposites and nacre by laser speckle for better toughness, *Advanced Science* 5(1) (2018), Article 1700635.

<https://doi.org/10.1002/advs.201700635>

[316] G. Tan, J. Zhang, L. Zheng, D. Jiao, Z. Liu, Z. Zhang, R.O. Ritchie, Nature-inspired nacre-like composites combining human tooth-matching elasticity and hardness with exceptional damage tolerance, *Advanced Materials* 31(52) (2019), Article 1904603.

<https://doi.org/10.1002/adma.201904603>

[317] Z.P. Shi, J.Q. Wang, Z.B. Wang, Y.X. Qiao, T.Y. Xiong, Y.G. Zheng, Cavitation erosion and jet impingement erosion behavior of the NiTi coating produced by air plasma spraying, *Coatings* 8(10) (2018), Article 346.

<https://doi.org/10.3390/coatings8100346>

[318] J. Li, B. Wu, H.S. Chen, Formation and development of iridescent rings around cavitation erosion pits, *Tribology Letters* 52(3) (2013), pp. 495-500.

<https://doi.org/10.1007/s11249-013-0234-7>

[319] C. Harges, F. Pohl, A. Rottger, M. Thiele, W. Theisen, C. Esen, Cavitation erosion resistance of 316L austenitic steel processed by selective laser melting (SLM), *Additive Manufacturing* 29 (2019), Article 100786.

<https://doi.org/10.1016/j.addma.2019.100786>

[320] J. Pu, Y.B. Sun, L. Wu, P. He, W.M. Long, Effect of CeO₂ content on microstructure and properties of Ni-based tungsten carbide layer by plasma arc cladding, *Coatings* 12(3) (2022), pp. 11Article 342.

<https://doi.org/10.3390/coatings12030342>

[321] M.X. Li, S.H. Zhang, H.S. Li, Y.Z. He, J.H. Yoon, T.Y. Cho, Effect of nano-CeO₂ on cobalt-based alloy laser coatings, *Journal of Materials Processing Technology* 202(1-3) (2008), pp. 107-111.

<https://doi.org/10.1016/j.jimatprotec.2007.08.050>

[322] Y.S. Tian, C.Z. Chen, L.X. Chen, Q.H. Huo, Effect of RE oxides on the microstructure of the coatings fabricated on titanium alloys by laser alloying technique, *Scripta Materialia* 54(5) (2006), pp. 847-852.

<https://doi.org/10.1016/j.scriptamat.2005.11.011>

[323] D. Shu, S.C. Dai, G. Wang, W.D. Si, P. Xiao, X.X. Cui, X. Chen, Influence of CeO₂ content on WC morphology and mechanical properties of WC/Ni matrix composites coating prepared by laser in-situ synthesis method, *Journal of Materials Research and Technology* 9(5) (2020), pp. 11111-11120.

<https://doi.org/10.1016/j.jmrt.2020.07.104>

[324] C. Lee, H. Park, J. Yoo, C. Lee, W. Woo, S. Park, Residual stress

and crack initiation in laser clad composite layer with Co-based alloy and WC plus NiCr, *Applied Surface Science* 345 (2015), pp. 286-294.

<https://doi.org/10.1016/j.apsusc.2015.03.168>

[325] J.S. Xu, X.C. Zhang, F.Z. Xuan, F.Q. Tian, Z.D. Wang, S.T. Tu, Tensile properties and fracture behavior of laser clad WC/Ni composite coatings with different contents of WC particle studied by in-situ tensile testing, *Materials Science and Engineering a-Structural Materials Properties Microstructure and Processing* 560 (2013), pp. 744-751.

<https://doi.org/10.1016/j.msea.2012.10.028>

[326] U. Jansson, E. Lewin, Sputter deposition of transition-metal carbide films - A critical review from a chemical perspective, *Thin Solid Films* 536 (2013), pp. 1-24.


<https://doi.org/10.1016/j.tsf.2013.02.019>

Appendix A – Excerpt of the product specification sheet of Belzona®-2141

PRODUCT SPECIFICATION SHEET

BELZONA 2141

FN10051



BELZONA[®]

Repair • Protect • Improve

ABRASION

Taber
The Taber abrasion resistance when tested in accordance with ASTM D4060 with 1 kg load is typically:

H18 Wheels (Wet) at 70°F (21°C)	39 mm ³ loss per 1000 cycles
H18 Wheels (Dry) at 70°F (21°C)	50 mm ³ loss per 1000 cycles

HARDNESS

Shore A Hardness:
Tested in accordance with ASTM D2240 typical value will be: 87.

HEAT RESISTANCE

For many typical anti-cavitation applications the product is suitable for operation at temperatures up to 104°F (40°C).

For other dry applications the product is thermally stable up to 212°F (100°C).

ADHESION

90° Peel Adhesion
When tested in accordance with ASTM D429 (modified), typical adhesion value achieved when the material is used in conjunction with the designated surface will be:
Mild steel 180 pli (3214 kg/m)

Note
Belzona Elastomer Conditioner is required to achieve adhesion.

TEAR STRENGTH

Tear Strength
Tested in accordance with ASTM D624 is typically 380 pli. (6786 kg/m).

CAVITATION RESISTANCE

The cavitation resistance of the product, when tested to a modified version of ASTM G32, using an ultrasonic transducer vibrating at 20 kHz, typically shows the following results:

Wave Amplitude (µm)	Volume Loss (mm ³ /hr)
36	0.07
50	5.50

Please contact Belzona for additional testing details.

SHELF LIFE

Separate base and solidifier components shall have a shelf life of 3 years from date of manufacture when stored in their original unopened containers between 41°F (5°C) and 86°F (30°C).

ELONGATION & TENSILE PROPERTIES

Elongation
Tested in accordance with ASTM D412 (Die C) typical value will be: 530%.

Tensile Strength:
Tested in accordance with ASTM D412 (Die C) typical value will be: 2200 psi (15.2 MPa).

ENCAPSULATION IMMERSION RESISTANCE

Testing has demonstrated that **Belzona 2141** in conjunction with **Belzona 2941** and **Belzona 8411**, will prevent corrosion on steel substrates in immersed conditions and can be peeled back when maintenance or inspection is required.

Appendix B – Physical properties of the materials in this thesis

Table A1 – Physical properties of related materials in this thesis.

Name	Formular	Mol. wt.	Mp [°C]	ρ [g/cm ³]
Cerium(IV) oxide	CeO ₂	172.115	2480	7.216
Chromium	Cr	51.996	1907	7.15
Nickel	Ni	58.693	1455	8.90
Tungsten carbide	WC	195.85	2785	15.6

Data from *CRC Handbook of Chemistry and Physics* (the 97th Edition).

Appendix C – The CS-400 sample processed by focused ion beam

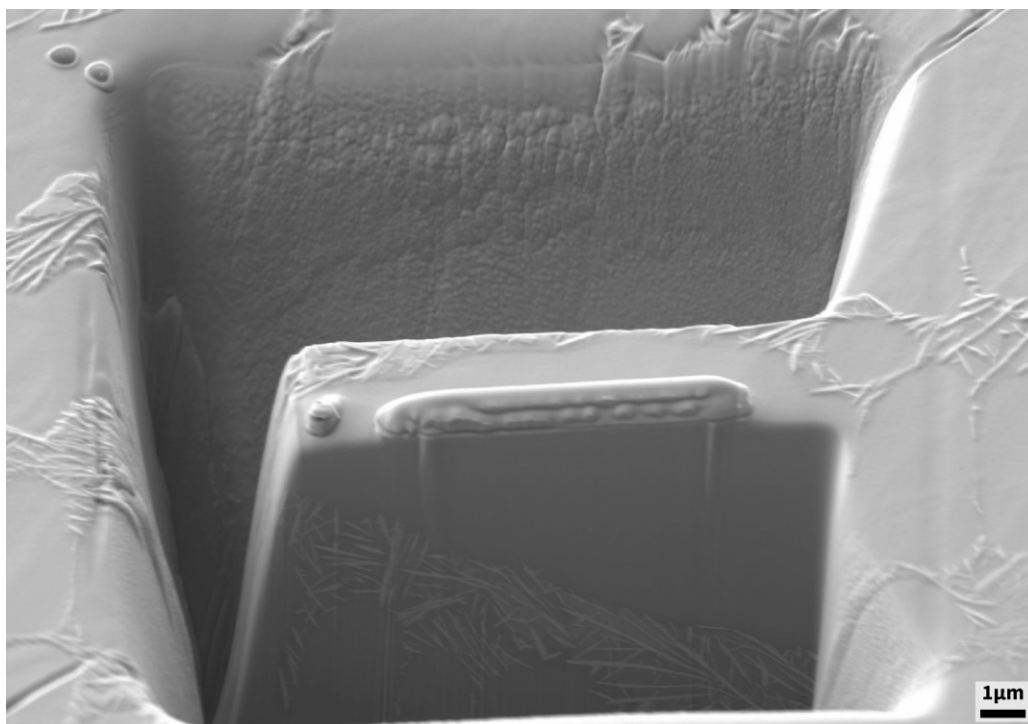


Fig. A1 – SEM image of the cross-section of the CS-400 sample being cut by focused ion beam. The probe of the focused ion beam was at 30 kV and 2 nA.

Appendix D – Cavitation erosion test on abalone shells

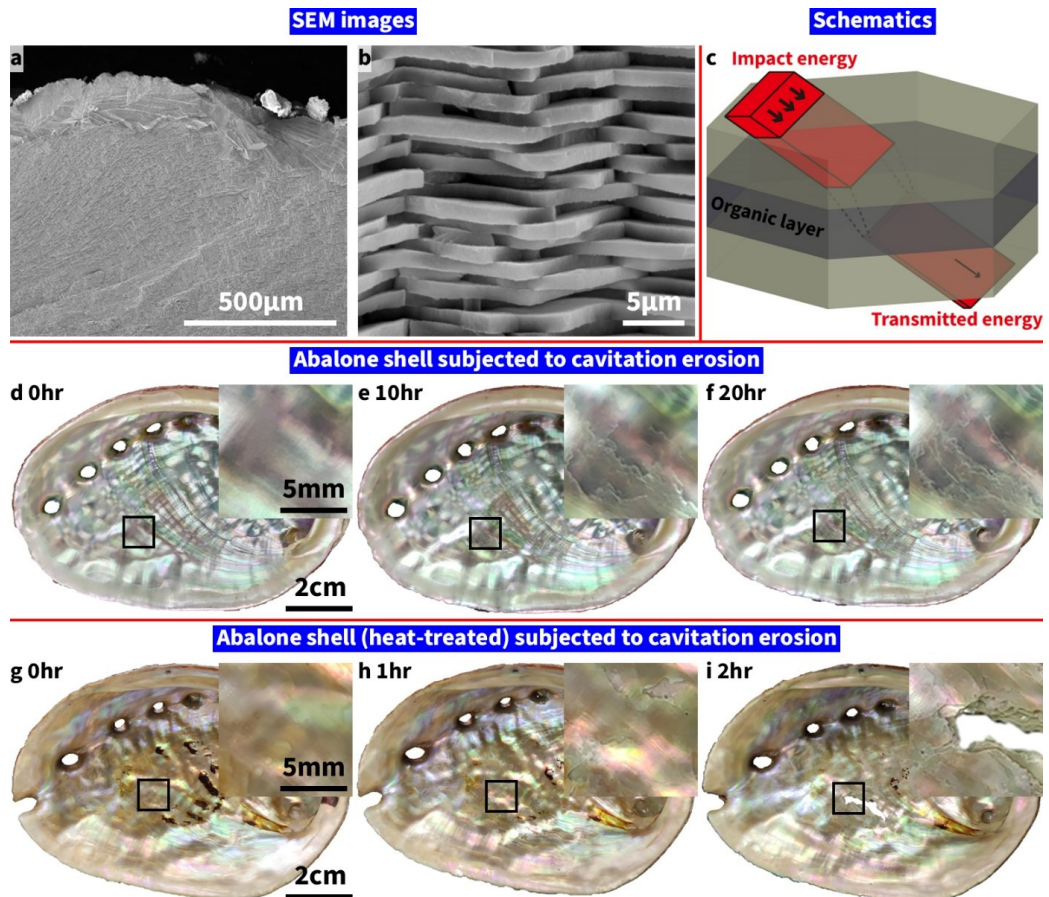


Fig. A2 – Cavitation erosion tests on abalone shells. a-b, SEM images showing the cross-section of the abalone shell. c, A schematic diagram showing the energy input to the shell is damped due to the sandwich structure. d-f, Images of the shell subjected to CE. The wear of the shell resulted from the limited stripping of the layers. The shell exposed to CE for 20 h did not exhibit any hole, implying that the shell had excellent resistance to CE. The SEM image of the cross-section of the abalone shell shows that it exhibits a highly ordered multiple sandwich structure. The energy applied to the structure could be dissipated among the layers of aragonite, which prevented the energy from transmitting to the deep layers. Thus, the abalone shell only took little damage when subjected to cavitation erosion. g-i, Images of the heat-treated shell (at 250 °C for 4 h) subjected to CE. The result shows that the resistance to CE of the heat-treated shell was significantly compromised. The heat-treated shell failed after 2 h and a large hole was observed due to the massive stripping of the aragonite layers. The organic materials in the shell were removed, resulting in a decrease in bonding strength. Thus, the strike of the cavitation impact could easily remove the aragonite layers, causing significant damage.

Appendix E – Ni-20/30vol.%Cr-WC MMCs treated by a 500-W laser

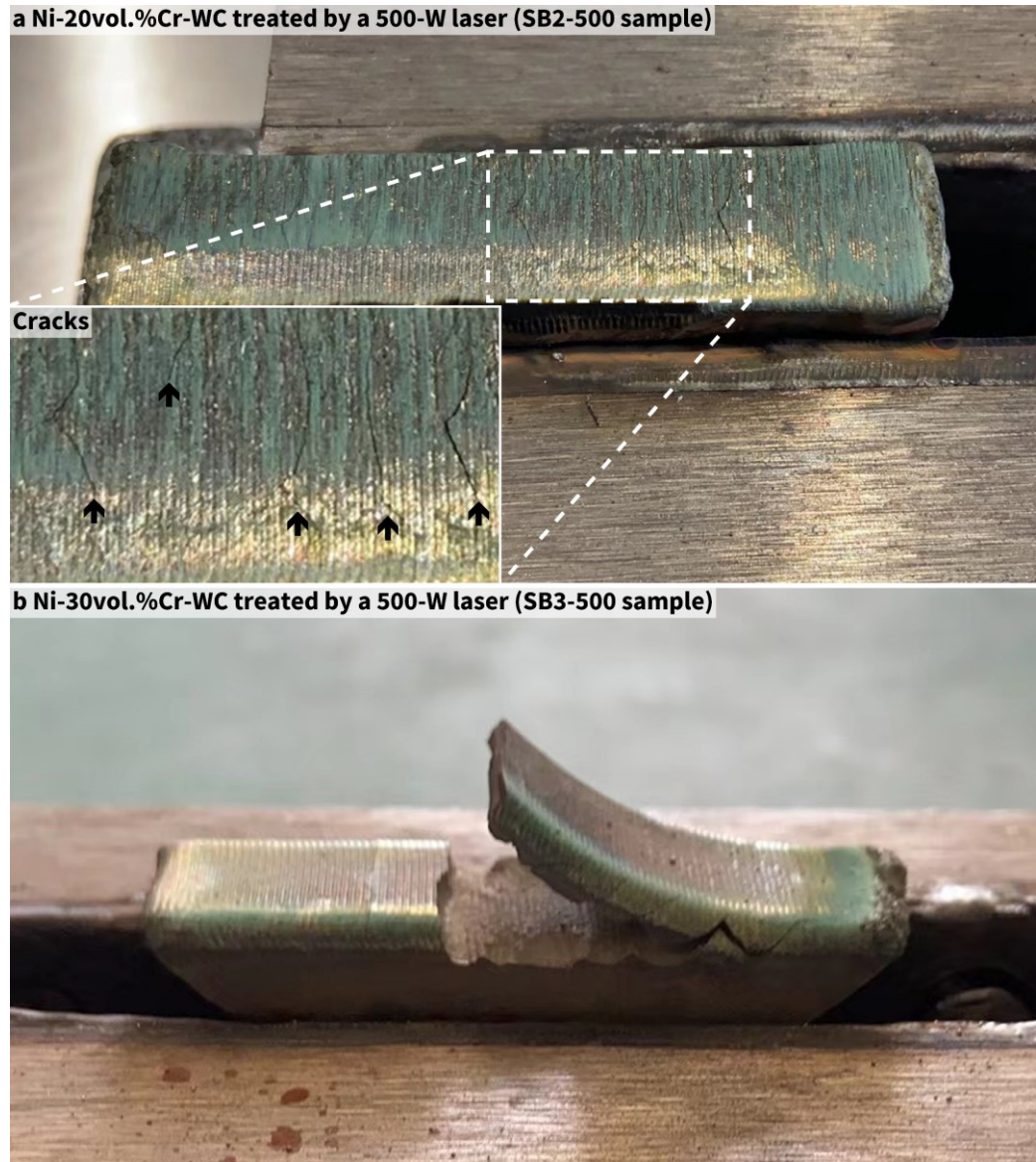


Fig. A3 – Photographs of the as-LSM Ni-20/30vol.%Cr-WC MMCs by a 500-W laser. a, Multiple cracks were found at the surface of the SB2-500 sample; b, A part of the laser-surface-melted layer of the SB3-500 sample was detached due to hot tearing.

Appendix F – Benchmarking the LSM MMCs against some engineering materials

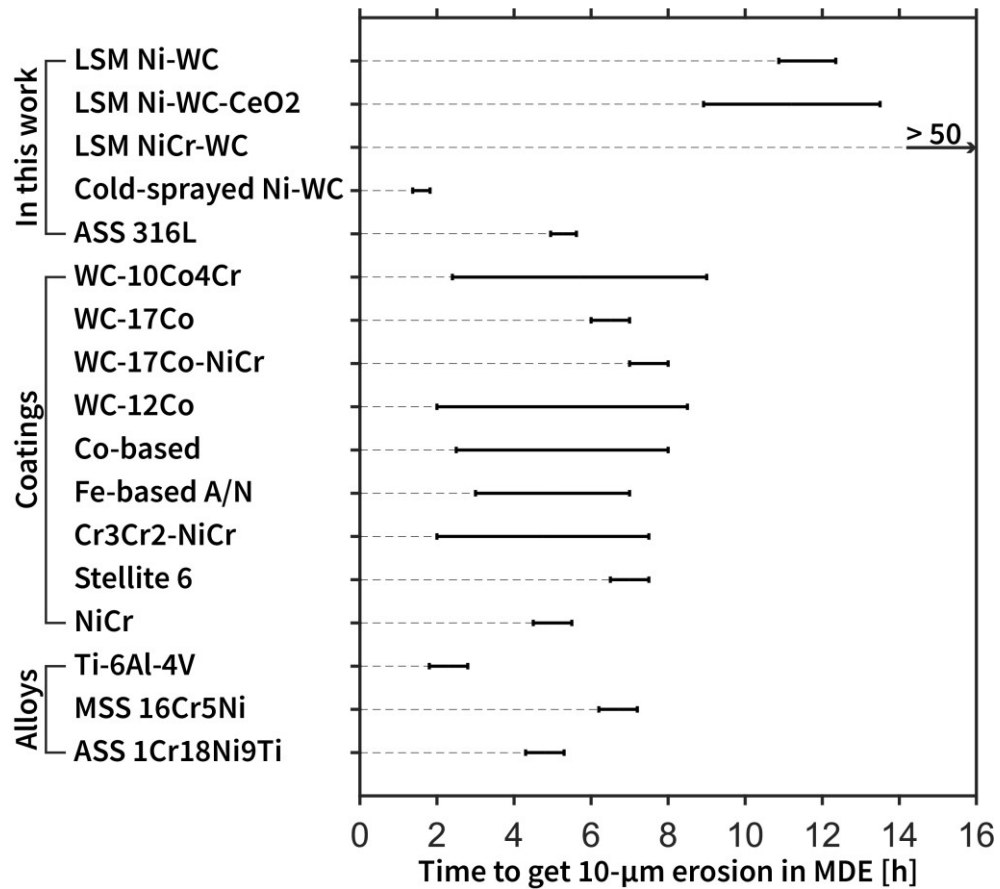


Fig. A4 – Benchmarking the LSM MMCs against other cavitation-erosion-resistant materials. This figure compares the LSM MMCs and the ASS 316L in this thesis with some common engineering CE-resistant materials. The horizontal axis shows how the time taken for the material to exhibit 10-µm erosion in MDE. The materials subjected to the CE test with similar parameters to this thesis were picked out. These materials include some coatings (WC-10Co4Cr [191, 194, 198, 208], WC-17Co [231], WC-17Co-NiCr [231], WC-12Co [191, 209], Co-based [289], Fe-based [230], Cr₃Cr₂-NiCr [67], Stellite 6 [159], and NiCr [231] coatings) and alloys (Ti-6Al-4V [231], 16Cr5Ni [31], and 1Cr18Ni9Ti [198]).